HIDRAULICA

HYDRAULICS-PNEUMATICS-TRIBOLOGY-ECOLOGY-SENSORICS-MECHATRONICS

2022

March

No. 1

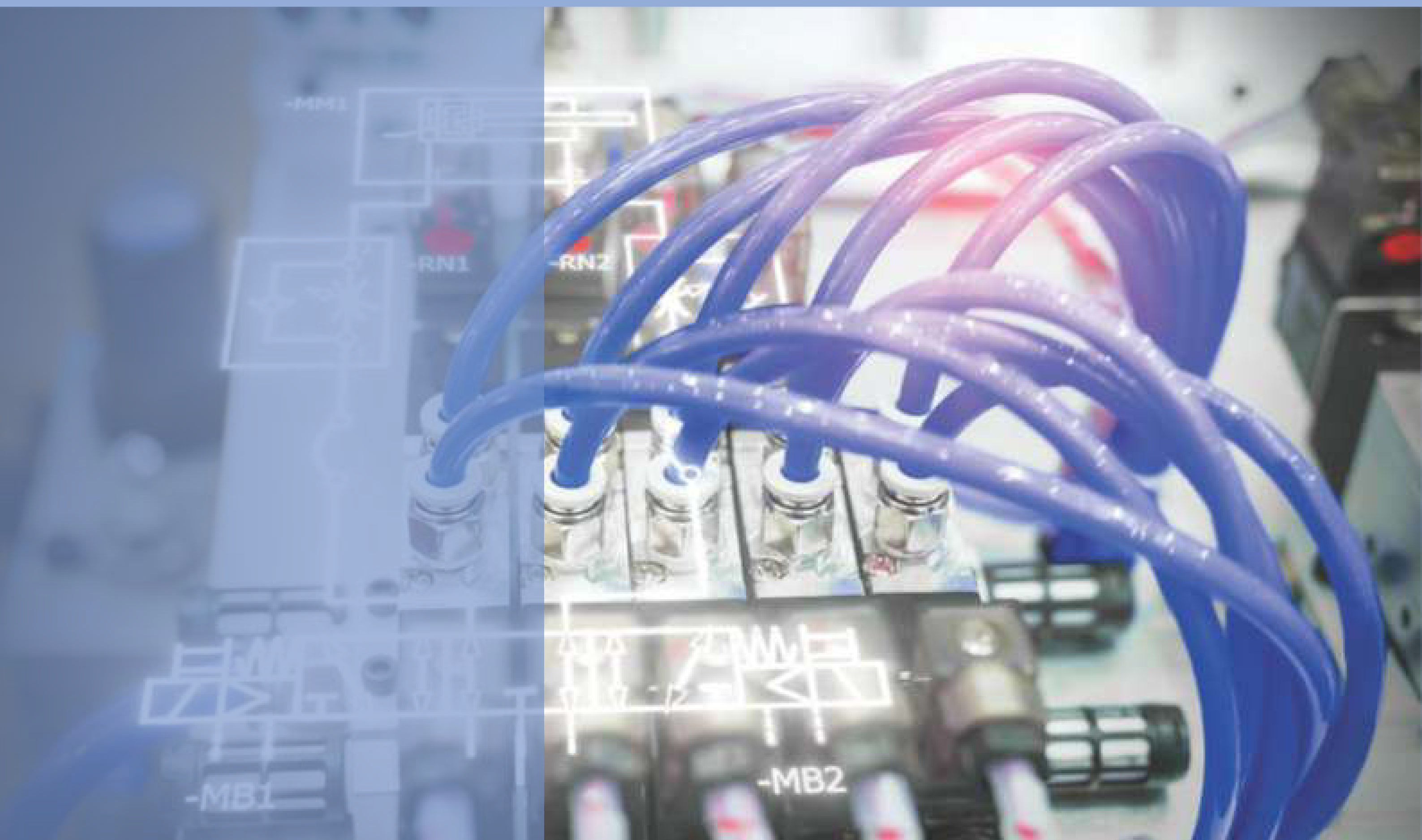

ISSN 1453 - 7303
ISSN-L 1453 - 7303

https://hidraulica.fluidas.ro

CONTENTS

Published by:
Hydraulics and Pneumatics Research Institute, Bucharest-Romania
Address: 14 Cuţitul de Argint, district 4, Bucharest, 040558, Romania
Phone: +40 21 336 39 91; Fax: +40 21 337 30 40; e-Mail: ihp@fluidas.ro; Web: www.ihp.ro
with support from:
National Professional Association of Hydraulics and Pneumatics in Romania - FLUIDAS
e-Mail: fluidas@fluidas.ro; Web: www.fluidas.ro

HIDRAULICA Magazine is indexed by international databases

ISSN 1453 – 7303; ISSN – L 1453 – 7303

EDITORIAL

Cercetarea hidraulică în vremuri dificile

Dr. Ing. Petrin DRUMEA
DIRECTOR PUBLICAȚIE

Cercetarea științifică, inclusiv cercetarea în hidraulică, din țara noastră este într-un declin permanent de câțiva ani, nu doar începând cu perioadele pandemiei sau cu conflictele grave din zonele apropiate. Declinul cercetării din România a început cu reducerea treptată a fondurilor alocate, cu reducerea numărului de cercetători și specialiști, dar și cu reducerea fondurilor pentru dotări.

Unitățile sau grupele de cercetare din institute, universități sau firme au funcționat și în ultimul timp, chiar dacă au existat și perioade de activitate on-line. Părțile de concepție și analiză au fost realizate și de acasă, acestea fiind activități individuale și care au nevoie de liniște și concentrare, în timp ce părțile de execuție și cele de experiment, care au nevoie de prezența fizică în baze de producție și în laboratoare, s-au derulat doar cu prezența fizică și cu respectarea precauțiilor indicate de specialiști. Din aceste motive, activitățile de cercetare nu au fost împiedicate vizibil de restricțiile pandemiei.

Și cu toate acestea, necazurile pandemiei și ale războiului au influențat masiv domeniul cercetării. Cum? Simplu! Prin reducerea cererilor industriei și ale altor domenii economice adresate unităților de cercetare. Pe lângă reducerile determinate de încetinirea activităților economice, au existat și există și reduceri cauzate de incompetența unor coordonatori ai domeniului. Sunt curios dacă aceste persoane înțeleg cum acționează ei asupra moralului lucrătorilor din cercetare și asupra menținerii și dezvoltării domeniului prin acțiunile lor ciudate, uneori chiar periculoase.

Cercetarea în domeniul hidraulicii, în România, mai dispune doar de câteva centre, dar foarte puține dispun de laboratoare funcționale. Cercetarea fără laborator și fără execuție nu reprezintă nimic, sau poate doar o variantă de a mima adevăratul proces. Deci, să repornim sau, în multe cazuri, să pornim activitatea laboratoarelor!

Cred că în domeniul cercetării, mai rău decât orice, este că prea mulți nepricepuți iau decizii în locul adevăraților specialiști. Adesea ne învață să brevetăm personaje care au cel mult o singură cerere de brevet, sau să facem cercetare științifică personaje care au lucrat oriunde, dar nu în zone specializate în cercetare, iar, mai nou, cum să facem digitalizare fără ca aceste personaje să înțeleagă sensul conceptului. În aceste condiții, nu mai e de mirare că numărul specialiștilor scade, iar rezultatele aplicate în economie se reduc la puține procente. A început să fie greu doar să înțelegem noutățile din domeniu, cu atât mai puțin reușim să lucrăm cu ele. Și, totuși, încă există șanse de redresare; altfel, o să mai adăugăm un domeniu despre care o să vorbim la trecut!

EDITORIAL

Hydraulic research during hard times

Ph.D.Eng. Petrin DRUMEA
MANAGING EDITOR

Scientific research, including research in hydraulics, in our country has been in a permanent decline for several years, not only since the pandemic periods or since the serious conflicts in nearby areas. The decline of research in Romania began with the gradual reduction of the allocated funds, with the reduction of the number of researchers and specialists, but also with the reduction of the funds for research infrastructure.

Research units or groups in institutes, universities or companies have continued to carry out their activity in these latter days, even though there have been periods of online activity, too. The design and analysis parts were also done from remote, these being individual activities that require tranquillity and concentration, while the execution parts and the experimental parts, which require in situ activity in shop floors and laboratories, were carried out only with the physical presence and with the observance of the precautions indicated by the specialists. For this reason, research activities have not been visibly hampered by pandemic restrictions.

Yet the plagues of the pandemic and the war have had a profound effect on research. How? Easy! By reducing the demands of industry and other economic areas addressed to the research units. In addition to the reductions caused by slowed-down economic activities, there have been - and still are - reductions caused by the incompetence of some coordinators in the field. I am curious if these people understand how they act on the morale of research workers and on maintaining and developing the field through their strange, sometimes even dangerous, actions.

Research in the field of hydraulics, in Romania, has only a few centers left, and very few of them have functional laboratories. Research without a laboratory and without physical development is nothing, or maybe just a way to mimic the real process. So, let's restart, or in many cases start from scratch, the activity in laboratories!

I think that in the field of research, worse than anything, is that too many inexperienced people make decisions instead of real specialists. We are often taught how to patent ideas by fellows who have filed at most one patent application, or how to conduct scientific research by fellows who have worked anywhere else but not in specialized areas of research, or, more recently, how to implement the digitalization while these fellows do not even understand the meaning of the concept. Under these conditions, it is no wonder that the number of specialists is decreasing, and the research results applied in the economy are reduced to a few percentage points. For many it is beginning to be difficult even to understand the news in the field, even less we manage to work with them. Yet, there are still chances for recovery; otherwise, we will add another area that we will talk about in the past tense!

ISSN 1453 – 7303 **“HIDRAULICA” (No. 1/2022)**
Magazine *of Hydraulics, Pneumatics, Tribology, Ecology, Sensorics, Mechatronics*

Experimental Research on a Savonius Helical Turbine with Integrated Transparent PV Cells

Assoc. Prof. PhD eng. **Sanda BUDEA**[1,*], Lecturer PhD eng. **Ștefan-Mugur SIMIONESCU**[1], Eng. **Octavian LAMBESCU**[1]

[1] University Politehnica of Bucharest, Romania, Energy Engineering Faculty; Department of Hydraulics, Hydraulic Machinery and Environmental Engineering

* Corresponding author’s e-mail address: sanda.budea@upb.ro; s.simionescu@upb.ro

Abstract: *Starting from the observation that the hybrid wind-solar systems are perfectly complementary both during a day and during a year, an experimental facility was designed and built, consisting of a Savonius wind turbine with helical blades, covered with thin, transparent film of flexible photovoltaic cells. The experimental results show a power coefficient of 0.265 for the Savonius helical rotor and operation starting from wind velocity of 0.65 m/s. This facility can produce energy from two sources, wind and sun, and even more, it ensures the cooling of the photovoltaic panel, which leads to better energy efficiency. The passive air cooling of the photovoltaic panel can achieve a reduction of its temperature by 10°C. When using the active cooling – resulting from the rotation of the Savonius rotor – a cooling with up to 40°C can be obtained. Regarding the efficiency of the photovoltaic panel, an improvement by 10-12% as effect of the cooling is recorded. The electrical energy obtained from the photovoltaic panel placed on the blades can ensure the wind propeller movement at lower wind velocities – it can give the propeller the impulse necessary to overcome the inertia, before entering the nominal working regime. The total power of this small hybrid system with D = 0.456 m, ranges between 20 ÷ 60 W.*

Keywords: *Savonius helical; wind turbine; flow spectrum; photovoltaic cells*

1. Introduction

Closely related to the concept of sustainable development and correlated with the express requirement to use energy from renewable sources, this project proposes the creation of a hybrid, innovative facility for capturing energy from wind and solar sources and converting it to electricity.
The facility consists of a small wind turbine, with vertical shaft and helical profiled blades, covered with a thin film of photovoltaic (PV) cells, on the principle 2 in 1 (wind and sun in one element).
Compared to the separate use of the two energy sources, the proposed system ensures a higher efficiency of the wind turbine by profiling the blade, estimating a power coefficient of 0.25 ÷ 0.3 and starting at low wind velocities, below 1 m/s. At the same time, a good efficiency is ensured to the photovoltaic source, through active air ventilation, which leads to superior performance.
The Savonius type vertical axis wind turbine was chosen for its advantages: simple construction, low tower height, no need for wind direction orientation and for defeating inertia very easily. The innovative idea was to cover the blades with photovoltaic cells and ensure a convenient exposure to the sun. The article presents the capture of wind and solar energy by designing the wind turbine blade, profiled-helical, slightly twisted, and wide enough to ensure a surface corresponding to the photovoltaic source.
The advantages of such a compact hybrid facility are:

- using the 2 wind and sun sources in one element;
- more uniform energy generation, more uniform distribution in winter and summer, the complementarity of the two solutions resulting from figure 1;
- the vertical wind turbine operates regardless of the wind direction;
- the turbine tower is much smaller compared to the horizontal variants;
- the turbine starts from low wind velocities;
- the hybrid facility uses a system of photovoltaic cells with parallel connections, to minimize losses;
- the surface required for the location of the hybrid solar wind facility is much smaller than in the case of separate use of the two components;

- the costs of energy obtained in hybrid systems are slightly higher than those of wind energy, but significantly lower than those obtained only from photovoltaics.

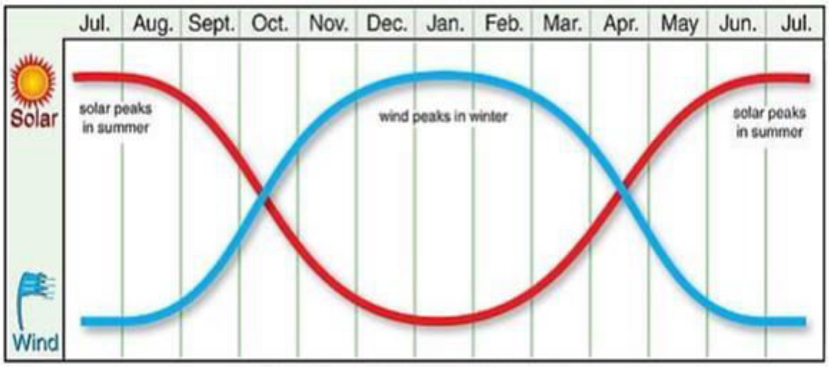

Fig. 1. Solar output peaks in summer and wind output peaks in winter

2. Experimental Set-up

Savonius wind turbines have many advantages, including a high value of starting torque, a simple design and the ability to operate regardless of wind direction, although they have low aerodynamic efficiency.
Savonius type vertical shaft wind turbines have been studied in terms of geometry and shape by Keum Soo Jeon [1], Akwa [2]. "Savonius rotor performance is affected by operational conditions, geometric and air flow parameters. Maximum averaged power coefficient includes values around 0.05 ÷ 0.30", [2]. In [3] Kacprzak et al. examine three cross-sections: classic, bach-type and elliptical. Power coefficients, torque coefficients and torque variation with the angle of incidence are also determined. Kumar et.al. [4] propose a hybrid design between Darrieus and Savonius turbines and test the prototypes with asymmetrical profile SH3055 and symmetrical NACA 0018. Helical Savonius Turbine with different blade type semi-circular (U), elliptical (S), and banesh (L) are tested in [5] by Wijianti and Saparin. Their tests show an influence of the blade design to the turbine performances: S type wind turbine rotors have a higher rotational speed than the ones of type L. Sobczak et al. [6] show the results from a set of numerical investigations on a Savonius turbine with deformable blades and found power coefficients exceeding 0.30.

2.1 Wind turbine design

Mendoza et al. in [7] investigated partial twisted blades for Savonius blades and Debnath et al. in [8] proposed a Savonius helical wind rotor for wind turbines with twist angles of 90º and 180º and investigated the effects of geometric parameters such as the overlap ratio, the effect of the twist angle on the turbine characteristics. Savonius wind turbines with helical blades have a positive static torque for all rotor angles and better performance than conventional Savonius wind turbines.
The following models are considered in the design/profiling of vertical axis wind turbine (VAWT) blades:
a) CFD aerodynamic modelling in order to obtain the optimal blade profile, a method approached more and more often lately;
b) Maximum momentum / torque theory (Blade Element Momentum BEM).
From aerodynamic modelling and analysis of multiple construction solutions, the vertical wind rotor must have minimum torque at low speed, to start easily (Savonius type) and high torque at high speed, to ensure driving force and extract the maximum power from the wind. However, for good aerodynamic performance, the blade must have a convenient profiling – for the present study, a helical profile was chosen, by correlating the two forces – lift and drag, and with a good power coefficient at higher wind velocities.
The velocity distribution on the Savonius helical rotor, with two and three blades [8], was analysed for different specific twisting angles. Static velocity and pressure distributions were obtained at rotor angles of 30°, 90° and 180° as shown in figures 2, 3 and 4 (results from CFD simulations [8]).

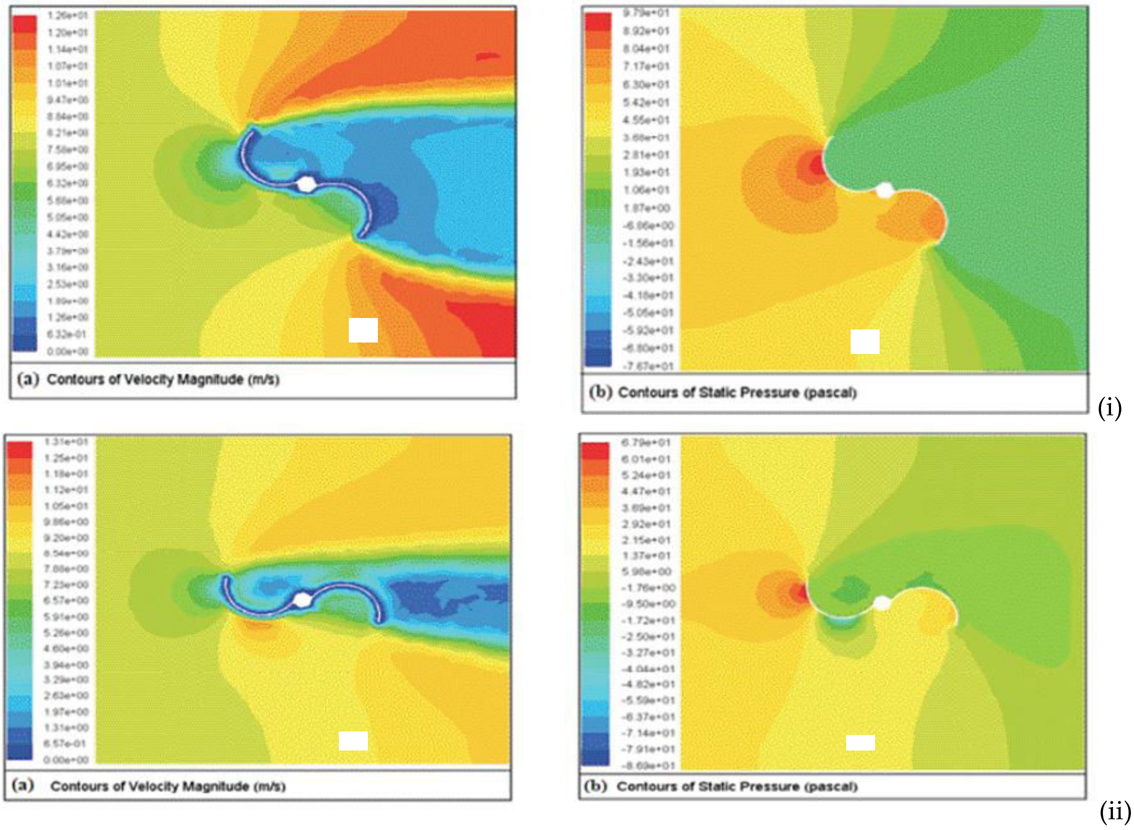

Fig. 2. Velocity and pressure distributions on the rotor, at rotor angles of 30° (i) and 90° (ii) [8]

Debnath's conclusions [8] were: the 2-blade rotor ensures a better power coefficient; the twisting of the helical blades with 180° ensures maximum torque.
The power coefficient (C_p) and the torque coefficient (C_t) can be calculated using the following equations:

- the power coefficient of any rotor can be expressed as: $C_p = \frac{P_{rotor}}{P_{max}}$; (1)
- the effective turbine power P_t can be expressed as: $P_t = \frac{1}{2}\rho A\left({V_1}^2 - {V_2}^2\right)R\omega$, (2)
  where V_1 and V_2 are the wind velocities upstream and downstream of the turbine rotor;
- P_{max} is the useful power extracted from the wind, given by the relation: $P_{max} = \frac{1}{2}\rho A\mathrm{v}^3$; (3)
- the power coefficient is: $C_p = \frac{\frac{1}{2}\rho A({V_1}^2 - {V_2}^2)R\omega}{\frac{1}{2}\rho AV^3}$; (4)
- the TSR or the wind rotor speed ratio is given by: $\lambda = \frac{u}{V} = \frac{R\omega}{V} = \frac{\pi Dn}{60\,v}$; (5)
- the torque coefficient of the rotor is: $C_t = \frac{C_p}{\lambda}$. (6)

The dimensions of the wind turbine are H = 0.8 m and D = 0.456 m. Figure 3 presents a picture of the wind turbine and a detail with the stiffening profiles of the blades. The twist between the four stiffening profiles is 180°. The low weight of the turbine and the well-executed mechanical parts ensure an overcoming of the rotor inertia at wind velocities of 0.65 m/s.

The working hypotheses and characteristics of the wind turbine were calculated as follows:

- wind velocity upstream the rotor: V = 5 m/s;
- turbine mass: m_t = 2.498 kg (consisting of blades with photovoltaic collector, shaft and bearing);
- theoretical power of the wind turbine: $P = \frac{\rho}{2}A\mathrm{v}^3$ = 27.81 W; (7)

- maximum force: $F_{max} = \frac{\rho}{2} v^2 DH$ = 22.78 N; (8)
- pressure and pressure force: p = 165.4 Pa, F_p = 74.43 N;
- torque: $M_t = mgR$ = 5.58 N·m. (9)

a)

b)
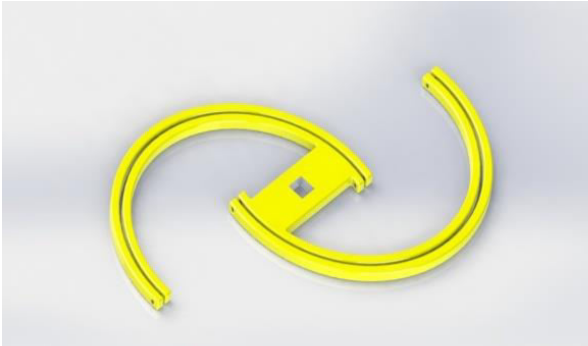

Fig. 3. Picture of the Savonius wind turbine (a) and detail with the stiffening profiles of the blades (b)

2.2. The Photovoltaic System

The innovative solution consists in the fact that the helical blades of the Savonius turbine are made of thin, flexible film of photovoltaic panel. A number of state-of-the-art technologies have led to the successful development and testing of various photovoltaic cell variants [9], [16]. Fluoropolymer-coated solar cells (a transparent film) [10] capture sunlight from any angle and can be applied to curved surfaces, making it possible to completely cover the curved blades of the wind turbine with solar cells. Tandem Semi-transparent Perovskite technology [11] ensures an efficiency of approximately 12.7%. Such a panel was tested in the Renewable Sources of Energy laboratory of the Hydraulics Department – University Politehnica of Bucharest within the current study.

The characteristics and structure of the photovoltaic panel are shown in Table 1, Figure 4 and Figure 5.

Table 1: Electrical characteristics of the flexible photovoltaic panel FWAVE 92W [16]

1000 W/m², 25°C		
Maximum output power	100	W
Maximum operating voltage	319	V
Intensity	0.313	A
Open circuit voltage	429	V
Short circuit	0.390	A
800 W/m², 25°C		
Maximum output power	80	W
Maximum operating voltage	298	V
Intensity	0.235	A
Open circuit voltage	393	V
Short circuit	0.317	A

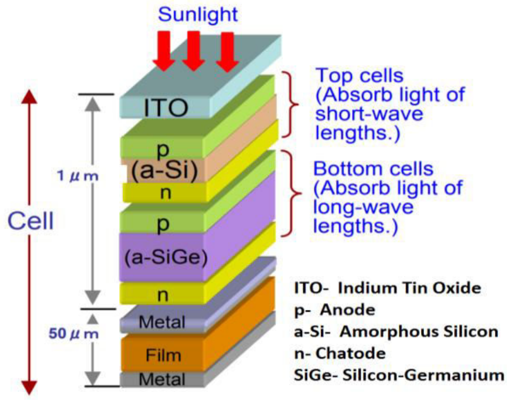

Fig. 4. The structure of the photovoltaic panel FWAVE 92W [16]

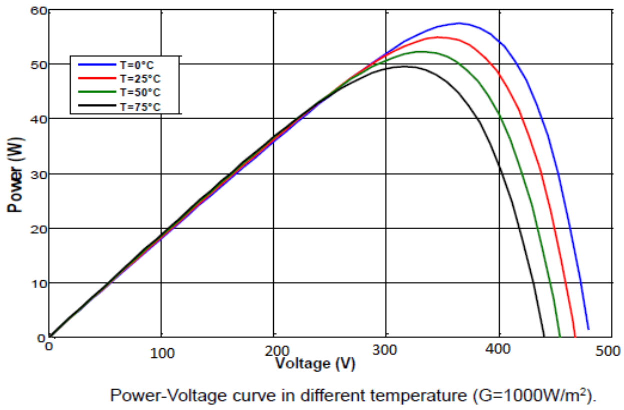

Fig. 5. Characteristic curves of the 92W flexible photovoltaic panel [16]

From the design data of the Savonius turbine, a sun exposure surface of the panel of 0.365 m^2 can be ensured with the two blades, so that at a maximum solar radiation of 1000 W/m^2 a power of 16.79W can be obtained. If the effect of active cooling is considered, a final power of up to 19W was obtained.

For photovoltaic panels to have good efficiencies, they must meet two conditions: their contact surface with incident sunlight must be clean; the temperature must be as low as possible.

A better option would be a transparent solar panel, so that there are no shading areas, with the disadvantage that these technologies still have low efficiencies, below 13% [11]. A two-sided (bifacial) solar panel [12] would be another option.

The cooling methods of photovoltaic solar panels are: air/wind cooling, ice cooling, water cooling or cold water vapor. Research has shown that the most efficient would be ice cooling [13], which can increase the energy efficiency by up to 60% [13].

When cooling the photovoltaic panel with air, previous studies have shown that the efficiency can be improved by 12 – 18%. Kaldellis et al. have found that the efficiency (or power) temperature coefficient increases between 0.30%/°C and 0.45%/°C when the temperature decreases [14].

3. Results

3.1. Operating characteristics

The operating characteristics of this wind turbine are represented graphically in Figure 6. Measurements were made up to wind velocities of 4.5 m/s, the values above this velocity resulted by polynomial extrapolation.

The measurements showed that the rotor overcomes inertia and rotates uniformly at velocities below 1 m/s, more precisely 0.65 m/s.

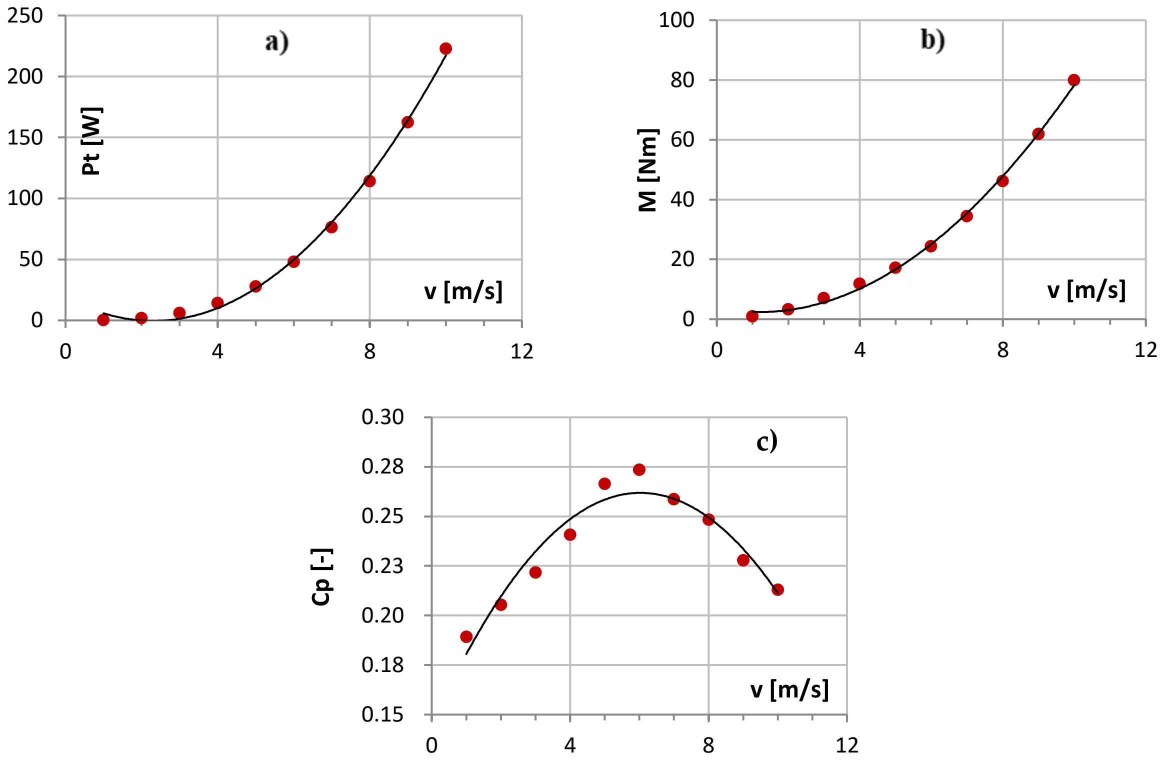

Fig. 6. Power (a), torque (b) and power coefficient (c) of the wind turbine

3.2. Visualization of the flow spectrum on the Savonius helical rotor

The air flow around the Savonius rotor was experimentally visualized using a smoke generator and a plane laser, and pictures were taken with a video camera. Images were obtained for two different rotational speeds of the turbine shaft, resulting from wind velocities of 3 m/s and 4.5 m/s respectivelly, as it can be seen in Fig. 7. An extensive study on this subject is presented in [15].

Fig. 7. Flow spectrum for wind velocity of 3 m/s (a) and 4.5 m/s (b)

3.3. Cooling efficiency

Using passive cooling with air of the photovoltaic panel, a reduction of its temperature by only 10° C can be obtained; by using active cooling, resulting from the rotation of the Savonius rotor, a cooling by over 40°C can be obtained for high wind velocity. The efficiency can increase by 12%, so for panels with an efficiency of 18%, by cooling it can exceed 20%, and for transparent or 2-sided panels with an efficiency of 9% it can reach 10.6%. This has the effect of producing additional electricity.

The effect of cooling the photovoltaic panel at different wind velocities was studied. If the effect of active cooling of the photovoltaic panel is considered, which increases by a maximum of 12% the efficiency of the panel, a final power resulting from the sun of 19 W can be obtained. This adds to the 19.95 ÷ 44.33 W generated by wind energy, which leads to a promising result for such a hybrid system, over to 60 W.

4. Conclusions

In this article, the authors propose a hybrid solar wind system in an innovative solution of Savonius wind turbine with helical blades, covered with thin film of photovoltaic panel.
Experiments were made on the wind turbine and a small twisting moment was obtained at wind velocity of 0.65 m/s. The operating characteristics of the wind turbine proposed in the article were outlined. The paper also includes the visualization of the flow spectrum for two wind speeds, confirmed by numerical studies from the literature.
The effect of cooling the flexible photovoltaic panel was checked. The total power of the hybrid system was between 20 ÷ 60 W.

Conflicts of Interest: The authors declare no conflict of interest.

References

[1] SooJeon, K., J. IkJeong, J.K. Pan, and K.W. Ryu. "Effects of end plates with various shapes and sizes on helical Savonius wind turbines." *Renewable Energy* 79*,* (July 2015): 167-176.
[2] Akwa, J.V., H.A. Vielmo, and A. Prisco Petry. "A review on the performance of Savonius wind turbines." *Renewable and Sustainable Energy Reviews* 16, no. 5 (2012): 3054-3064.
[3] Kacprzak, K., G. Liskiewicz, and K. Sobczak. "Numerical investigation of conventional and modified Savonius wind turbines." *Renewable Energy* 60 (December 2013): 578-585.
[4] Kumar, P.M., S. Anbazhagan, N. Srikanth, and T.C. Lim. "Optimization, design, and construction of field test prototypes of adaptive hybrid Darrieus turbine." *J Fundam Renewable Energy Appl* 7, no. 6 (2017): 1000245.
[5] Wijianti, E.S., and S. Saparin. "The effect of blade type variations on Savonius wind turbine performance." *IOP Conf. Series: Earth and Environmental Science* 353 (2019): 012015.
[6] Sobczak, K., D. Obidowski, P. Reorowicz, and E. Marchewka. "Numerical Investigations of the Savonius turbine with deformable blades." *Energies* 13, no. 14 (2020): 3717.
[7] Mendoza, V., E. Katsidoniotaki, and H. Bernhoff. "Numerical study of a novel concept for manufacturing Savonius turbines with twisted blades." *Energies* 13, no. 8 (2020): 1874.
[8] Debnath, P., R. Gupta, and K.M. Pandey. "Performance analysis of the helical Savonius rotor using computational fluid dynamics." *ISESCO Journal of Science and Technology* 10, no. 18 (2014): 17-28.
[9] Husain, A., W.Z. Hasan, S. Shafie, M. Hamidon, and S.S. Pandey. "A review of transparent solar photovoltaic technologies." *Renewable and Sustainable Energy Reviews* 94 (October 2018): 779-791.
[10] Ito, Seigo, Peter Chen, Pascal Comte, Mohammad Khaja Nazeeruddin, Paul Liska, Péter Péchy, and Michael Grätzel. "Fabrication of screen-printing pastes from TiO_2 powders for dye-sensitised solar cells." *Progress in Photovoltaics: Research and Applications* 15, no. 7 (November 2007): 603-612.
[11] Bailie, C.D., M.G. Christoforo, J.P. Mailoa, A.R. Bowring, E.L. Unger, W.H. Nguyen, et al. "Semi-transparent perovskite solar cells for tandems with silicon and CIGS." *Energy Environ Sci* 8, no. 3 (2015): 956–963.
[12] Guerrero-Lemus, R., R. Vega, K. Taehyeon, A. Kimm, and L.E. Shephard. "Bifacial solarphotovoltaics – A technology review." *Renewable and Sustainable Energy Reviews* 60 (July 2016): 1533-1549.
[13] Peng, Z., M.R. Herfatmanesh, and Y. Liu. "Cooled solar PV panels for output energy efficiency optimization." *Energy Conversion and Management* 150 (2017): 949-955.
[14] Kaldellis, J.K., M. Kapsali, and K. Kavadias. "Temperature and wind speed impact on the efficiency of P.V. installations. Experience obtained from outdoor measurements in Greece." *Renew. Energy* 66 (2014): 612–624.
[15] Ciocănea, Adrian, Sanda Budea, Ştefan Mugur Simionescu, and Octavian Lambescu. "Experimental research on increasing the static torque for a small Savonius rotor of helical type." *IOP Conference Series: Earth and Environmental Science*, *664* (2021): 012033.
[16] Fuji electric. Accessed October 15, 2021. https://www.fujielectric.com/?ui_medium=jp_glnavi.

Synchronization of the Travel of Hydraulic Cylinders. Modeling and Simulation

Prof. PhD Eng. **Anca BUCUREȘTEANU**[1*]

[1] University POLITEHNICA of Bucharest

* ancabucuresteanu@gmail.com

Abstract: *In this paper, the authors present the theoretical research and simulations performed for establishing some variants of hydraulic drive for the units that require two or more cylinders. Two simple and affordable methods that do not entail special expenses are shown comparatively. The solutions can be applied for systems that do not require very precise positioning, but which must have a good repeatability.*

Keywords: *Hydraulic cylinders, synchronous travel*

1. Introduction. Need for Synchronization

Let us consider the actuation diagram in Figure 1.

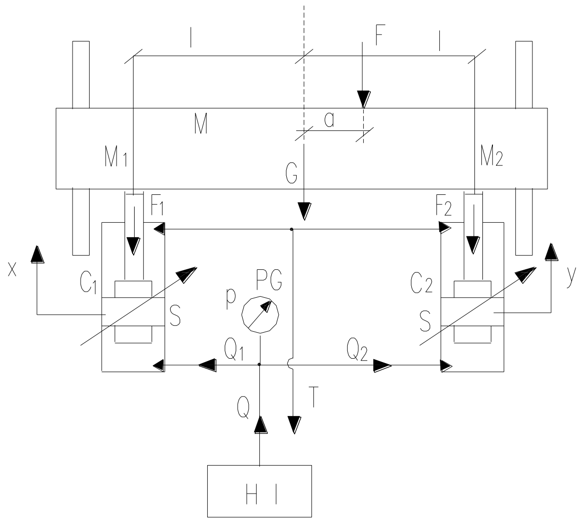

Fig. 1. Simplified hydraulic diagram of a system with two synchronized cylinders

Cylinders C_1 and C_2 – with the distance 2 *l* between them - lift a load of mass *M* and a weight *G*. The load travels on two vertical guideways against a force *F* positioned at a distance *a* related to the axis of symmetry. The cylinders are of the same type but, even in this case, there are inherent differences between them: different coefficients of friction at the rod and piston, different values of the flow losses coefficients proportional to pressure (a_1 and a_2) and of the coefficients of force loss proportional to speed (b_1 and b_2) [1, 2, 3].

Initially the cylinders are in lower position. The hydraulic unit (HI) transmits a flow *Q* to the lower surfaces *S* of the two cylinders. The pressure provided by the source has the common value *p*, visualized by means of the pressure gauge PG [4]. The specific forces F_1 and F_2 and masses M_1 and M_2 correspond to the cylinders C_1 and C_2. The positions of the cylinders C_1 and C_2 are defined by the dimension *x* and *y*, respectively [1, 3, 5, 6]. When the cylinders go upwards, it is necessary to meet at all times the condition:

$$|x - y| < \varepsilon \tag{1}$$

In the relation (1), the allowable difference of size was noted by ε. During the lifting, the oil behind the two pistons passes freely to the tank T.
The hydraulic unit is supplied by a classic pressure source consisting of a constant flow rate pump and a pressure valve [4].
Under these conditions, the mathematical model of this system is:

$$F_1 = \frac{l(F+G)-Fa}{2l} \tag{2}$$

$$F_2 = \frac{l(F+G)+Fa}{2l} \tag{3}$$

$$Q_1 + Q_2 = Q \tag{4}$$

$$Q_1 = S\frac{dx}{dt} + a_1 p_1 + \frac{V_0 + xS}{E}\frac{dp_1}{dt} \tag{5}$$

$$Q_2 = S\frac{dy}{dt} + a_2 p_2 + \frac{V_0 + yS}{E}\frac{dp_2}{dt} \tag{6}$$

$$M_1\frac{d^2x}{dt^2} + b_1\frac{dx}{dt} + F_1 + F_{F1} = p_1 S \tag{7}$$

$$M_2\frac{d^2y}{dt^2} + b_2\frac{dy}{dt} + F_{12} + F_{F2} = p_2 S \tag{8}$$

In the relations (2) - (8) it was also noted: t – time; F_{F1} and F_{F2} – the reduced total friction forces at each cylinder; V_0 - the initial volume of liquid in the circuit of each cylinder; E – the modulus of elasticity of the oil; p_1 and p_2 - instantaneous pressures on the S surfaces of the cylinders C_1 and C_2.
The synchronous travel in terms of position is ensured by the condition specified in the relation (1). As soon as both cylinders reach the maximum upper position, the lowering command can be given. In this case, the mathematical model is similar to the one shown above.
These mathematical models can be extended to more cylinders. High accuracy synchronization involves the use of expensive equipment, servo or proportional type and of position transducers (resistive, inductive, optical ones etc.) [4]. The subject of this article refers to the less accurate synchronized systems, such as the ones for auxiliary kinematic chains of the machine tools [4]. These ones use the classic equipment and do not require position transducers.
In order to study the different variants of actuation, a real case was taken into consideration: the protective guard of the working area of a vertical lathe [7]. The up and down movement of this protective guard is actuated by two cylinders. The cylinders have the working surface S = 12.56 cm^2 (diameter of 40 mm), stroke c = 900 mm, M_1 = 100 Kg, M_2 = 150Kg, F_1 = 60 daN, F_2 = 80 daN. The pressure valve is set to p = 20 bar and the pump supplies a flow of Q_P = 9 l/min. In static conditions, the pressures necessary for the two cylinders are: p_1 = 12.73 bar and p_2 = 18.31 bar. It can be noticed that these values are lower than the value set at the pressure valve. In this case, the time required to achieve the complete stroke at both cylinders is:

$$t = \frac{2Sc}{Q_P} \tag{9}$$

Making the substitutions in the relation (9) one can get t = 15 s.
In order to observe the behavior of this system in dynamic conditions, specific simulation programs were used [8].
Figure 2 shows the results of this simulation.
The lifting command was given 10 s after starting the pump. The total lifting time is about 18 s. Therefore, the lifting time resulted from the static calculation is exceeded by 3 s. In the studied case, this fact does not mean any trouble. But a real trouble and a nunacceptable fact is that the cylinder C_1 finishes its entire stroke before the cylinder C_2 starts. In the case of such a construction, it is certain that the phenomenon of blocking on the guideways appears.

Fig. 2. Results of simulating the operation of two unsynchronized cylinders

Flow dividers can be used to avoid these situations.

2. Use of Resistive Flow Dividers

Flow dividers are devices that allow a division of the input flow in a well-defined ratio for two consumers [5]. They can divide the flow into different ratios, such as: 50%/50%, 40%/60% or 30%/70%. They can operate in one direction of the flow or in both directions [5]. Figure 3 shows the construction and symbol of a flow divider that works in one direction.

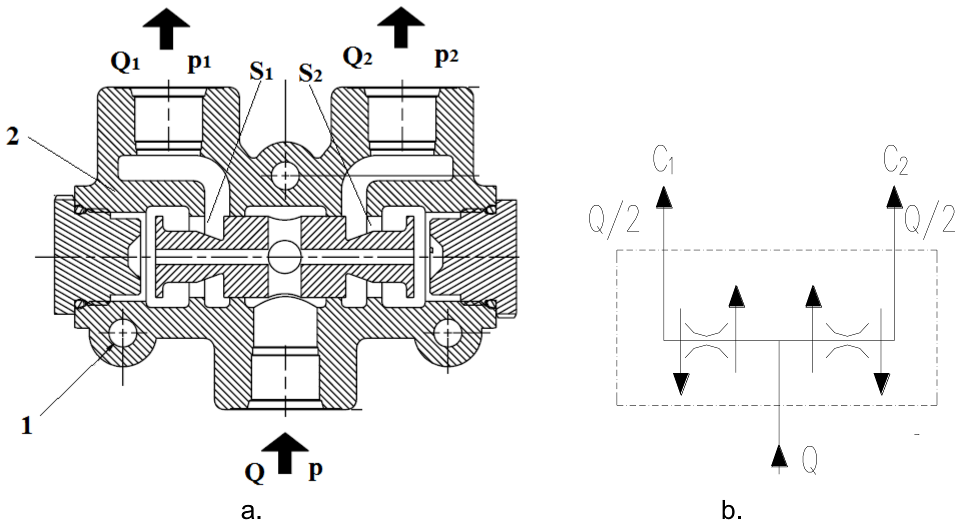

Fig. 3. Resistive flow divider

The source supplies the divider with the flow rate Q at the pressure p in the lower part of the body 1. The piston 2 works freely in this part. Depending on the values of the local pressures p_1 and p_2, the piston oscillates so that the variations of the flow surfaces S_1 and S_2 ensure the equality, or the imposed ratio, of the flows Q_1 and Q_2 sent to the cylinders C_1 and C_2.
If the diagram in Figure 1 is supplemented with a resistive flow dividerof 50%/50% type, the characteristics in Figure 4 are obtained after the simulations.
The time required to complete the stroke is ~16 s, but on this occasion it can be observed that the movement of the two cylinders is simultaneous at the pressure of p = 18.5 bar and there is no more the danger of blocking the system.
The advantage of using flow dividers compared to the use of flow regulators [2] is obvious especially in the cases where the movements of going up and going down are performed in unrepeatable conditions: change of the forces value, change in mass distribution, variations of friction forces etc. If precision flow regulators are used, the adjustment once made for certain

conditions becomes useless when changes occur. The flow dividers perform automatically the adjustmentand the imposed conditions, at anytime.

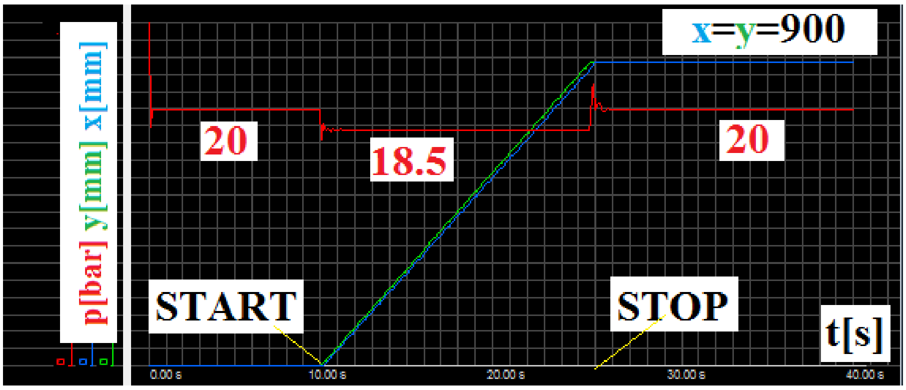

Fig. 4. The results of simulating the operation of two cylinders synchronized by means of a resistive flow divider

In some cases, it is necessary for the load moving UP-DOWN to be secured against accidental falling because of the weight or the occurrence of external forces. For these cases, it is possible to use the diagram in Figure 5 for ascent, descent and STOP phase.

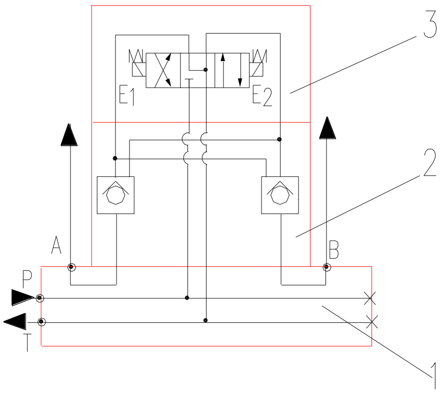

Fig. 5. Securing system against the accidental falling of the actuated load

To reduce the need for pipes, it is recommended to make a modular assembling of the plate 1, double unlockable check valve 2 and directional valve 3. When it is not actuated, the directional valve 3 has a connection of A - B - T type for an efficient locking. The ascent is performed by actuating the electromagnet E_1 and the descent is made by controlling the electromagnet E_2. In order to increase the operation safety, but also for the actuations in case of failure, hydro-pneumatic accumulators can be used [1, 2, 5, 9, 10].

3. Synchronization of the Travel of the Hydraulic Cylinders Working in "Pliers" System

The lathes intended for the simultaneous machining of the two wheels of an axle used for railroad cars and locomotives are usually specialized machine-tools and lately have become CNC machines [11].

The process of bringing the semi-finished product to the position of machining and evacuation is ensured by two identical hydraulic cylinders that raise/lower and clamp/unclamp the workpiece in the required conditions of accuracy and safety. The clamping will always be done in the same position, as the axis of the semi-finished product must be identical to the axis described by the driving system represented by the two tables (specific to this type of machine). Regardless of the weight of the semi-finished product and its clamping diameter, the two cylinders will ensure the conditions mentioned above. It is basically a pair of power "pliers" with hydraulic actuation. Figure 6 shows the actuation diagram of the two cylinders for such a case.

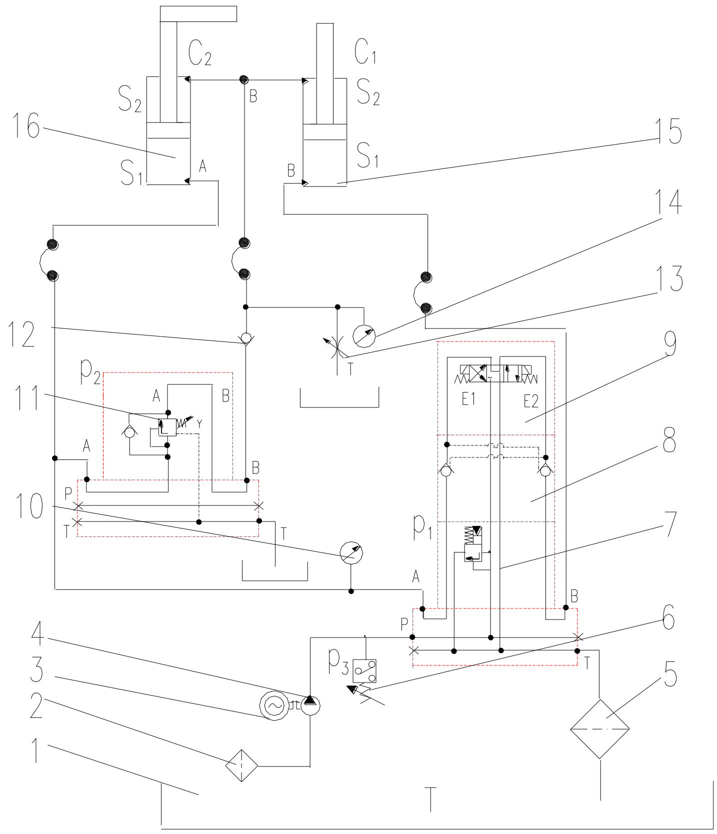

Fig. 6. Actuation diagram of a "pliers" type synchronization system

Pump 4, driven by the electric motor 3, sucks the oil from the tank 1 (T) by means of the suction filter 2. The maximum pressure in the system p_1 is adjusted by means of the pressure valve 7 and is confirmed by the pressure switch 6, adjusted to the pressure p_3 ($p_3 < p_1$). The pressure p_1 is permanently displayed on the pressure gauge 10. A pressure p_2 at least by 10 bar lower than the pressure p_1 is set at the sequence valve 11. This pressure can be read on the pressure gauge 14 during the clamping and unclamping operations. The check valve 12 ensures the compensation of the eventual losses from the upper chambers of the cylinders 15 and 16. Those ones have the surfaces S_2. The lower surfaces of the cylinders are also identical and have the value S_1. The throttle valve 13 allows the initial adjustments and the ventilation of the circuit at the initial start. The cylinder C_1 (15) is the one that supports the weight of the semi-finished product that it raises and lowers. Cylinder C_2 (16) is that part of the "pliers" that comes and clamps the semi-finished product from the top down. The electromagnets E_1 and E_2 of the directional valve 9 are powered in order to actuate the cylinders 15 and 16. The accidental pressure drops are avoided by means of the hydraulic latch 8.

In the STOP phase, the cylinders remain in the last set position thanks to the latch 8. If the electromagnet E_1 is actuated, the oil is sent through the path B of the directional valve 9 on the surface S_1 of the lifting cylinder 15. The oil on the surface S_2 of this one feeds the similar surface of cylinder 16. In the absence of flow losses, the clamping cylinder 16 descends at the same speed as the cylinder 15 raises.

If the electromagnet E_2 is actuated, the oil is sent through the path A of the directional valve 9 on the surface S_1 of the clamping cylinder 16, but also to the sequence valve 11. This one only opens if the pressure in the system reaches at least the value p_2. The flow passing through this is added to the output flow from the surface S_2 of the clamping cylinder 16 and supplies the surface S_2 of the cylinder 15 which goes down. Due to the difference in the surfaces $S_1 - S_2 > 0$, the cylinder 16 goes up and the cylinder 15 goes down. In this case too, they travel at the same speed which, in the absence of flow losses, will ensure a correct positioning related to the axis of the lathe.

To check the operation of the system, a simulation was performed in AUTOMATION STUDIO [8].

The result of this simulation is shown in Figure 7.

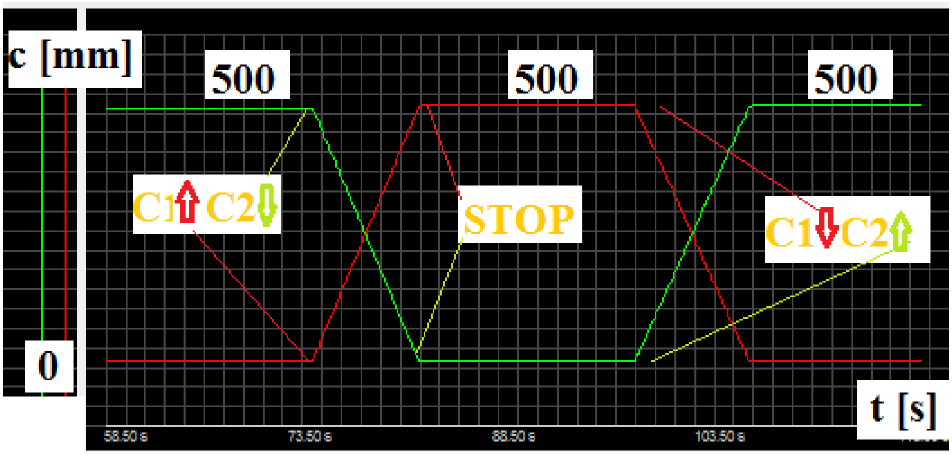

Fig. 7. Simulation of the clamping/unclamping function of cylinders working in "pliers" system

It was considered that the flow rate of the pump 4 is Q = 30 l/min, the set pressures are p_1 = 45 bar, p_2 = 35 bar and p_3 = 42 bar. The cylinders are identical and they have the stroke c = 500 mm, S_1 = 78.5 cm^2, S_2 = 59 cm^2.
It is considered that the semi-finished product has the weight G = 1000 daN.
Due to the way in which the two cylinders operate, the total stroke of clamping/unclamping is made with the value 2xc = 1000 mm. Under these conditions, the necessary time for the clamping and unclamping during a fixed stroke and in a repeatable position, regardless of the workpiece, is ~18 s. Given the overall size of these machines, but also the weight of the semi-finished products, this value of time is considered acceptable. The power of the electric drive motor will be about 4 kW.
Figure 8 shows the cylinders C_1 and C_2 before the assembling in the unit.

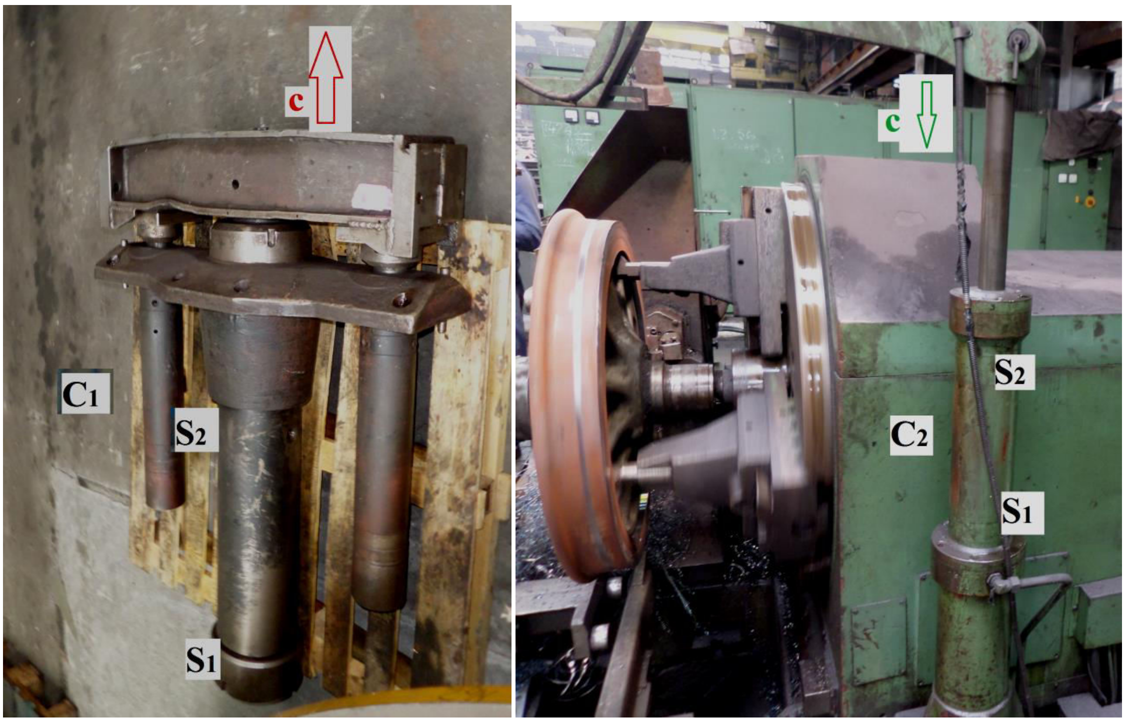

a. b.

Fig. 8. Cylinders C_1 and C_2 before assembling

4. Use of Volumetric Flow Dividers

The volumetric flow dividers have a construction similar to the one of the gear pumps [1]. Figure 9 shows the construction and assembly diagram of such a divider for the supply of three consumers.

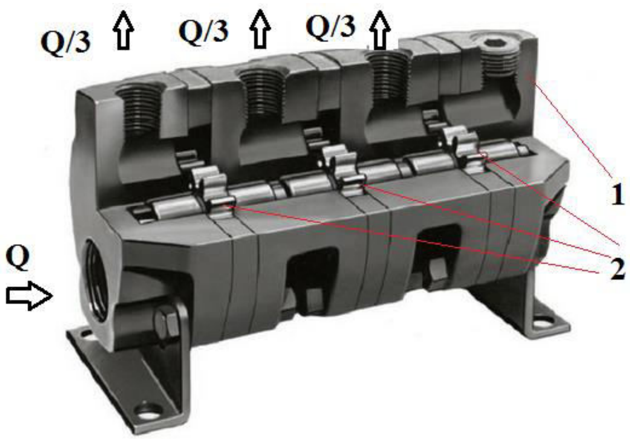

a.

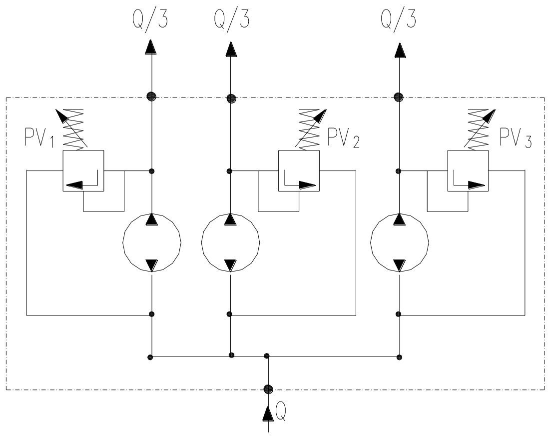

b.

Fig. 9. Volumetric flow divider for three consumers

Pinions 2 rotate synchronously in housing 1. For each outlet there is a pressure valve, marked PV_1, PV_2 and PV_3.
These dividers are supplied by a pump Q_P with a flow rate higher than the required flow Q ($Q_P > Q$). For the example shown in Figure 1, a divider with two outputs (50%/50%) is chosen. If the pressure regulated at the pressure valves is not reached in each circuit, the differences that appear between the flows supplied to the two cylinders are caused by possible losses or oil compressibility.
The results of the operation simulation in this case are presented in Figure 10.

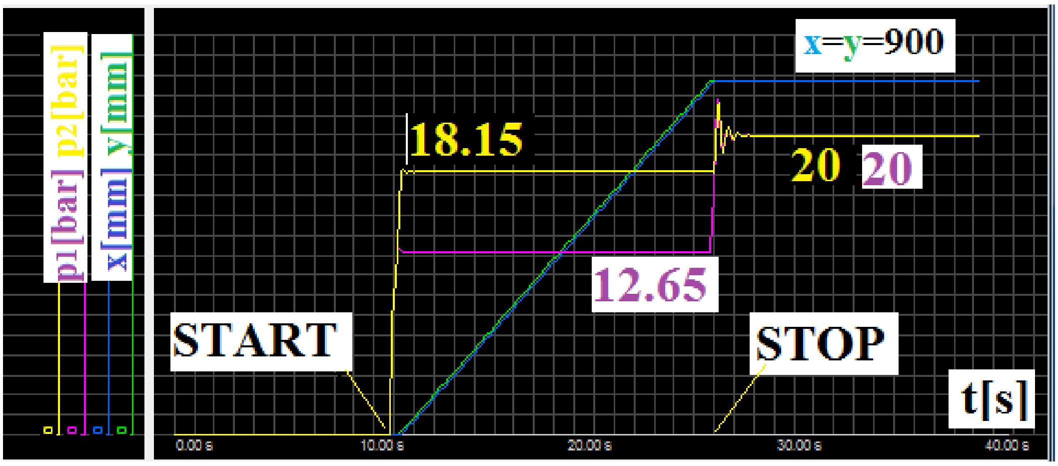

Fig. 10. Results of simulating the operation of two synchronized cylinders using a volumetric flow divider

In this case, too, the travel of the cylinders is synchronously made at different pressures: $p_1 = 12.65$ bar and $p_2 = 18.15$ bar. After the stroke of both cylinders, the pressure becomes, in both cylinders, $p_1 = p_2 = p = 20$ bar.

5. Conclusions

The synchronous movement of two or more hydraulic consumers (cylinders or rotary hydraulic motors) is difficult to achieve by using throttles or flow control valves. Even if a proper adjustment of these ones is performed, it will become inefficient in time because of the changes that occur during operation.
For the synchronous travel of two or more hydraulic systems that do not require positioning accuracy of the order of tenths of a millimeter, it is recommended to use flow dividers. If only two identical cylinders are operated, and the flows are small (in order of magnitude below 10 l/min), resistive flow dividers can be used successfully. These ones can also provide uneven flow rates to the two cylinders.
In case of higher flow rates or when several cylinders are operated, the recommended solution is to use volumetric flow dividers.
If it is intended to avoid the uncontrolled movement of the load due to weight, unforeseen forces or failures, the "hydraulic latch" type securing systems will be used.

References

[1] Bucureşteanu, Anca. *Hydraulic and Pneumatic Driving/Acţionări hidraulice şi pneumatice*, Bucharest, Printech Publishing House, 2003.
[2] Prodan, Dan, Mircea Duca, Anca Bucureşteanu, and Tiberiu Dobrescu. *Hydrostatic Drives - Machine Parts/Acţionări hidrostatice - Organologie*, Bucharest, AGIR Publishing House, 2005.
[3] Guibert, Ph. *Applied Industriel Hydraulics/Hydraulique industrielle appliquee*, Université de Metz, 1991.
[4] Prodan, Dan. *Machine-Tools Hydraulics/Hidraulica Masinilor-Unelte*. Bucharest, Printech Publishing House, 2004.
[5] ***. Catalogues and leaflets PARKER, BOSCH REXROTH and MTC.
[6] Bucureşteanu, Anca. "Dynamics of Hydraulic Cylinders. Classical Mathematical Models and Simulations" *HIDRAULICA Magazine of Hydraulics, Pneumatics, Tribology, Ecology, Sensorics, Mechatronics*, no. 2 (June 2017): 14-20.
[7] Prodan, Dan. *Heavy machine tools. Mechanical and Hydraulic Systems/Maşini-unelte grele. Sisteme mecanice si hidraulice*. Bucharest, Printech Publishing House, 2010.
[8] ***. Software package AUTOMATION STUDIO.
[9] Bucureşteanu, Anca. *Hydro-Pneumatic Accumulators. Use and Modeling/Acumulatoare pneumohidraulice. Utilizare si modelare*. Bucharest, Printech Publishing House, 2001.
[10] ***. Hydraulic Trainer BOSCH REXROTH.
[11] Prodan, Dan, George Constantin, and Anca Bucureșteanu. "Retrofitting of the Hydraulic Installation of a CNC Lathe for Re-Profiling Railway Wheelset." *Proceedings in Manufacturing Systems* 12*,* no. 1*,* (2017): 3–8.

Examination of Losses in Fire Extinguisher System Operated from Centrifugal Pump

Full Professor PhD. **Rajmund KUTI[1],** Associate Professor PhD. **Péter HORVÁTH[2],**
Assistant Professor PhD. **Flóra HAJDU[3],** Department Engineer **Csenge PAPP[4],**
PhD Student **Gabriella LÁSZLÓ[5]**

[1] Széchenyi István University, Department of Mechatronics and Machine Design H-9026 Győr, Egyetem Square 1. kuti.rajmund@sze.hu

[2] Széchenyi István University, Department of Mechatronics and Machine Design, H-9026 Győr, Egyetem Square 1. horvathp@sze.hu

[3] Széchenyi István University, Department of Mechatronics and Machine Design, H-9026 Győr, Egyetem Square 1. hajdfl@sze.hu

[4] Széchenyi István University, Department of Mechatronics and Machine Design, H-9026 Győr, Egyetem Square 1. papp.csenge@sze.hu

[5] Széchenyi István University, H-9026 Győr, Egyetem Square 1. gabriella.laszlo30@gmail.com

Abstract: *Nowadays, the most often used fire extinguisher material for fire extinguishing is still water, whom transportation can be conducted in different fire extinguishing systems to the spot of fire. The quantity of the water mass, which can be extracted of the fire extinguisher system depends on the applied unit, and is influenced by losses that occur during water transportation. It is very important to examine the losses occurring inside the water supply system, since they influence the quantity of extracted water, thus the fire extinguishing itself. To be aware with this topic in more detail, to increase the efficiency of fire extinguishing in practice, we examine in our paper the terms of occurring losses in the most commonly used centrifugal pump operated fire extinguisher systems, particularly regarding effective fluid movement. The aim of our research is to determine the optimal conditions for fire extinguisher systems, and further to help the work of firefighters.*

Keywords: *Fire fighting system, operation parameters, losses, effective fluid flow, optimization*

1. Introduction

The transportation of fire extinguisher water from the source is made possible most of the times by the fire extinguisher system assembled by firefighters. Its parts are the pump, hose, manifolds and nozzles. According to the requirements of usage, numerous equipment were developed. Among pumps that are capable of water transportation, fire extinguisher pumps constitute a separate group, these can withstand due to their structure, operation in non-optimal conditions [1]. However, it has to be in consideration, that there can be severe differences between the nominal liquid movement performance given by the manufacturer and the extracted water mass from the fire extinguisher system [2]. These can derive from the attributes of the area and the losses that occur in the water transporting system. It is inevitable to take the occurring losses into consideration while examining the effective liquid movement in fire extinguisher systems. The achieved results help in practice to ensure safety operation in long-term.

2. Creating a calculation model

In case of fire extinguisher pumps, performance parameters are measured in most cases along with 1.5 – 3 meters pumping depth, with a measuring unit placed directly onto the discharge port of the pump, they measure it between different speed boundaries. During fire extinguishing tasks, these conditions cannot be realized, changing the intake and pressure height mean performance variation in case of centrifugal pumps, the water mass can decrease in a given time period. To realize optimal operating conditions during fire extinguishing tasks is inevitable, however, on-spot conditions, equipment available do not always enable these, thus real pressure and water mass values cannot meet the desired ones. After studying data in available literature, we found only the part of solutions, but we have not found a unique and obvious answer to the problem. There is a strong need for complex calculations while every possible loss is taken into account. This cannot be conducted during an accident due to time factor. As a solution, we decided to compile a simplified calculation model, that represents the necessary elements for conducting fire extinguishing tasks, as system. The necessary data and formula for the calculations, we have collected, is also published in this paper. To ease the calculations, we assembled a simple fire extinguisher system and used it. The elements of the base model can be extended, if necessary. The elements of the system assembled are the following:

- Centrifugal pump,
- Standard inlet and discharge fire hoses,
- Manifold,
- Nozzle.

The examined and assembled fire extinguisher from the elements mentioned above, consists of a centrifugal pump and ray “C”. As pump, a Rosenbauer Fox III. Portable pump is examined that is used in EU countries everyday, its supply comes from artificial water tank, in intake operation mode. As requirement that has to be met in case of the arranged fire extinguisher system, it is determined that the pump should support the water mass necessary to operate the DIN EN 15182-3 type nozzles and to ensure 5 bar water pressure to create a proper ray in 10 meter fire fighting. The next figure shows vertical image of the assembled fire extinguisher system.

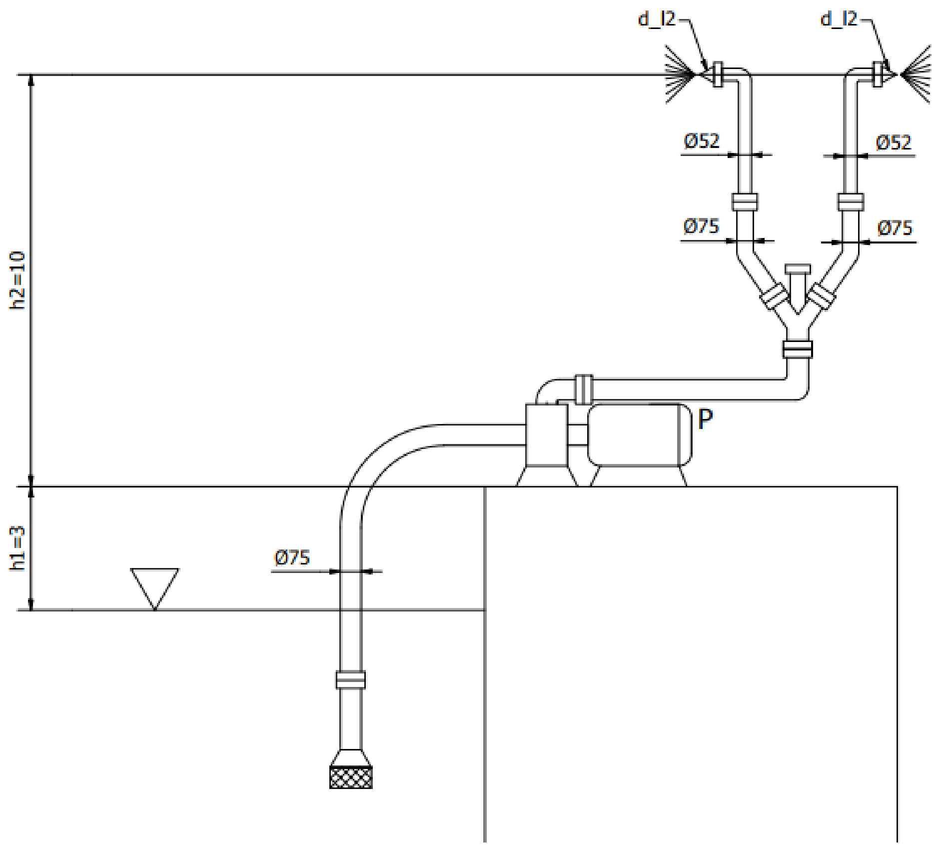

Fig. 1. The vertical structure of fire extinguisher system (Source: authors’ compilation, marking of [3] used)

To meet our demands, all rays of the system have to ensure a water ray of $Q=0.00343$ m^3/s (206 l/p) volume flow, with a nozzle operated in h= 10 m height whose nozzle has an outlet with $d_{L2}=12$ mm diameter. The length of water supply hoses is L=40 m. To examine the fire extinguisher system, we have to determine the operation point to the operation speed of the pump.

Further task is to calculate the impulse force that impacts on the nozzle and on the fire fighter who holds it. According to Paul Spurgeon [4] the pressure of the liquid in the discharge port of the pump can be defined as the sum of pressure losses:

$$\Delta p = \Delta p_L + \Delta p_t + \Delta p_h + \Delta p_o \tag{1}$$

In the equation:

- Δp :pump pressure
- Δp_L : pressure at nozzle
- Δp_t : friction loss of fire hoses
- Δp_h : pressure loss coming from lifting
- Δp_o : pressure loss of units (for e.g. manifold, transfer piece, pressure stabilizer unit)

In the following, we represent the calculation method for certain pressure losses in case of one ray.

2.1 Pressure loss of fire hoses

After studying the available literature about the pressure losses of fire hoses, we could determine, that data show differences, thus we calculated the pressure loss in meters in correspondence to volume flow, accordint to data in [3]. After converting the data from anglo-saxon measurement units to the SI units, the two most frequent dimensions were 2" and 3", so 52 and 75 mm as hose diamater. We edited the diagrams that contain the pressure loss for every meters, these are in Figure 2. Parabolas can be fitted on the measurement points with a good estimation.
The ratio in case of the 52 mm diameter "C" hose: $c_{52} = 3.4 \cdot 10^7 \ Pas^2/m^6$.
In case of 75 mm diameter "B" hose $c_{75} = 5.1 \cdot 10^6 \ Pas^2/m^6$.
We have to mention, that these values can differ in a small extent depending on the manufacturers and age of hose – although they have to meet the requirements of the standards.

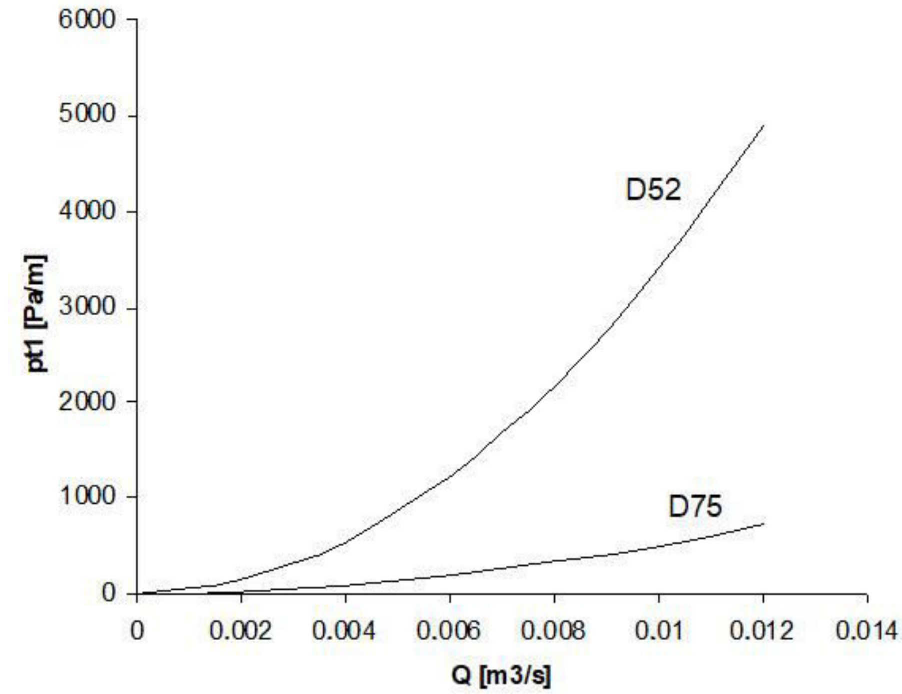

Fig. 2. Pressure loss to every meter of 52 and 75 mm diameter (Source: authors' compilation)

2.2 Pressure difference of nozzle

A key element in the system, is the nozzle, which actually is, two confusors connected into two, in-between them a combined closing unit is assembled. The following figure shows a DIN EN 15182-3 type confusor used with nozzle.

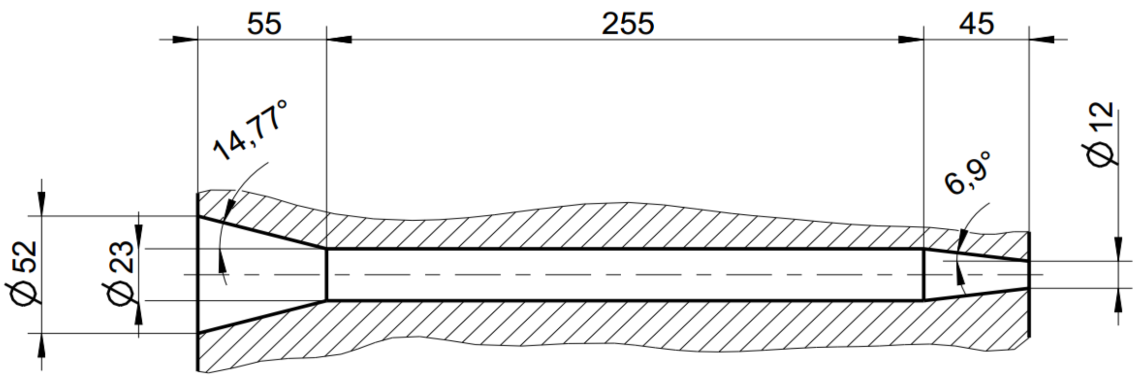

Fig. 3. Drawing of confusor and the cross-section of nozzle (Source: authors' compilation and [5])

The pressure drop and volume flow data of nozzles are represented as a table format in MSZ 1059 standard. A 12 mm diameter nozzle has a pressure drop of $\Delta p_L = 5 \cdot 10^5$ Pa in case of m Q=206 l/min=0.00343 m^3/s volume flow. We have to mark, that pressure difference is not totally a loss, since kinetic and pressure energy in the inlet cross-section of the nozzle convert into velocity energy. If the pressure-volume flow data for the appropriate type of hose is not available, we can it calculate with a good estimation only with the known geometries.
As we write the Bernoulli-formula between the in- and outlet of the nozzle, pressure and kinetic energy convert into pure kinetic energy [5]:

$$\frac{\Delta p_L}{\rho} + \frac{v_{L1}^2}{2} = \frac{v_{L2}^2}{2} \tag{2}$$

Velocities are determined by the volume flow, the pressure difference existing between the in- and outlet cross-section of the nozzle, the following correlation can be determined:

$$\Delta p_L = \underbrace{\frac{\rho}{2}\left(\frac{1}{A_{L2}^2} - \frac{1}{A_{L1}^2}\right)}_{k_L} Q^2 = \frac{1000}{2} \cdot \frac{4^2}{\pi^2}\left(\frac{1}{0.012^4} - \frac{1}{0.052^4}\right) 0.00343^2 \approx 460\ kPa \tag{3}$$

The standard calculates with 96 percentage discharge loss, thus $\Delta p_L \approx 480$ kPa.
This value barely differs from the value presented in the table – probably rounded – 500 kPa.
Pressure drop that occurs in the nozzle – similarly to the pressure loss of the hose – is proportional to the volume flows quadriatic. The ratio for the given nozzle: $k_L = 4 \cdot 10^{10}\ \ \mathrm{Pas}^2/\mathrm{m}^6$

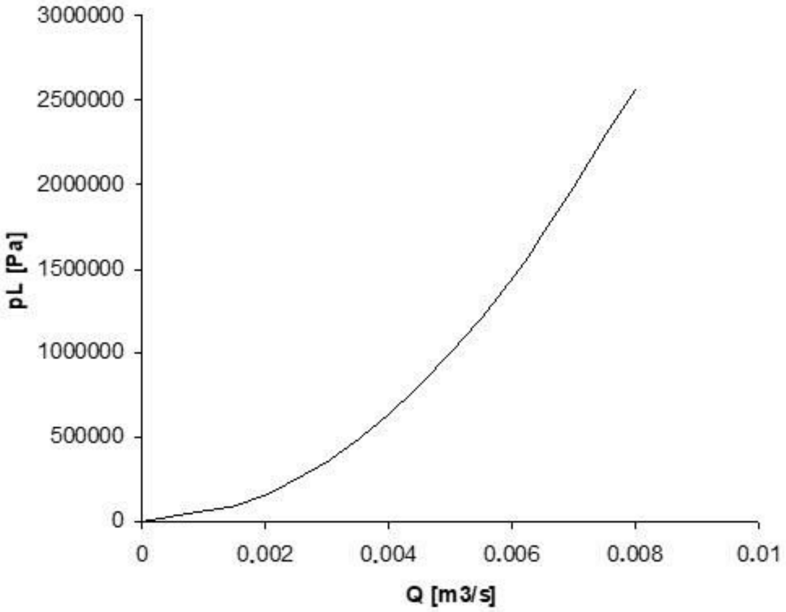

Fig. 4. The pressure drop of the 12 mm diamater nozzle in correspondance of volume flow (Source: authors' compilation)

In case of the nozzle, it is necessary to mention, that an impulse force acts on the nozzle and it cannot be neglected. This force is originated by the narrowing cross-section of the hose and so the impulse of the liquid changes.
Impulse force can be calculated from

$$F = \dot{m}(v_2 - v_1) = \rho \frac{A_1 - A_2}{A_1 A_2} Q^2 \tag{4}$$

correlation. Impulse force is represented in correspondence of volume flow, in case of the 12 mm diameter nozzle:

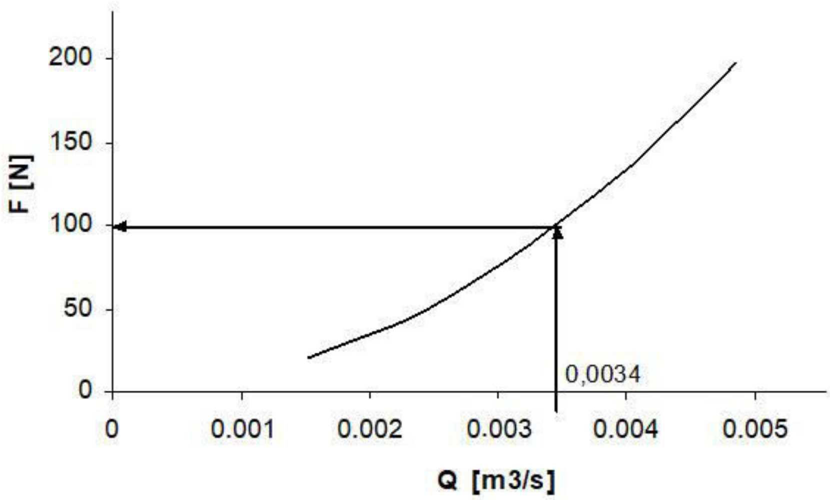

Fig. 5. Impulse force in correspondence of volume flow, in case of nozzle with 12 mm diameter (Source: authors' compilation)

2.3 Pressure loss due to lifting and the pressure loss of the manifold

In case of the pressure loss coming from lifting, we can calculate with 1 bar per meter, so 10^5 Pa loss [6]. Manufacturers usually do not, or just in certain cases, define the resistance coefficient of the unit, that has to be determined with calculation later [3]. According to the referred source, in case of the manifolds, pressure drop has to be considered with 10 PSI, so 0.69 bar losses [6].

3. Conclusions

In our research work we determined the losses occuring in fire extinguisher systems. After executing the calculations, represented earlier and evaluating the results, we determined that the fire extinguisher system, we created, can be operated in practice. The required water yield and pressure at the nozzles could be supplied by the pump. By analysing our results, we determined, that there are differences between the extracted water masses in case of rays operated on different levels. This has to be taken into account during fire fighting. We could conclude, that inside fire hoses during operation, signifiant losses occour. The examination of the pump is also inevitable, because without it, there is no obvious conclusion, whether our pump is capable of operation in given condition with the required water yield and pressure supply. During result analysis, with the proper conclusions, the operation of water supply systems can be supported. With the application of the represented calculations, the examination of assembled fire extinguisher systems can be easily carried out and experiences can be adapted to practice, so as, water supply problems can be prevented that are originated from inproper operation.

References

[1] Fecser, Nikolett. ”Examining the Characteristics of Pedrollo_CP130 Centrifugal Pump in Simulated Service Conditions.” *Hidraulica Magazine*, no. 2 (June 2017), pp. 40-49.
[2] Fecser, Nikolett, and Rajmund Kuti. ”Examining Fire Pump Metz Fp 24/8 on Cavitation.” *Hidraulica Magazine*, no. 4 (December 2017), pp. 98-104.
[3] Béla, Szabó L. *Water Supply Studies*/*Vízellátási ismeretek*. Budapest, BM Publishing House/BM Könyvkiadó, 1983.
[4] Spurgeon, Paul. “Every Pump Operators’ Basic Equation.” *Fire Engineering* 165, no. 10 (October 2012): pp. 51-65.
[5] Lajos, Tamás. *Fundamentals of Fluid Dynamics*/*Az áramlástan alapjai*. Budapest, Technical University Publisher / Műegyetemi Kiadó, 2004.
[6] Pázmándy, Mihály. *Water supply for firefighting*/*A tűzoltás vízellátása*. Budapest, BM Publishing House/BM Könyvkiadó, 1979.

ARX Models as a Useful Tool to Generate Design Hydrograph with Rainfall

Dra. **Maritza ARGANIS[1*]**, M.Eng. **Margarita PRECIADO[2]**

[1] National Autonomous University of Mexico, MArganisJiingen.unam.mx

[2] Mexican Institute of Water Technology, preciado@tlaloc.imta.mx

*Corresponding Author: MArganisJ@iingen.unam.mx

Abstract: *ARX-type parametric autoregressive models were used to identify the best fit to precipitation effective data and direct statistical runoff corresponding to a 100 years return period, under assumption that a runoff rain process can be treated as a linear system; this model was validated with data from another rain runoff event corresponding to a 10,000 years return period; the best model obtained was the ARX 1 1 1 type. It consists of two correspondence rules, one hydrograph for rise branch and another for recession, since in this way the highest model adjustment percentages (76%) were achieved with both the measured data and those of the validation.*

Keywords: *Return period, Rainfall-Runoff, ARX models, Canseco Dam*

1. Introduction

The problem to estimating direct runoff hydrograph generated by an effective precipitation event associated with a return period has a lot importance in hydraulic and hydrological studies for hydraulic design structures [1]. Recently, many studies are focused to estimating runoff for forecasting purposes and considering real-time systems; in these cases, the problem of non-linearity is argued [2, 3]. Selecting variables, one of the most influence a rain-runoff process has led to the implementation of sensitivity analysis procedures [4]. In [5] three types of rainfall runoff models are identified: physically based ones that take into account rainfall, runoff, soil moisture, soil type and use, and basin physiography; somewhat more simplified conceptual models that group the concepts of infiltration and retention losses in shrubs and theoretical or data-driven models that only find the correspondence rule between the rain process and runoff. In this study we will highlight models of this nature.

Rainfall runoff process can be analyzed as a system with an input signal to a system (excess precipitation) and an output from the system (direct runoff hydrograph). Runoff commonly occurs with a certain time delay with respect to the occurrence of precipitation and its behavior comes to depend both on the rain in the time analyzed and on the rain and the runoff itself in previous times. Under this conception, an analogy can be made with a parametric identification of systems and applied to the case of statistical rains, that is, data from a mean hyetogram of the basin and direct runoff that it would produce, for a given return period (previously obtained with help for example, a distributed model physically based or conceptual type to which a theoretical data-drive model is applied to map rainfall in runoff and this model in turn applied to estimation of direct runoff hydrographs for storms. corresponding to another return period for the same analyzed basin.

This paper describes the Matlab software toolbox tools use [6, 7], to obtain with an optimization process, the best fit ARX model for the transformation of effective rain into direct runoff. Input data correspond to the hyetogram of mean precipitation corresponding to a 10 years return period and the inflow to Canseco reservoir dam located in Veracruz, Mexico [8, 9]; which is identified as a closed basin. Validation data are from another statistical event corresponding to an effective rainfall hyetogram corresponding to a 10,000 years return period. In a first stage, 50 percent of the data were considered to identify the best AX model and 50% data from same event for validation; but in that case, ARX model gave high adjustment errors, barely a 42% fit, so it was decided to separate problem considering a function defined with two correspondence rules, one for ascent branch of the hydrograph up to time peak and another correspondence rule for descent leg to base time. With this consideration applied to the event with a 10 years return period, an ARX model was obtained that gave a 76% correspondence in adjustment in ascending branch with used data to identify (Tr = 10 years) and a similar value when applying data model for validation (Tr = 10,000 years), while in the descending branch the percentage of adjustment was 98%.

2. Methodology

2.1 Study site

In this paper, we used as a starting mean hyetogram point data for basin and runoff, corresponding to 100 and 10,000 years return periods (Table 1), they were obtained with a statistical procedure and a runoff rain model for the Canseco Dam. located in Laguna de Catemaco, that is, it is a closed basin (see Fig. 1), located in Los Tuxtlas Volcanic Massif, in the southeast of the state of Veracruz, Mexico. It is located at the coordinates 95 ° 04 '6.98"W, 18 ° 24' 6.71"N, limited by the extreme geographic coordinates 18º 21 'and 18º 27' of northern latitude and 95º 01 'and 95º 07' of western longitude, 332 m above sea level. It is part of the Rio Papaloapan basin [8, 9].

Table 1: Mean basin hyetogram (effective rainfall hpe) and direct runoff (Qd) for return period Tr = 100 and 10,000 years

	Tr=100 years		Tr=10000 years	
Tr	**hpe**	**Qd**	**hpe**	**Qd**
h	**(mm)**	**(m^3/s)**	**(mm)**	**(m^3/s)**
1	0.55	0	0.9	0
2	0.86	1.76	1.4	2.88
3	1.19	9.57	1.94	15.61
4	1.53	23.11	2.5	37.68
5	1.98	39.36	3.21	64.16
6	2.99	57.97	4.86	94.47
7	3.5	79.86	5.68	130.12
8	3.96	106.89	6.43	174.02
9	5.07	136.89	8.22	222.64
10	7.15	168.64	11.6	274.05
11	14.73	208.49	23.93	338.64
12	156.85	276.04	255.07	448.3
13	37.04	639.11	60.29	1039.15
14	15.24	1641.23	24.81	2669.33
15	9.27	2585.45	15.1	4204.42
16	8.37	2828.08	13.63	4598.63
17	6.13	2554	9.99	4153.31
18	3.96	2062.49	6.44	3354.46
19	3.8	1634.43	6.19	2658.55
20	2.64	1287.27	4.3	2094.06
21	1.48	1011	2.42	1644.79
22	0.34	791.91	0.55	1288.45
23	0	614.5	0	999.86
h	**(mm)**	**(m^3/s)**	**(mm)**	**(m^3/s)**
24	0	467.12	0	760.09
25	0	345.48	0	562.17
26	0	250.13	0	407.02

	Tr=100 years		Tr=10000 years	
Tr	**hpe**	**Qd**	**hpe**	**Qd**
27	0	179.13	0	291.48
28	0	127.95	0	208.2
29	0	91.39	0	148.72
30	0	65.28	0	106.23
31	0	46.63	0	75.88

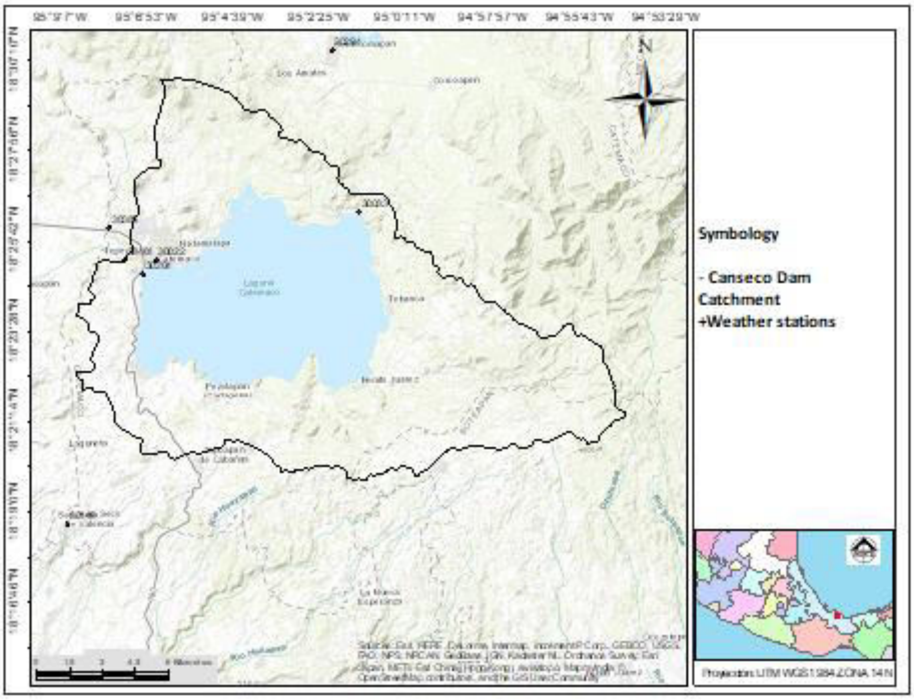

Fig. 1. Canseco Dam basin and climatologic weather stations. Source [8]

2.1 Parametric models for linear systems

For simplicity, parameter models general form for linear systems identification is given by equation 1 [6], which is known as the prediction error model (PEM)

$$A(q^{-1})y(t) = \frac{B(q^{-1})}{F(q^{-1})}u(t) + \frac{C(q^{-1})}{D(q^{-1})}e(t) \tag{1}$$

Where u (t), y (t) and e (t) are input, output and system noise respectively; A, B, D and F are polynomials as a shift operator function (q-1).

By choosing a structure from previous general model, simplified models are obtained, of which following ARX (exogenous autoregressive model), ARMAX (Autoregressive Moving Average Exogenous), OE (Output Error) and Box-Jenkins structures are for practical use:

2.1.1 ARX Model

$$A(q^{-1})y(t) = B(q^{-1})u(t) + e(t) \tag{2}$$

2.1.2 ARMAX Model

$$A(q^{-1})y(t) = B(q^{-1})u(t) + C(q^{-1})e(t) \tag{3}$$

2.1.3 OE Structure

$$y(t) = \frac{B(q^{-1})}{F(q^{-1})}u(t) + e(t) \tag{4}$$

2.1.4 Box-Jenkins Structure

$$y(t) = \frac{B(q^{-1})}{F(q^{-1})}u(t) + \frac{C(q^{-1})}{D(q^{-1})}e(t) \tag{5}$$

In this paper, only ARX models use is highlighted.

2.2 Parametric models identification in Matlab software Functions

Within Matlab editor, you can call functions that allow linear models generation; this is a general way to obtain vector model is:

$$th = \text{model}([output \quad imput], ths) \tag{6}$$

Where: model: it will be ARX if you are looking for ARX model shape, ARMAX, if you want to identify an ARMAX model; column vector output with system output data, column vector input with system input data and *ths* row vector containing parameters number of the model being tested and in its the most general form it and has the elements:

$$ths = [na \quad nb \quad nc \quad nd \quad nf \quad nk] \tag{7}$$

Where na, nb, nc, nd, nf are polynomials coefficients number of A, B, C, D and F of ec 1 or chosen structure (2 to 5) and nk is input and output delay times number.

2.3 Optimal structure selection

To select the model order to choose, tests can be made with different coefficients and delays in *ths* vector to make a comparison with a criterion help, for example, mean square error or by checking model parameters number to choose the best. Matlab software basin with functions designed to perform a several models automated test, obtaining their loss functions (which corresponds to the case in which mean square error between observed data and calculated with model gives minimum value) and between them indicates one that provides the smallest adjustment error; For this, it must consider data to make identification or obtain from model and data to make model validation; necessary instructions for this are highlighted in Fig. 2

```
nn=struc([1:10],[1:10],[1:10]);

v=arxstruc(datos_ident, datos_val,nn);


nn=selstruc(v)
```

Fig. 2. Instructions for obtaining optimal structure for ARX models.

In Fig. 2 struc is a matrix that contains structures result from combinations na, nb and nk in case of ARX models, arxstruc returns loss functions given vector that contains t input and output data to identify, vector that contains data for model validation and matrix struc and instruction selstruc returns the model that has the lowest loss function value.

Once the optimal model is identified, vector th of equation 6 is formed to generate it.

For model validation, instruction comparison is used (vector to identify or vector to validate, th) to presents the figure of to fit between data used to estimate model and data calculated by model or fit between data for validation and data that model calculates for those validation points.

We can also obtain residuals or errors that model commits graphically with instruction resid (vector to identify or to validate, th).

The following section highlights an example of the application of these procedures.

3. Application and results

3.1 Test 1 with ARX model and 50% storm 1 data for identification and 50% for validation

Statistical storm data were used for the return period Tr = 100 years and data first half was used for identification vector and next half for validation vector, when using instructions to optimize it was obtained that the best model is:

$$Q(t) = 1.654Q(t-1) + 1.741Pe(t-1) \tag{8}$$

When we applied validation data model to compare instruction, a 42% adjustment percentage was observed, but when we comparing against data entered for identification, an 88% adjustment percentage was observed. (Fig. 3).

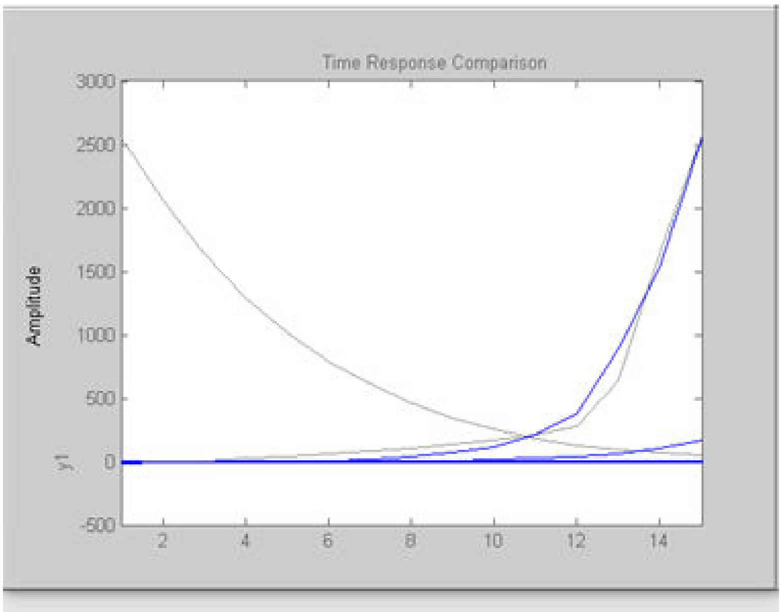

Fig. 3. Data Comparison used to identify and validate vs ARX model calculations

Given that direct runoff hydrograph upward and downward branches pass through an extreme point, identifying two behaviors; it problem can be analyzed with a function defined by two correspondence rules.

3.2 Test 2 with ARX model

Data in table 1 were divided into two groups considering storm 1 hydrograph of ascending branch (Tr = 100 years) as data to identify and storm 2 ascending branch (Tr = 10000 years as data to validate first model correspondence rule to estimate runoff; and the other hand, hydrograph of storm 1 descending branch (Tr = 100 years) was considered to identify and storm 2hydrograph of descending branch (Tr = 10000 years) to identify validate second model correspondence rule to estimate runoff.

With these considerations and when did optimization process for ascending and descending branch, the following function was obtained with two correspondence rules:

$$Q(t) = \begin{cases} 1.258Qd(t-1) + 3.041Pe(t-1); 0 \le t \le tp \\ 0.7508Q(t-1) + 21.17Pe(t-1); tp < t \le tb \end{cases} \tag{9}$$

Ascending and descending branches comparison with data for identification and with data for validation we can observed in Figs. 4 to 7.

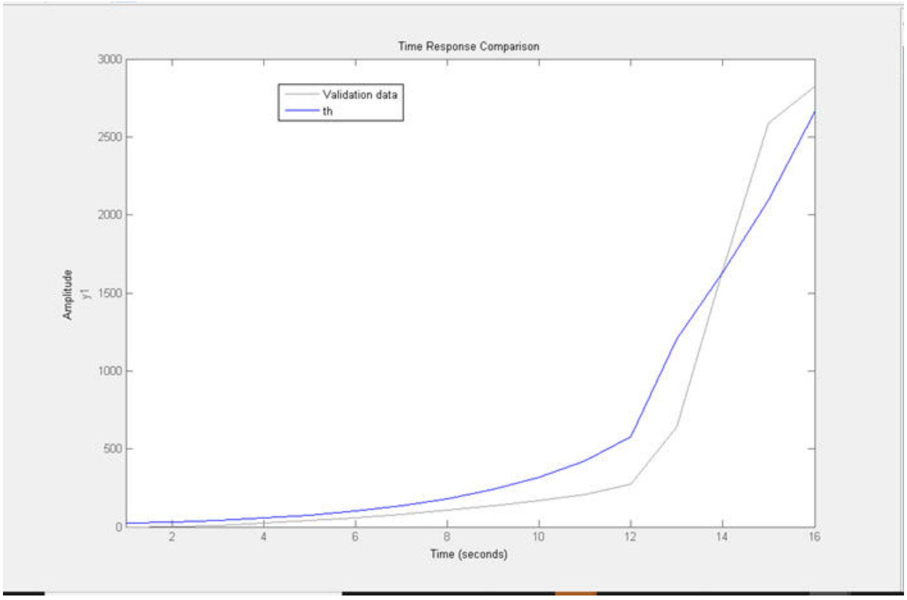

Fig. 4. Ascending branch comparison with identification data

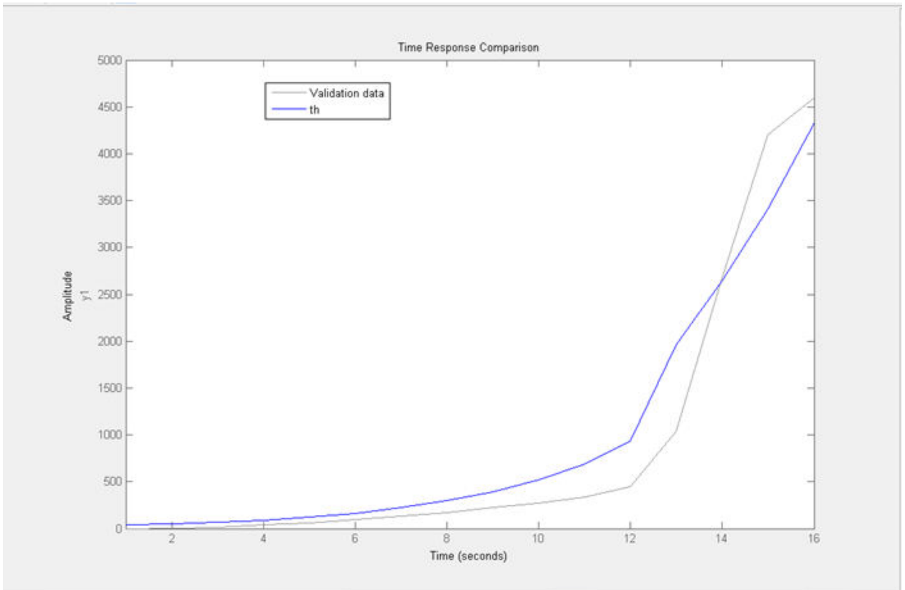

Fig. 5. Ascending branch validation with validation data

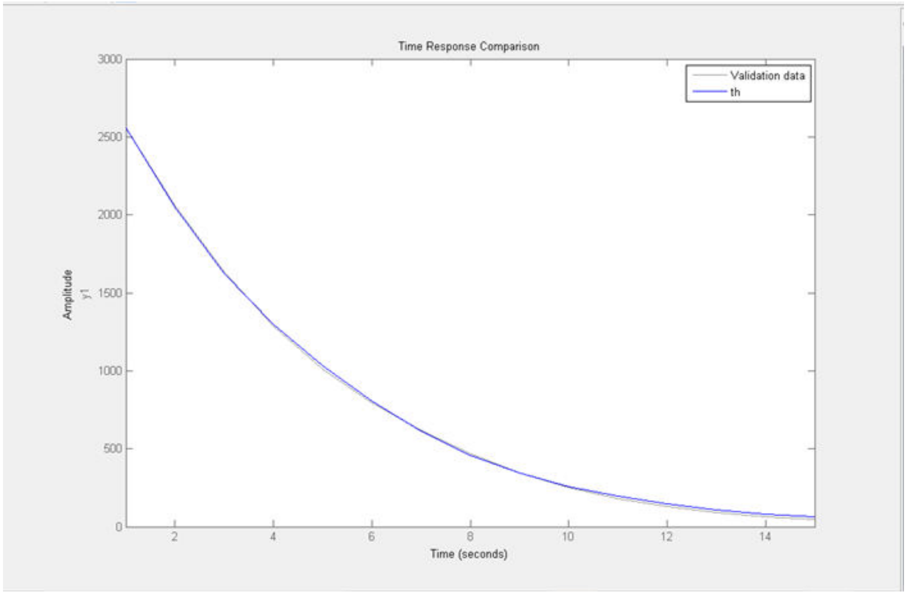

Fig. 6. Descent branch Comparison with identification data

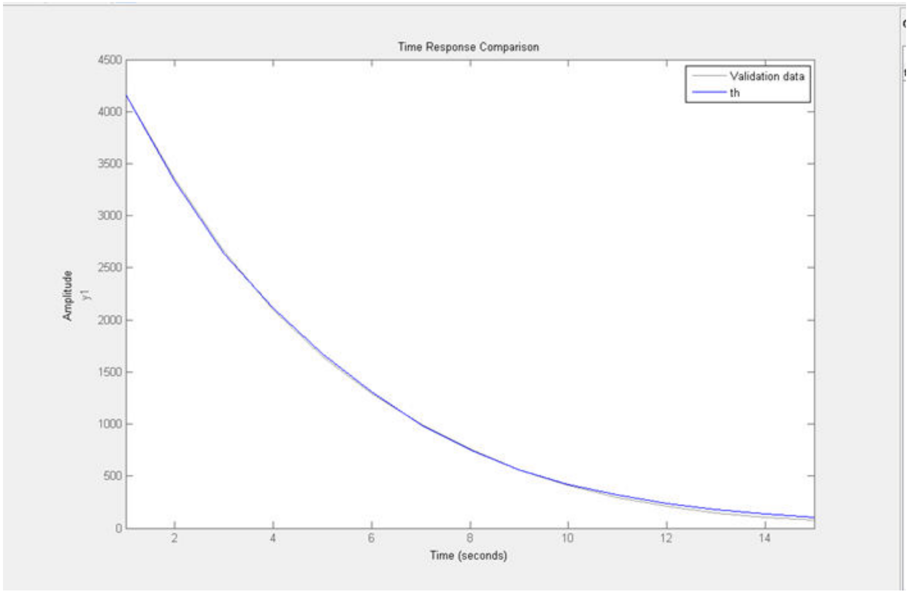

Fig. 7. Descent Branch Comparison with Validation Data

Figures 4 to 7 show a model better fit for descending hydrograph branches.
Residuals of each correspondence rule with validation data appear in Figs. 8 and 9.

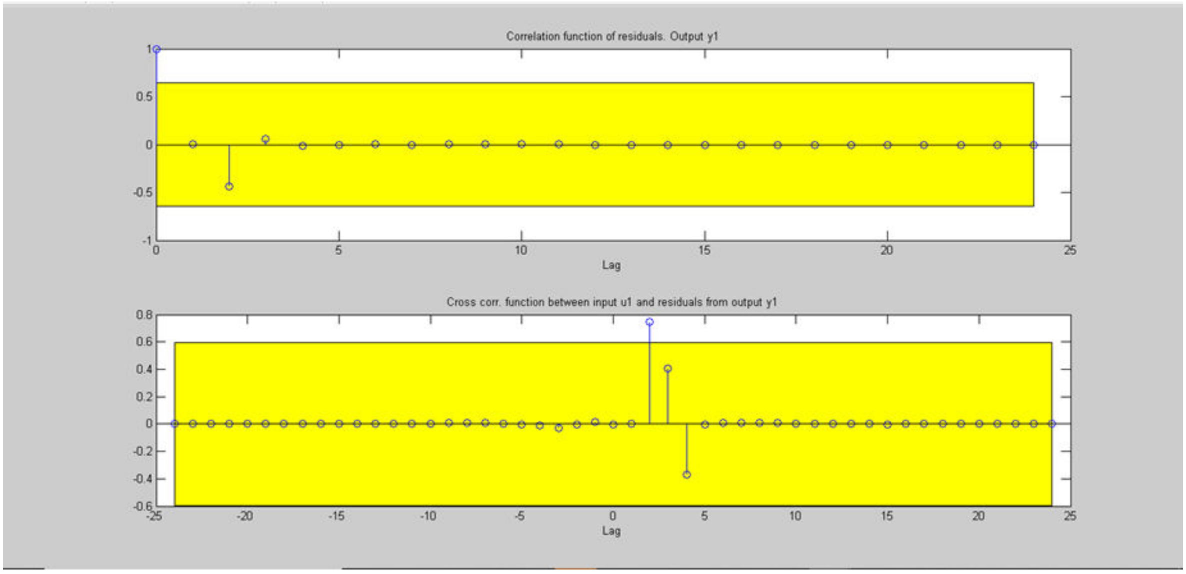

Fig. 8. Validation data residuals and those calculated by ascent branch model

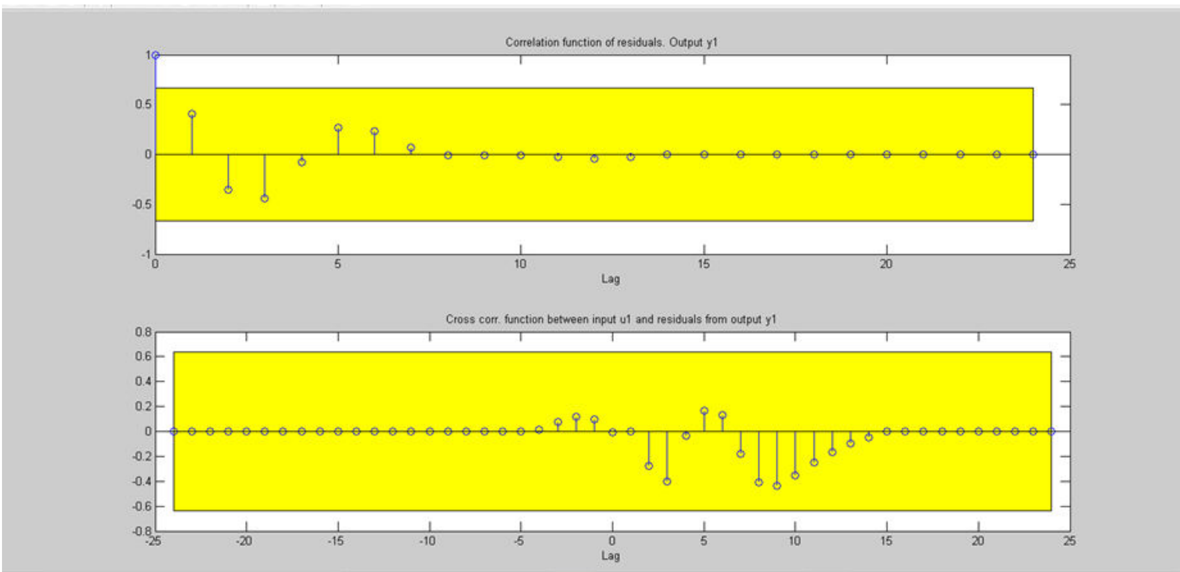

Fig. 9. Validation data residuals and those calculated by ascending branch model

From Figs. 8 and 9 above, it is observed that in ascent branch model validation presents less difficulties in reproducing data, while for descending, greater differences are observed between is estimated by model and validation data.
Hydrograph calculated complete drawing for Tr = 100 years using original input data (rainfall and runoff in previous step) is in Fig. 10 and calculated hydrograph for Tr = 100 years using runoff data that is calculating model appears in Fig. 11.

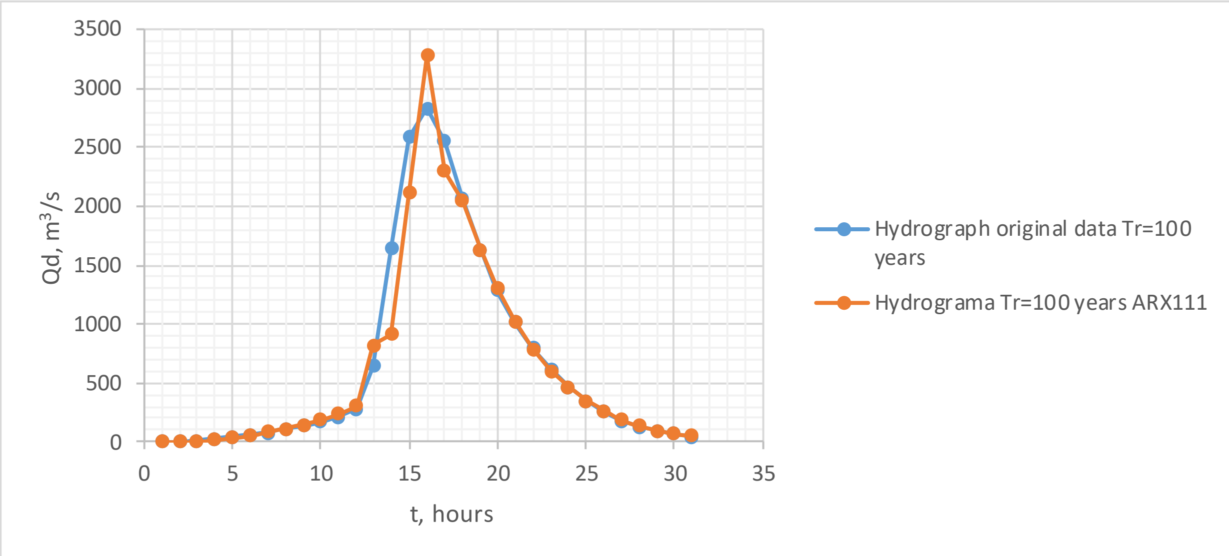

Fig. 10. Identification hydrograph comparison and the calculated hydrograph model with two correspondence rules and identification runoff data. Event Tr = 100 years

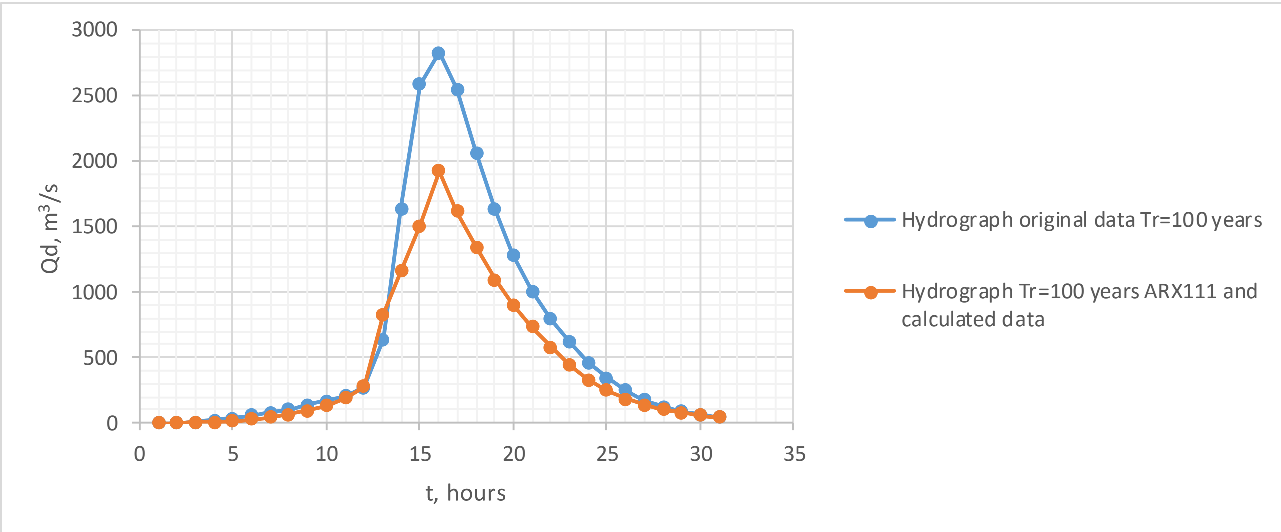

Fig. 11. Identification hydrograph Comparison and hydrograph model calculated with two correspondence rules and runoff data calculated with the model. Event Tr = 100 years

Estimated hydrograph with model for Tr = 10000 years using original rainfall and runoff data appears in Fig. 12 and the hydrograph calculated for Tr = 10000 years with given rainfall and runoff generated by the model appears in Fig. 13.

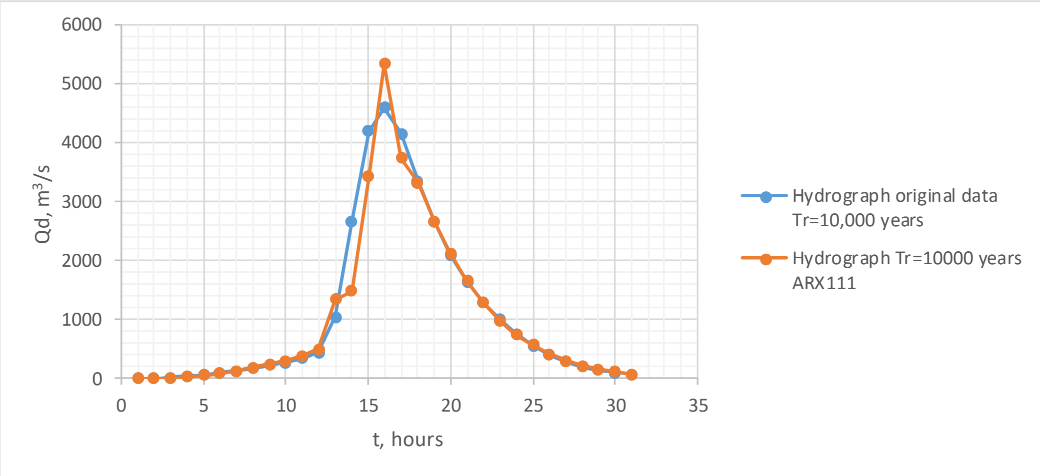

Fig. 12. Validation hydrograph comparison and calculated model hydrograph with two correspondence rules and validation runoff data. Event Tr = 10000 years

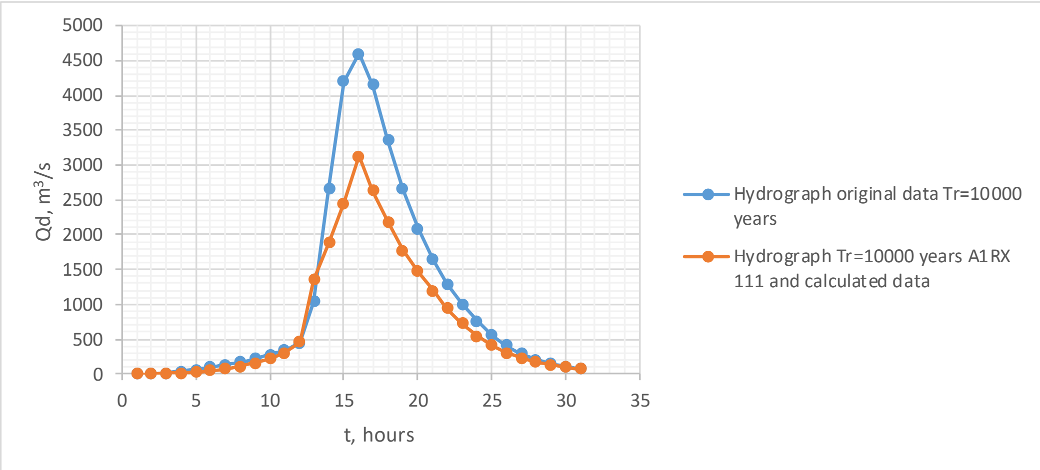

Fig. 13. Validation hydrograph comparison and calculated hydrograph model with two correspondence rules and validation runoff data. Event Tr = 10000 years

From Figures 10 to 13 an underestimation in hydrograph is observed, peak flow and therefore in runoff volume in two calculated storm cases.

Table 2 indicates peak flow and volumes obtained in each cases from Figures 10 to 13 and difference percentages found in said variables.

Table 2: Differences percentages in peak flow and hydrographs volume with original data and model calculated with two correspondence rules of equation 8

Tr	**Original Data**	**ARX**	**$Qp_{calcdcalc}$**	**% difference**	**$Qp_{calcdcalc}$**
	Qp	**$Qp_{calc\ dorig}$**		**Qpcalc dorig**	
years	**m³/s**	**m³/s**	**m³/s**		
100	2828.08	3280.69	1922.70	16	32
10000	4598.63	5335.08	3126.87	16	32
	Original Data	**ARX**		**% difference**	
Tr	**V**	**V_{Qdorig}**	**V_{Qdcalc}**	**V_{Qdorig}**	**V_{Qdcalc}**
years	**hm³**	**hm³**	**hm³**		

Tr	Original Data	ARX	$Qp_{calcdcalc}$	% difference	$Qp_{calcdcalc}$
	Qp	$Qp_{calc\ dorig}$		Qpcalc dorig	
100	73.11	70.55	51.10	3	30
10000	118.91	114.75	83.12	3	30

4. Conclusions

ARX Linear parametric models type was obtained to estimate direct runoff hydrograph from design precipitation data and a previously known runoff value (in this case, they were hourly rainfall and runoff data).
ARX optimal model when considering 50% of data for identification and 50% of data for validation and the storm itself presented difficulty in fully hydrograph reproducing, so it was decided to assume hydrograph shape with function behavior a definiteness by two correspondence rules, one for its ascending branch and other for its descendent branch.
Optimal models determined for each correspondence rule were of the same order na = 1, nb = 1 and nx = 1, and they were able to ascending branches reproduce with adjustments of 76% and 98%, respectively, when original data using, although in general, there is an underestimation in calculated hydrographs peak flow.
When hydrographs are calculated from known precipitation data and calculated runoff data, it is observed that model manages to reproduce ascending branch with a better fit than descending branch.
Model shape suggests that dependence that naturally occurs in basin rain runoff process, since a runoff time dependence is observed, on rainfall that occurred in a previous instant of time but also on existing runoff at instant previous.

References

[1] Aparicio Mijares, Francisco J. *Fundamentals of Surface Hydrology / Fundamentos de Hidrología de Superficie*. Ciudad de México, Limusa Publishing House, 2011.
[2] Hadid, Baya, Eric Duviella, and Stéphane Lecoeuche. "Data-driven modeling for river flood forecasting based on a piecewise linear ARX system identification." *Journal of Process Control* 1, no. 8 (February 2020): 44-56. https://doi.org/10.1016/j.jprocont.2019.12.007.
[3] Gautam, D. K., and K. P. Holz. "Rainfall-runoff modelling using adaptive neuro-fuzzy systems." *Journal of Hydroinformatics* 3, no. 1 (January 2001): 3–10. doi: https://doi.org/10.2166/hydro.2001.0002.
[4] Tang, Y., P. Reed, K. Van Werkhoven, and T. Wagener. "Advancing the identification and evaluation of distributed rainfall-runoff models using global sensitivity analysis." *Water Resour. Res.* 43, no. W06415 (June 2007): 1-14. doi:10.1029/2006WR005813.
[5] Chang, Tak K., Amin Talei, Lloyd H.C. Chua, and Sina Alaghmand. "The Impact of Training Data Sequence on the Performance of Neuro-Fuzzy Rainfall-Runoff Models with Online Learning." *Water* 11, no. 1 (December 2019): 52. https://doi.org/10.3390/w11010052.
[6] López Guillén, María Elena. "Systems Identification. Application to the modeling of a DC motor / Identificación de Sistemas. Aplicación al modelado de un motor de continua." July 28, 2021. Accessed October 22, 2021.
http://www.ie.tec.ac.cr/einteriano/control/Laboratorio/3.7Identificacion%20de%20sistemas.PDF.
[7] Mathworks. (2018). Available at: https://la.mathworks.com/help/ident/ug/what-are-polynomial-models.html.
[8] Domínguez Mora, Ramón, Maritza Liliana Arganis Juárez, E.E. Carrizosa, C.A. Jiménez, R. Mendoza, G.G. Esquivel, A.J.L. Herrera, G.J.C. Ramírez, and Edgar Antonio Sotomayor Suárez. *Hydrological study and determination of the operation policy of the Catemaco lagoon / Estudio hidrológico y determinación de la política de operación de la laguna de Catemaco.* C.H. Chilapan, for Federal Electricity Commission (CFE). Final report, 2016.
[9] Sotomayor Suárez, Edgar Antonio. *Hydrological study of the Laguna de Catemaco basin and review of the operating policy at C. H. Chilapan / Estudio hidrológico de la cuenca de la Laguna de Catemaco y revision de la politica de operación en la C. H. Chilapan*. Postgraduate Master's Thesis in Engineering, UNAM, México, 2018.

Modification of the Cavitation Resistance by Hardening Heat Treatment at 450 °C Followed by Artificial Aging at 180 °C of the Aluminum Alloy 5083 Compared to the State of Cast Semi-Finished Product

Eng. **Alexandru Nicolae LUCA[1],** Prof.PhD.Eng. **Ilare BORDEAȘU[2*],**
Prof.PhD.Eng. **Brândușa GHIBAN[3],** Lecturer PhD.Eng. **Cristian GHERA[4],**
Eng. **Dionisie ISTRATE[5],** Lecturer PhD.Eng. **Daniel-Cătălin STROIȚĂ[6]**

[1] Politehnica University of Timisoara, alexandru.luca2@student.upt.ro

[2] Politehnica University of Timisoara, ilarica59@gmail.com

[3] Politehnica University of Bucharest, ghibanbrandusa@yahoo.com

[4] Politehnica University of Timisoara, cghera2000@yahoo.com

[5] Politehnica University of Bucharest, dionisieistrate@yahoo.com

[6] Politehnica University of Timisoara, daniel.stroita@upt.ro

* Corresponding author: Ilare Bordeasu, ilarica59@gmail.com

Abstract: *The paper presents the results of the experiment of behavior and resistance to vibration cavity erosion, carried out on cast aluminum alloy 5083 heat treated by hardening at 450 ˚C and maintained for 12 hours at the artificial aging temperature of 180 ˚C. Following the experiment carried out in the Cavitation Erosion Research Laboratory of the Politehnica University of Timișoara, it is found that the duration of 12 hours is insufficient to increase the resistance to cavitation erosion, as evidenced by the destruction of caves in the shape of pits.*

Keywords: *Alloy 5083 aluminum, erosion of cavitation, mean depth erosion, erosion rate, microstructure, mechanical properties*

1. Introduction

Aluminum-based alloys have a very high industrial application due to their low weight and acceptable mechanical property values [1-3]. Among these applications, for our study, is of interest in the field of vehicles and river vessels [1], where there are demands of hydrodynamic currents with erosion by cavitation [4, 5]. Such parts are the rotors of the pumps for cooling the car engines and the propellers of the boats and engines for the propulsion of pleasure boats [6, 7, 8, 9], which after a number of hours of operation have surfaces with pitting erosion, sometimes with very large caverns, which requires the repair of the eroded area, or even the replacement of the part.

2. Researched material

The experimental program was carried out on samples taken from 5083 cast aluminum alloy and heat treated by volumetric hardening at 450 ˚C followed by artificial aging at 180 ˚C (see the cyclogram of the heat treatment, in fig. 1). Data on the chemical composition and mechanical properties of the researched semi-finished alloy can be found in [1, 3, 6, 7].

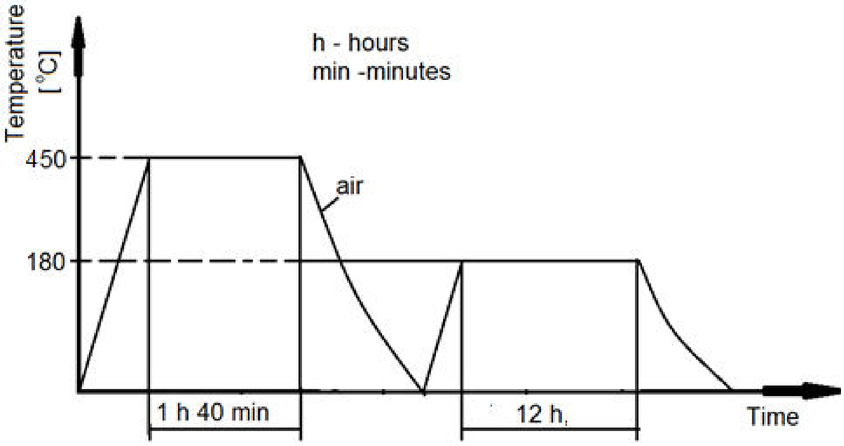

Fig. 1. Cyclogram of volume heat treatment

For the analysis of the data obtained in the detailed experiment, this paper preserves the symbolism given in the bibliographic references and mentioned in the web pages [1], (Witness (H)) for the sample taken from the semi-finished product and HNL for the heat treated sample.

3. Research equipment and method

The experimental research program was carried out in the Cavitation Erosion Research Laboratory on the vibrating device with piezoceramic crystals [4], fig. 2, within the Politehnica University of Timișoara, using the stationary sample method (fig. 2b) [4, 10].

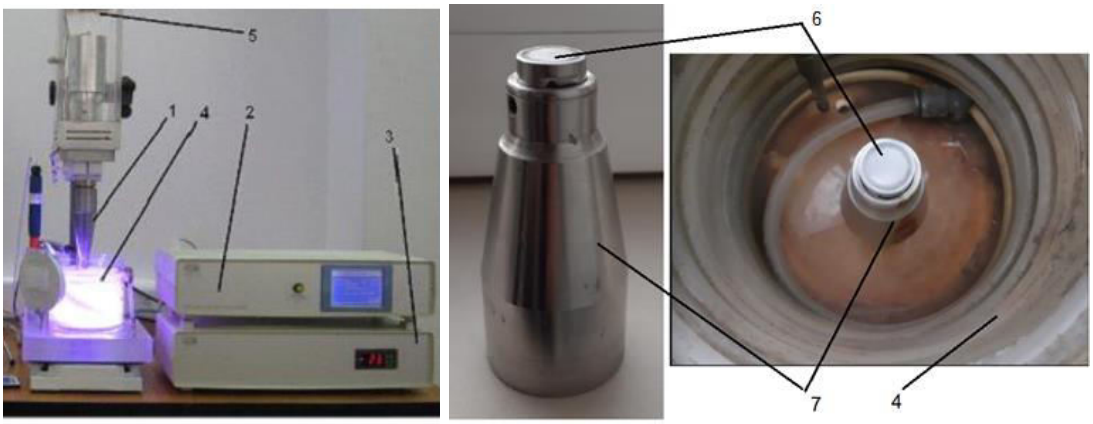

Fig. 2. Standard vibrating device
1- sonotrode; 2- electronic ultrasound generator; 3- electronic device for regulating the water temperature; 4- the vessel with liquid and the cooling coil; 5- piezoceramic transducer 20 KHz and 500 W; 6- computer for parameter control; 7- test for cavitation testing (d = 15.8 mm, length = 16 mm); 8- sample fixing device for performing the experimental test

The total duration of a test, the intermediate periods, the liquid environment, the processing and interpretation of the recorded data are in accordance with the custom of the laboratory [4, 10, 11, 12] and those prescribed in the international standard ASTM G32-2016 [13].
For the purpose, three samples were tested in double distilled water, according to the requirements imposed by ASTM G32-2016.
According to the rigors related to the appearance of the surfaces at the beginning of the cavitation test, they were polished to a roughness, Rz = 0.2 ÷ 0.8 µm.
Throughout the cavitation test, the functional parameters of the device (double vibration amplitude of 50 µm, oscillation frequency of 20 ± 0.1 KHz, electric power supply of the electronic ultrasonic generator of 500 W) and distilled water temperature of 22 ± 1 ˚C, which determines the hydrodynamic regime of the cavitation, respectively the intensity of destruction by micro-jets and

shock waves produced by the implosion of cavitation bubbles, were kept at constant values, due to the fact that the whole operation program is computer controlled and controlled specially built for this purpose [12].

4. Experimental results

4.1 Specific curves and parameters

Construction of specific cavitation curves (analytical curves), which serve to determine the values of the cumulative average depth (MDE_{max}) achieved by eroding the vibrating cavity in the surface structure, as well as the final bearing speed $MDER_s$ (known as stabilization rate of surface erosion [4, 10, 13]), was made starting from the algebraic mean values of the mass losses (Δmi) determined at the end of the intermediate periods Δt_i (5, 10 and 15 minutes) with the analytical balance type Zatklady which has an accuracy of 10^{-5} grams.
The analytical relations of the curves, detailed as a way of constructing in [14], have the form:

- for the variation of the cumulative average depth

$$MDE(t) = A \cdot t \cdot (1-e^{-B \cdot t}) \tag{1}$$

- for average erosion rate (erosion rate)

$$MDER(t) = A \cdot (1-e^{-B \cdot t}) + A \cdot B \cdot t \cdot e^{-B \cdot t} \tag{2}$$

where:
A - is the scale parameter, statistically established for the construction of the approximation/mediation curve, provided that the deviations of the experimental points (values) from it are minimal;
B - is the shape parameter of the curve.

The values of these coefficients can be seen in the diagrams in fig. 3 and 4 containing the curves MDE (t) and MDER (t).
The areas delimited by the dark red curves define the time interval in which the mass loss or destruction of the structure is pronounced. These variations are very well highlighted by the photographic images (macro) and SEM in fig. 5 and 6.

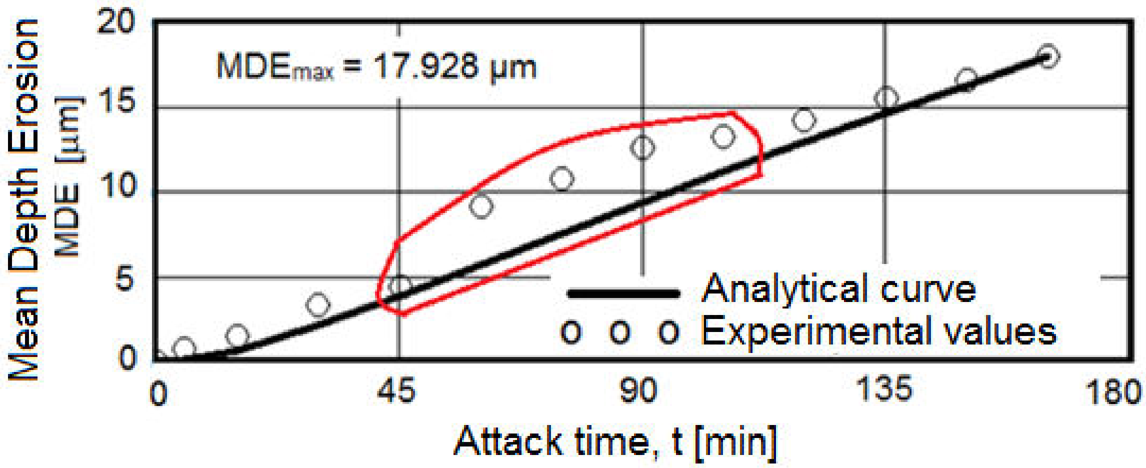

Fig. 3. Variation of the average erosion depth with the duration of exposure to cavitation ((A = 0.109, B = 0.035)

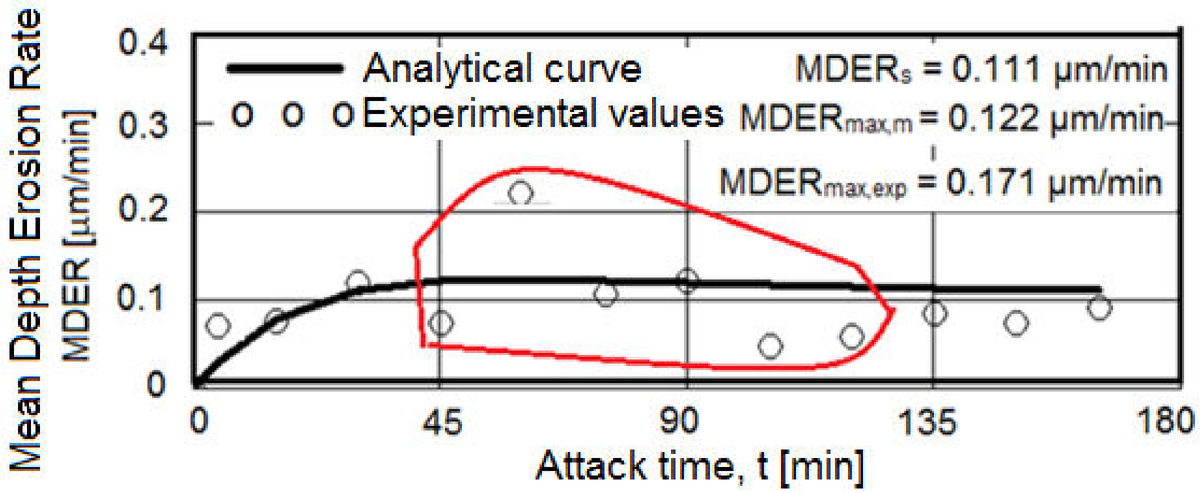

Fig. 4. Variation of the average erosion rate with the duration of exposure to cavitation
((A = 0.109, B = 0.035)

The data in Fig. 3 and 4 show:

1- The most significant mass losses, with important differences between the values of the speeds between two successive measurements, are recorded in the range 45-120. These speed jumps are in accordance with the macro-photographic images in fig. 5 and SEM (profilogram) in fig. 6;

2- The erosive mechanism of the first 30 minutes is observed, in which the mass losses are caused by the elimination of the roughness tips and the abrasive dust. The actual material losses are reduced, in the structure developing elasto-plastic deformations and crack networks [5, 7, 9, 10, 13, 14];

3- The shape of the approximation / mediation curve of the experimental values, with a difference of 11 µm / min between the maximum value ($MDER_{max,m}$= 0.122 µm/min) and the one towards which it tends to stabilize ($MDER_s$= 0.111 µm/min), is specific to surfaces with average mechanical properties in value (Brinell Hardness = 80.7 HB and Resilience = 18 J, $R_{p0.2}$ = 144.5 MPa, R_m = 311.21 MPa), which gives this condition a behavior specific to materials with low resistance to cavitation [5, 10, 15, 16];

4- After 120 minutes and until the end of the test, the erosion process takes place at approximately constant speed (the differences between the experimental, successive values of erosion rates are insignificant, within the range of deviations, specific to this hydrodynamic process), reason for which the variation of the MDE(t) curve over this time interval is approximately linear, and of the MDER(t) curve is asymptotically decreasing towards the stabilization value of the $MDER_s$. The explanation given in the literature [5, 16] is put on the hardening of the superficial layer of the cavity surface and on the attenuation of the impact forces by the air penetrated in the caverns;

5- Significant difference, of about 40%, between the maximum value obtained by experiment ($MDER_{max.\ exp}$ = 0.171 µm/min) and the one defined by the mediation curve ($MDER_{max,m}$= 0.122 µm/min), even if it is recorded at the same cavitation duration (90 minutes, fig. 4). This aspect is another proof of the complexity of the mechanism by which the structure responds to the cavitation request and by which the effect of the duration of maintenance on the heat treatment of aging on the structure and mechanical properties, as value and mode of distribution in the sample volume.

4.2 Morphology of surface degradation

The evolution of the surface structure degradation, obtained as a result of the mentioned heat treatment, is shown in the photographic images from fig. 5, made with the Canon Power Shot A 480 camera.

The erosion profile, created by the caverns in the area of the surface destroyed by the cavitation, is shown in fig. 6 by the SEM image, recorded after the end of the test (the 165 minutes of exposure of the cavitation attack).

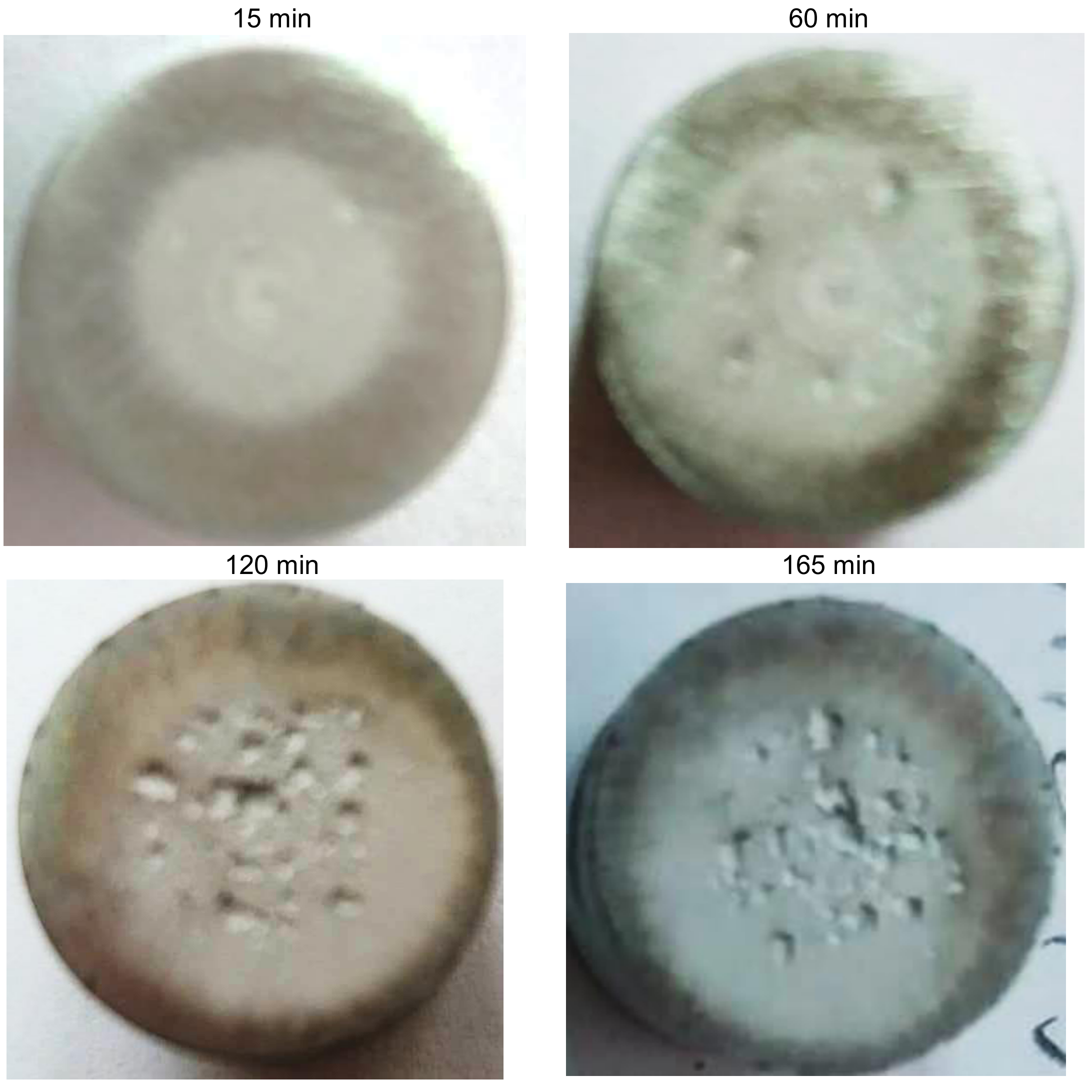

Fig. 5. Macro-photographed images after different times

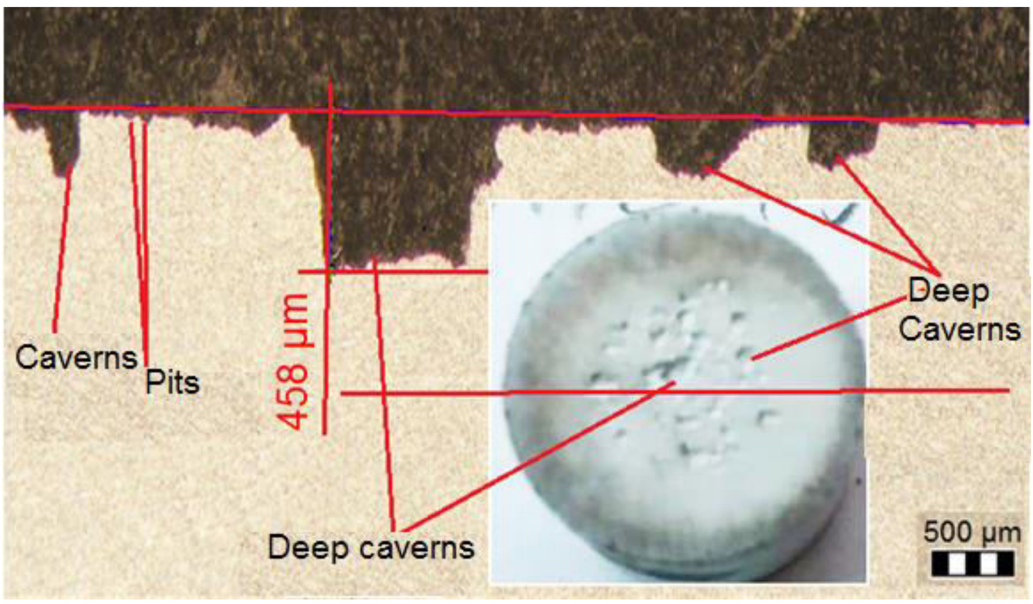

Fig. 6. Structural aspect in transversal cross-section and frontal section

The images in fig. 5 and 6 lead to the following findings:
- the photo images in fig. 5 show that the cavitational erosion of the surface starts as early as 15-30 minutes, as shown in fig. 3 and 4, but substantial, large losses, with the creation of deep caverns in depth, shape After 45 minutes of exposure to cavitation, the caverns deepen and material losses are close, causing approximately constant erosion rates. The causes have been set out above;
- from fig. 6 shows an enormous difference (over 25 times) between the value of the maximum depth of the cave caught in the section plan (451 µm, fig. 6) and the maximum average cumulated after 165 minutes (17.928 µm, fig. 3). Therefore, this difference reaffirms the conclusions of [11]; to evaluate the behavior and strength of a structure at the request of the cavity it is recommended to use the average value on the surface MDE_{max} and not the maximum of a cave, in an arbitrary area. However, it should be noted that the very high value of the pit caught in the sectioning plan raises a big question mark about the degree of fineness and the constitution of the structure resulting from this heat treatment of aging.

5. Comparison of results

The influence of the maintenance duration of 12 hours, of the heat treatment carried out at tempering temperature 450 ˚C, followed by artificial aging at 180 ˚C, on the resistance of the structure to the vibrating cavity, is presented, comparatively, in fig. 7, through the values of the parameters of the cumulative average depth of erosion MDE_{max} and of the three erosion rates.

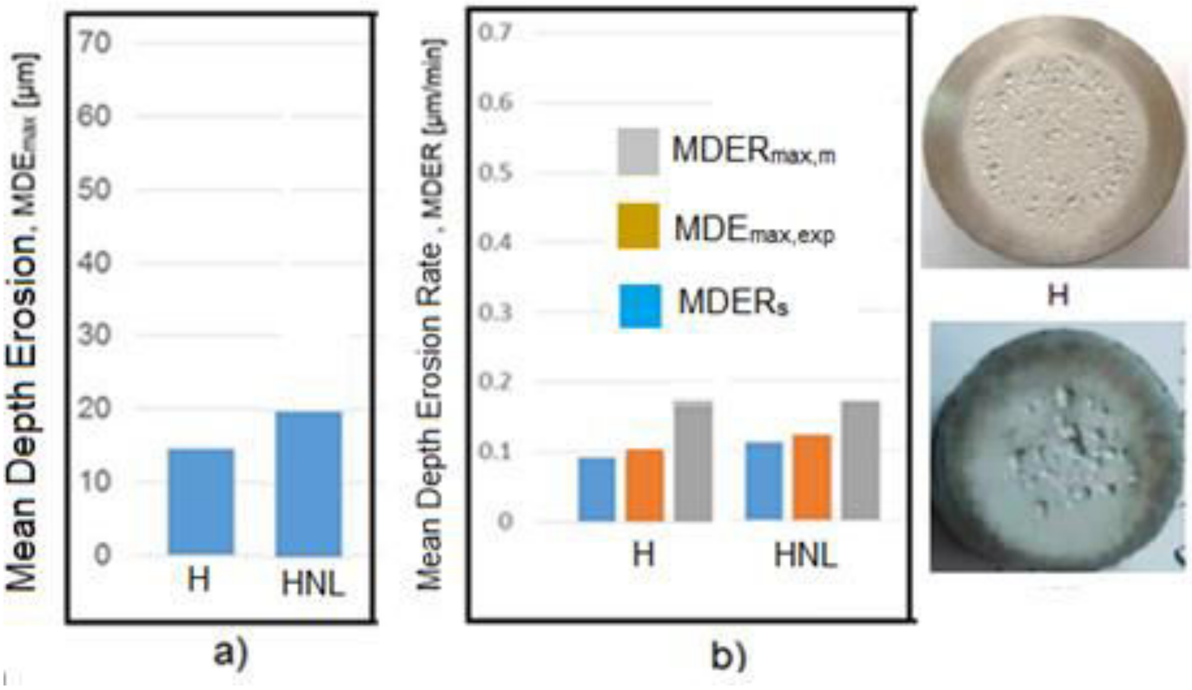

Fig. 7. Comparison between erosion parameters

The data in the two histograms, to which the photo images were attached, show:
1. according to the values of the two parameters MDE_{max} and $MDER_s$, recommended by ASTM G32 standards and used in the Cavitation Erosion Research Laboratory, the best strength is the H sample taken from the semi-finished product (MDE_{max} = 14.572 µm, $MDER_s$ = 0.092 µm/min [6, 7]);
2. Reconfirms that the maximum values of the erosion rate ($MDE_{max,exp}$), obtained from the experimental measurements and the maximum defined by the analytical curve of mediation of the experimental values ($MDER_{max,m}$) cannot be recommended to be used as comparison parameters, as due to the fact that the first does not objectively reflect the behavior and strength of the structure during the duration of exposure to cavitation (from 0 to 165 minutes), and the second does not offer the objectivity of using the speed of $MDER_s$.

6. Conclusions

1. The destruction of the structure, starting with the 135 minute of the cavitation attack and until the completion of the erosion test (165 minutes), is performed at an approximately constant speed, leading to the linear variation of the MDE(t) curve and a smooth, asymptotic decrease. MDER(t) curve to the stabilization value ($MDER_s$). The explanation is related to the hardening of the cyclically impacted layer by the cavitation microgrids and the air entering the gaps left by the expulsion of the material, which attenuates the impact force and consequently widens the cracks, breaking the bonds between the grains and expelling them.
2. The heat treatment applied determines the modification of the structure that suffers a pronounced degradation in the period 45-120 minutes, by increasing the number and geometric dimensions of the caverns.
3. The shapes of caverns, from pinching to large pits, are mainly determined by the shape of the microstructure resulting from the heat treatment regime applied.
4. The heat treatment of hardening at 450 ˚C and aging at 180 ˚C does not increase the resistance to cavity erosion, compared to the semi-finished state, but changes the way of destruction, by reducing the number of caves, increasing them in size, which requires the study continued on other regimes such as time durations and aging temperatures.

References

[1] https://www.amari.ro/images/catalog-produse/Catalog-INDUSTRIE-Amari-2012.pdf.
[2] http://www.placi-aluminiu.ro/en-aw-5083-almg45mn07.
[3] https://fdocumente.com/document/aluminiu-catalog.html.
[4] Bordeasu, Ilare. *Monograph of the Cavitation Erosion Research Laboratory of the Politehnica University of Timisoara (1960-2020) / Monografia laboratorului de cercetare a eroziunii prin cavitaţie al Universităţii Politehnica Timişoara: (1960-2020).* Timisoara, Politehnica Publishing House, 2020.
[5] Garcia, Ramon. “Comprehensive Cavitation damage Data for Water and Various Liquid Metals Including Correlation with Material and Fluid Properties.” Technical Report No. 6. University of Michigan, 1966.
[6] Istrate, Dionisie, Cristian Ghera, Laura Salcianu, Ilare Bordeasu, Brandusa Ghiban, Dumitru Viorel Bazavan, Lavinia Madalina Micu, Daniel-Catalin Stroita, and Daniel Ostoia. “Heat Treatment Influence of Alloy 5083 on Cavitational Erosion Resistance.” *Hidraulica Magazine*, no. 3 (September 2021): 15-25.
[7] Bordeasu, Ilare, Cristian Ghera, Dionisie Istrate, Laura Salcianu, Brandusa Ghiban, Dumitru Viorel Bazavan, Lavinia Madalina Micu, Daniel-Catalin Stroita, Alexandra Suta, Ileana Tomoiaga, and Alexandru Nicolae Luca. “Resistance and Behavior to Cavitation Erosion of Semi-Finished Aluminum Alloy 5083.“ *Hidraulica Magazine*, no. 4 (December 2021): 17-24.
[8] Szala, Miroslaw, Leszek Łatka, Mariusz Walczak, and Marcin Winnicki. “Comparative Study on the Cavitation Erosion and Sliding Wear of Cold-Sprayed Al/Al2O3 and Cu/Al2O3 Coatings, and Stainless Steel, Aluminium Alloy, Copper and Brass.” *Metals* 10*,* no. 7 (June 2020): 856.
[9] Tong, Zhaopeng, Jiafei Jiao, Wangfan Zhou, Yu Yang, Lan Chen, Huaile Liu, Yuzhou Sun, and Xudong Ren. “Improvement in cavitation erosion resistance of AA5083 aluminium alloy by laser shock processing.” *Surface and Coatings Technology* 377 (November 2019): 124799.
[10] Bordeasu, Ilare. *Cavitation erosion of materials* / *Eroziunea cavitaţională a materialelor.* Timişoara, Politehnica Publishing House, 2006.
[11] Micu, Lavinia Madalina. *Cavitation erosion behavior of duplex stainless steels* / *Comportarea la eroziune prin cavitatie a otelurilor inoxidabile duplex.* Doctoral thesis. Timisoara, 2017.
[12] Oanca, Victor Octavian. *Techniques for optimizing the resistance to cavitation erosion of CuAlNiFeMn alloys for the execution of naval propelle*rs / *Tehnici de optimizare a rezistenţei la eroziunea prin cavitaţie a unor aliaje CuAlNiFeMn destinate execuţiei elicelor navale*. Doctoral thesis. Timișoara, 2014.
[13] ***. “Standard method of vibratory cavitation erosion test.” *ASTM Standard G32*, 2016.
[14] Bordeasu, Ilare, Mircea Octavian Popoviciu, Victor Balasoiu, and Constantin Patrascoiu. “An Analytical Model for the Cavitation Erosion Characteristic Curves.” *Scientific Bulletin “Politehnica” University of Timişoara, Transaction of Mechanics* 49(63) (2004): 253-258.
[15] Franc, Jean-Pierre, François Avellan, Brahim Belahadji, Jean-Yves Billard, Laurence Briançon-Marjollet, Didier Fréchou, Daniel-H. Fruman, Ayat Karimi, Jean-Louis Kueny, and Jean-Marie Michel. *Cavitation. Physical mechanisms and industrial aspects / La Cavitation. Mécanismes physiques et aspects industriels*. Grenoble, Press Universitaires de Grenoble, 1995.
[16] Hammitt, Frederick G., and N.R. Bhatt. *Cavitation damage resistance of hardened steels*. Univ. Michigan, 1970: 1-36.

Experimental Research on the Influence of Factors on the Electricity Production of Thin-Film Photovoltaic Panels

Assoc. Prof. PhD. Eng. **Adriana TOKAR**[1*], Assis. Prof. Eng. **Dănuț TOKAR**[1], Eng. **Filip STOIAN**[2], R. A. PhD. student Eng. **Daniel MUNTEAN**[1]

[1] University Politehnica Timisoara

[2] Business Expert S.R.L.

* Corresponding author's e-mail address: adriana.tokar@upt.ro

Abstract: *Given the current context regarding environmental pollution, in which conventional installations also participate, the aim of this article is to analyse whether photovoltaic systems are a viable solution to help solve this problem. Thus, the article analyses the way in which the electricity production of photovoltaic installations is influenced by the aging of the photovoltaic cells that make it up, but also by certain natural factors (water droplets, shading caused by clouds). Experimental measurements were performed on a new ZY-S100 thin-film photovoltaic panel and then on an aged one (7 years of operation) using an MI 3109 EurotestPV Lite METREL. When it comes to the main problem addressed in the paper, the influence of the aging of photovoltaic cells on the efficiency of the photovoltaic panels, the measurements indicated that the aged panel suffered a 25% decrease in efficiency in the seven years of operation, which comes to a decrease of 3.57% for each year.*

Keywords: *Electricity, photovoltaic panels, thin-film, aging, natural factors influence*

1. Introduction

The utilisation of renewable energy sources (RES), together with the improvement of energy efficiency (EE), can contribute to the energy consumption reduction, greenhouse gas emission reduction and in consequence, to the prevention of dangerous climate changes. The advantages of using solar energy emerge from the fact that it is an endless energy source that is also non-polluting. The disadvantages of using solar energy are that the caption technology is yet insufficiently performant. Another disadvantage is solar panels have a low efficiency, and the solar energy varies depending on the time of the day, or year, the angle of incidence of the solar panels or the atmospheric conditions [1, 2, 3, 4].
The last decades had brought a radical change in the concept plan by becoming aware of the necessity to durably develop social and economic life and to promote renewable energy sources that are considered a key element. From all these sources, electricity that is obtained by converting solar energy seems one of the most promising energy sources, that in the present is based on the technology of three generations of photovoltaic panels built to resist a wide range of exterior temperature (-40ºC…80ºC) and can also withstand various environmental factors (rain, hail or snow). On the flip side, the shade from clouds and the low levels of radiation, due to cloudy skies, has up until this moment a considerable effect on the capacity of the panels to generate electrical energy due to their low efficient in these conditions [5, 6, 7, 8, 9, 10].
The article proposes an assessment of the production of energy when exposed to solar radiation and an estimation of the decreasing efficiency of electrical energy production of 7-year-old panels, but also of the effects made by clouds and rain droplets.

2. The evolution of photovoltaic panels

Currently, photovoltaic generators are a reality, functioning all around the globe, and even more, being the only energy source of energy for satellites and the International Orbital Station. Also, in many countries extensive programmes of research and subsidy to determine attractive prices for the selling electrical energy from solar panels. Both the problem of the availability of energy, it's cost and the negative influence of the energetic industry on the environment stimulated research and innovation in the renewable domain [11]. Lately, the conversion of solar energy with the help of

photovoltaic technology was often addressed by researchers under various aspects [12, 13, 14]. Thus, photovoltaic panels are built in a various range, starting from crystalline silicon panels (the first generation of cells) [15, 16, 17, 18], , panels with Thin Film photovoltaic cells made by applying a thin layer (thick of about several μm, in comparison with crystalline silicon panels that have a thickness of several hundreds of μm) of semiconductor material(amorphous silicon, cadmium telluride- Cadmium sulphide (CdTeS), gallium arsenide (GaAs)) and up to copper, indium and selenite (CIS) modules, copper, indium, gallium and selenite (CIGS) and copper, indium, gallium, selenite and sulphur (CIGSS) modules, technologies under study and development, in which silicon is replaced with special alloys [8, 9, 10].
The research and development of photovoltaic cells in the last 2 decades have led to the appearance on the market of third generation panels / modules, the technologies used being promising. Examples are organic photovoltaic (OPV) and hybrid pigmented sensitized (DSSC) cells. The third generation can be classified as follows: advanced inorganic thin film such as (CIS), organic solar cells that include fully organic and hybrid cells; and thermo-photovoltaic (POS) cells with low bandwidth potential but which can be used for both heat and power (CHP) systems [11].

3. The influence of the aging of thin-film photovoltaic panels and environmental factors upon the electrical energy production. CASE STUDY

3.1 Description of the experimental installation

The experimental arrangement was located in the courtyard of the Faculty of Constructions of the Polytechnic University of Timișoara. The stand that was used to perform the measurements consisted of: a metal support to position at a 45° inclination a new thin-film photovoltaic panel (module) ZY-S100 and later an aged one (that was operating for 7 years) of the same type and a test apparatus MI 3109 EurotestPV Lite METREL (from the LE laboratory, specializing in CONSTRUCTION INSTALLATIONS). To perform the experimental measurements, an ammeter clamp was used to measure current (cc / ac), a test probe, a probe for measuring the temperature of photovoltaic cells and a probe for measuring solar radiation, a resistance and two multimeters to be able to measure voltage, current and resistance when the installation is under load. The orientation of the stand used was towards the east (the only option available for the placement of the panels for a concrete installation).
The ZY-S100 thin-film photovoltaic panel can deliver a maximum power of 100W ± 3%, and the characteristics are presented in ANNEX 1. The type of panel for which the measurements were made, the preparation of the installation and the equipment used are shown in Fig.1, and the measurement diagram and connections is represented in Fig. 2 [19].

Fig. 1. Preparation of the test installation

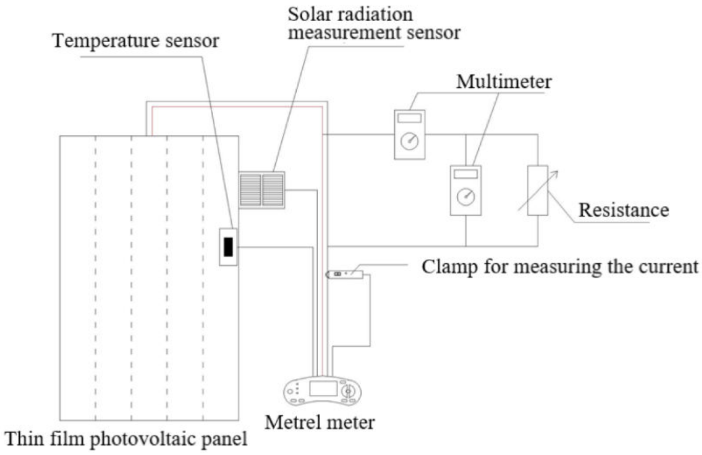

Fig. 2. The measurement and connection scheme

Thus, to obtain the experimental results was used a test device MI 3109 EurotestPV Lite METREL, two multimeters and a resistance that allowed the following measurements of the following parameters: direct current in photovoltaic installations, insulation resistance, continuity of PE conductors, open circuit voltage Uoc and current short circuit Isc, plotting the current-voltage curve IU of photovoltaic modules, irradiation, temperature of photovoltaic module, measurement of alternating current in photovoltaic installations, voltage, current and power, efficiency of photovoltaic modules [19].

3.2 The influence of environmental factors on efficiency

Two thin-film photovoltaic modules were tested for outdoor conditions for 4 days and the output power was monitored every hour. One of these modules was previously cleaned, having a free surface, without obstruction factors, and the other was affected by water droplets on its surface.
Temperature is a significant determining factor that affects the speed of electric flows through any given electric circuit. The daily power output, short circuit current and open circuit voltage of each studied module exposed to water droplets are illustrated in Fig. 3 showing the effects of raindrops on the output power, comparatively, between a new panel and an aged panel [19].

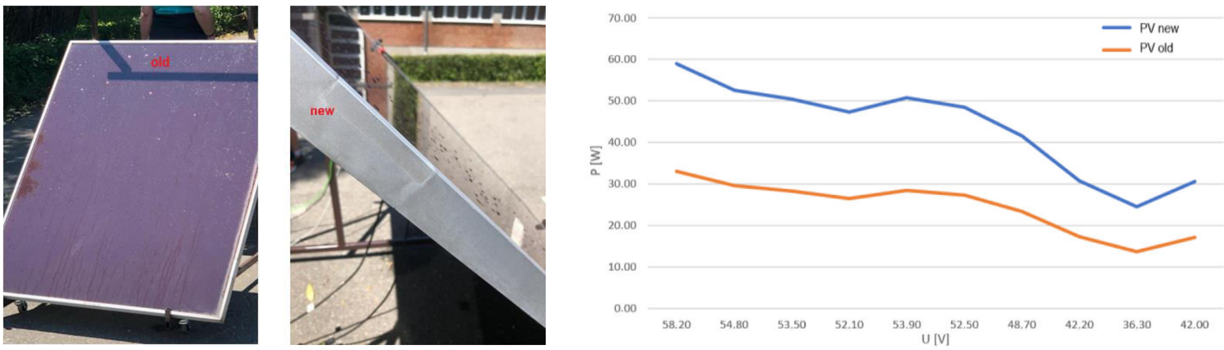

Fig. 3. The output power of a new panel and an old one both covered with water droplets

The water droplets lower the temperature of the photovoltaic module, which in turn increases the potential difference, thus improving the output power. To describe the impact of temperature on the efficiency of a photovoltaic module, the output voltage of a photovoltaic module can be estimated at a given temperature using the relation (1) [19]:

$$U_{oc,amb} = T_{coef} \cdot [(T_{STC} - T_{amb})] + U_{OC,STC} \quad (1)$$

where:

$U_{oc,amb}$ - open circuit voltage at the ambient temperature T_{amb}
$U_{oc,STC}$ - open circuit voltage at STC(standard testing conditions)

T_{STC}- temperature of the open circuit at STC

If $U_{oc,amb} = 0.33 \cdot (25 - T_{amb}) + 22.06$, the relation shows that, for the low ambient temperature, a high voltage would be obtained. There are two advantages to running water on the surface of the panel, namely: cooling and cleaning the panel. The cooling rate for photovoltaic cells is 2 °C / min, depending on the operating conditions. It can be seen that, regardless of the condition of the panel, new or old, the effects of the water droplets are the same [19].

3.3 The influence of the aging of photovoltaic cell on the efficiency

Azidi et al. [20] points out that in order to take into account the aging of photovoltaic modules, the effects of optical and electric degradation are taken into account. The degradation rate of αopt transmissivity (optical glass loss and encapsulation loss) and series resistance (damage of electric parts) αRs are defined with accelerated test results. Optical losses for both EVA encapsulant and glass are assessed by measuring the spectral hemispheric transmittance after 10 years of exposure with an annular sample extracted from outdated field modules. The transmittance reduction is calculated with spectral values in the wavelength range of 450-1200 nm. The rate of degradation of series strength is determined by taking into account a linear variation of the measured values obtained every 500 hours for an accelerated test at 85 ° C heat / 85% humidity performed on encapsulated silicon cells, assuming that 1000 hours of testing are equivalent to 20 years of use. The dispersion of the experimental values is ± 10% [19].

$$\tau(T) = \tau_0(-\alpha_{opt} \cdot T + 100\%) \quad (2)$$

$$R_S(T) = R_{S0}(+\alpha_{R_S} \cdot T + 100\%) \quad (3)$$

It should be noted that aging is a long-term phenomenon, and the laws of aging are defined on a large scale compared to the instant detection of MPP: ΔT >> Δt. The lifespan of a photovoltaic module is between 20 and 25 years, and that of an inverter is around 10 years. The results between the initial time and T = 20 years are compared. The DC / DC converter and the inverter should keep their properties constant over time to appreciate the effect of the degraded photovoltaic module [20].
As for the resistance of the photovoltaic module, it is increased due to the aging effect, and then it limits the output power. The decrease in power as a function of voltage is shown in Fig. 4 for a panel that operated for a period of t = 7 years.

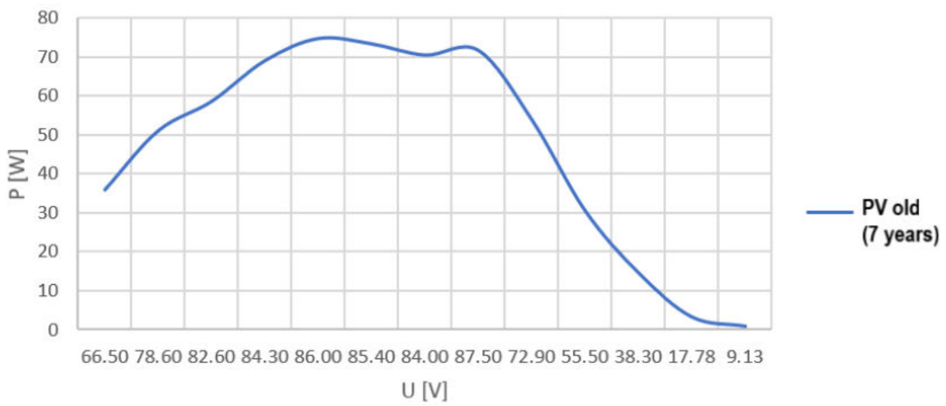

Fig. 4. Power in relation to voltage (t=7 year)

The temperature of the cells was also monitored, which led to the conclusion that the decrease in power is influenced when the module temperatures are higher. Temperatures measured at the surface of the panel are up to 50.8 ℃. The specialized literature indicates as a percentage the decrease of the efficiency of 1% / year for photovoltaic panels [20]. The appearance of the curves drawn for the period in which the recordings were made (4 days) is approximately the same, being comparable to the specialized literature, and for this reason it was represented in Fig. 4 power curve in relation to the voltage for a high degree of sunshine (cloudless sky).

3.4 The influence of clouds on the efficiency

During the days when the measurements took place, there were also periods when the sky was covered by clouds, which influenced the efficiency of the photovoltaic panels, which can be seen in Fig. 5. The measurements were performed hourly on a new photovoltaic panel.

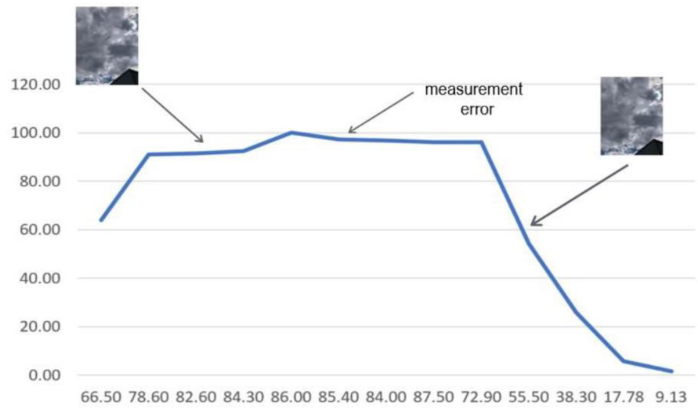

Fig. 5. The influence of clouds on the efficiency of a new photovoltaic panel

Cloud shading tends to be detrimental to the performance of photovoltaic modules. The cloud shading condition was considered one of the most significant sources of loss for photovoltaic installations. The best solution to this problem is to avoid shading as much as possible. The impact that shading has on the performance of the photovoltaic module depends on certain parameters such as the level of solar radiation and the distribution of shadows on the surface of the panel. The obtained results indicate that the output voltage of the photovoltaic panel decreases as the shaded surface increases. The maximum voltage value for the photovoltaic panel without shading was 86 V, and in the presence of shade due to clouds, the maximum voltage was 82.6 V, which indicates a decrease of 3.95% (Fig. 5.). The effects of clouds on the power curve are highlighted by images in Fig. 5 at the time they occurred [19].

3.5 The comparative analysis between the efficiency of old and new thin-film photovoltaic panels

Fig.6 compares the voltage variation and the voltage for a new panel and an old panel.

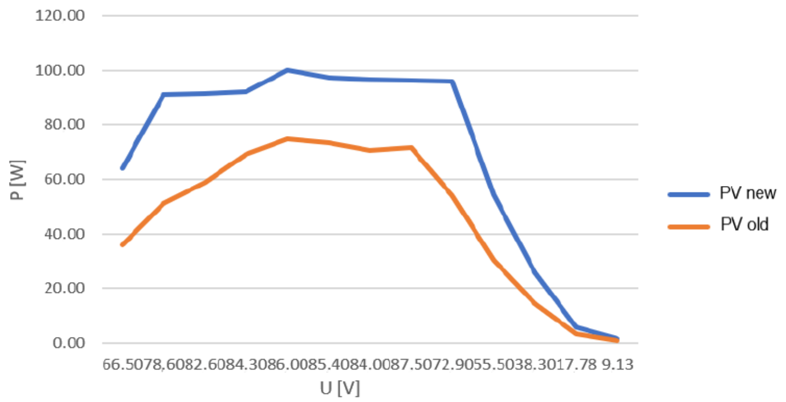

Fig. 6. The output power for a new and old panel

A decrease in the efficiency of the ZY-S100 thin-film panel of 25% can be observed, which means a decrease of 3.57 % for each year of operation [19].

Although the literature indicates a 1% decrease in yield per year for photovoltaic panels, the study shows that it is important to specify the type of panel and photovoltaic cells for which experimental measurements were performed.

4. Conclusions

In this paper, the impact of the aging of photovoltaic cells, the impact of clouds and the impact of water droplets on the surface of the panel on the electricity production of photovoltaic panels were studied. In order to achieve this goal, measurements were made regarding the output power of a new ZY-S100 thin-film photovoltaic panel and later on an identical (7 years) aged panel. Measurements and calculations have taken into account both the laws of aging and the uncertainty of the data.

Regarding the impact of water droplets on the surface of the panel, it was concluded that water droplets lower the temperature of the photovoltaic module, which in turn increases the potential difference, thus improving the output power. It has also been observed that regardless of the condition of the panel, new or old, the effects of water droplets are the same.

Measurements on the photovoltaic panel when the sky was overcast indicated that cloud shading tends to be detrimental to the performance of photovoltaic modules, with the panel's output voltage decreasing as the shaded area increases. At the same time, from measurements and calculations it was observed that, for the panels used in the presence of clouds, there was a decrease of the output voltage of 3.95%.

The test results regarding the impact of the aging of photovoltaic cells on the electricity production of ZY-S100 thin-film panels show a 25% decrease in panel efficiency in the 7 years of operation, which means a decrease of 3.57% for each year of operation. Although the literature indicates a 1% decrease in efficiency per year for photovoltaic panels, the study shows that it is important to specify the type of panel and photovoltaic cells for which experimental measurements were performed.

References

[1] European Commission. "Climate change consequences." Accessed February 11, 2022. https://ec.europa.eu/clima/climate-change/climate-change-consequences_en.

[2] ***. "What is global warming"/"Ce este incalzirea globala." Accessed February 2, 2022. https://meteo.ro/articole/Ce-este-incalzirea-globala/33.

[3] Dumitrescu, Alexandru. "Determining the potential of energy resources"/"Determinarea potențialului resurselor de energie." Administratia Nationala de Meteorologie. *Project: "The Green Path to Sustainable Development"/Proiect: "Calea Verde spre Dezvoltare Durabilă"*, 2016. Accessed February 10, 2022. http://caleaverde.ro/wp-content/uploads/2016/08/Determinarea-potentialelor-resurselor-de-energie-eoliene-si-solare.pdf.

[4] Habbane, A.Y., J.C. McVeigh, and S.O.I. Cabawe. "Solar radiation model for hot dry arid climates." *Applied Energy* 23, no. 4 (1986): 269-279.

[5] Proctor, Darrell. "New Technology Keeps Solar on Track." *Power Magazine*, 2020. Accessed February 8, 2022. https://www.powermag.com/new-technology-keeps-solar-on-track/.

[6] Ibn-Mohamed, T., S. C. L. Koh, I.M. Reaney, A. Acquaye, G. Schileo, K. B. Mustapha, and R. Greenough. "Perovskite solar cells: An integrated hybrid lifecycle assessment and review in comparison with other photovoltaic technologies." *Renewable and Sustainable Energy Reviews* 80 (December 2017): 1321-1344.

[7] So, Franky. "The Evolution of Solar Technology - How Photovoltaic Technology Has Developed and Why Nanotechnology May Influence the Future." *AltEnergyMag*, May 26, 2020. Accessed February 14, 2022. http://www.becker-posner-blog.com/2012/02/is-capitalism-in-crisis-becker.html.

[8] Guillemoles, J. F., T. Kirchartz, D. Cahen, and U. Rau. "Guide for the perplexed to the Shockley–Queisser model for solar cells." *Nature Photonics* 13, no. 8 (August 2019): 501–505.

[9] Alley, Nigel John. *New Architectures and Designs for Organic Photovoltaics*. Doctoral thesis. Dublin City University, 2012.

[10] Kaltenbrunner, M., M. S. White, E.D. Głowacki, T. Sekitani, T. Someya, N. S. Sariciftci, and S. Bauer. "Ultrathin and lightweight organic solar cells with high flexibility." *Nature Communications* 3 (April 2012): 770.

[11] Bică, Marin. *Sisteme fotovoltaice (Suport de curs) Partea I* /*Photovoltaic systems* (*Course support) Part 1*. Bucharest, 2019.

[12] Banu, Ioan Viorel. *Scientific research report: Current state of research on the integration of photovoltaic sources in electricity networks/Raport de cercetare ştiinţifică: Stadiul actual al cercetărilor ce privesc integrarea surselor fotovoltaice în rețelele electrice*. Doctoral thesis. Technical University "Gheorghe Asachi" Iasi, 2013.

[13] ABB. "Technical Application Papers No.10. Photovoltaic plants." Accessed January 14, 2022. https://search.abb.com/library/Download.aspx?DocumentID=1SDC007109G0202&LanguageCode=en&DocumentPartId=&Action=Launch.
[14] Greenpeace. "energy - [r]evolution. A Sustainable EU 27 Energy Outlook." Accessed February 21, 2022. https://www.greenpeace.org/static/planet4-slovenia-stateless/2019/03/a0493fe0-a0493fe0-er-2012-embargo.pdf.
[15] Dias, Pablo Ribeiro, Mariana Gonçalves Benevit, and Hugo Marcelo Veit. "Photovoltaic solar panels of crystalline silicon: Characterization and separation." *Waste Management & Research: The Journal for a Sustainable Circular Economy* 34, no. 3 (March 2016): 235-245.
[16] Taşçıoğlu, Ayşegül, Onur Taşkın, and Ali Vardar. "A Power Case Study for Monocrystalline and Polycrystalline Solar Panels in Bursa City, Turkey." *International Journal of Photoenergy*, vol. 2016 (March 2016): Article ID 7324138.
[17] Enaganti, Prasanth K., and Sanket Goel. "Study of Submerged Mono-and Poly-Crystalline Silicon Solar Cells with Split Spectral Ranges Using Optical Filters." *ECS Journal of Solid State Science and Technology* 9, no. 7 (August 2020): Article ID 075005.
[18] Lojpur, Vesna, Miodrag Mitrić, and Ivana Lj Validžić. "The improved photovoltaic response of commercial monocrystalline Si solar cell under natural and artificial light by using water flow lens (WFL) system." *International Journal of Energy Research* 43, no. 8 (March 2019): 3507-3515.
[19] Stoian, Filip, and coordinator Adriana Tokar. *The influence of aging thin-film photovoltaic panels on electricity production*. Dissertation thesis, 2021, University Politehnica of Timisoara.
[20] Azizi, Amina, Pierre-Olivier Logerais, Amar Omeiri, Adel Amiar, Abderafi Charki, Olivier Riou, Fabien Delaleux, and Jean-Felix Durastanti. "Impact of the aging of a photovoltaic module on the performance of a grid-connected system." *Solar Energy* 174 (2018): 455 – 454.

ISSN 1453 – 7303 **"HIDRAULICA" (No. 1/2022)**
Magazine *of Hydraulics, Pneumatics, Tribology, Ecology, Sensorics, Mechatronics*

Determining the Relation between the Size of the Air Bubble Immersed in Water and the Dissolved Oxygen Concentration

PhD Std. **Marilena Monica BOLTINESCU (ROZA)**[1], Prof. Dr. Eng. **Nicolae BĂRAN**[1], ȘI. Dr. Eng. **Mihaela CONSTANTIN**[1]*

[1] University Politehnica of Bucharest

* i.mihaelaconstantin@gmail.com

Abstract: *Starting from the equation of oxygen transfer rate to water, a mathematical connection is established between the concentration of dissolved oxygen in the water and the diameter of the air bubble introduced in water.*
For diameters of the oxygen introduction orifice in water between 0.05 ÷ 0.1 mm, the diameter of the air bubble entering the water is calculated and the variation of the dissolved oxygen concentration in the water as a function of time is exposed.

Keywords: *Water aeration, dissolved oxygen, fine bubbles, oxygen transfer.*

1. Introduction

Aeration is necessary to improve water quality, to avoid the occurrence of oxygen deficiency in systems where there is a biochemical consumption of oxygen above the self-aeration capacity of water, to eliminate toxic gases that can be found in water and in the water treatment process [1].
The main purpose of water aeration, regardless of the industry and the reason for its use, is to increase or maintain an optimal level of dissolved oxygen in a body of water.
The oxygen needed for the aeration process is taken from the atmospheric air and introduced into the water. For this aeration to be effective, a uniform dispersion of air must be ensured throughout the body of water in a tank or basin; the air must be evenly distributed to provide the required oxygen. Dissolved oxygen content is the most important indicator of water quality. Fish, for example, need up to 5mg / dm^3 of dissolved oxygen to survive. The amount of oxygen in the water is consumed by various biological or chemical processes. The amount of water left in these processes depends on the rate of deoxygenation and the rate of oxygenation (aeration), which can occur naturally or artificially. By aeration of water is meant the transfer of oxygen from atmospheric air to water, which is, in fact, a phenomenon of the transfer of a gas into a liquid. The most common method of removing organic impurities under the action of an aerobic bacterial biomass is to introduce gaseous oxygen into the wastewater. By introducing air into the water there is an oxygenation of the water, a process called aeration.
The term oxygenation is mainly used when introduced into water [1]:
- A mixture of air + pure oxygen from a cylinder.
- Pure oxygen from cylinders.
- Air with low nitrogen content (95% O_2 and 5% N_2) delivered by oxygen concentrators.
- Air + ozone given by ozone generators.

The notion of dissolved oxygen in water becomes clear from the analysis of Figure 1.

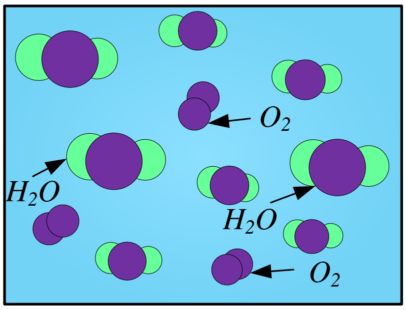

Fig. 1. View of molecular structure: dissolved oxygen

Figure 1. shows that each molecule of water consists of one molecule of oxygen connected to two molecules of hydrogen (the green sphere coupled to two purple spheres).
Dissolved oxygen molecules (purple spheres) can be found among water molecules. The maximum amount of oxygen that can be dissolved in water depends on several physical and chemical parameters, such as: atmospheric pressure, water temperature, water salinity, the degree of water turbulence [2] [3].
Water temperature is an important factor, so the warmer the water, the lower the dissolved oxygen concentration. Therefore:
- at t = 10ºC, in clean, fresh water, an amount of 11.3 mgO_2 / dm^3 can be absorbed;
- at t = 25ºC, in clean water, only 8.3 mgO_2 / dm^3 can be absorbed.

2. The equation of the oxygen transfer rate to water

The rate of transfer of dissolved oxygen in water is given by the relation [3] [4]:

$$\frac{dC}{d\tau} = a \cdot k_L \cdot \left(C_s - C_0\right)\ [kg / m^3 s] \tag{1}$$

where:
dC / dτ - rate of change of dissolved oxygen concentration in water (rate of oxygen transfer to water);
ak_L - volumetric mass transfer coefficient [s^{-1}];
C_s - mass concentration of oxygen at saturation in the liquid phase [kg / m^3];
C - current mass oxygen concentration in the liquid phase [kg / m^3].
The term "ak_L" includes:
k_L- mass transfer coefficient [m / s];
a - specific interphase contact surface:

$$a = \frac{A}{V}\left[\frac{m^2}{m^3}\right] \tag{2}$$

where:
A- gas bubble area [m^2];
V - the volume of the biphasic system (air + water) [m^3];
If boundary conditions C = C_0 are imposed for τ = 0, equation (1) can be integrated [5] [6] [7]:

$$\frac{dC}{C_s - C} = a \cdot k_L\, d\tau \tag{3}$$

In the hypothesis that C <C_s, after integration, it results:

$$-ln\left(C_s - C\right) = a \cdot k_L \cdot \tau + ct \tag{4}$$

The constant is obtained from the limit condition: C = C_0 for τ = 0
and has the value:

$$ct = -ln\left(C_s - C_0\right) \tag{5}$$

Introducing (5) in (3) one can obtain:

$$-ln\left(C_s - C\right) = a \cdot k_L \cdot \tau - ln\left(C_s - C_0\right) \tag{6}$$

$$ln\left(C_s - C\right) = ln\left(C_s - C_0\right) - a \cdot k_L \cdot \tau \tag{7}$$

$$ln\left(C_s - C\right) = ln\left(C_s - C_0\right) + ln\, e^{-a \cdot k_L \cdot \tau} \tag{8}$$

$$ln\left(C_s - C\right) = ln(\left(C_s - C_0\right) \cdot e^{-a \cdot k_L \cdot \tau}$$

$$C_s - C = ln(\left(C_s - C_0\right) \cdot e^{-a \cdot k_L \cdot \tau}$$

$$C = C_s - \left(C_s - C_0\right) \cdot e^{-a \cdot k_L \cdot \tau} \tag{9}$$

τ=0

3. Determining the mathematical relation between the diameter of the air bubble at the orifice exit and the variation of the dissolved oxygen concentration in the water as a function of time

The equation for the rate of oxygen transfer to water is rewritten as follows:

$$C_o = C_s - \frac{C_s - C_0}{e^{a \cdot k_L \cdot \tau}} \tag{10}$$

The value of the interfacial area, considering the air bubble as a small sphere of radius R, is [1] [8]:

$$a = \frac{A}{V} = \frac{4\pi R^2}{\frac{4}{3}\pi R^3} = \frac{4\pi (d_b/2)^2}{\frac{4}{3}\pi (d_b/2)^3} = \frac{6}{d_b} \tag{11}$$

where d_b = the bubble diameter immediately at the orifice exit.
The equation of the rate of oxygen transfer to water is rewritten as follows:

$$C_o = \frac{C_s - (C_s - C_0)}{e^{a \cdot k_L \cdot \tau}} = C_s - \frac{C_s - C_0}{e^{a \cdot k_L \cdot \tau}} \tag{12}$$

Given that C_s, C_0, k_L, are constant, the relation (10) can be written as:

$$C_{o_2} = C_{t,1} - \frac{C_{t,2}}{e^{C_{t,3} \cdot \frac{\tau}{d_b}}} \tag{13}$$

where $C_{t,1}$, $C_{t,2}$, $C_{t,3}$ is constant.
From this relation one can see the following:
- When d_0 decreases from 0.1 mm to 0.05 mm, the value of d_b will decrease and τ will increase from 1 to 120 minutes.
- As a result, the size $e^{C_{t,3} \cdot \frac{\tau}{d_b}}$ will increase during aeration (τ = 1 ,,,,,, 120 min).
- As a result, the fraction in relation (13) will decrease during aeration, so C_{o_2} will increase during aeration if d_b decreases [9].

Thus, it is mathematically demonstrated that when the water inlet decreases (d_0 = 0.1 → 0.05 mm) the value of the dissolved oxygen concentration in the water will increase [10] [11].

4. Determining the mathematical relation between the orifice diameter (d_0) in the perforated plate and the air bubble diameter (d_b) at the water entrance

The air bubble radius at the exit of the orifice (R_b) is given by the relation [8] [9]:

$$R_0 = \left(\frac{3}{2} \cdot \frac{r_0 \cdot \sigma}{\rho_l \cdot g} \right)^{\frac{1}{3}} \tag{14}$$

where: σ = surface tension water coefficient; σ = $73 \cdot 10^{-3}$ N / m
ρ_l = water density: ρ = 10^3 kg / m^3
g = gravitational acceleration; g = 9.81 m / s^2
r_0 = orifice radius [m].

$$d_b = 2 \cdot R_0 = 2 \cdot \left(\frac{3}{2} \cdot \frac{r_0 \cdot \sigma}{\rho_l \cdot g} \right)^{\frac{1}{3}} \tag{15}$$

Replacing d_0, the data in table 1 results in:

Table 1

Version no.	1	2	3	4	5	6
$d_o \cdot 10^{-3}$ [m]	0.05	0.06	0.07	0.08	0.09	0.10
$d_b \cdot 10^{-3}$ [m]	1.324	1.407	1.461	1.528	1.589	1.646

Table 1 shows that as the orifice diameter (d_0) in the perforated plate increases by 0.05 → 0.1 mm, the diameter of the air bubble when detached from the plate increases from 1.324 mm to 1.646 mm.

5. The results of theoretical and experimental researches

a) For version I, in which the orifice diameter in the perforated plate is 0.1 mm, the initial data used for the theoretical calculation and for performing the experimental measurements are presented:
V_{H2O} = 0.125 m^3; d_b = 0.1 mm
H = 500 mm H_2O
C_0 = 5.84 mg / dm^3
t_{H2O} = 24 ° C → C_s = 8.4 mg / dm^3
p_{air} = 573 mm H_2O; t_{air} = 24.1 °C
τ = 120 min
b) For version II, the same data are maintained, only d_b = 0.05 mm is modified.
To determine the change over time in the dissolved oxygen concentration in water, a computation program was prepared, the logical diagram of which is shown in Figure 2.

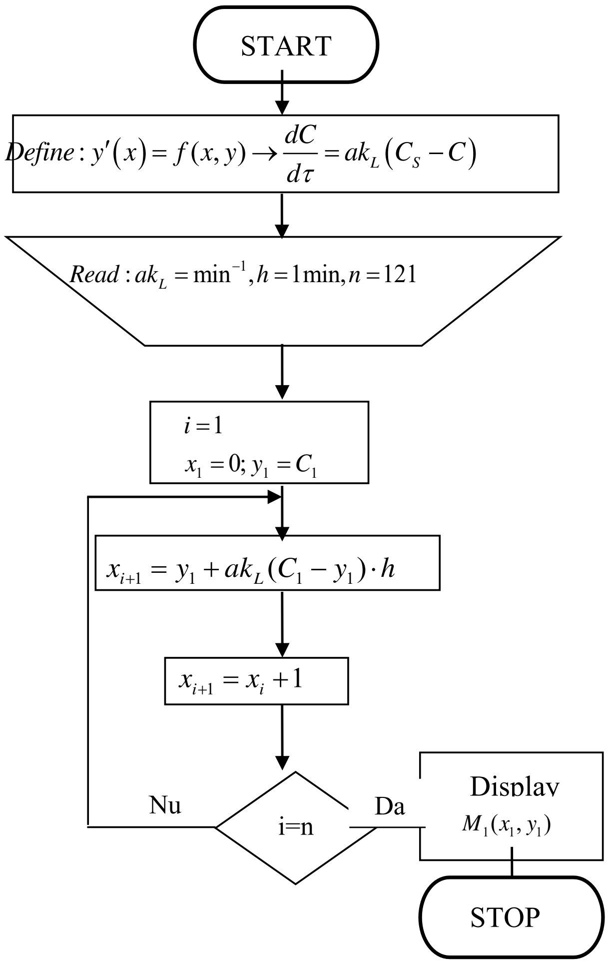

Fig. 2. Logical computation scheme for the numerical integration of the differential oxygen transfer rate equation

Following the computation program, curves 1 from figures 5 and 6 were constructed.
The scheme of the experimental installation and the operation of a fine bubble generator are shown in Figures 3 and 4.

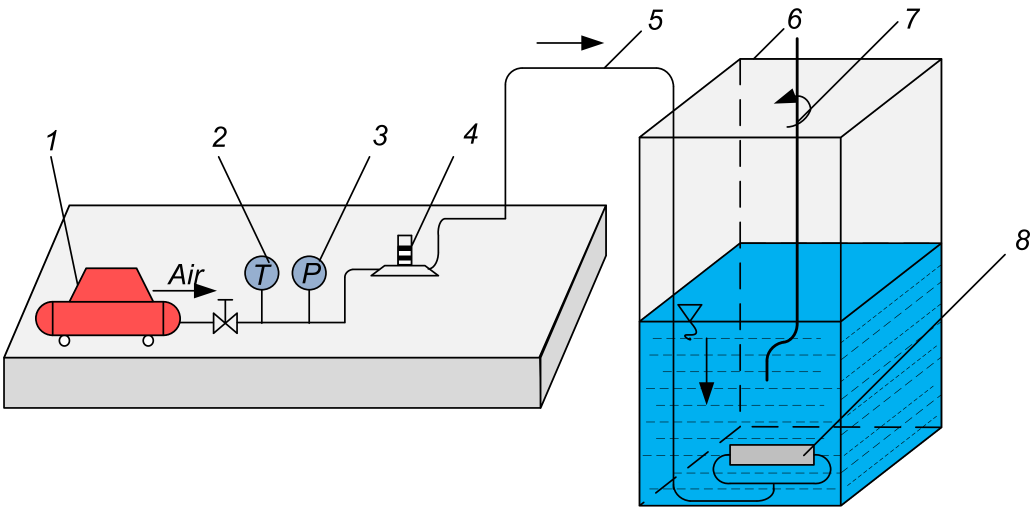

Fig. 3. Scheme of the installation for the introduction of atmospheric air into water:
1 - electrocompressor; 2 - digital thermometer; 3 - digital manometer; 4 - rotameter; 5 - air transport pipe; 6 - water tank; 7 - oxygenometer probe; 8 - fine bubble generator

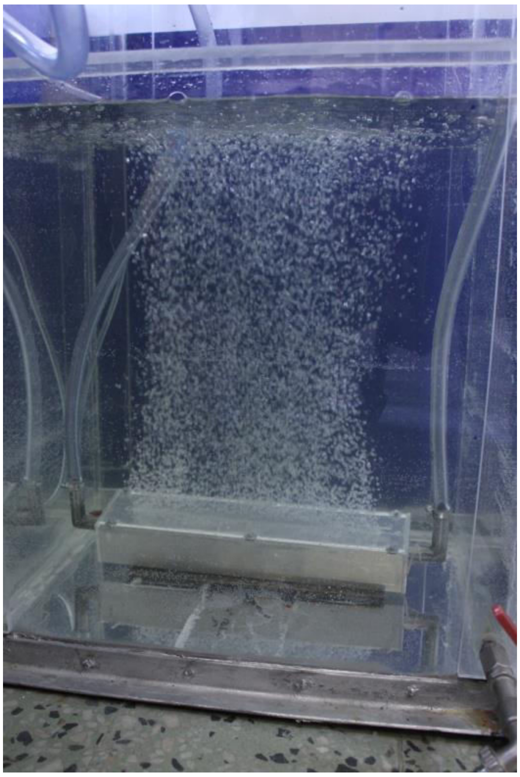

Fig. 4. Fine bubble generator in function

6. Researches methodology

Performing the measurements involves the following steps:

1. Check that the 132 orifices function, i.e., the atmospheric air is introduced into the bubble generator;
2. Fill the tank with water up to H = 500 mm H_2O;
3. Measure C_0, tH2O, t_{air};
4. Insert the fine bubble generator into the water tank and note the time (τ);
5. Every 15 minutes, take the fine bubble generator out of the tank and measure the dissolved oxygen concentration; subsequently, reinsert the fine bubbles generator in the water tank.

6. When a horizontal level of the function C = f (τ) is reached, the measurements stop, with the condition: C ≈ Cs;
7. From previous researches [14] [15][16], the concentration of dissolved oxygen in water tends to saturate after two hours. Therefore, the measurement of the oxygen concentration will be performed at the moments: 15, 30, 45, 60, 75, 90, 105, 120 minutes.
8. At the end of the measurements, clean the oxygenometer probe and drain the water from the tank.
Following the experimental measurements for version I, the data in Table 2 were obtained.

Table 2: Values of dissolved oxygen concentration in water as a function of time

τ [min]	0	15	30	45	60	75	90	105	120
$\dot{V}_{air}[dm^3/h]$	600	600	600	600	600	600	600	600	600
$\dot{V}_{IO_2}=0.21\cdot 600=126\,[dm^3/h]$	126	126	126	126	126	126	126	126	126
$\dot{V}_{O_2}$ from other sources	0	0	0	0	0	0	0	0	0
t_{H2O} [°C]	23.7	23.7	23.7	23.7	23.7	23.7	23.7	23.7	23.7
t_{air} [°C]	24.1	24.1	24.1	24.1	24.1	24.1	24.1	24.1	24.1
C_0 [mg/dm³]	5.84	5.84	5.84	5.84	5.84	5.84	5.84	5.84	5.84
C_s [mg/dm³]	8.4	8.4	8.4	8.4	8.4	8.4	8.4	8.4	8.4
C [mg/dm³]	5.84	6.89	7.65	8.01	8.10	8.26	8.31	8.35	8.39

Based on the theoretical and experimental calculation results, curves 1 and 2 were drawn in Fig.5.

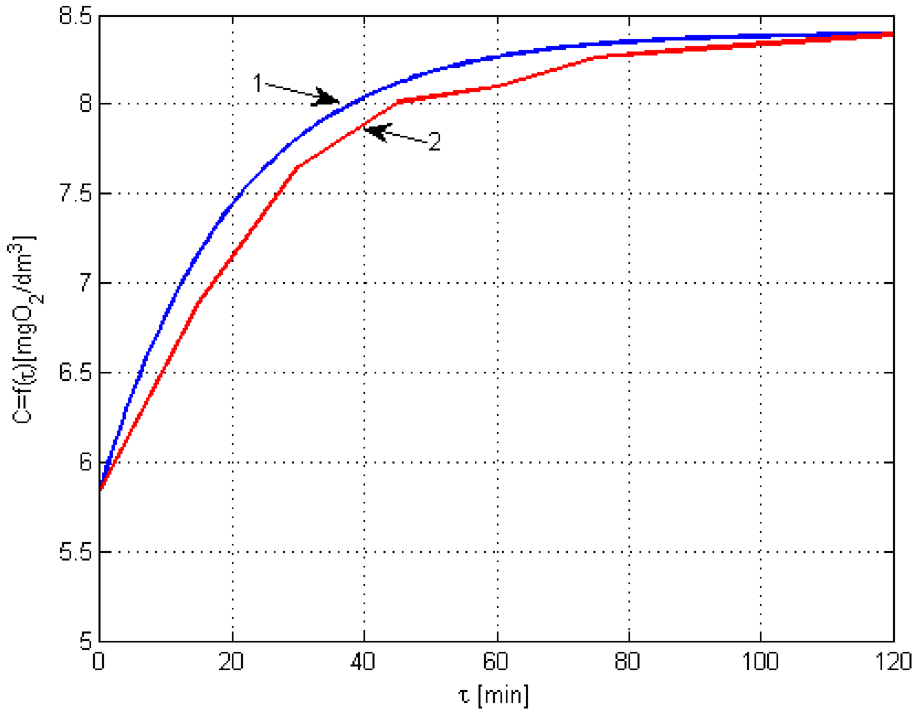

Fig. 5. Variation of the dissolved oxygen concentration in water over time for version I.
1 - curve drawn based on theoretical data (for Φ = 0.1);
2 - curve drawn based on experimental data (for Φ = 0.1)

Figure 5 shows that the differences between the two curves are very small, which demonstrates the correctness of the researches.
For version II (d_0 = 0.05 mm), following the experimental measurements, the data from table 3 were obtained:

Table 3: Values of dissolved oxygen concentration in water as a function of time

τ [min]	0	15	30	45	60	75	90	105	120
$\dot{V}_{air}[dm^3/h]$	600	600	600	600	600	600	600	600	600
$\dot{V}_{IO_2} = 0.21 \cdot 600 = 126\,[dm^3/h]$	126	126	126	126	126	126	126	126	126
$\dot{V}_{O_2}$ from other sources	0	0	0	0	0	0	0	0	0
t_{H2O} [°C]	19.5	19.5	19.5	19.5	19.5	19.5	19.5	19.5	19.5
t_{air} [°C]	23.5	23.5	23.5	23.5	23.5	23.5	23.5	23.5	23.5
C_0 [mg/dm³]	5.84	5.84	5.84	5.84	5.84	5.84	5.84	5.84	5.84
C_s [mg/dm³]	9.2	9.2	9.2	9.2	9.2	9.2	9.2	9.2	9.2
C [mg/dm³]	5.84	7.9	8.2	8.35	8.53	8.71	8.75	8.85	9.00

Based on the theoretical and experimental calculation results, curves 1 and 2 were drawn in Fig. 6.

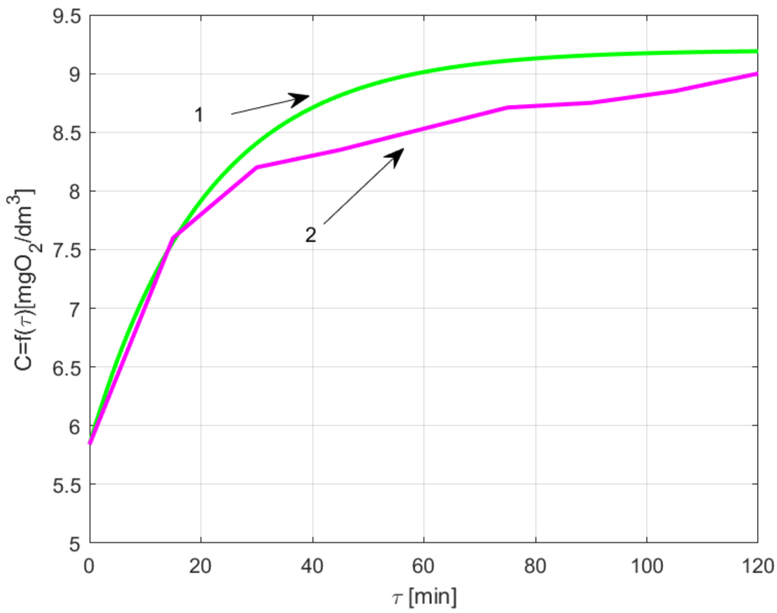

Fig. 6. Variation of dissolved oxygen concentration in water over time for version II
1 - curve drawn based on theoretical data Φ = 0.05;
2 - curve drawn based on experimental data Φ = 0.05

By comparing the experimental data obtained for the two versions, the following graph was obtained, shown in Figure 7:

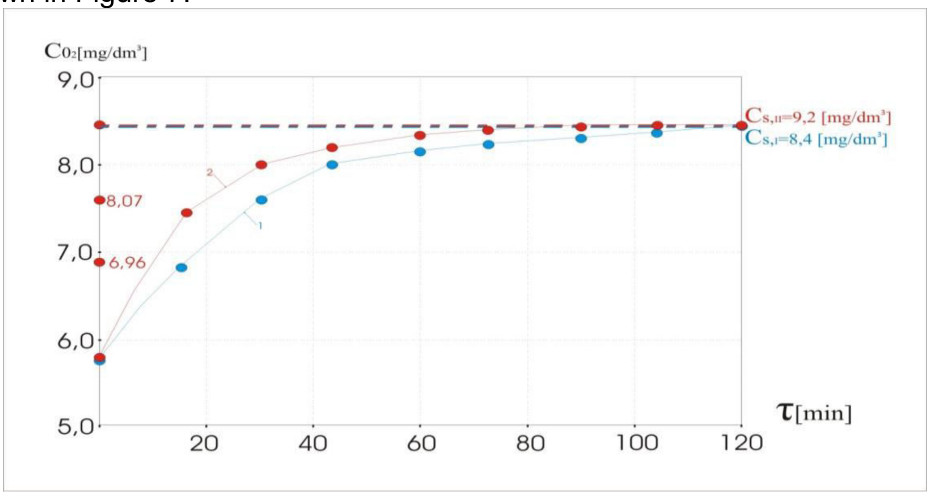

Fig. 7. The modification in time of the dissolved oxygen concentration in water C_{O2} = f (τ) for the two versions

7. Conclusions

- From the previous calculations, one can notice that as the orifice diameter in the perforated plate of the FBG increases, the diameter of the bubble immersed in water also increases. This leads to a change in the allure of the curve C = f (τ).
- The dissolved oxygen concentration in the water increases rapidly as the diameter of the air bubble that enters the water decreases.
- The realization of the fine bubble generator was made possible using micro technologies, which made it possible to make orifices with ø = 0.1 mm and ø = 0.05 mm, respectively, in the FBG perforated plate.
- The aim is to achieve a new stage, namely the use of nanotechnologies in the construction of water aeration equipment.

References

[1] Tănase, E. Beatrice*. The influence of the composition of the gas blown in water on the dissolved oxygen content / Influența compoziției gazului insuflat în apă asupra conținutului de oxigen dizolvat*. Doctoral thesis, Politehnica University of Bucharest, Faculty of Mechanics and Mechatronics, 2017.
[2] Căluşaru, I. M. *The influence of the physical properties of the liquid on the efficiency of the oxygenation processes* / *Influenţa proprietăţilor fizice ale lichidului asupra eficienţei proceselor de oxigenare*. Doctoral thesis, Politehnica University of Bucharest, Faculty of Mechanics and Mechatronics, 2014.
[3] Pătulea*,* Al. S. *The influence of functional parameters and the architecture of fine bubble generators on the efficiency of aeration installations* / *Influenţa parametrilor funcţionali şi a arhitecturii generatoarelor de bule fine asupra eficienţei instalaţiilor de aerare*. Doctoral thesis, Politehnica University of Bucharest, Faculty of Mechanics and Mechatronics, 2012.
[4] Oprina, G. *Contributions to the hydro-gas-dynamics of porous diffusers* / *Contribuţii la hidro-gazo-dinamica difuzoarelor poroase*. Doctoral thesis, Politehnica University of Bucharest, Faculty of Power Engineering, 2007.
[5] Antia, H. M. *Numerical Methods for Scientists and Engineers*. Basel, Birkhauser Publisher, 2nd edition, 2002.
[6] Shampine, L. F., and M. K. Gordon. *Computer Solution of Ordinary Differential Equations: The Initial Value Problem*. San Francisco, W.H. Freeman Press, 1975.
[7] Recktenwald, G. *Numerical Integration of Ordinary Differential Equations for Initial Value Problems*. Portland, Oregon, Portland State University, Department of Mechanical Engineering, 2006.
[8] Oprina, G., I. Pincovschi, and Gh. Băran. *Hydro-Gas-Dynamics Aeration systems equipped with bubble generators* / *Hidro-Gazo-Dinamica Sistemelor de aerare echipate cu generatoare de bule*. Bucharest, Politehnica Press, 2009.
[9] Droste, L. R. *Theory and Practice of Water and Wastewater Treatment*. Hoboken, New Jersey, John Wiley & Sons, Inc., 1996.
[10] Miyahara, T., Y. Matsuha, and T. Takahashi. "The size of bubbles generated from perforated plates." *International Chemical Engineering* 23 (1983): 517-523.
[11] Băran, N., I. M. Căluşaru, and G. Mateescu. "Influence of the architecture of fine bubble generators on the variation of the concentration of oxygen dissolved in water." *Buletinul Stiintific al Universitatii Politehnica din Bucuresti, seria D, Inginerie Mecanică* 75, no. 3 (2013): 225-236.
[12] Houcque, David. *Applications of MATLAB: Ordinary Differential Equations (ODE)*. Ilinois, Robert R. McCormick School of Engineering and Applied Science, Northwestern University, 2007.
[13] Pătulea, Alexandru, Ionela Mihaela Căluşaru, and Nicolae Băran. "Reasearches regarding the measurements of the dissolved concentration in water." *Advanced Materials Research* 550-553 (*Advances in Chemical Engineering II*) (2012): 3388-3394 doi:10.4028/www.scientific.net/AMR.550-553.3388.
[14] Căluşaru-Constantin, M., E. B. Tănase, N. Băran, and Rasha Mlisan-Cusma. "Researches Regarding the Modification of Dissolved Oxygen Concentration in Water." *IJISET - International Journal of Innovative Science, Engineering & Technology* 1, no. 6 (2014): 228-231.
[15] Constantin, M., N. Băran, and B. Tănase. "A New Solution for Water Oxygenation." *International Journal of Innovative Research in Advanced Engineering (IJIRAE)* 2, no. 7 (2015): 49-52.

ISSN 1453 – 7303 “HIDRAULICA” (No. 1/2022)
Magazine of Hydraulics, Pneumatics, Tribology, Ecology, Sensorics, Mechatronics

Use of a Cylinder with Two Piston Rods

Eng. **Cătălin FRĂȚILĂ**[1], Dr. eng. **Tiberiu AXINTE**[1,*], Eng. **Roxana DAMIAN**[1],
Dr. math. **Elena CURCĂ**[1], Eng. **Diana DUMITRAȘ**[1]

[1] Research and Innovation Center for Navy, Romania

* tibi_axinte@yahoo.com

Abstract: *This paper presents aspects related to the use of cylinders with two piston rods. Beside the cylinder with two piston rods, there is also a pneumatic actuator. This actuator is a cylindrical metal machine, which guides with two piston rods in a straight-line, a reciprocating movement in a cylinder. In this article, four circuits for cylinders with two piston rods, both pneumatic and electro-pneumatic circuits are presented. The first pneumatic circuit is a simple one and has only one cylinder with two piston rods. The second pneumatic circuit has two cylinders with two piston rods. Furthermore, the first electro-pneumatic scheme is endowed with logical modules. The second electro-pneumatic scheme is equipped with Grafcet PLC. It should be noted that all circuits have various pneumatic devices: air supply, lamps in cold, strong wind or storm fishing conditions. The design and simulation of the pneumatic circuits in this manuscript is done using FluidSim software from Festo.*

Keywords: *Piston, rod, pneumatic, electrical, scheme, circuit*

1. Introduction

In practice, a cylinder with two piston rods can be used twofold: it can replace other types of pneumatic cylinders and also can be used in various industrial machinery and pneumatic tools.
Moreover, because the advantage it has, having the same construction height, the cylinder with two piston rods transmits at least twice the force compared to standard cylinders, [1].
Construction of this pneumatic actuator is compact, Fig. 1.

Fig. 1. Cylinder with two piston rods

In pneumatic and electro-pneumatic schemes, the cylinders with two rods is represented by a specific symbol, Fig. 2.

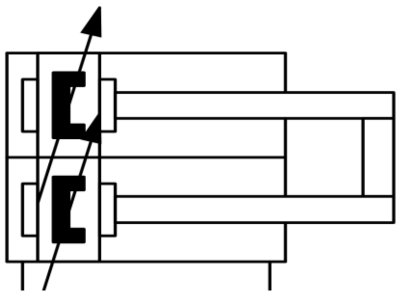

Fig. 2. Symbol of cylinder with two piston rods

This cylinder has two piston rods that move in parallel and that are coupled by a double trestle, [1].

The main characteristics of the cylinder with two piston rods are: low noise emission, dust emission, compact units, corrosion-resistant, easy and ready-to-install, etc.
The actuator guarantees small torsion when positioning and moving assemblies and tools.
Therefore, coming along in the same construction height, the cylinder with two piston rod conveys a double force as compared to standard cylinders.

2. The cylinder with two piston rods in the pneumatic circuits

A pneumatic installation is an interconnected set of devices that converts compressed air into mechanical work, [2].
In the table below there are given the component devices used in the first pneumatic scheme.

Table 1: The devices of the first pneumatic scheme

Description	Number of components
Compressed air supply	1
5/2 way valve	1
Air filter	1
Throttle valve	2
Cylinder with two piston rods	1

The first pneumatic circuit studied by authors has one cylinder with two piston rods, Fig. 3.

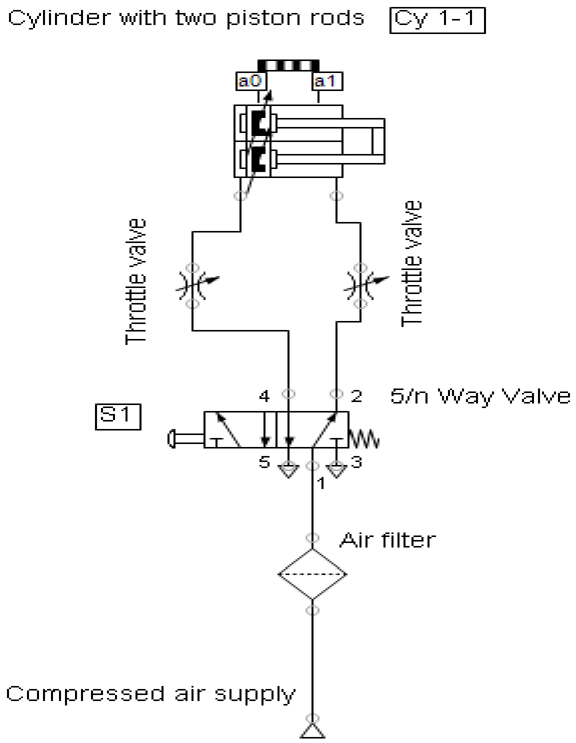

Fig. 3. First pneumatic circuit using one actuator

The first pneumatic circuit operates only if operator presses S1 button. This button belongs to the 5/2 way valve with spring. Then, two piston rods move from point a0 to point a1. After that, those two piston rods return from point a1 to point a0, because the 5/2 way valve has a spring, Fig.4.

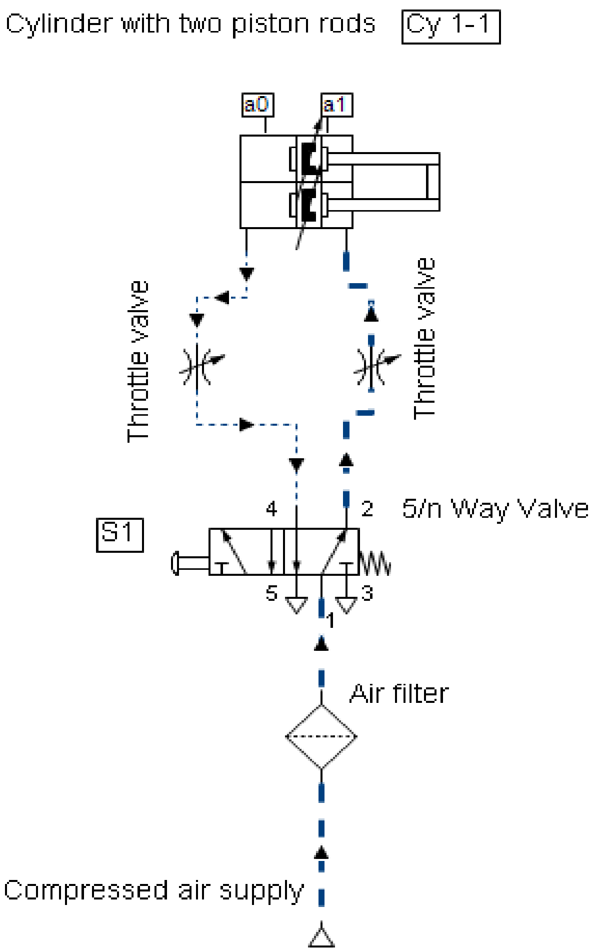

Fig. 4. First pneumatic scheme with one actuator

The diagrams below show variation of the position and velocity. These functional parameters belong to a cylinder with two piston rods (Cy 1-1), Fig. 5.

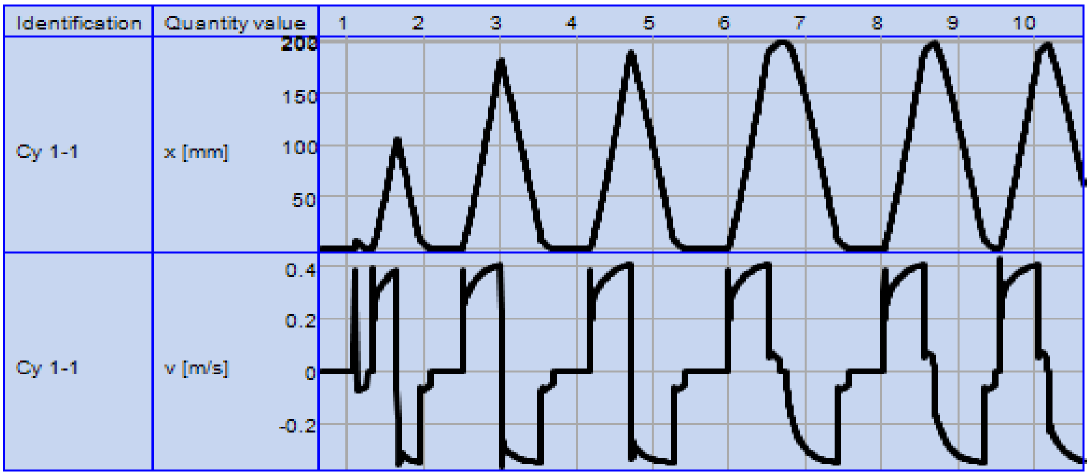

Fig. 5. Diagrams of parameters variations from the Cy 1-1

The data in Table 2 shows the component devices used in the second pneumatic circuit.

Table 2: The devices of the second pneumatic scheme

Description	Number of components
Compressed air supply	1
5/2 way valve	1
Air service unit	1
Throttle valve	4
Cylinder with two piston rods	2

The second pneumatic scheme studied uses two actuators (Cy 2-1 and Cy 2-2), Fig. 6.

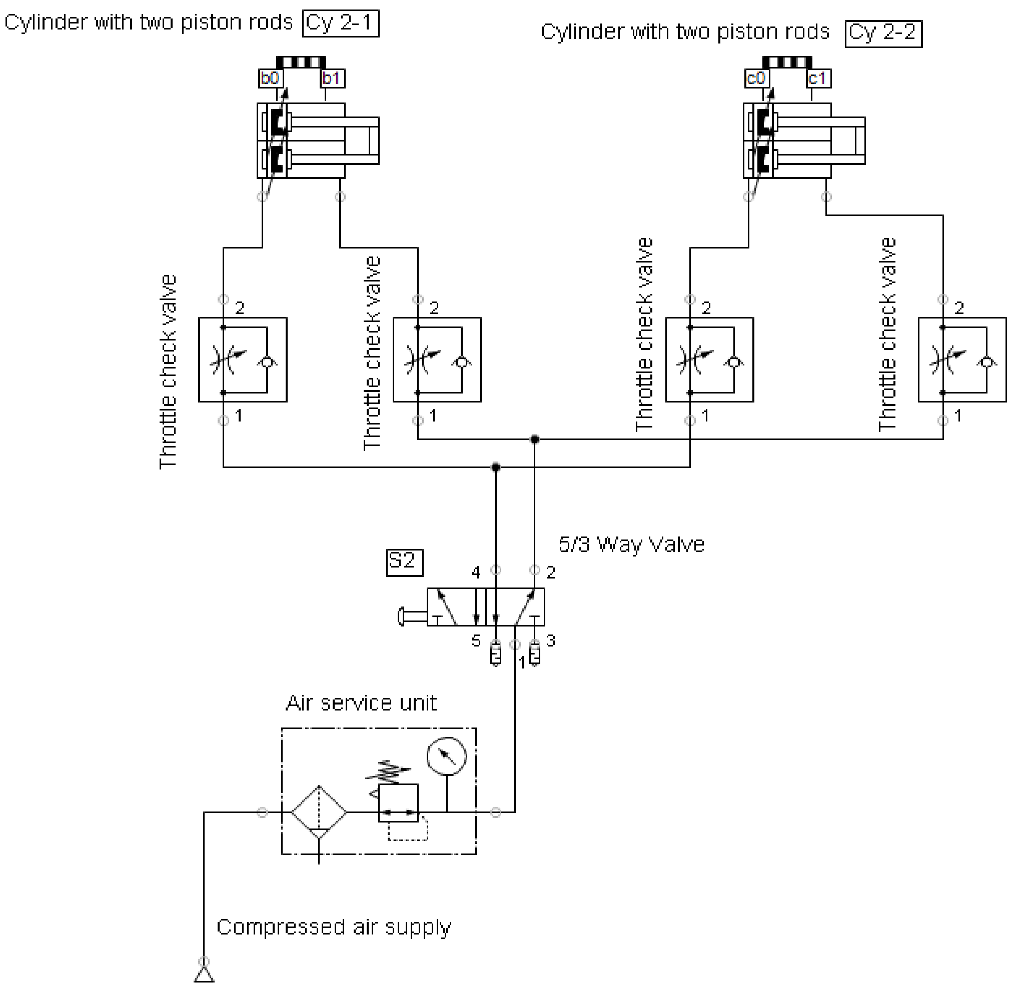

Fig. 6. Second pneumatic scheme with two actuators

When operator presses S2 button, the cylinders with two rods open together. Thereby, the piston rods which belongs to the cylinder (Cy 2-1) move from point b0 to point b1 and the piston rods which belong to the cylinder (Cy 2-2) move from point c0 to c1, [3].

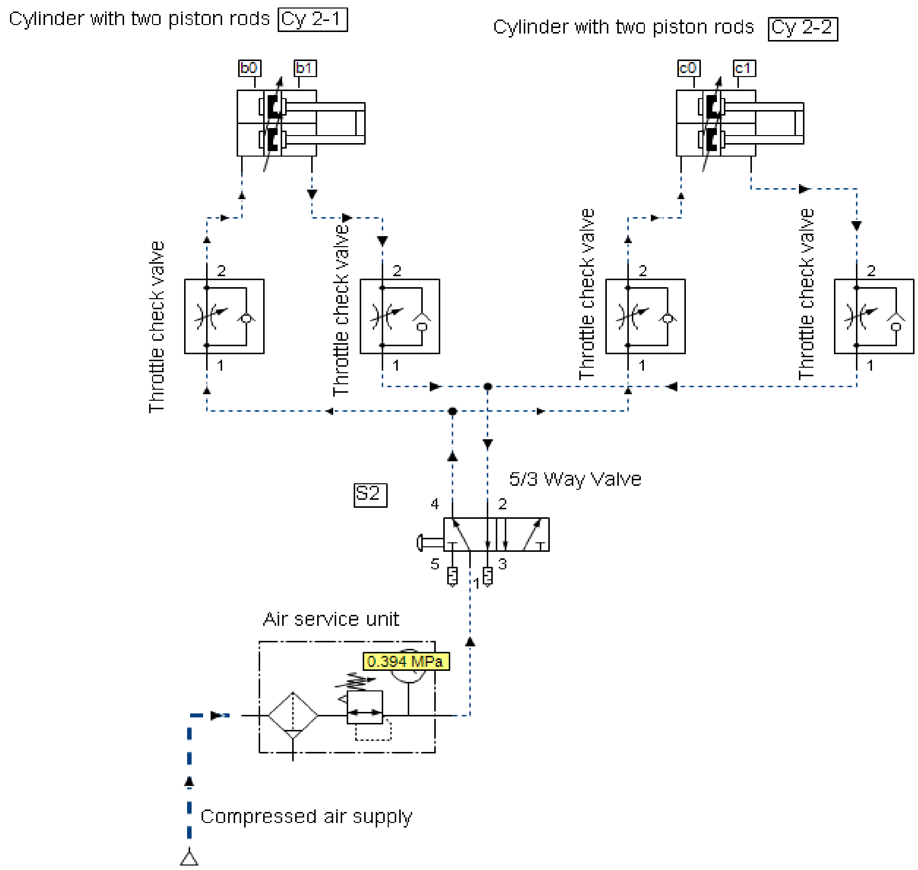

Fig. 7. Second pneumatic scheme - Simulation

To close the pneumatic circuit, the operator has to press the S2 button again. In this case, both pistons return to their starting points, Fig. 7.

3. The cylinder with two piston rods in the electro-pneumatic circuits

An electro-pneumatic scheme consists of an electrical or electronic part controlling the pneumatic power part of the circuit, [4].
Table 3 shows the components used in the pneumatic circuit.

Table 3: The devices of the first electro-pneumatic scheme

Description	Number of components
Compressed air supply	1
5/2 way solenoid valve	1
Air filter	1
Throttle valve	2
Cylinder with two piston rods	1
Relay	2
Lamp	2
Valve solenoid	2

The first electro-pneumatic scheme analyzed has one cylinder with two piston rods, Fig. 8.

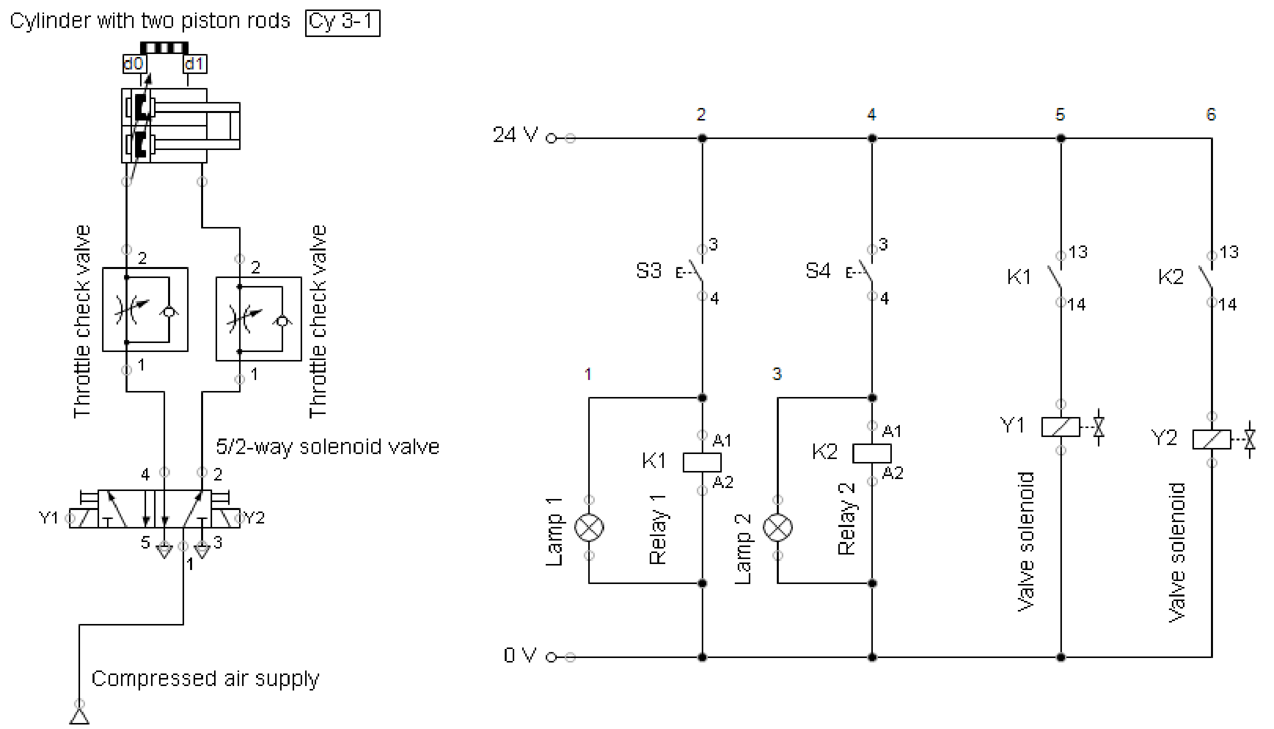

Fig. 8. First electro-pneumatic scheme

This first electro-pneumatic circuit operates only if operator presses S3 button. This button belongs to the 5/2 way solenoid valve. Then, the two piston rods move from point d0 to point d1. In this case, lamp 1 shows a pink signal, Fig. 9.

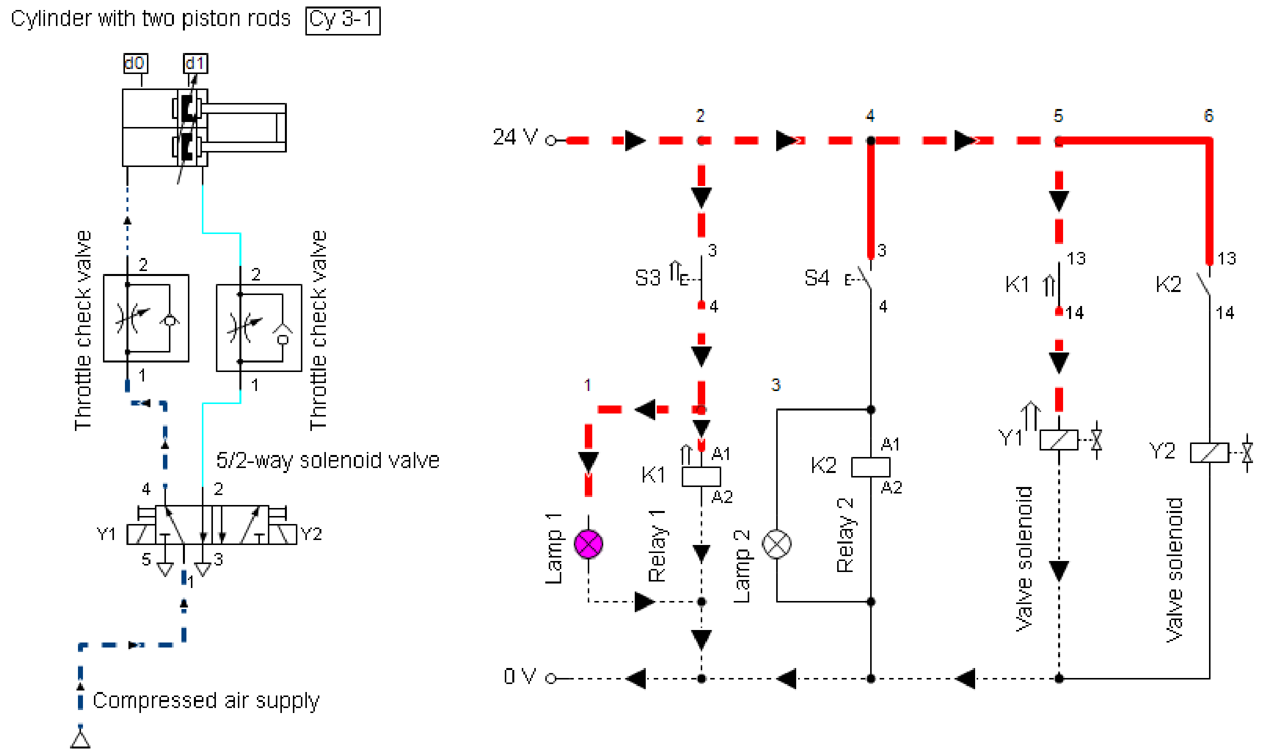

Fig. 9. First electro-pneumatic scheme – Simulation I

After that, the two piston rods return from point d1 to point d0 and lamp 2 shows a blue signal in electro-pneumatic circuit, Fig. 10.

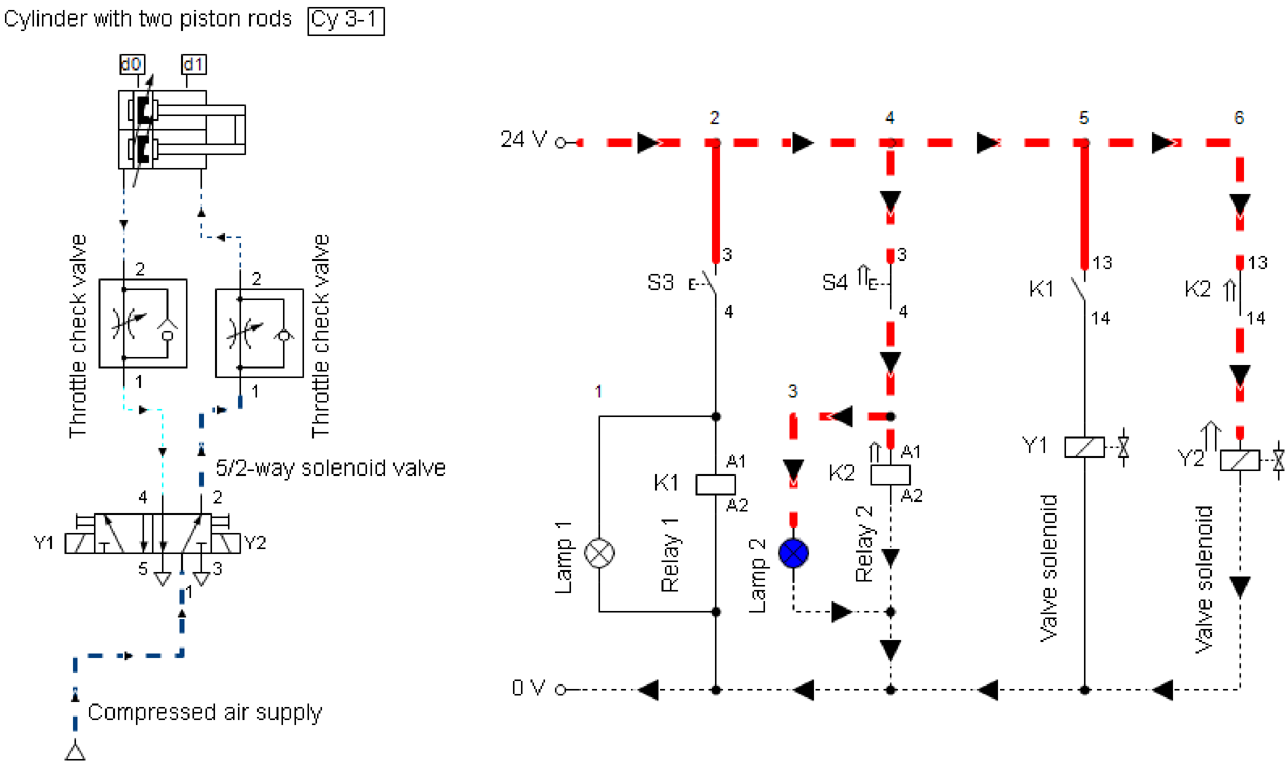

Fig. 10. First electro-pneumatic scheme – Simulation II

Table 4 shows the components used in the second electro-pneumatic circuit, [5].

Table 4: The devices of the second electro-pneumatic scheme

Description	Number of components
Compressed air supply	1
5/2 way solenoid valve	1
Cylinder with two piston rods	1
Logic module	1
Valve solenoid	2

A development of a second electro-pneumatic scheme consists in further improvement with logic module, Fig. 11.

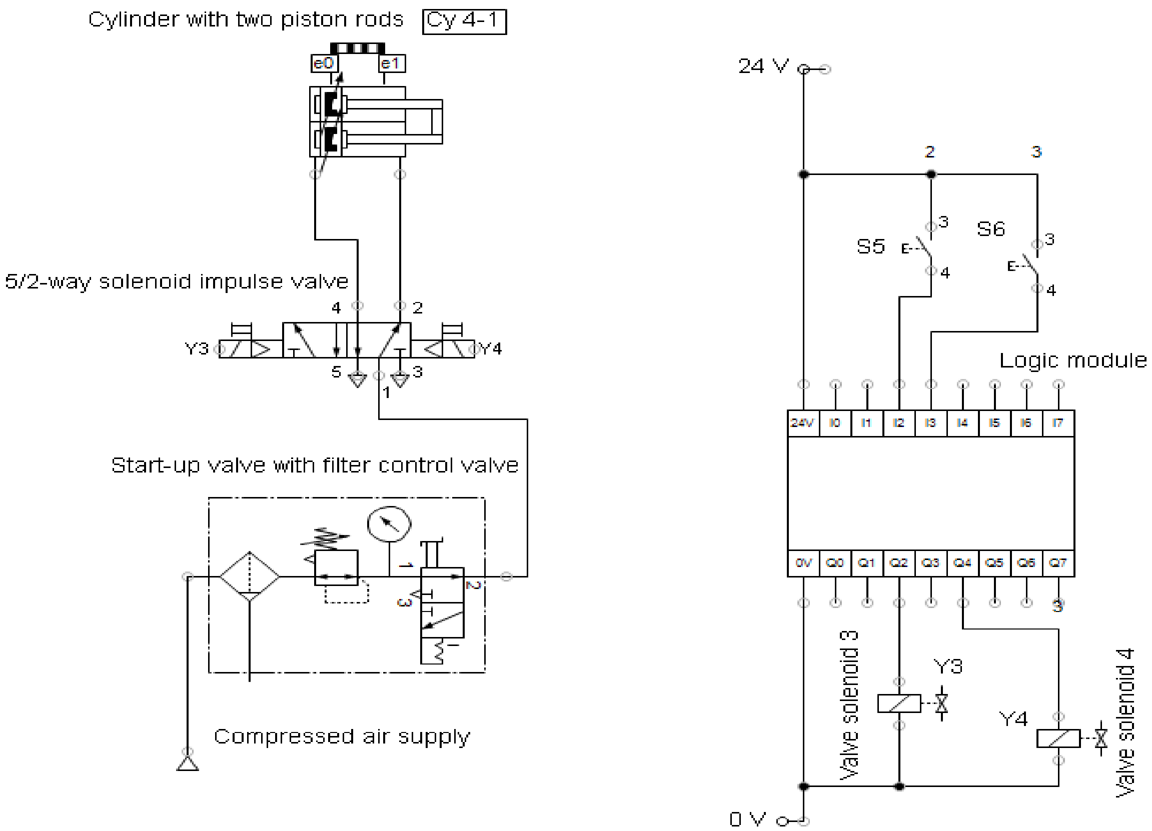

Fig. 11. Second electro-pneumatic scheme

The operator has to press the S 5 button to open the second electro-pneumatic scheme. In this case, the cylinder with two piston rods (4-1) moves from point e0 to point e1, Fig. 12.

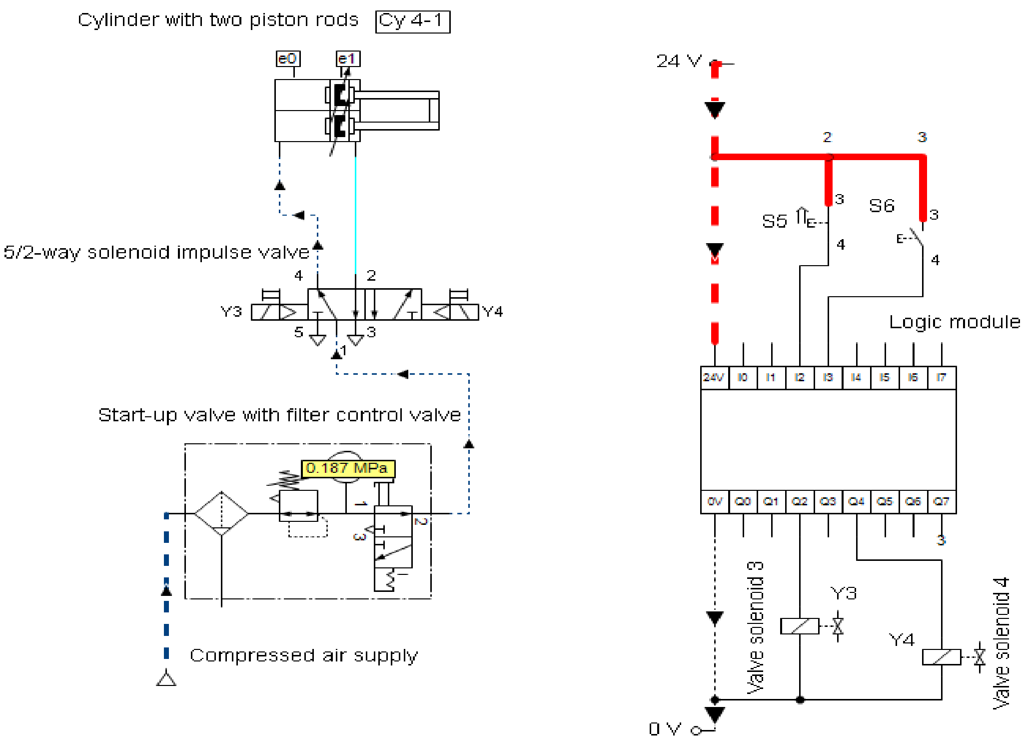

Fig. 12. Second electro-pneumatic scheme – Simulation I

Afterwards, the operator presses S6 button, [6].
This causes the cylinder with two piston rods (4-1) to move from point e1 to point e2, Fig. 13.

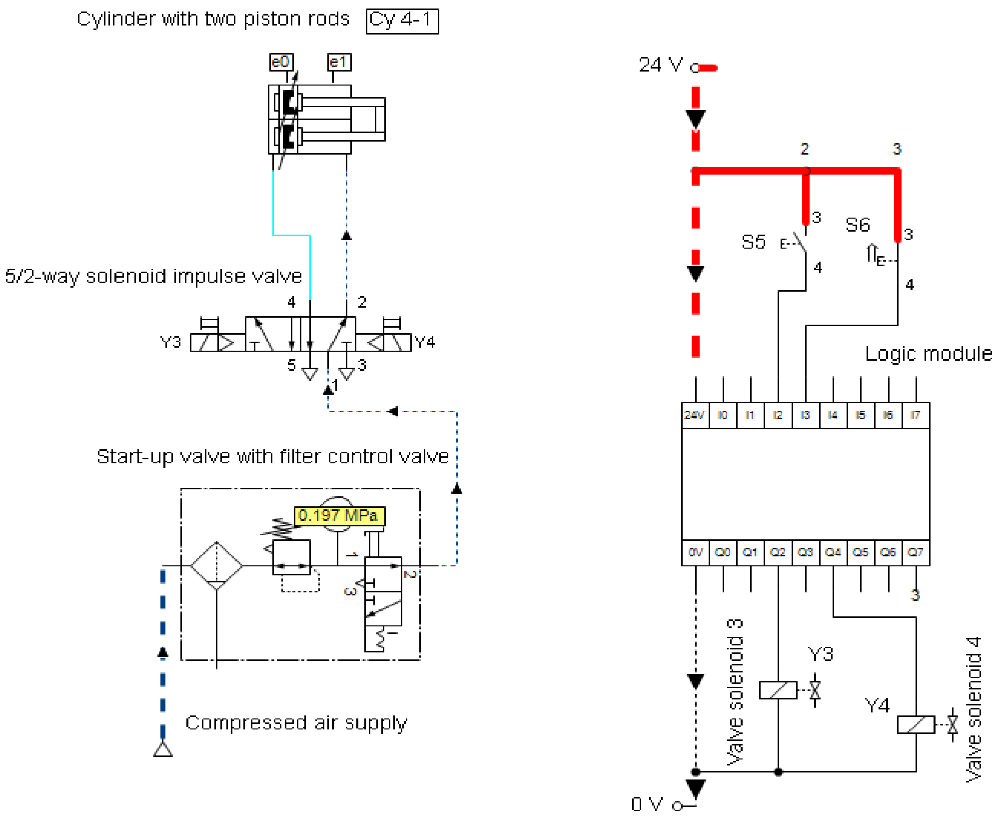

Fig. 13. Second electro-pneumatic scheme – Simulation II

4. Conclusions

The circuits shown in this paper allow the experimental verification of cylinder with two piston rods used in pneumatic installations based on these above presented circuits. Moreover, these installations can be used for practical training at any level (students, operators, workers, etc.) of persons who specialize and/or improve in the field of pneumatic components.
Cylinders with two piston rods, logic module and electrical equipment used for automatic system design have a high degree of performance and accessibility.
For a better choice of investment in such devices using the presented pneumatic installations, it is recommended that similar simulation methods should also be used beforehand.

References

[1] www.festo.com
[2] Jimenez, M., E. Kurmyshev, and C.E. Castaneda. "Experimental Study of Double-Acting Pneumatic Cylinder." *Experimental Techniques* 44 (2020): 355-367.
[3] Abreu, Paulo, Maria de Fátima Chouzal, Jacobo Sáenz Valiente, Luis de la Torre, and Maria Teresa Restivo. "Remote experiments with pneumatic circuit using a double rod cylinder." Paper presented at 2019 5th Experiment@ International Conference (exp.at'19), Funchal (Madeira Island), Portugal, June 12-14, 2019.
[4] Rădoi, R., M. Blejan, I.C. Duțu, Gh. Șovăială, and I. Pavel. "Determining the step response for a pneumatic cylinder positioning system." *Hidraulica Magazine*, no. 2 (June 2014): 25-31.
[5] Parambath, Joji. *Electro-pneumatics and Automation*. (Pneumatic Book Series (in the SI Units)). Independently published, 2020.
[6] Dumitrache, C.L., B. Hnatiuc, and D. Deleanu. "Exhaust Gas Recirculation (EGR) valve, design and computational fluid dynamic analysis." *IOP Conference Series: Materials Science and Engineering, ModTech* 1182 (2021): 012022. DOI: 10.1088/1757-899X/1182/1/012022.

Hydraulic Station for a Railway Track Welding Machine

PhD Eng. **Ioan LEPĂDATU[1,*]**, PhD Stud. Eng. **Liliana DUMITRESCU[1]**,
PhD Stud. Eng. **Ștefan ȘEFU[1]**, Ec. **Laurențiu Valentin NICOLAE[2]**,
Dipl. Eng. **Dănuț Florin MATEESCU[2]**

[1] National R&D Institute for Optoelectronics, Subsidiary Hydraulics and Pneumatics Research, Bucharest

[2] S.C. Proflex Automotive S.R.L.

* lepadatu.ihp@fluidas.ro

Abstract: *The welding head of the containerized and completely independent mobile machines for flash-butt welding of train and tram tracks is operated with the help of a hydraulically actuated rotary crane. The article shows a hydraulic station that provides the hydraulic energy needed to operate the rotary crane of a railway track welding machine.*

Keywords: *Hydraulic station, rail welding machine, rotary crane, flash-butt welding*

1. Introduction

Flash-butt welding of train or tram tracks is done by a complex mechanical - electrical equipment called "welding head" which has a hydraulically actuated mechanism for positioning and alignment of the rails.
The hydraulic installation of the welding head includes two hydraulic cylinders for vertical alignment of rails, two hydraulic cylinders for horizontal alignment of rails, and two hydraulic cylinders for positioning the rails so that between their ends the electric arc that makes the welding possible is created.
Positioning of the welding head above the rails, at the welding point, is performed by a rotary crane located on the platform of the mobile welding machine chassis.
The welding head is suspended from the crane hook.
The hydraulic installation of the rotary crane consists of two cylinders for the extension arm, two cylinders for the lifting arm and a rotary hydraulic motor with speed reducer for rotation of the crane arm.
Hydraulic power required for the welding head and rotary crane is given by the hydraulic station placed on the platform of the mobile welding machine chassis.
Below is presented the construction and operation of the hydraulic station of the railway track welding machine.

2. Technical characteristics and performance of the hydraulic station

2.1. Double electric pump

a) Main pump, PPA :
- Capacity .... V_g 71 cm^3 / rev;
- Maximum flow rate …………………………..….. Q_{max} 104 l / min;
- Maximum pressure …………………………..…. p_{max} 250 bar;

b) Recirculation pump, PRD:
- Capacity .... Vg 16 cm^3 / rev;
- Maximum flow rate ………………………….... Q_{max} 24 l / min;
- Maximum pressure …………………………… p_{max} 16 bar;

c) Electric motor:
- Power …………………………………………..…. N 30 kW;
- Speed ……………………………………...……. 1460 rpm.

2.2. Emergency electric pump

a) Emergency pump (gear pump), PU

- Capacity .... Vg 10.8 cm^3 / rev;
- Maximum flow rate ……………………….... Q_{max} 16 l / min;
- Maximum pressure ………………………..… p_{max} 250 bar;

b) Electric motor

- Power ………………………………………… 7.5 kW;
- Speed ………………………………………… n 1460 rpm;

2.3. Safety block, PP

- Nominal opening …………………………… Dn 10 mm;
- Maximum pressure ………………………… p_{max} 310 bar;

2.4. Safety block, PR

- Nominal opening …………………………… Dn 06 mm;
- Maximum pressure ………………………… p_{max} 25 bar;

2.5. Safety block, PU

- Nominal opening …………………………… Dn 06 mm;
- Maximum pressure ………………………… p_{max} 250 bar;

2.6. Reducing valves block

- Nominal opening …………………………… Dn 10 mm;
- Maximum pressure ………………………… p_{max} 250 bar;

2.7. Oil cooling block

- Nominal opening …………………………… Dn 06 mm;
- Maximum pressure ………………………… p_{max} 25 bar;

2.8. Equipped tank

- Tank volume …………………………….…. V 400 l;
- Return filter flow rate …………..……..…. Q 100 l/ min;
- Return filter filtering fineness ……………..... 10 μm.

3. Structure of the hydraulic station

The hydraulic station (fig. 1) consists of eight subassemblies: pumping group - *1*; emergency electric pump - *2*; safety block, PP - *3*; safety block, PP - *4*; safety block, PU - *5*; reducing valves block- *6*; oil cooling block – *7* and equipped tank - *8*.

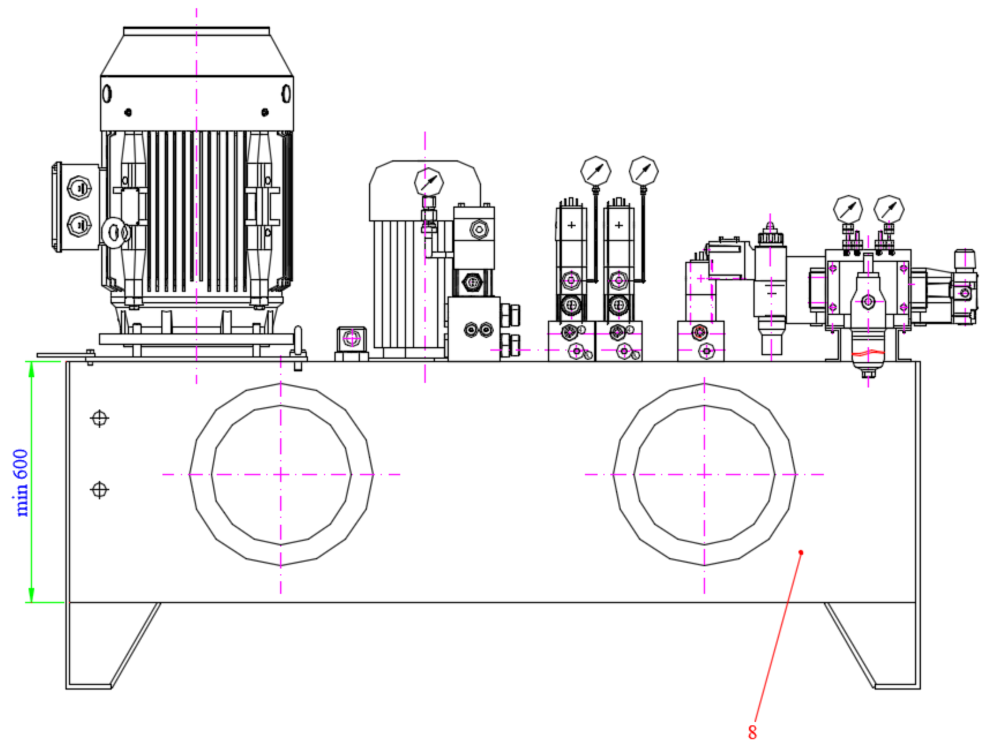

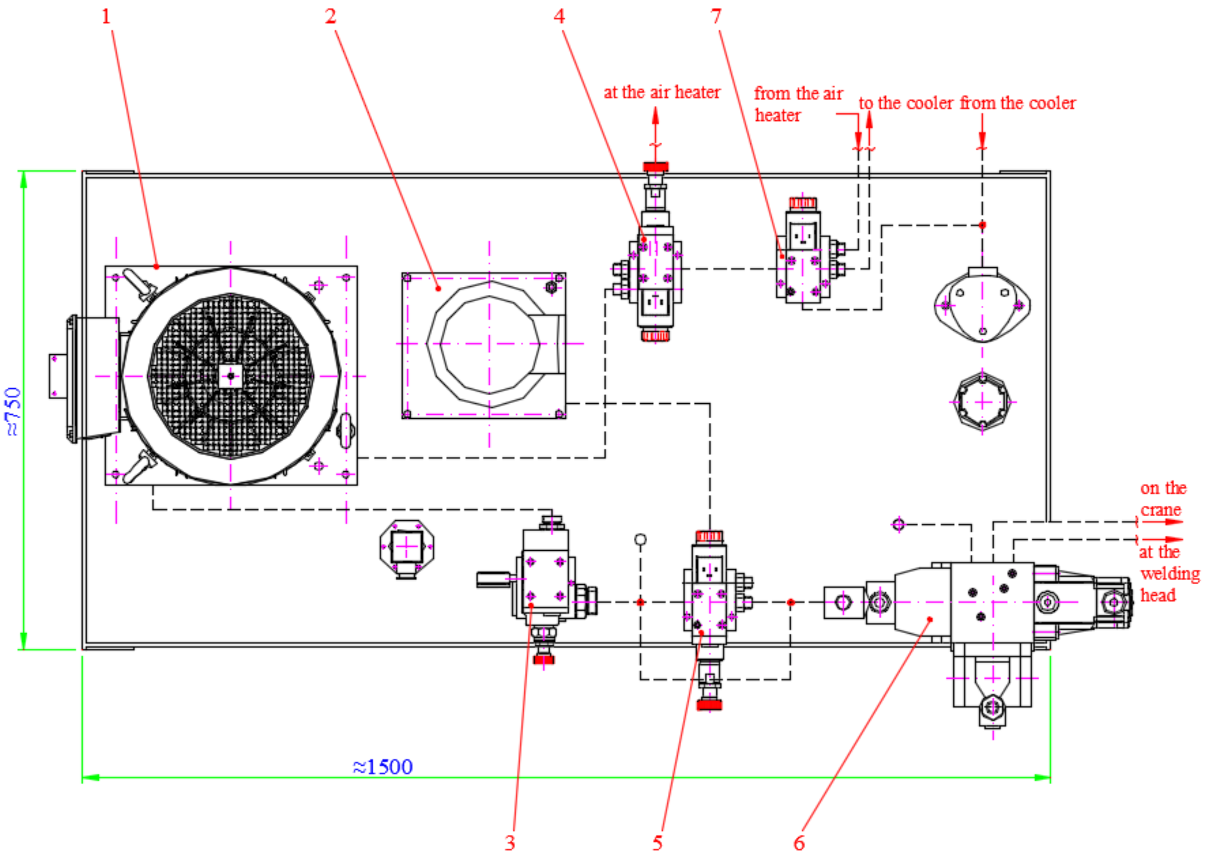

Fig. 1. Structure of the hydraulic station

1. Pumping group; 2. Emergency electric pump; 3. Safety block, PP; 4. Safety block, PR, 5. Safety block, PU; 6. Reducing valves block; 7. Oil cooling block; 8. Equipped tank

The pumping group *1* is fixed to the cover of the tank and provides hydraulic power (flow rate and pressure) for all hydraulically operated mechanisms. Pumping group contains a double pump, consists from an axial pistons pump and one with gears, both immersed in tank and is driven by an asynchronous electric motor of 30 kW at 1500 rpm.
Emergency electric pump *2* consists of a 7.5 kW asynchronous electric motor that drives at a speed of 1500 rot /min a gear pump with a capacity of 108 cm^3/ rot immersed in oil.
The safety block, PP - position *3*, contains devices that limit the maximum pressure on the main circuit: it is located on the oil tank cover.
The safety block, PR - position *4*, contains devices that limits the maximum pressure on the cooling circuit.
The safety block, PU - position *5*, contains the devices that limits the maximum pressure on the emergency hydraulic circuit.
The reducing valves block *6* contains two valves that maintain the working pressure at the set value on the two hydraulic circuits that supply the welding head and the rotary crane.
The oil cooling block *7* contains the devices that ensure the interconnection between the air/oil cooler and the water/oil cooler.
The equipped tank *8* contains the oil tank with the return filter and the filling and venting filter.
All subassemblies are located on the oil tank cover. The connections between the devices are done with metal pipes.

4. Hydraulic station operation

The role of the hydraulic station is to supply hydraulic power [1, 2, 3, 4, 5] to the welding head and the rotary crane.
The diagram of the hydraulic station is presented in fig. 2 below.

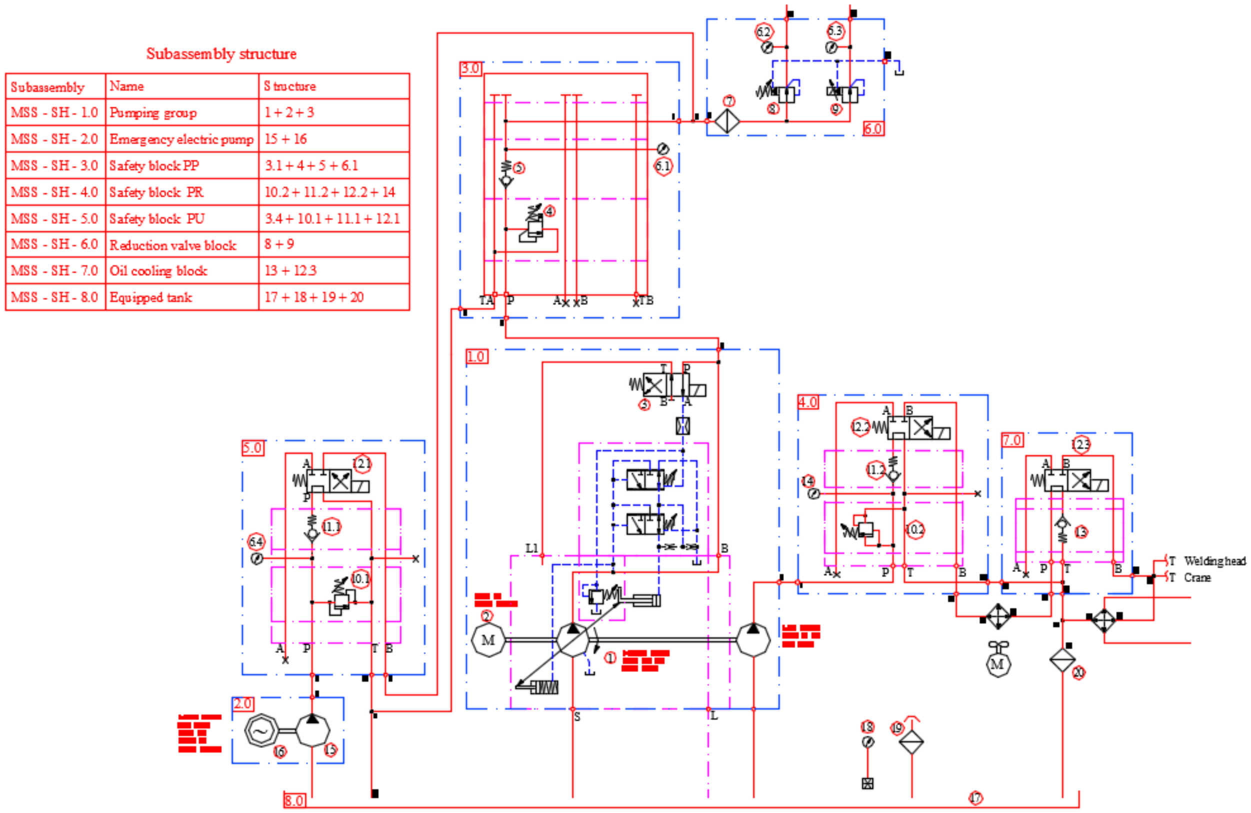

Subassembly	Name	Structure
MSS - SH - 1.0	Pumping group	1 + 2 + 3
MSS - SH - 2.0	Emergency electric pump	15 + 16
MSS - SH - 3.0	Safety block PP	3.1 + 4 + 5 + 6.1
MSS - SH - 4.0	Safety block PR	10.2 + 11.2 + 12.2 + 14
MSS - SH - 5.0	Safety block PU	3.4 + 10.1 + 11.1 + 12.1
MSS - SH - 6.0	Reduction valve block	8 + 9
MSS - SH - 7.0	Oil cooling block	13 + 12.3
MSS - SH - 8.0	Equipped tank	17 + 18 + 19 + 20

Fig. 2. Hydraulic diagram of the hydraulic station

4.1. Pumping group - 1.0

Pumping group [1] *1.0* consists of double pump *1*, electric motor *2* and directional control valve *3*. Double pump *1* consists of an axial piston pump with variable flow rate, PPA and gear pump, PRD. The PPA pump supplies hydraulic power (flow rate x pressure) to the two hydraulically operated pieces of equipment: the welding head and the rotary crane. The PRD pump ensures cooling and filtration of hydraulic oil. Directional control valve *3* switches the flow rate of the PPA pump to "zero" or "maximum".

4.2. Emergency electric pump - 2.0

The emergency electric pump goes into operation when the pumping group *1.0* fails during operation. Its role is to remove from load and bring to "zero" the mechanisms of the hydraulic head and rotary crane. It consists of gear pump *15* and electric motor *16*.

4.3. Safety block, PP - 3.0.

The safety block [2], PP consists of pressure valve *4*, one-way valve *5* and pressure gauge *6.1*. Safety valve *4* limits the pressure on the discharge circuit of the PPA pump. One-way valve *5* ensures the circulation of the working fluid in one direction, from the PPA pump to the two consumers - the welding head and the rotary crane. Pressure gauge *6.1* indicates the pressure on the discharge circuit of the PPA pump.

4.4. Safety block, PR - 4.0.

The functional role of the safety block [2], PR is to limit the pressure on the oil cooling and filtration circuit. The block consists of pressure valve *10.2*, one-way valve *11.2*, directional control valve *12.2* and pressure gauge *14*. Pressure valve *10.2* limits the pressure of the PRD pump. One-way valve *11.2* allows the working fluid to flow only from the PRD pump to the cooler and filter, not the other way around. If the oil has a temperature below 50˚ C, then it is directed by the directional control valve *12.2* directly into the filter *20*. If the oil temperature exceeds 50˚ C, then the directional control valve *12.2* is switched automatically and the oil is first passed through the air/oil cooler (air heater) and then, after cooling, it is filtered by filter *20*. Pressure gauge *14* indicates the pressure on the discharge circuit of the PRD pump.

4.5. Safety block, PU - 5.0.

The functional role of this block [2] with devices is to limit the maximum pressure on the hydraulic discharge circuit of the emergency electric pump and to ensure starting on no-load, disconnected from the load of electric motor *16*. The safety block, PU contains pressure valve *10.1*, one-way valve *11.1*, directional control valve *12.1*, and pressure gauge *6.4*. Safety valve *10.1* limits the pressure on the discharge circuit of pump *15*. One-way valve *11.1* allows oil to flow only from the pump to the consumer. Directional control valve *12.1* ensures starting on no-load of electric motor *16* because on its P to T field, the pumped discharge oil is sent to the tank without load. Manometer *6.4* indicates the pressure on the discharge circuit of emergency pump *15*.

4.6. Reducing valves block - 6.0.

The functional role of this block is to reduce the pressure exerted by the PPA pump or pump *15* to the value required for functioning of the welding head and rotary crane mechanisms. The block contains filter *7*, proportionally controlled reducing valves *8* and *9*, as well as pressure gauges *6.2* and *6.3*. Filter *7* ensures the filtration of the oil that enters the proportional valves to a fineness of 10 µm. Reducing valve *8* is dedicated to the hydraulic circuit of the control head, while reducing valve *9* is dedicated to the hydraulic circuit of the rotary crane. The pressure on the two circuits is measured by means of pressure gauges *6.2* and *6.3*.

4.7. Oil cooling block - 7.0.

When the oil heating is strong and the air/oil cooler (air heater) does not cope, the water/oil cooler enters the circuit, too [3]. This function is performed by the oil cooling block with the help of directional control valve *12.3*. On the P to T field of the directional control valve, the oil is only cooled by the air/oil cooler. On the other side of the directional control valve, the air/oil cooler is linked in series with the water/oil cooler and thus it increases the oil cooling capacity. Check valve *13* allows oil to flow only from the PRD filtration and cooling pump to oil tank *17*.

4.8. Equipped tank - 8.0.

The working fluid is stored in oil tank [4, 5] *17*. On the cover of tank *17* there is also level and temperature transducer *18*, filling and venting filter *19*, and return filter *20*. Level and temperature transducer *18* signals the situation in which the oil level in basin goes down below the minimum level and commands the activation of the cooling circuit if the oil temperature rises above 50˚ C.
The oil is introduced into the tank through filter *19*, which also allows the circulation of ambient air from the outside to the inside of the tank and vice versa due to the variation of the oil level, which is caused by handling of the hydraulic cylinders. Return filter *20* retains the impurities with which the hydraulic oil is contaminated during the functioning of the welding head and rotary crane hydraulic installation.

5. Conclusions

The hydraulic station for a railway track welding machine is designed so that:

- It ensures the operation of the hydraulically actuated mechanisms of the welding head and the rotary crane at optimal parameters;

- It ensures operation in case of failure to complete the duty cycle;
- It ensures the filtration and cooling of the hydraulic oil for a long and trouble-free operation of the railway track welding machine.

Acknowledgments

This paper has been developed in INOE 2000-IHP, as part of a project co-financed by the European Union through the European Regional Development Fund, under Competitiveness Operational Programme 2014-2020, Priority Axis 1: Research, technological development and innovation (RD&I) to support economic competitiveness and business development, Action 1.2.3 – Partnerships for knowledge transfer, project title: *Development of energy efficient technologies in niche applications of the manufacture of on-demand mechanical-hydraulic subassemblies and maintenance of mobile hydraulic equipment*, project acronym: MENTEH, SMIS code: 119809, Financial agreement no. 6 /25.06.2018, subsidiary contract no. 46 /17.01.2022.

References

[1] Dumitrescu, L., Al.P. Chiriță, Șt.M. Șefu, and R.M. Oprescu. "Innovative stand for testing of hydraulic pumps and motors." Paper presented at the 24th International Conference on Hydraulics and Pneumatics HERVEX, Băile Govora, Romania, November 7-9, 2018.
[2] Dumitrescu, L., Șt.-M. Șefu, I.M. Baciu, and M. Blejan. "Stand for Experimental Verification of Components in the Structure of Hydraulic Drive Systems." *Hidraulica Magazine*, no. 4 (December 2021): 57-63.
[3] Duțu, I.C., and R.I. Rădoi. "Automated hydraulic oil cooling system driven by a variable speed hydraulic motor." Paper presented at the 23rd International Conference on Hydraulics and Pneumatics HERVEX, Băile Govora, Romania, November 8-10, 2017.
[4] Ioniță, N., N. Dimitriu, and L. Dumitrescu. "Endurance comparative test bench for rotary hydrostatic pumps." / "Stand de testare comparativă la anduranță a pompelor hidrostatice rotative." Paper presented at the 15th International Salon on Hydraulics and Pneumatics HERVEX, Calimanesti-Caciulata, Romania, November 14 – 16, 2007.
[5] Assofluid. *Hydraulics in Industrial and Mobile Applications*. Brugherio (Milano), Grafiche Parole Nouve s.r.l. Publishing House, 2007.

Simulations regarding the Modernization of the District Heating System in Timisoara by Controlling the Supply and Regulating the Temperature of the Heating Agent

PhD. student Eng. **Daniel MUNTEAN**[1], PhD. student Eng. **Matei MÎRZA**[1],
Assoc. Prof. PhD. Eng. **Adriana TOKAR**[1,*], Assis. Prof. Eng. **Dănuț TOKAR**[1]

[1] University Politehnica Timisoara

* Corresponding author's e-mail address: adriana.tokar@upt.ro

Abstract: *The current context of climate change requires the efficiency of district heating systems. The article proposes the implementation of modernization solutions for district heating systems in order to reduce heat loss on the distribution system and implicitly CO2 emissions at the level of thermal agent production. The case study analyses the supply of the Forestry Technical College from Timisoara, which has a heat demand for the building of 1MW and is located at a distance of 1200m from the nearest thermal point. Simulations were performed for several efficiency stages of the central heating system, which before efficiency, operated without any control over the supply with thermal agent.*
The first stage of efficiency involves the transition from the uncontrolled continuous supply of the final consumer to an adjustable supply according to the thermal energy requirement, and the second stage represents the reduction of supply temperatures on the supply and return pipes from the high temperature regime (t_t = 80°C and t_r = 60°C), to an average temperature regime (t_t = 60°C and t_r = 40°C).

Keywords: *District heating, modernization, efficiency, reduction of heat loss*

1. Introduction

District heating systems have been known since the 14th century, and have been using various energy sources since the beginning: geothermal, fossil fuels, biomass and waste incineration. The thermal transport agent for heat for district heating systems until the 1930s was steam. This system used pipes made of concrete and was characterized by high energy losses through the transport system [1].
The second generation of district heating systems appeared after 1930 and used hot water under pressure at temperatures above 100 ° C, systems characterized by high consumption of materials with poor thermal properties (pipes in concrete ducts, massive counter current heat exchangers). These systems have shown an inability to control heat demand, but have shown improved fuel economy [1], [2], [3].
In the 1970s, the third generation of centralized energy transmission systems was developed. It also used pressurized water, but at lower temperatures than the previous generation and was often referred to as the "Scandinavian district heating technology" [1], [2]. During this period, the switch to prefabricated components buried in the ground (pre-insulated pipes) and to plate heat exchangers, which generated a reduction in material consumption was made [1], [2], [3].
The fourth generation of systems is a natural evolution of the previous one which, in the context of the requirements regarding the quality in constructions, regarding energy saving and thermal insulation, highlights both the characteristics oriented towards efficiency and sustainable use of natural resources. The main features of this generation refer to the fact that the temperatures of the thermal agent for transporting or distributing thermal energy continue to decrease (40-60 ° C), the equipment used is more and more modular, and the materials are increasingly flexible and have low energy losses, but the most important aspect is that the system makes it easier to integrate renewable energy sources (heat pumps, solar panels) and excess heat from communities and industry [3], [4].
The evolution of district heating systems is presented in Table 1 in terms of the method of heat production and energy source associated with the technological period [1].

Table 1: Production and energy sources for district energy [1]

Characteristic	1st Generation	2nd Generation	3rd Generation	4th Generation
Peak Technology Period	1880–1930	1930–1980	1980–2020	2020–2050
Heat Production	Steam boilers	CHP and heat- only boilers	Large-scale CHP	Heat Recycling
Energy Source	Coal	Coal and oil	Biomass, waste and fossil fuels	Renewable sources

Today, district heating systems allow the long-distance distribution of thermal energy and the increasing use of renewable energy, thus increasing the fight against global warming and the energy crisis. For this reason, sustainable district heating systems will have to provide planning structures, low costs correlated to efficient operation and strategic investments, an aspect illustrated in Fig. 1 [2].

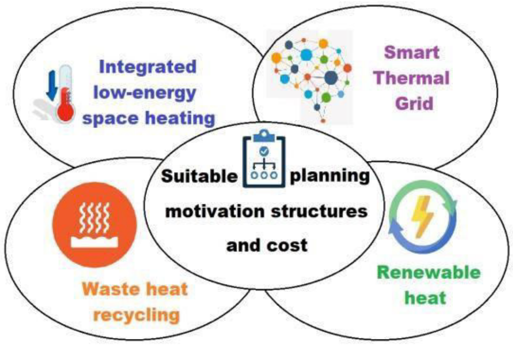

Fig. 1. The concept of 4th Generation District Heating [2]

Given both the massive expansion of newly built areas characterized by buildings equipped with low temperature heating systems, and the existence of consumers located at a great distance from the thermal points, but also the current issue of central heating systems in Romania and in particularly of the district heating system in Timișoara (pipes with an advanced degree of wear, insulated in the classical solution), which even in the case of massive investments to replace existing pipes with pre-insulated pipes, some problems remained unresolved [3].
In this sense, for the transition from generation III to generation IV, the article proposes as efficiency solutions the zoning of the centralized system according to the type of consumer, in the sense that the primary distribution network to transport heat on a main route at a maxim temperature necessary for the most disadvantaged consumer, from which areas with a lower temperature requirement are supplied, or certain isolated consumers (at a great distance from the thermal point) [3].

2. Solutions for reducing energy consumption by regulating the temperature, in the transition from the 3rd to the 4th generation

The district heating system in Timișoara is part of the category of third generation systems that use as solid energy source solid fuel (coal) with natural gas contribution. The thermal agent used by district heating plants is hot water (90ºC-115ºC) transported through the primary circuit to the zonal thermal points where the energy is transferred to the secondary circuit using plate heat exchangers. From the thermal points the thermal agent is transported to the final consumers [3].
District heating with low temperature of the thermal agent offers new possibilities for a higher energy efficiency and a lower consumption of energy produced from fossil fuels. In terms of demand, low temperature thermal agent is commonly available as a basis for energy efficient heating of the building and preparation of hot water for consumption. Low temperature heat can be integrated into district heating by using large-scale efficient heat pumps, solar thermal collectors and combined heat and power plants on biomass.

In general, the use of lower temperatures reduces pipeline transport losses and can increase the overall efficiency of the total energy chains used in district heating. In order to achieve maximum efficiency, not only district heating networks but also energy conversion must be optimal, and indoor installations of final consumers must be adapted to allow the use of low temperatures provided by the network (e.g., by radiant heating). For this reason, the implementation of solutions based on high levels of renewable energy requires an adaptation of the technical infrastructure and buildings. A typical district heating network supplies areas with different temperature needs for heating buildings, such as individual residential areas or condominiums characterized by old buildings with a high temperature demand, administrative buildings and residential areas of individual type or condominium characterized by new buildings with a lower temperature demand (Fig.2a). If we consider the entire district heating system, the total heat loss is significant, as well as the potential for savings. In each zone, the afferent supply network is practically a branch of the main primary network (Fig. 2a), and in these branching points it is proposed to change the temperature by installing a mixing loop (Fig. 2b) [5], adapting the temperature to correspond to the real heat demand in the area, minimizing the heat loss on the respective branch [3]. Another common situation is that we have a zonal thermal point that produces thermal energy for nearby consumers or for more distant consumers (Fig. 3a). The temperature regulation solution for the distant consumer is for it to be supplied on a dedicated route from the nearest thermal point, thus having the possibility to regulate the temperature according to its energy requirement (Fig. 3b).

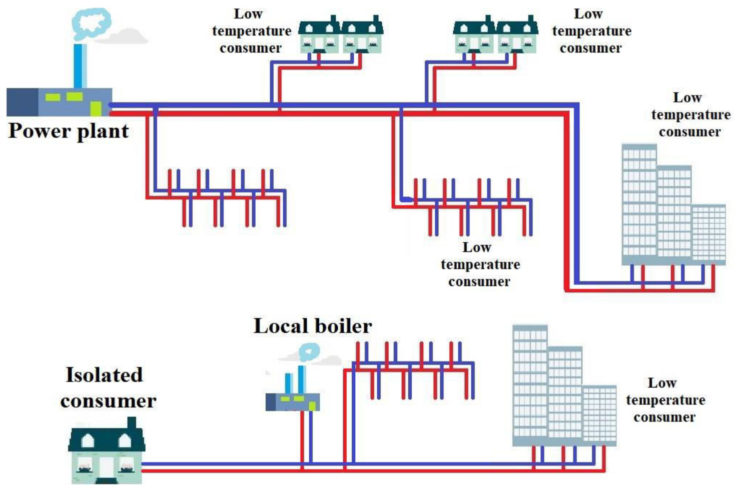

a)

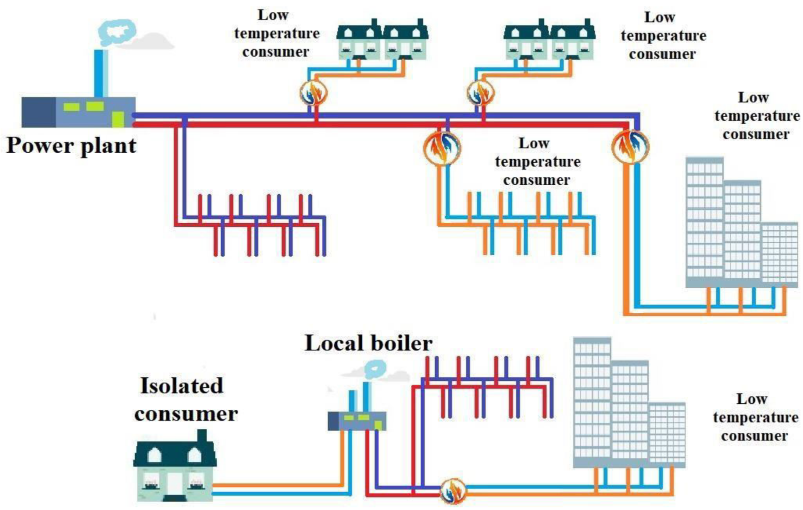

b)

Fig. 2. Temperature regulation solutions for the district heating network
a) Before temperature regulation, b) After temperature regulation [5]

3. Adapting the existing system and transitioning from the IIIrd to the IVth generation, for an isolated consumer from Timisoara. Case Study

In general, the district heating systems in our country (which contain in interdependence, the source, the hot water network, the connection installations and the powered buildings) use two temperature regulation steps. Thus, at the source the temperature in the supply pipe in the primary network is fixed based on the forecast data (outdoor temperature and wind speed for a period of 612 hours). At the thermal points, a second regulation step is operated by correlating the temperature of the thermal agent in the indoor installations with the outdoor temperature.
Therefore, from the thermo-hydraulic point of view in the heat supply using in practice, the qualitative-quantitative (mixed) regulation based on the use of the theoretical quality graph at sources and on the correction of the thermal power taken from the final consumers by modifying the thermal points, automatically or manually the primary heat sink flow.
This change of flow aims both to correlate the temperature of the secondary thermal agent with the temperature of the outside air and to achieve the condition regarding the temperature of the hot water for consumption. Thus, it can be said that the adjustments in the two stages regarding the temperature / flow of the thermal agent finally ensure an additional correction of the heat consumption at the final consumer. In the operation of the system, a correlation is actually established between the temperature of the thermal agent and the climatic factors (especially the temperature of the outside air) [6].
The reason for this correlation, contained in the adjustment chart, is related to the heating process of the buildings. The process of preparing hot water, as a result of the connection schemes of the consumers, contributes to the decrease of the water temperature in the return pipe but also to the lower limitation of the water temperature in the supply pipe, to the value of 65°C, as a result of the requirement to be able to obtain even during the relatively warm transition periods hot drinking water at a temperature of 50 - 55°C [3].
Given the fact that the primary and secondary thermal network does not cover the total area of the city of Timisoara, which is constantly developing and expanding, there is the problem of finding solutions that are as economical and technically efficient as possible, with which to feed the new buildings or neighborhoods to the needs of final consumers. One of the classic solutions is the extension of the primary heating network and the creation of a new heating point to serve as the connection for new area of buildings. Given that the primary thermal circuit supplies the entire city, the thermal agent transported through the primary network has a fairly high temperature, with a variation between 90-115^{o}C on the supply pipe and 50-65^{o}C on the return pipe, generating a considerable energy loss. [3].
The evolution from the 3rd to the 4th generation district heating system requires a decrease in the temperature of the transport thermal agent, so we have to choose a supply solution that supports this principle. In Timisoara, at the moment, the temperature regulation of the thermal agent is made from the unit thermal point for the whole served consumption area, and the supply regime is 24 hours.
The case study analyzes the heat supply of the Forestry Technical College from Timișoara, which has a heat demand of 1MW [7]. The proposed modernization aims both to reduce energy losses through the transport of thermal agent and to reduce CO2 emissions.
The Forestry Technical College is supplied from the PT UMT thermal point, as can be seen in (Fig. 3), through a dedicated route, made with pre-insulated steel pipes D.139.7x250mm with insulation class "1 x reinforced" [7], with a length of 1200 meters, through which the thermal agent is transported with a flow temperature of 80^{o}C and a return temperature of 60^{o}C, Heat exchange between the thermal agent delivered from the UMT thermal point and the thermal agent circulated through the consumer's indoor installation it is made with the help of a thermal module [7].

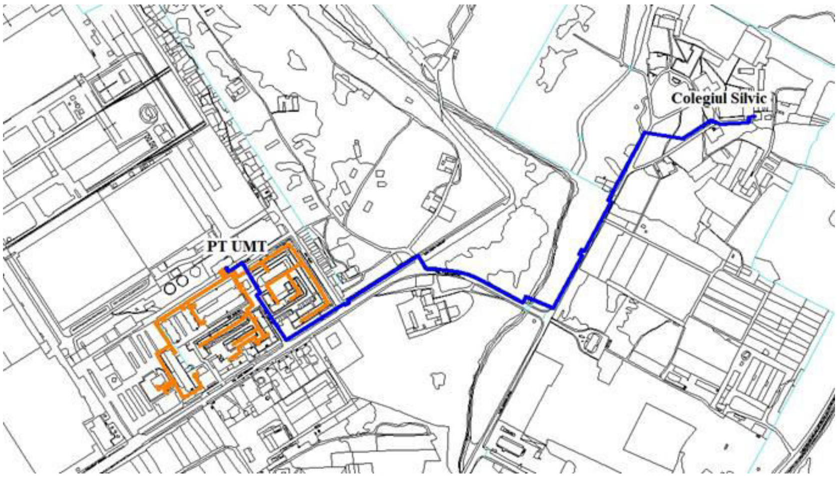

Fig. 3. Heat supply of the Technical Forestry College from Timișoara [7]

Thermal supply network of the Forestry Technical College
Thermal supply network of the residential buildings

The reduction of thermal energy loss on district heating pipes can be done in two ways, the use of thermally insulated pipes and reducing the temperature of the thermal agent to a temperature as low as possible without affecting the necessary thermal parameters to the final consumer. Considering the fact that the thermal network route we are referring to in this case is made from good quality pre-insulated pipes, we propose a solution to reduce energy loss by lowering the transport temperature of the thermal agent.

In the studied situation considering the long length of the district heating route to the final consumer, as well as the destination of the educational building, we identified a first stage of modernization of the district heating system which involves the transition from a continuous supply of heat during the day to a supply correlated with the final consumer's requirement.

The simulation for the supply with thermal agent of the Forestry Technical College was performed with the help of the Polysun calculation program [8] which is based on the analytical relation (1), according to the design regulations of the heating installations [9], [10].

$$Q = m \cdot c_p \cdot (t_1 - t_2) \tag{1}$$

where:

m - mass flow, in kg / s;

c_p - specific heat of water, in kJ / kg · K;

t_1 - indoor water temperature, in ° C;

t_2 - outdoor ambient temperature, in ° C.

The principle diagram of the consumer supply installation in the existing situation is presented in Fig. 4.

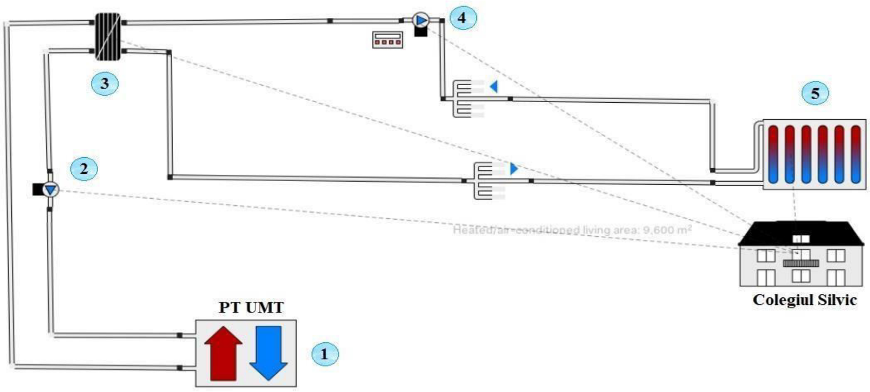

Fig. 4. Schematic diagram of the existing installation
1 – District Heating Substation, 2 – Circulating pump DH, 3 – Heat exchanger
4 – Circulating pump end-user, 5 – End-user

For the existing heat supply situation of the Forestry Technical College, at the supply / return temperatures of 80/60 ° C, the heat losses were simulated according to the average outdoor temperature for Timișoara [11], [12], for the year 2022. Fig. 5 shows the variation of heat loss (Fig. 5a) and the monthly energy consumption (Fig. 5b).

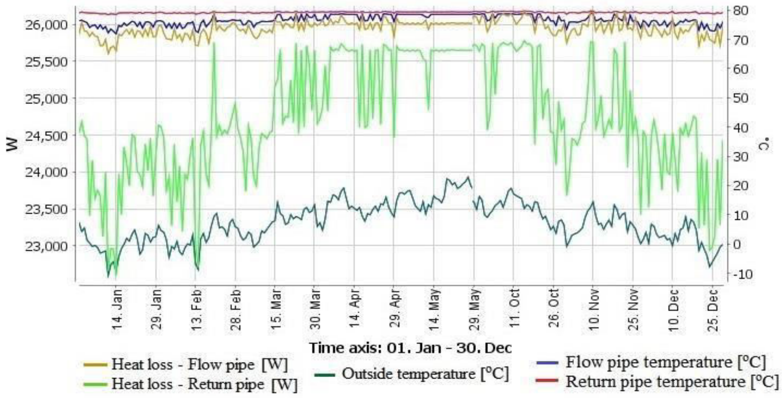

a)

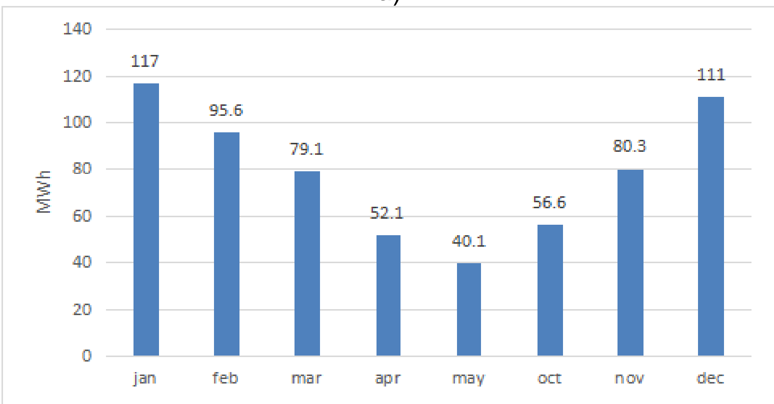

b)

Fig. 5. Heat loss and energy consumption for the existing situation [8]

The first stage involved a modernization of the PT-UMT thermal point by introducing an automation for the circulation pump of the thermal agent to the studied consumer, so that on the transmission network the circulation of the thermal agent is realized only during the period when there is circulation in the interior heating installation of the consumer.

At this stage of modernization at the flow / return temperatures of 80/60°C, heat losses were simulated under the same conditions depending on the average outside temperature. In Fig. 6 shows the variation of heat loss (Fig. 6a) and the monthly energy consumption (Fig. 6b).

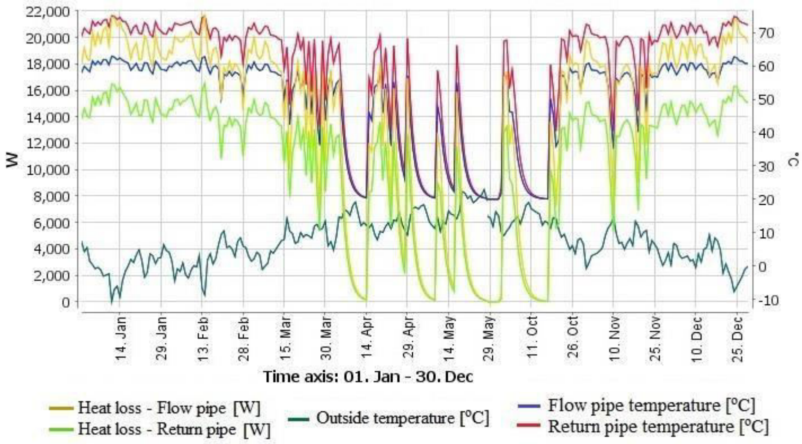

a)

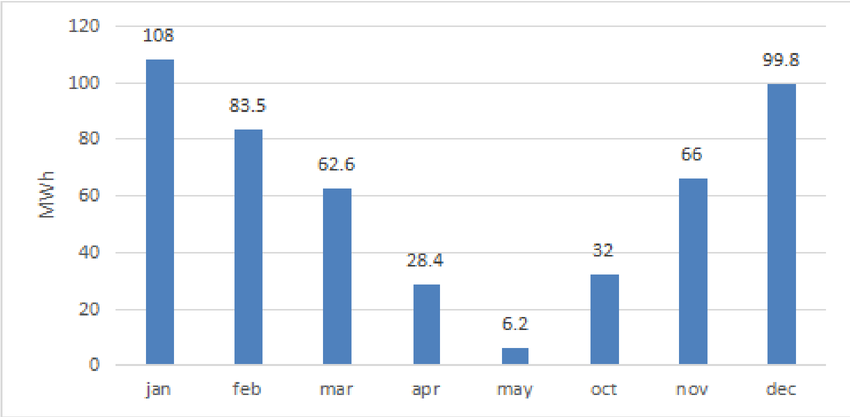

b)

Fig. 6. Heat loss and energy consumption for modernization situation (pumping automation) [8]

Considering the supply solution of the final consumer on a dedicated route, the possibility of implementing a new stage of efficiency of the supply system was studied by reducing the temperature of the supplied thermal agent from the initial situation 80/60°C to 60/40°C. The results can be seen in Fig. 7 showing the variation of heat loss (Fig. 7a) and the monthly energy consumption (Fig. 7b).

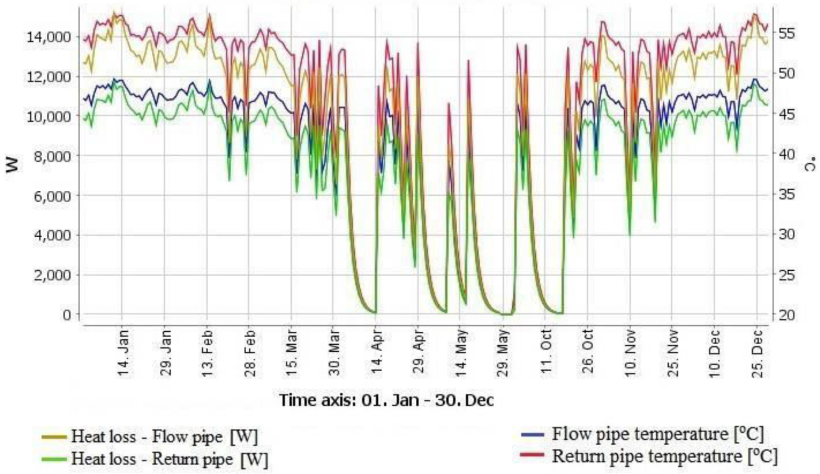

a)

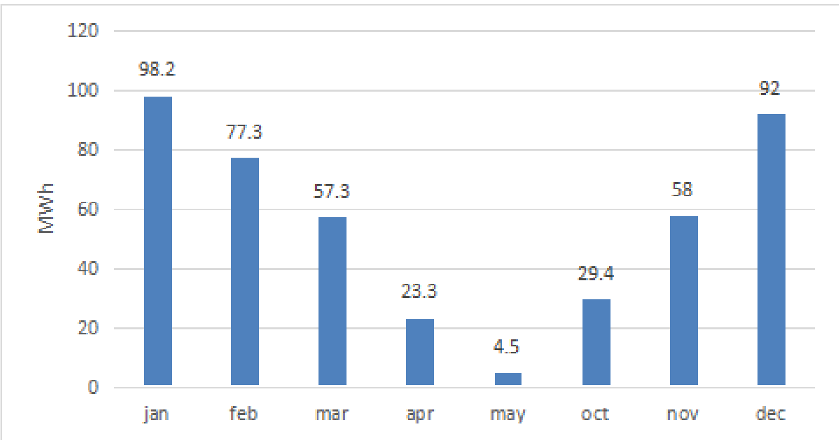

b)

Fig. 7. Heat loss and energy consumption for the efficiency situation (reduction of supply / return temperatures) [8]

Compared to the existing situation, the modernization stage can contribute to the reduction of energy loss on the supply route by a percentage of 51.12%, and the efficiency stage can contribute to the reduction of energy loss on the supply route by a percentage of 65.87%, according to Table 2. In addition, one can observe that for the modernization and efficiency stage, respectively, a saving of 145.3 MWh can be achieved by applying the pumping automation and 191.8MWh respectively by reducing the temperature of the thermal agent.

Table 2: Analysis of annual consumption and reduction of heat loss

Characteristics	Unit	Existing situation	Modernized situation	Streamlined situation
Annual heat loss	[MWh]	295.60	144.50	100.87
Heat loss reduction	[%]	-	51.12	65.87
Annual energy consumption	[MWh]	631.8	486.5	440
Annual energy reduction	[MWh]	-	145.30	191.80

A comparative analysis obtained by simulating the operating parameters, between the three variants of heat supply (during the cold period of the year) of the analysed isolated consumer is presented in Fig. 8.

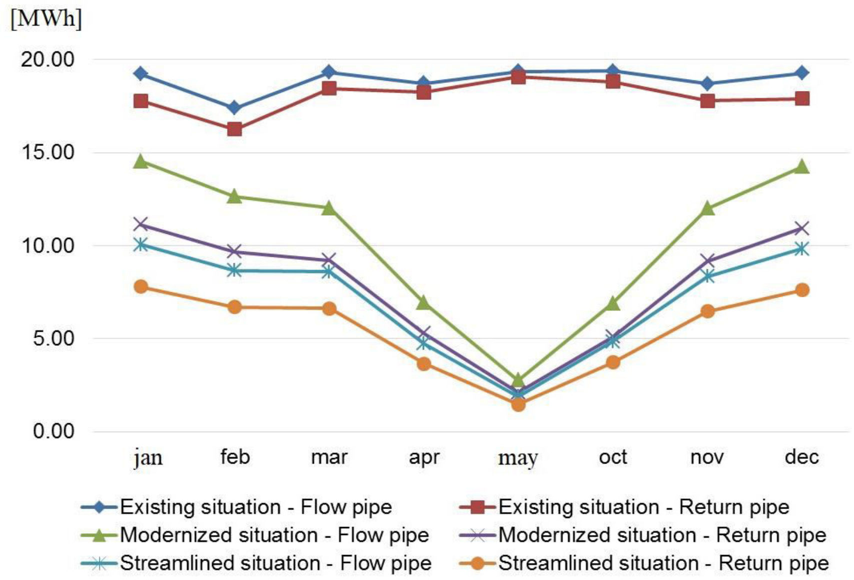

Fig. 8. The comparison between the heat losses of all three analysed variants

From the analysis of the graphical representation in Figure 8, one can notice that in the existing situation the heat loss curves on the supply and return of the system keep their allure throughout the year, while in the situation of the modernized system by automating pumping and the system considered efficient energetically, they change their shape, having a decreasing tendency as the outside temperature increases.

4. Conclusions

For the transition from generation III to generation IV, modernization and efficiency measures can be multiple and can be carried out in several stages depending on the particular situations of final

consumers, measures aimed at the realization and sustainable use of district heating networks, in accordance with policy to reduce energy consumption and CO_2 emissions.
For the case study, based on the results obtained by simulation, it can be seen that for the first stage of modernization a reduction of energy losses of 51.12% was obtained compared to the existing situation (continuous circulation), and for the efficiency stage by reducing the supply/return temperatures of the thermal agent obtained a reduction of energy losses of 65.87% compared to the existing situation. On the other hand, an important aspect is the reduction of the annual thermal energy consumption materialized by a reduction of 145.3 MWh by automating the pumping and respectively 191.8 MWh by streamlining the system by reducing the supply/return temperatures of the thermal agent.
As future directions, the authors intend to carry out a study on the use of heat pumps for the production of heat for this case study and to assess the reduction of CO2 emissions.

References

[1] Lake, Andrew, Behnaz Rezaie, and Steven Beyerlein. "Review of district heating and cooling systems for a sustainable future." *Renewable and Sustainable Energy Reviews* 67 (2017): 417–425.
[2] Lund, Henrik, Sven Werner, Robin Wiltshire, Svend Svendsen, Jan Eric Thorsen, Frede Hvelplund, and Brian vad Mathiesen. "4th Generation District Heating (4GDH) Integrating smart thermal grids into future sustainable energy systems." *Energy* 68 (2014): 1-11.
[3] Muntean, Daniel, Matei Mirza, and Adriana Tokar. "Soluții de reducere a pierderilor de căldură în sistemele de termoficare prin zonarea temperaturii de livrare." *Ingineria Instalatiilor*, no. 1 (2021): 27-31.
[4] International Energy Agency (IEA). Renewables 2019, "Market analysis and forecast from 2019 to 2024", "Report extract. Heat" Fuel report — October 2019. Accessed March 02, 2022. https://www.iea.org/reports/renewables-2019/heat.
[5] Nielsen, Anders, and Charles Winther Hansen. "Grundfos iGrid temperature zone, District Heating – Grundfos white paper." 2019. Accessed March 02, 2022.
https://net.grundfos.com/Appl/ccmsservices/public/literature/filedata/Grundfosliterature-6289184.pdf
[6] Isoplus manufacturer's technical documentation. Accessed March 07, 2022. www.isoplus.org.
[7] COLTERM S.A. Timisoara Local Heating Company / Compania Locală de Termoficare COLTERM S.A. Timișoara, 2022. Accessed March 04, 2022. https://www.colterm.ro.
[8] Polysun software from Vela Solaris.
[9] ASRO. SR 1907-1:2014, "Instalaţii de încălzire. Necesarul de căldură de calcul. Metodă de calcul".
[10] ASRO. SR 1907-2:2014, "Instalaţii de încălzire. Necesarul de căldură de calcul. Temperaturi interioare convenţionale de calcul".
[11] Ilina, Mihai (coord.). *Technical Encyclopedia of Installations. Installations Handbook. Heating Installations / Enciclopedia Tehnica de Instalatii. Manualul de Instalatii. Instalatii de Incalzire*. 2nd edition. Bucharest, Artecno Publishing House, 2010.
[12] Duță, Gheorghe (coord.). *Technical Encyclopedia of Installations. Installations Handbook. Ventilation and Air Conditioning Installations / Enciclopedia Tehnica de Instalatii. Manualul de Instalatii. Instalatii de Ventilare si Climatizare*. 2nd edition. Bucharest, Artecno Publishing House, 2010.

ISSN 1453 – 7303 **"HIDRAULICA" (No. 1/2022)**
Magazine *of Hydraulics, Pneumatics, Tribology, Ecology, Sensorics, Mechatronics*

Experimental Demonstrations of Extension of Technical Applications for Pumping Units Equipped with Miniboosters

Ph.D. Eng. **Teodor Costinel POPESCU[1,*]**, Ph.D. Stud. Eng. **Alexandru-Polifron CHIRIȚĂ[1]**, Dipl. Eng. **Alina Iolanda POPESCU[1]**, Dipl. Eng. **Andrei VLAD[2]**, Dipl. Eng. **Ionel Daniel VOCHIN[2]**, Res. Assist. **Ana-Maria Carla POPESCU[1]**

[1] National R&D Institute for Optoelectronics, Subsidiary Hydraulics and Pneumatics Research, Bucharest, Romania

[2] S.C. HESPER S.A., Bucharest, Romania

* popescu.ihp@fluidas.ro

Abstract: *The authors of this article have developed three high-pressure pumping modules, composed of low-pressure electric pumps, equipped with oscillating hydraulic pressure intensifiers (miniboosters), which they intended to use to supply hydraulic cylinders of small dimensions and high forces. Due to the flow and pressure pulsations that occur at the outlet of the minibooster secondary side, such pumping modules are recommended for applications with static loads, which imply generating and maintaining high pressures in the volumes of closed spaces (pipes, tanks), or at the end of the stroke of hydraulic cylinders (presses). The authors have demonstrated, on an experimental test bench, which includes a 700 bar hydraulic test cylinder and a load simulation hydraulic cylinder, that the three pumping modules can also be used for the relatively uniform displacement of the dynamic load test cylinder over its entire stroke.*

Keywords: *High-pressure pumping module, minibooster, dynamic load, hydraulic cylinder, uniform displacement*

1. Introduction

A **high-pressure pumping module** may be equivalent to a **low-pressure pumping group** (oil tank + fixed flow electric pump + pressure valve + hydraulic directional control valve + pressure filter) **equipped with an oscillating hydraulic pressure intensifier** (minibooster).
The classic application for the use of these pumping modules, whose hydraulic operating diagram is shown in Figure 1, is the supply of single or double acting hydraulic cylinders, which move with no load over the entire advance stroke, except at the end of the stroke, where they have to achieve and maintain high clamping / pressing forces. Basically, the high-pressure pumping module **operates at low pressure during the displacement of hydraulic cylinder**, with maximum flow, which produces high speed of displacement of the cylinder; **high-pressure operation only takes place at the stroke end** of the cylinder, where the displacement is zero, and the high-pressure flow is only necessary to cover any internal losses on the high-pressure circuit.
When the slide valve of the pumping module hydraulic directional control valve switches to the left position of the hydraulic symbol (Fig. 1), fixed pump flow reaches the piston chamber of the (single or double acting) hydraulic cylinder directly, bypassing low / high-pressure pistons (**LP**, **HP**) and bistable distribution valve (**BV1**), the two check valves (**KV1**, **KV2**) and unlockable check valve (**DV**) being open, and the cylinder starts its **advance stroke** at full speed.
When the cylinder piston reaches the end of the advance stroke, or on the onset of the load, the three check valves (**KV1**, **KV2**, **DV**) get closed, and the minibooster starts up and pumps oil at high pressure, namely:
- The two pistons (**LP**+**HP**) move in both directions;
- Through the hydraulically operated distribution valve the oil discharged by the fixed pump fills **volume 2** (when pistons **LP**+**HP** move upwards) or **volume 2** is discharged through **volume 3** to the tank (when pistons **LP**+**HP** move downwards);
- The oil at low pressure is sucked into the volume V1 (**KV1** open, **KV2** closed), when pistons move downwards;
- The oil at high pressure is pumped out of the volume V1 (**KV1** closed, **KV2** open), when pistons move upwards.

Up and down displacement of the pistons stops (the minibooster stops working) when the pressure on fitting **H** of the minibooster reaches the set value of the safety valve (not shown in fig.1) of the pump (the pump discharges through the safety valve to the tank). The pressure on fitting **IN** of the minibooster is amplified on fitting **H**, with a value equal to the amplification ratio **i**. If the pressure in fitting **H** decreases due to internal oil leaks, the minibooster starts working again to restore high pressure.
To start the **retraction stroke** of the cylinder, the slide valve of the pumping module hydraulic directional control valve switches to the right position of the hydraulic symbol; unlockable check valve **DV** receives the command to open from the pump, and the hydraulic cylinder piston chamber is discharged via **DV** to the tank.

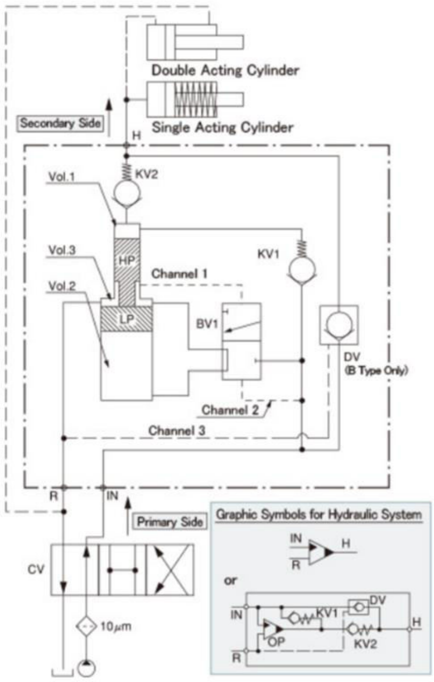

Caption:
LP = low-pressure piston;
HP = high-pressure piston;
BV1 = bistable distribution valve, hydraulically controlled through pilot channels *1* and *2*, for changing the direction of displacement of the pistons;
DV = unlockable check valve, controlled through pilot channel *3*, for discharging high-pressure oil from the chamber of the consumer;
KV1, **KV2** = check valves for oil inlet / outlet in / from high-pressure chamber **Vol.1**;
Vol.2 = volume of oil discharged to the tank by distribution valve **BV1**, via volume **Vol.3**;
IN = inlet fitting to the primary side of the minibooster;
R = outlet (return) fitting from the primary side of the minibooster;
H = secondary side of the minibooster outlet fitting;
CV = hydraulic directional control valve for changing the direction of displacement of the hydraulic cylinder, single or double acting, supplied via high-pressure outlet fitting **H**, from the secondary side of the minibooster.

Fig. 1. Classic application for using pumping modules equipped with minibooster [1]

2. High-pressure pumping modules equipped with miniboosters

Figure 2 below shows the three high-pressure pumping modules developed by the authors (MP1, MP2, MP3), of different power, pressure amplification ratios and flow rates.

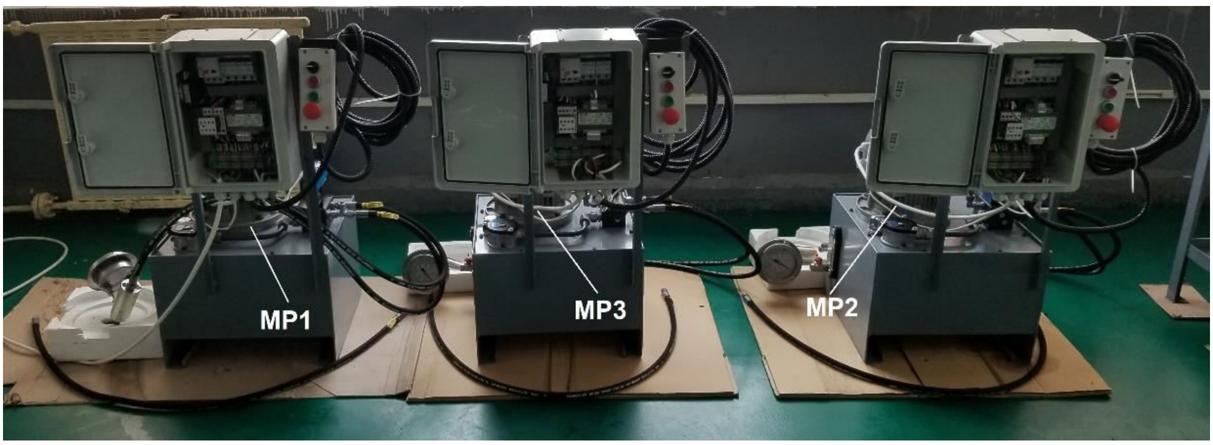

Fig. 2. The three high-pressure pumping modules equipped with miniboosters

Table 1: Technical characteristics of high-pressure pumping modules

Technical characteristics	Pumping module MP1	Pumping module MP2	Pumping module MP3
Overall dimensions [mm]	443 x 425 x 880	443 x 425 x 880	443 x 425 x 880
Geometric volume of the pump $V_g[cm^3/rev]$	8	6	4.20
Pump flow rate *Q[l/min]*	11.77	8.95	6.10
Oil tank volume *V[l]*	38	38	38
Pump drive electric motor power *N[kW]*	4	3	2.2
Pump drive electric motor speed *n[rev/min]*	1460	1455	1455
Rated pump pressure (IN minibooster) $p_{IN}[bar]$	adjustable 0...200	adjustable 0...200	adjustable 0...200
Pressure amplification ratio $i = p_{H1} / p_{IN}$ [-]	5	6.6	7.6
Amplified pressure p_{H1} [bar]	adjustable 0...1000	adjustable 0...1320	adjustable 0...1520
Flow rate at amplified pressure Q_{H1} [l/min]	11.77...0.75	8.95...0.40	6.10...0.30
High-pressure outlet fitting of minibooster *H1*	internal thread M22 x 1.5	internal thread M22 x 1.5	internal thread M22 x 1.5

The technical characteristics of these products are shown in Table 1, and their hydraulic operating diagram in Figure 3.

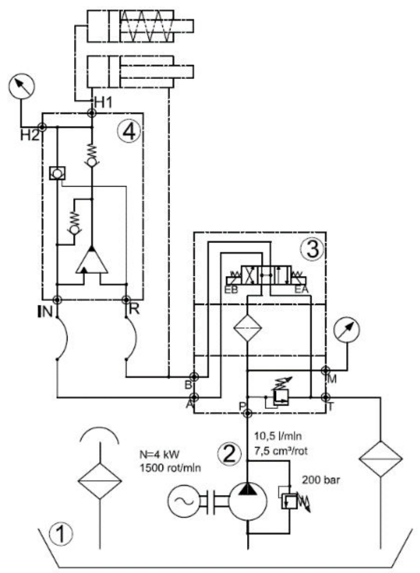

Caption:

1 = hydraulic tank with return filter and filling and venting filter;
2 = electric pump (*4 kW, 3 kW, 2.2 kW*);
3 = block with hydraulic devices (direct pressure control valve, modular pressure filter, 4/3 electrohydraulic directional control valve, low pressure gauge);
4 = minibooster (*i=5, i=6.6, i= 7.6*);
IN = low-pressure inlet fitting of the minibooster (primary side of the minibooster);
H1 = high-pressure outlet fitting of the minibooster (secondary side of the minibooster);
H2 = high pressure gauge fitting (secondary side of the minibooster);
R = return fitting (primary side of the minibooster).

Fig. 3. Hydraulic operating diagram of the three high-pressure pumping modules

3. Experimental tests on high-pressure pumping modules equipped with miniboosters

Static load tests and dynamic load tests on the high-pressure fitting of the minibooster have been carried out for each of the three pumping modules [2]...[7].

3.1 Static load tests on the pumping modules

Static load tests on pumping modules MP1, MP2, and MP3 have been carried out with an M22x1.5 plug, mounted on fitting *H1* of the minibooster and adjusting the pressure in the primary side in the range 0 ... 200 bar. Figure 4 shows the maximum pressure values achieved by the three pumping modules (p_{Hmax}).

Pumping module MP1
Product code:
MPIP-HP1-8.0-HC7-5.0-0.0

On the large pressure gauge:
p_{H2} = 960 bar
On the small pressure gauge:
p_{IN} = 200 bar
Amplification ratio:
i = 960 / 200 = 4.80

Pumping module MP2
Product code:
MPIP-HP1-6.0-HC7-6.6-0.0

On the large pressure gauge:
p_{H2} = 1290 bar
On the small pressure gauge:
p_{IN} = 200 bar
Amplification ratio:
i = 1290 / 200 = 6.45

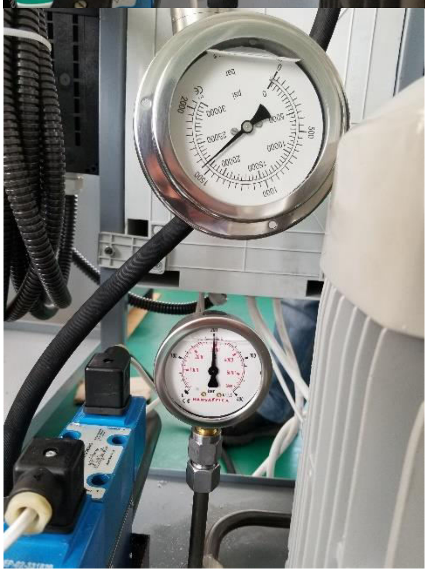

Pumping module MP3
Product code:
MPIP-HP1-4.3-HC7-7.6-0.0

On the large pressure gauge:
p_{H2} = 1540 bar
On the small pressure gauge:
p_{IN} = 200 bar
Amplification ratio:
i = 1540 / 200 = 7.70

Fig. 4. Maximum pressure values achieved with the three pumping modules (MP1, MP2, MP3)

3.2 Dynamic load tests on the pumping modules

The dynamic load tests of the three pumping modules have been carried out on the test bench for high-pressure pumping modules and systems, product code SPMS-0.0, which is shown in fig. 5.

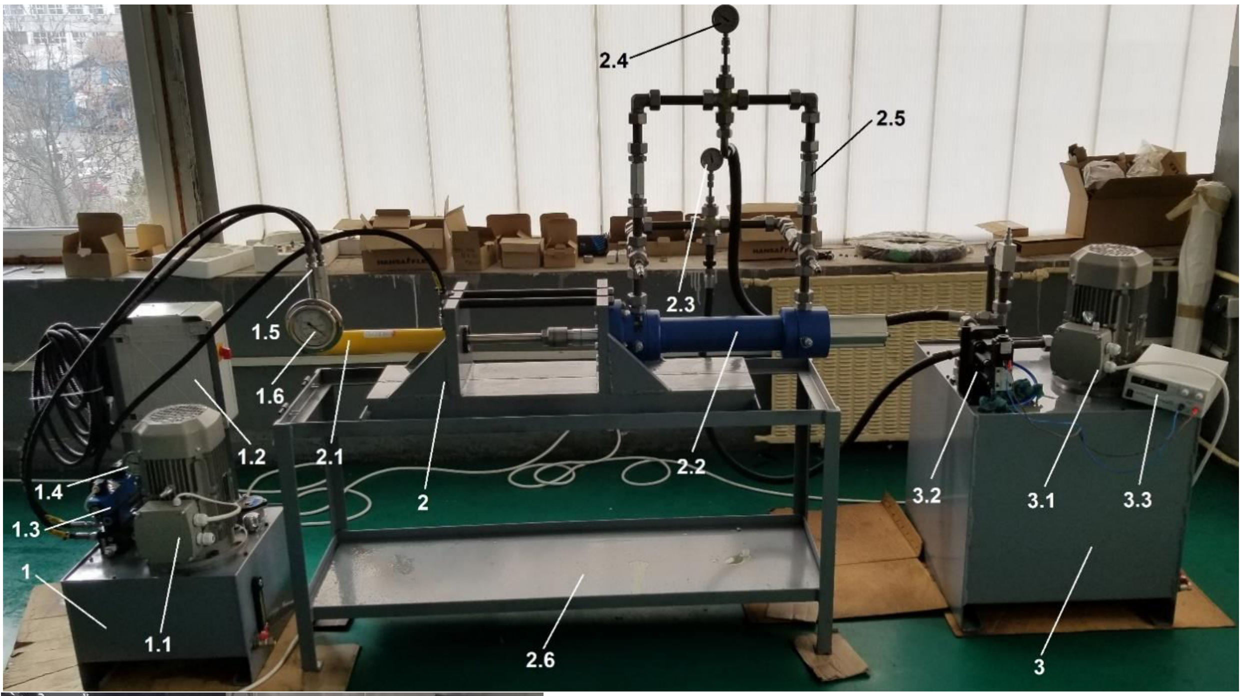

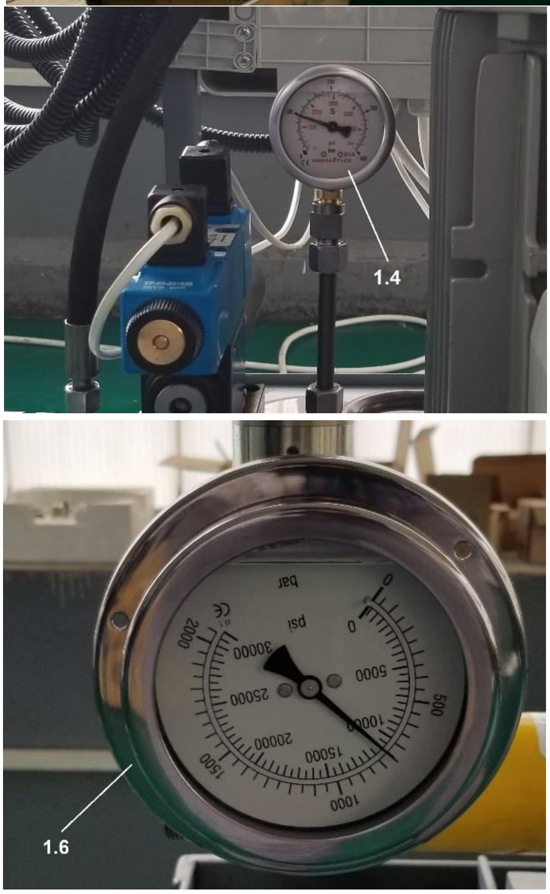

Caption:

1 = Pumping module under tests (MP1, MP2, **MP3**);
1.1 = Electric pump (4 kW, 3 kW, **2.2 kW**);
1.2 = Electric panel;
1.3 = Block with hydraulic devices (**direct pressure control valve**, modular pressure filter, 4/3 electrohydraulic directional control valve, low pressure gauge);
1.4 = Low pressure gauge (it reads **100 bar**);
1.5 = Minibooster (i=5, i=6.6, **i=7.6**);
1.6 = High pressure gauge (it reads **750 bar**);
2 = Hydraulic cylinder fastening module;
2.1 = Test cylinder Ø38.1/ Ø25.4 x 257 (p_{max}= 700 bar);
2.2 = Load cylinder Ø80/ Ø45 x 300;
2.3, 2.4 = Pressure gauges for measuring pressure in the load cylinder chambers;
2.5 = Check valves (4 pcs.);
2.6 = Support frame;
3 = Hydraulic station for filling the load cylinder;
3.1 = Electric pump 2.2 kW, 60 cm^3/rev;
3.2 = Normally closed proportional pressure valve;
3.3 = Power supply for proportional electromagnet of normally closed pressure valve.

Note:
The pictures have been taken during experimental tests on pumping module MP3.

Fig. 5. Test bench for high-pressure pumping modules and systems with dynamic load

3.2.1 Dynamic load tests on module MP1

Module MP1 was connected hydraulically to the 700 bar test cylinder (HC) of the bench, with fitting H1 of the minibooster fixed to the piston chamber fitting and fitting B of the 4/3 electrohydraulic directional control valve fixed to the rod fitting. Seven measurements were performed, as follows:

Measurement 1: Maximum flow rate of pumping module MP1, idle, with no load, was determined by using a graded beaker and stopwatch (11.77 l / min);

*For the next measurements, the safety valve (SV) of the module was set to **160 bar**, taking into account two aspects: maximum working pressure of the test cylinder of the bench (700 bar); the safety valve of the module must not open during the displacement of the load cylinder of the bench (for Qs = 0, it results* $Qp_{ump} = Q_{IN} = Q_H + Q_R$*).*

Measurement 2: Flow rate of pumping module MP1, idle, with no load, with zero supply current of the normally closed proportional valve that simulates the load, was determined by measuring the time of a complete advance stroke of the test cylinder (stroke = 257 mm);

Measurements 3-7: Flow rates of pumping module MP1, with load, were determined for the normally closed proportional valve supply currents of 0.5A, 0.7A, 0.9A, 1.1A, 1.3A, simulating the load, by measuring the time of a complete advance stroke of the test cylinder. The results of the measurements are shown in Table 2 and Figure 6.

Table 2: Results of experimental tests with dynamic load on module MP1

Item no.	Measured values			Calculated values						
	Pressures [bar] *(p)*		Time / stroke [s/ 257 mm] *(t)*	Speed of HC [mm/s] *(V=c/t)*	HC Piston area [mm²] *(A_p)*	Flow rates [l/min] *($Q=A_p x V$)*			Force of HC [kN] *($F=p/A_p$)*	Ampl. ratio i [-]
	Setting of SV (primary side)	Load of HC secondary side)				on H1	max.	on R		
1	0	0	-	-	-	11.770	11.77	0.000	0.00	5
2	160	30	2.670	96.254	1140	6.583	11.77	5.186	3.42	5
3	160	150	16.145	15.918	1140	1.088	11.77	10.681	17.1	5
4	160	255	16.860	15.243	1140	1.042	11.77	10.727	29.07	5
5	160	375	17.860	14.389	1140	0.984	11.77	10.785	42.75	5
6	160	510	19.260	13.343	1140	0.912	11.77	10.857	58.14	5
7	160	625	23.265	11.046	1140	0.755	11.77	11.014	71.25	5

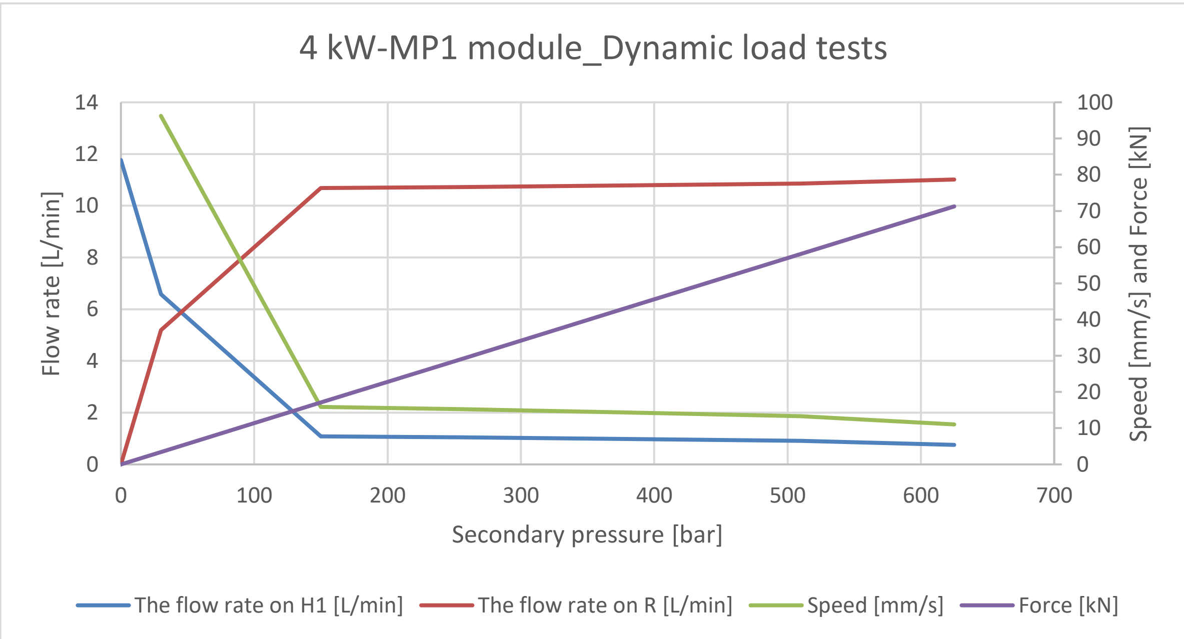

Fig. 6. Module M1: Variation of Q_{H1}, Q_R, speed, and force of test cylinder depending on p_{H1}

3.2.2 Dynamic load tests on module MP2

Module MP2 was connected hydraulically to the 700 bar test cylinder (HC) of the bench, with fitting H1 of the minibooster fixed to the piston chamber fitting and fitting B of the 4/3 electrohydraulic directional control valve fixed to the rod fitting. Seven measurements were performed, as follows:
Measurement 1: Maximum flow rate of pumping module MP2, idle, with no load, was determined using a graded beaker and stopwatch (8.955 l / min);
*For the next measurements, the safety valve (SV) of the module was set to **120 bar**, taking into account two aspects: maximum working pressure of the test cylinder of the bench (700 bar); the safety valve of the module must not open during the displacement of the load cylinder of the bench (for Qs = 0, it results $Qp_{ump} = Q_{IN} = Q_H + Q_R$).*
Measurement 2: Flow rate of pumping module MP2, idle, with no load, with zero supply current of the normally closed proportional valve that simulates the load, was determined by measuring the time of a complete advance stroke of the test cylinder (stroke = 257 mm);
Measurements 3-7: Flow rates of pumping module MP2, with load, were determined for the normally closed proportional valve supply currents of 0.4A, 0.7A, 0.9A, 1.1A, 1.3A, simulating the load, by measuring the time of a complete advance stroke of the test cylinder. The results of the measurements are shown in Table 3 and Figure 7.

Table 3: Results of experimental tests with dynamic load on module MP2

Item no.	Measured values			Calculated values						
	Pressures [bar] *(p)*		Time / stroke [s/ 257 mm] *(t)*	Speed of HC [mm/s] *(V=c/t)*	HC Piston area [mm²] *(A_p)*	Flow rates [l/min] *($Q=A_pxV$)*			Force of HC [kN] *($F=p/A_p$)*	Ampl. ratio i [-]
	Setting of SV (primary side)	Load of HC secondary side)				on H1	max.	on R		
1	0	0	-	-	-	8.955	8.955	0.000	0.00	6.6
2	120	30	3.373	76.193	1140	5.211	8.955	3.743	3.42	6.6
3	120	100	26.500	9.698	1140	0.663	8.955	8.291	11.40	6.6
4	120	200	30.770	8.352	1140	0.571	8.955	8.383	22.80	6.6
5	120	365	33.190	7.743	1140	0.529	8.955	8.425	41.61	6.6
6	120	500	36.280	7.083	1140	0.484	8.955	8.470	57.00	6.6
7	120	650	43.470	5.912	1140	0.404	8.955	8.550	74.10	6.6

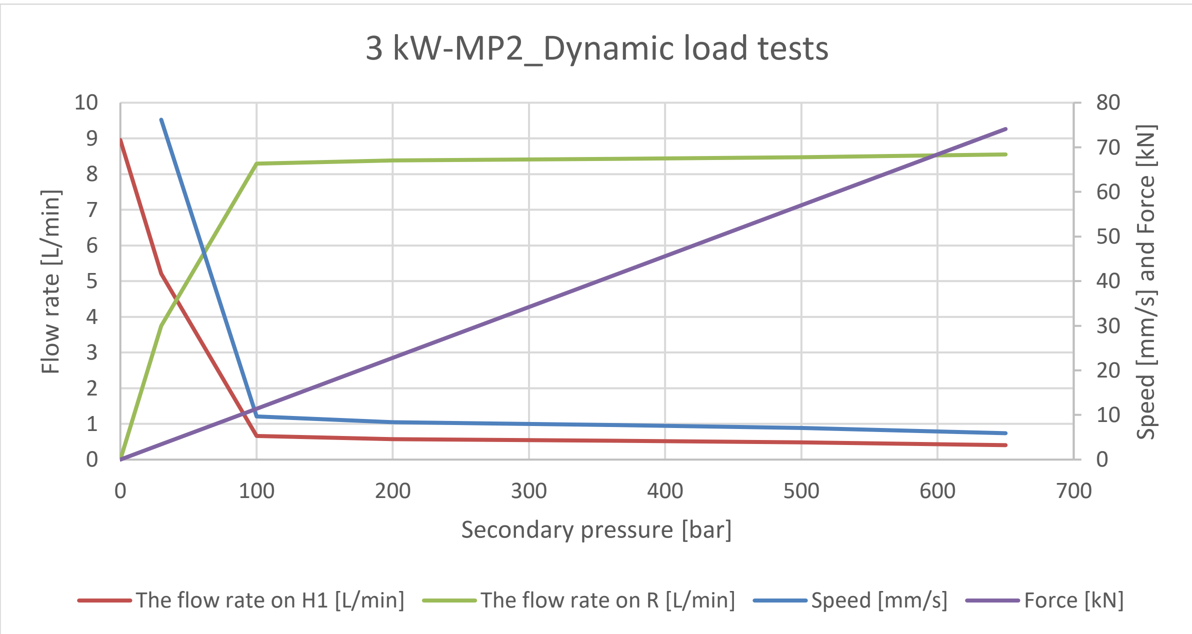

Fig. 7. Module M2: Variation of Q_{H1}, Q_R, speed, and force of test cylinder depending on p_{H1}

3.2.3 Dynamic load tests on module MP3

Module MP3 was connected hydraulically to the 700 bar test cylinder (HC) of the bench, with fitting H1 of the minibooster fixed to the piston chamber fitting and fitting B of the 4/3 electrohydraulic directional control valve fixed to the rod fitting. Seven measurements were performed, as follows:

Measurement 1: Maximum flow rate of pumping module MP3, idle, with no load, was determined using a graded beaker and stopwatch (6.10 l / min);

For the next measurements, the safety valve (SV) of the module was set to ***120 bar****, taking into account two aspects: maximum working pressure of the test cylinder of the bench (700 bar); the safety valve of the module must not open during the displacement of the load cylinder of the bench (for Qs = 0, it results* $Qp_{ump} = Q_{IN} = Q_H + Q_R$*).*

Measurement 2: Flow rate of pumping module MP3, idle, with no load, with zero supply current of the normally closed proportional valve that simulates the load, was determined by measuring the time of a complete advance stroke of the test cylinder (stroke = 257 mm);

Measurements 3-7: Flow rates of pumping module MP3, with load, were determined for the normally closed proportional valve supply currents of 0.5A, 0.8A, 1A, 1.2A, 1.3A, simulating the load, by measuring the time of a complete advance stroke of the test cylinder. The results of the measurements are shown in Table 4 and Figure 8.

Table 4: Results of experimental tests with dynamic load on module MP3

Item no.	Measured values			Calculated values						
	Pressures [bar] *(p)*		Time / stroke [s/ 257 mm] *(t)*	Speed of HC [mm/s] *(V=c/t)*	HC Piston area [mm²] *(A_p)*	Flow rates [l/min] *($Q=A_p x V$)*			Force of HC [kN] *($F=p/A_p$)*	Ampl. ratio i [-]
	Setting of SV (primary side)	Load of HC secondary side)				on H1	max.	on R		
1	0	0	-	-	-	6.100	6.10	0.000	0.00	7.6
2	100	30	5.176	49.652	1140	3.396	6.10	2.703	3.42	7.6
3	100	180	41.65	6.170	1140	0.422	6.10	5.677	20.52	7.6
4	100	340	45.96	5.591	1140	0.382	6.10	5.717	38.76	7.6
5	100	460	50.31	5.108	1140	0.349	6.10	5.750	52.44	7.6
6	100	580	54.22	4.739	1140	0.324	6.10	5.775	66.12	7.6
7	100	630	56.45	4.552	1140	0.311	6.10	5.788	71.82	7.6

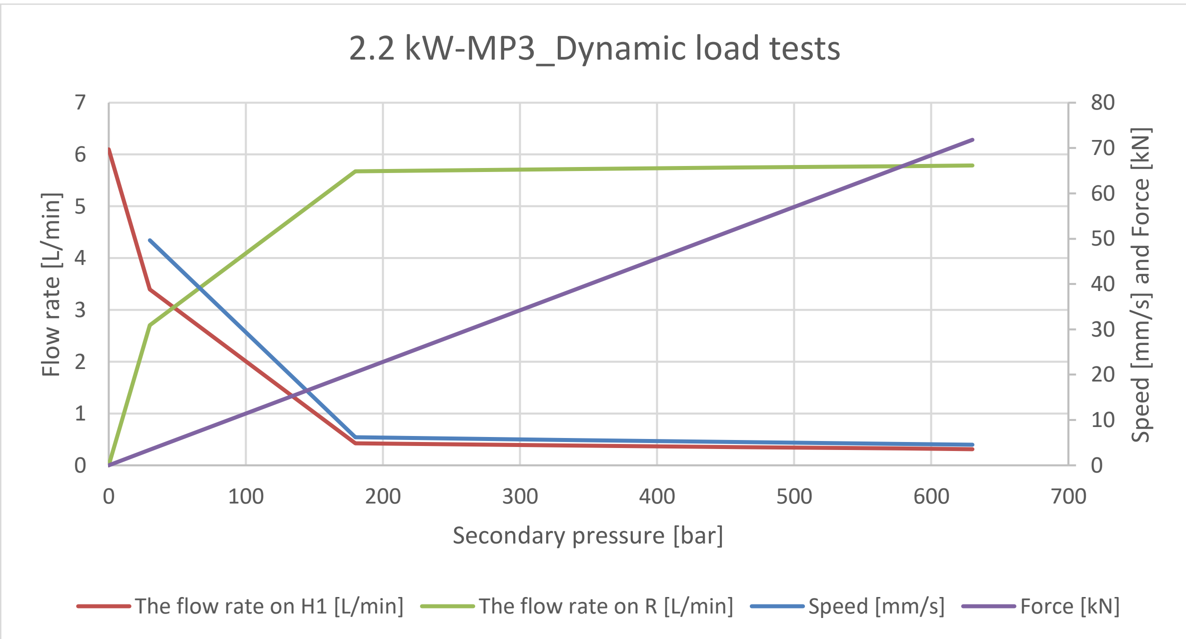

Fig. 8. Module M3: Variation of Q_{H1}, Q_R, speed, and force of test cylinder depending on p_{H1}

3.2.4 Comparison of flow rates of the pumping modules at equal dynamic loads

The three pumping modules (MP1, MP2, MP3) are characterized by increasing pressure amplification ratios (5, 6.6, 7.6) and decreasing flow rates at high pressures. As a result, the test cylinder has high speed and creates low force when it is supplied by module MP1, and vice versa, low speed and high force when it is supplied by module MP3. A comparison of flow rates at the secondary output of the minibosters of the three pumping modules (fitting **H1**), which determines the speed rates on the advance stroke of the test cylinder of the bench depending on its load, is plotted in Figures 9 and 10.

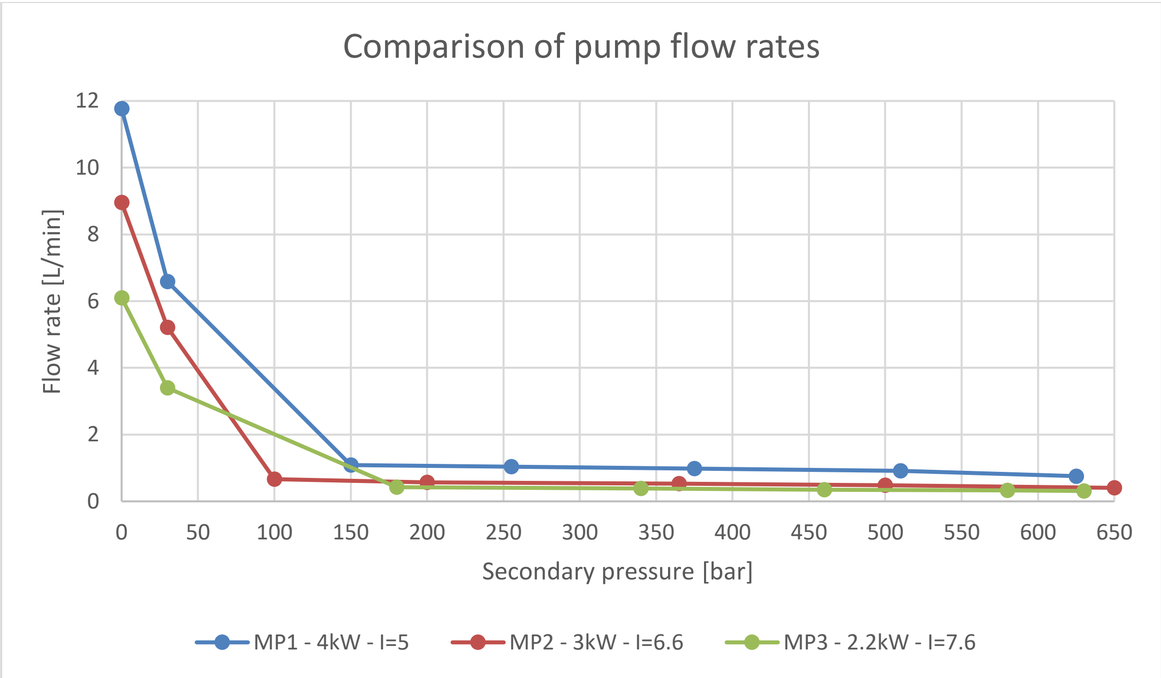

Fig. 9. Comparison of dynamic load flow rates of the three pumping modules

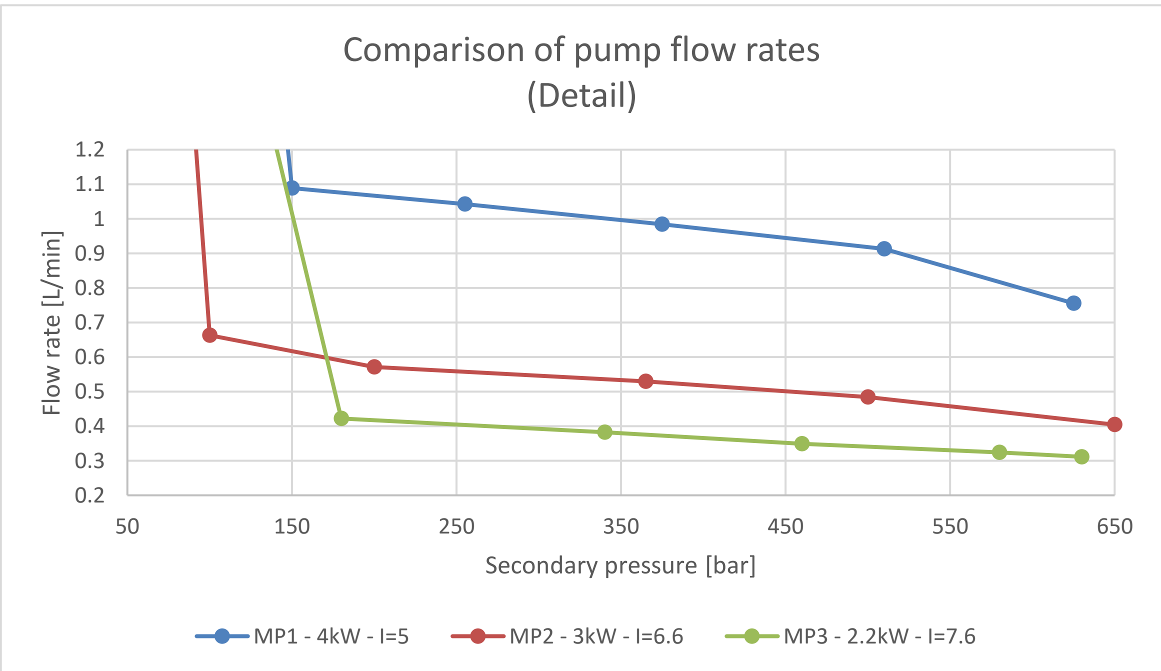

Fig. 10. Comparison of dynamic load flow rates of the three pumping modules (Detail)

4. Conclusions

- *Static load tests* have shown the ability of the pumping modules to achieve, on the high pressure fitting within the secondary side of the oscillating hydraulic amplifier, high, adjustable, static pressures (MP1 = 0 ... 1000 bar; MP2 = 0 ... 1320 bar; MP3 = 0 ... 1420 bar) through the direct pressure control valve in the primary side. This technical characteristic of the three pumping modules makes them recommendable for use in *static resistance tests of metal pipes and tanks; long-term maintenance of high pressure in hydraulic presses*.
- *Dynamic load tests* have shown the ability of the pumping modules to drive single and double acting hydraulic cylinders, of high pressures and small dimensions, on their entire advance stroke, the displacement being relatively uniform and continuous, with small pulsations. This technical characteristic of the three pumping modules makes them recommendable for use when driving hydraulic cylinders in the structure of *extrication rescue equipment and intervention tools used in case of road accidents; installations for lifting and getting back on the rails the derailed rolling stock; hydraulic lifting equipment used in mines and other narrow spaces.*
- *Dynamic load tests* have shown that the set of low-pressure (**LP** in Fig. 1) and high-pressure (**HP** in Fig. 1) pistons, together with the hydraulically controlled bistable distribution valve (**BV1** in Fig. 1) oscillates inside minibosters even if there is only the resistive load given by internal frictions in the seals of hydraulic cylinders of the bench (approx. 30 bar on output **H** of the miniboster). For such low loads, the flow rates on return **R** of the minibosters being appreciable (5.186 l / min, for module M1; 3.743 l / min, for module M2; 3.420 l / min, for module M3), the displacement speeds of hydraulic cylinders decrease significantly compared to the case when they are supplied with a pumping module without minibooster.
- For a qualitative assessment of uniformity of displacement of the hydraulic cylinders in the structure of the bench, measurements will be carried out by using an acceleration transducer fixed on the coupling between the rods of the cylinders.

Acknowledgments

The research presented in this paper has been developed under Financial Agreement no. 272/24.06.2020, signed by the Ministry of European Funds / Ministry of Education and Research and S.C. HESPER S.A. Bucharest for the Innovative Technological Project titled “Digital mechatronic systems for generating pressure of 1000 bar, using hydraulic pressure intensifiers” (SMGP), project under implementation from 01.07.2020 to 30.06.2023.

References

[1] P.M.P. Pioneer Machine Tools. “The increase pressure actuation system of hydraulic boosters HC series.” Accessed February 21, 2022. http://pmt-pioneer.com/en/product-detail5.html.
[2] Bartnicki, Adam. “The Research of Hydraulic Pressure Intensifier for Use in Electric Drive System.” *IEEE ACCESS* 7 (2019): 20172-20177.
Accessed February 22, 2022. https://ieeexplore.ieee.org/stamp/stamp.jsp?tp=&arnumber=8633832.
[3] Popescu, T.C., A.P. Chiriță, and A.-M.C. Popescu. “Research on the assessment of flow and pressure pulses in oscillating hydraulic intensifiers.” *Mining Machines, no. 4* (164) (2020): 14-23; DOI: 10.32056/KOMAG2020.4.2.
[4] Espersen, C. “Pressure Boosters in Hydraulic Systems A Solution Which Is Often Overlooked.”
Accessed February 21, 2022. https://nanopdf.com/download/pressure-boosters-in-hydraulic-systems_pdf.
[5] https://www.minibooster.com/hc7/ Accessed February 10, 2022.
[6] Levinsen, A. “Scanwill fliud power Unique hydraulic pressure intensifier solutions. ”
Accessed February 22, 2022. https://www.luvra-hydraulik.de/fileadmin/web_data/downloads/Luvra-Hydraulik-Scanwill-0915.pdf .
[7] Günaydın, A.C., M. Halkacı, F. Ateş, and H.S. Halkacı. “Experimental Research of the Usability on Double Acting Intensifiers in Hydroforming.” *MATEC Web of Conferences 220* (2018): 04001. Accessed February 22, 2022.
https://www.matec-conferences.org/articles/matecconf/pdf/2018/79/matecconf_icmsc2018_04006.pdf.

Researches on Water Aeration Using Fine Bubbles Generators

PhD Std. **Marilena Monica BOLTINESCU (ROZA)**[1], Prof. Dr. Eng. **Nicolae BĂRAN**[1], Dr. Eng. **Albertino Giovani ROZA**[1], Șl. Dr. Eng. **Mihaela CONSTANTIN**[1]*

[1] University Politehnica of Bucharest

* i.mihaelaconstantin@gmail.com

Abstract: *The paper presents the constructive solution of a fine air bubble generator that is used to aerate waters. This generator is provided with a perforated plate, which has orifices for the introduction of air into the water, as follows:*
- Variant I: the diameter of the orifice is 0.1 mm
- Variant II: the diameter of the orifice is 0.5 mm.
A computation program is being developed showing the change in the concentration of dissolved oxygen in the water as a function of time in which air is introduced into the water.
Theoretical and experimental data for the two variants are compared; it is concluded that as the diameter of the orifice in the perforated plate decreases, the water aeration process becomes more efficient.

Keywords: *Fine bubble generator, water aeration, dissolved oxygen, orifice.*

1. Introduction

The gaseous mixture that can be introduced into the water to increase the oxygen concentration can be [1] [2]:
1. atmospheric air (21% O_2 + 79% N_2);
2. atmospheric air + oxygen taken from a cylinder in certain proportions;
3. low nitrogen air supplied by oxygen concentrators.

In case 1 it can be stated that an aeration process takes place which aims at oxygenating the waters.
In cases 2 and 3, as the oxygen content of the gas mixture changes, the notion of water oxygenation is introduced, i.e., a distinction must be made as follows:
• water aeration takes place by introducing atmospheric air into the water (1);
• oxygenation of water takes place by introducing oxygen-enriched air (2) + (3)

Aeration and oxygenation of water are biphasic mass transfer processes, the gaseous phase passes into the liquid phase (water). Applications of these processes are used for the following purposes:
- for wastewater treatment;
- for biological wastewater treatment;
- when collecting and separating emulsified fats from wastewater;
- in maintaining an optimal level of oxygen concentration for underwater plants or animals;
- in some of the processes of treating the water captured from a source, to make it drinkable.

Gas bubbles immersed in water can be classified according to their diameter as follows (figure 1):

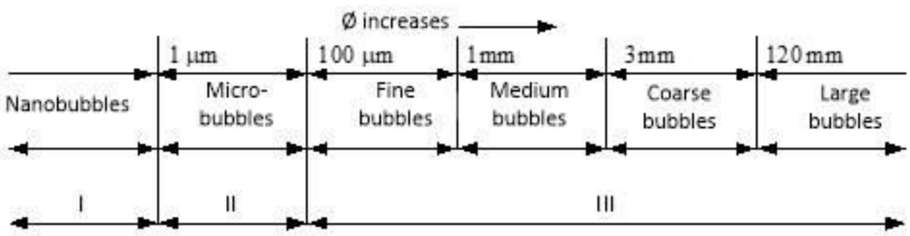

Fig. 1. Classification of gas bubbles according to their diameter (ø):
I - the area where the gas bubbles can be observed under the microscope;
II - the area where gas bubbles can be observed with difficulty;
III - the area where gas bubbles can be observed with the naked eye.

In figure 2, one can observe that the oxygen in the water appears in two forms:
• O_2 bound to H_2;
• Free O_2, called dissolved oxygen in water.

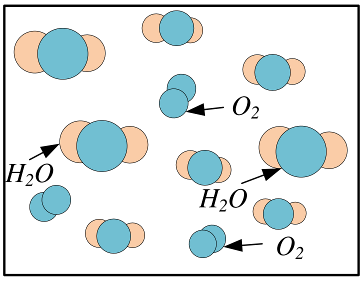

Fig. 2. Oxygen dissolved in water

The solubility of oxygen in water is dependent on temperature, atmospheric pressure, the size of the air-water contact surface and water turbulence. The oxygen needed for the aeration process is taken from the atmospheric air and introduced into the water by three methods: pneumatic, mechanical, and mixed. The pneumatic method uses aeration devices that introduce fine air bubbles into the water; these devices are classified into three categories, as follows [3] [4]:
I. fine bubble generators constructed of ceramic, plastic materials;
II. fine bubble generators constructed of perforated elastic membranes;
III. fine bubble generators with perforated plates made with the help of micro-machines for drilling in coordinates, with drills of ø <0.5mm.
Oxygen transfer in wastewater is an important issue in treatment technology; using fine bubble aeration, the amount of air introduced is optimized, obtaining significant energy savings. Fine air bubbles are obtained with the help of fine bubble generators (FBG) made of ceramic materials (porous diffusers) or perforated plates.
The use of porous diffusers has the following disadvantages:
• emitted air bubbles have unequal diameters;
• air bubbles appear irregularly, only on certain parts of the surface of the porous diffusers;
• porous diffusers have high pressure losses [5].
In recent years, researches on water oxygenation have focused on obtaining fine bubble generators whose orifices for the air introduction into the water have a diameter d <1 mm. FBGs were built which has the perforated plate made by an unconventional technological process (EDM); this process ensures a uniform distribution of the orifices on the surface of the plate and an equal diameter of the orifices. The size and dimension of the orifices are an important parameter of the FBG because it directly affects the air inlet pressure in the FBG, and the size of the air bubble blown into the water.

2. Mathematical model- the oxygen transfer rate equation

The rate of transfer of dissolved oxygen in water is given by the relation [6] [7]:

$$\frac{dC}{d\tau} = a \cdot k_L \cdot \left(C_s - C_0\right) \; [kg / m^3 s] \tag{1}$$

where:
$dC / d\tau$ - rate of change of dissolved oxygen concentration in water (rate of oxygen transfer to water);
ak_L - volumetric mass transfer coefficient [s^{-1}];
C_s - mass concentration of oxygen at saturation in the liquid phase [kg / m^3];
C - current mass oxygen concentration in the liquid phase [kg / m^3].
The term "ak^L" includes:
k_L- mass transfer coefficient [m / s];
a - specific interphase contact surface:

$$a = \frac{A}{V}\left[\frac{m^2}{m^3}\right] \tag{2}$$

where: A- gas bubble area [m^2];
V - the volume of the biphasic system (air + water) [m^3];
If boundary conditions C = C_0 are imposed for τ = 0, equation (1) can be integrated [8] [9] [10]:

$$\frac{dC}{C_s - C} = a \cdot k_L \, d\tau \tag{3}$$

In the hypothesis that C <C_s, after integration, it results:

$$-ln\left(C_s - C\right) = a \cdot k_L \cdot \tau + ct \tag{4}$$

The constant is obtained from the limit condition: C = C_0 for τ = 0
and has the value:

$$ct = -ln\left(C_s - C_0\right) \tag{5}$$

Introducing (6) in (4) one can obtain:

$$-ln\left(C_s - C\right) = a \cdot k_L \cdot \tau - ln\left(C_s - C_0\right) \tag{6}$$

$$ln\left(C_s - C\right) = ln\left(C_s - C_0\right) - a \cdot k_L \cdot \tau \tag{7}$$

$$ln\left(C_s - C\right) = ln\left(C_s - C_0\right) + ln\, e^{-a \cdot k_L \cdot \tau} \tag{8}$$

$$ln\left(C_s - C\right) = ln(\left(C_s - C_0\right) \cdot e^{-a \cdot k_L \cdot \tau}$$

$$C_s - C = ln(\left(C_s - C_0\right) \cdot e^{-a \cdot k_L \cdot \tau}$$

$$C = C_s - \left(C_s - C_0\right) \cdot e^{-a \cdot k_L \cdot \tau} \tag{9}$$

τ=0

To determine theoretically the increase in the concentration of dissolved oxygen in water as a function of the oxygenation time of water, the following quantities must be known:

Table 1: Variation of saturation concentration with temperature at p_{atm} = 760 mm Hg

t°C	**Cs**	t°C	**Cs**	t°C	**Cs**	t°C	**Cs**
0.0	**14.60**	10.0	**11.30**	20.0	**9.10**	30.0	**7.50**
0.5	**14.40**	10.5	**11.10**	20.5	**9.00**	30.5	**7.50**
1.0	**14.20**	11.0	**11.00**	21.0	**8.90**	31.0	**7.40**
1.5	**14.00**	11.5	**10.90**	21.5	**8.80**	31.5	**7.30**
2.0	**13.80**	12.0	**10.80**	22.0	**8.70**	32.0	**7.30**
2.5	**13.60**	12.5	**10.60**	22.5	**8.60**	32.5	**7.20**
3.0	**13.40**	13.0	**10.50**	23.0	**8.60**	33.0	**7.20**
3.5	**13.30**	13.5	**10.40**	23.5	**8.50**	33.5	**7.10**
4.0	**13.10**	14.0	**10.30**	24.0	**8.40**	34.0	**7.00**
4.5	**12.90**	14.5	**10.20**	24.5	**8.30**	34.5	**7.00**
5.0	**12.70**	15.0	**10.10**	25.0	**8.20**	35.0	**6.90**
5.5	**12.60**	15.5	**10.00**	25.5	**8.20**	35.5	**6.90**
6.0	**12.40**	16.0	**9.80**	26.0	**8.10**	36.0	**6.80**
6.5	**12.30**	16.5	**9.70**	26.5	**8.00**	36.5	**6.80**
7.0	**12.10**	17.0	**9.60**	27.0	**7.90**	37.0	**6.70**
7.5	**12.00**	17.5	**9.50**	27.5	**7.90**	37.5	**6.70**
8.0	**11.80**	18.0	**9.40**	28.0	**7.80**	38.0	**6.60**
8.5	**11.70**	18.5	**9.30**	28.5	**7.70**	38.5	**6.60**
9.0	**11.50**	19.0	**9.30**	29.0	**7.70**	39.0	**6.50**
9.5	**11.40**	19.5	**9.20**	29.5	**7.60**	39.5	**6.50**

a) Initial oxygen concentration for a given water temperature (t = 25 ° C), C_0 = 5.12 mg / dm^3;
b) The saturation concentration C_s = 8.2 mg / dm^3 for the same water temperature t = 25 ° C can be read from Table 1 [11].
c) Integration step: a research duration of about two hours is estimated; the step: h = 1 min is chosen (n = 121); $=\tau = 120$ min.
From the literature [12] [13], for a constant airflow of 540 dm^3 / h, a value for ak_L of 0.09 is adopted.

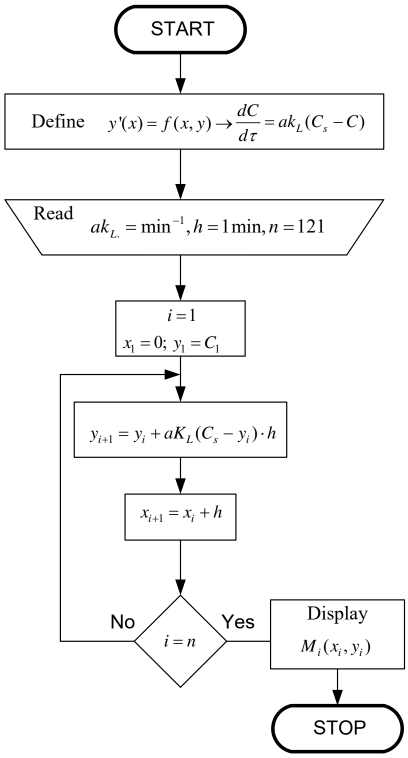

Fig. 3. Logical computation scheme for the numerical integration of the differential equation of the oxygen transfer rate

The scheme (figure 3) is based on the Euler method, the method with separate steps and explicit algorithm [14] [15].

2.1. Establishing the architecture of the orifice plate of the fine air bubbles generator

Two categories of parameters intervene in the water oxygenation process:
I. geometric parameters of the fine bubble generator, more precisely of the plate with fine orifices (D, s, d_o, d); (figure 4).
II. operating parameters ($\dot{V}$, Δp_{FBG}, H, C_0).
Notations:
D - the diameter of the bubble at its detachment from the orifice [m];
s - thickness of the perforated plate [m];
d_o – orifice diameter [m];
d - the distance between two orifices on the same line [m].

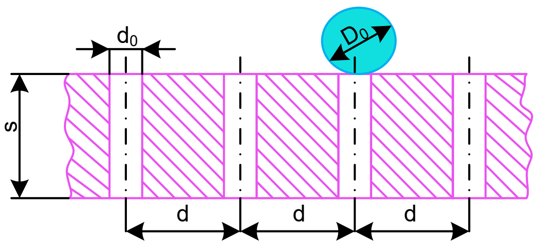

Fig. 4. Logical computation scheme for the numerical integration

In the design and construction of the FBG, the following two conditions must be met: [16] [17]:

$$I - \quad \frac{s}{d_0} > 3, \tag{10}$$

$$II - \quad \frac{d}{d_0} > 8 \tag{11}$$

In the experimental researches for the two variants are obtained:

$$I - \ d_0 = 0.1mm;\ s\ /\ d_0 = 2\ /\ 0.1 = 20;\ d\ /\ d_0 = 2\ /\ 0.1 = 20 \tag{12}$$

$$II - \ d_0 = 0.5mm;\ s\ /\ d_0 = 2\ /\ 0.5 = 4;\ d\ /\ d_0 = 10\ /\ 0.5 = 20 \tag{13}$$

One can observe that for the two variants the ratio s / d_0> 3, and the ratio d / d_0 = 20, so d / d_0> 8.
From the previous researches and considering the architecture of the installation for experimental research on FBG, an outlet air section in water of A = $1.2 \cdot 10^{-6}$m^2 was chosen.
The number of orifices for the two variants results:

$$I - \ d_0 = 0.1mm;\ n_{0.1} = \frac{A}{\left(\pi \cdot d_0^2\right)/4} = \frac{1.2 \cdot 10^{-6}}{\frac{\pi \cdot \left(0.1 \cdot 10^{-3}\right)^2}{4}} = 152\, orifices \tag{14}$$

$$I - \ d_0 = 0.5mm;\ n_{0.5} = \frac{A}{\left(\pi \cdot d_0^2\right)/4} = \frac{1.2 \cdot 10^{-6}}{\frac{\pi \cdot \left(0.5 \cdot 10^{-3}\right)^2}{4}} = 6\ orifices \tag{15}$$

A new generation of FBG is proposed in which the air dispersion orifices in the water are processed by micro-drilling, and the diameters of the orifices are of the dimensions: d_{0I} = 0.1 mm, d_{0II} = 0.5 mm.
Other types of FBG obtained by unconventional technologies are presented in the papers [18] [19].
The following are the two constructive variants of FBG, namely:
Variant I: FBG with a perforated plate with 152 orifices, ø 0.1 mm;
Variant II: FBG with a perforated plate with 6 orifices, ø 0.5 mm.
I. FBG presentation for variant I.
Figure 5 shows the plate with orifices.

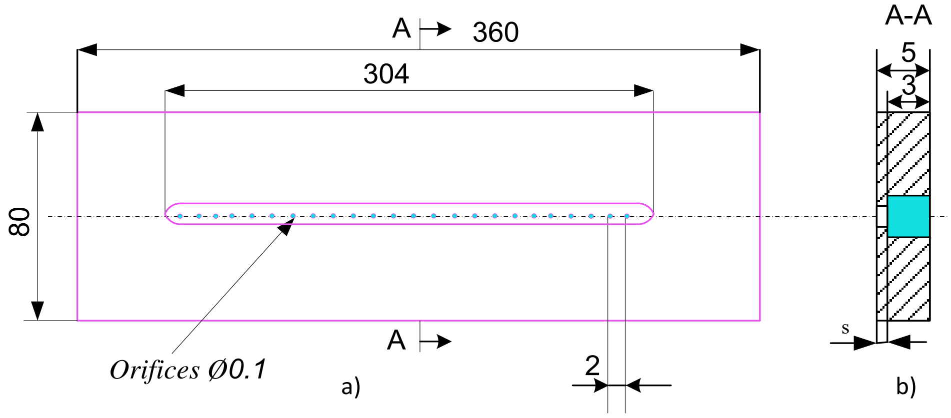

Fig. 5. FBG orifices plate
a) plan view; b) cross section

To perform the orifices in the plate (figure 5), an alveolus (a channel) 3 mm deep and 304 mm long was created. Subsequently, with the help of a C.N.C (numerically controlled machine), a special machine for microprocessors type KERN Micro 152 orifices were made in channel with Ø 0.1 mm. This machine has an accuracy of ± 0.5 µm, which ensured the creation of a FBG which is an original construction solution.
Figure 6 shows the constructive solution of the FBG for variant I.

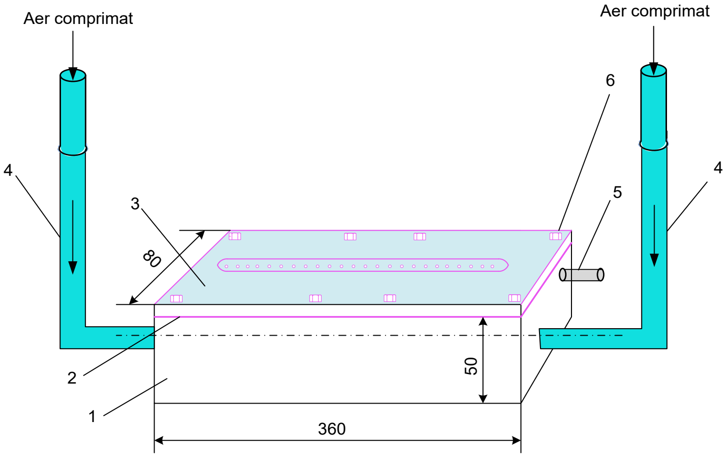

Fig. 6. Fine air bubble generator
1- compressed air tank; 2- sealing gasket; 3- plate with orifices; 4- FBG Ø 18mm compressed air supply pipe; 5-connection for measuring compressed air pressure; 6- screws for fixing the plate with orifices in the tank frame

Following the running of the computation program, for the FBG in variant I the curve C = f (τ) presented in figure 7 was constructed (Initial data: $\dot{V}=600\,dm^3/h$; C_0 = 5.48 mg / dm^3, τ = 120 minutes; $t_{H_2O}=24\,^{\circ}C$; C_s = 8.4 mg / dm^3).

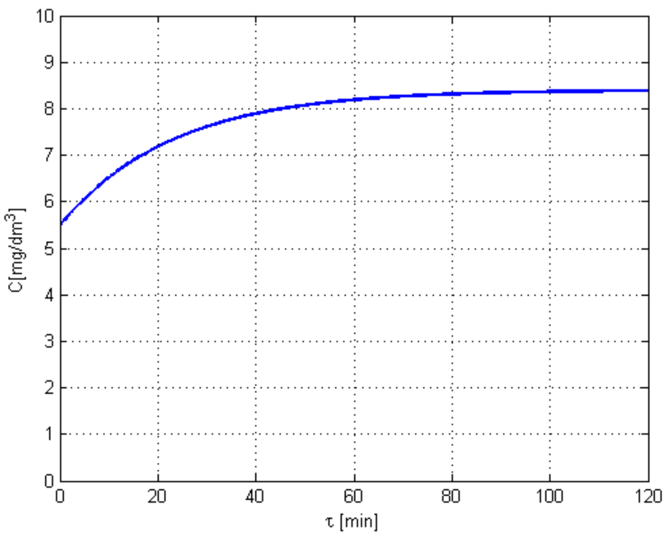

Fig. 7. Variation of the dissolved O_2 concentration in water as a function of time for FBG in variant I with ø 0.1 mm

II. FBG presentation for variant II.

A rectangular plate is chosen as the construction form for the orifice plate. A sketch of this plate is shown in Figure 8:

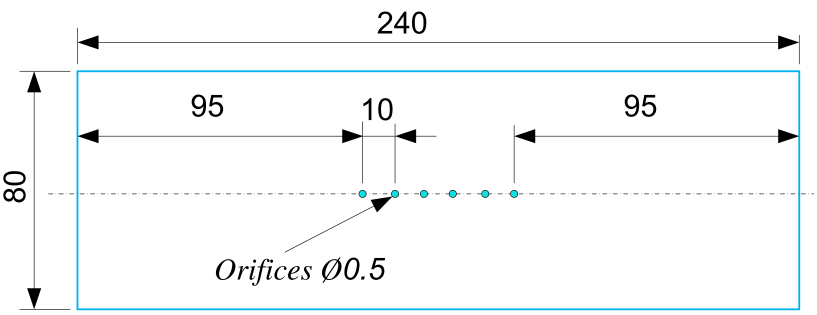

Fig. 8. Perforated plate with 6 orifices of Ø 0.5 mm

For this variant, the distance between the orifices is 10 mm and the thickness of the aluminum plate is 2 mm. The variation of the dissolved O_2 concentration in time for FBG in variant II is shown in figure 9.

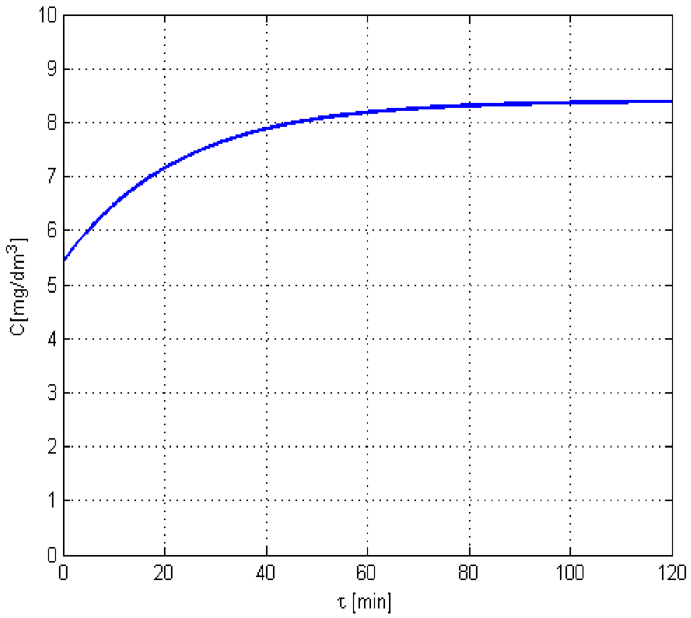

Fig. 9. Variation of the dissolved O_2 concentration in water as a function of time for FBG in variant **II** with ø 0.5 mm

To highlight the influence of the diameter of the air introducing orifice in the water on the concentration of dissolved oxygen, a comparison of the theoretical researches carried out for the two types of fine bubble generators was made.

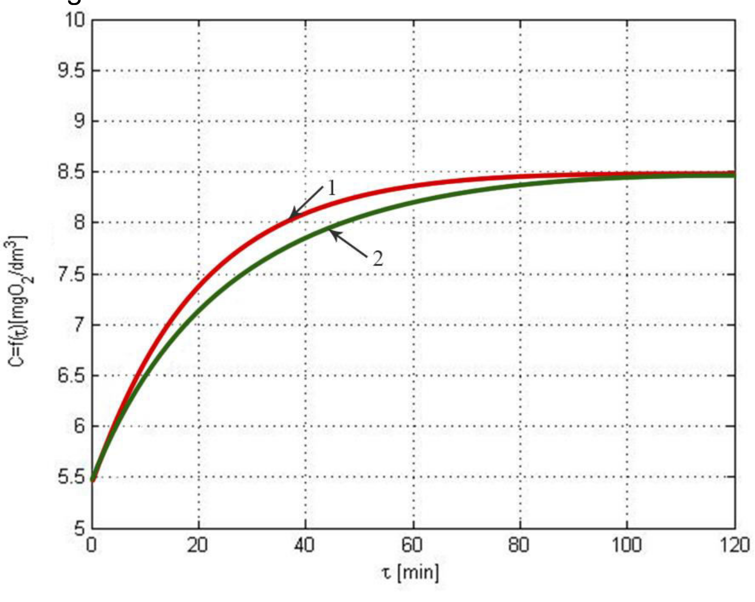

Fig. 10. Variation in the dissolved O_2 concentration in water as a function of time
1- FBG in variant **I** (Ø 0.1 mm), 2 - FBG in variant **II** (Ø 0.5 mm)

Analyzing figure 10, the following conclusions can be drawn:
- the increase of the dissolved oxygen concentration in the water is faster in the case of the fine bubble generator with orifices Ø 0.1 mm compared to the generator of fine bubbles with orifices Ø 0.5 mm.
- it is confirmed that a smaller diameter of the air introducing orifices in the water leads to a more efficient oxygenation of the water volume.

2.2. Presentation of the experimental installation

The scheme of the experimental installation corresponding to variants I and II, is presented in figure 11 [20] [21].

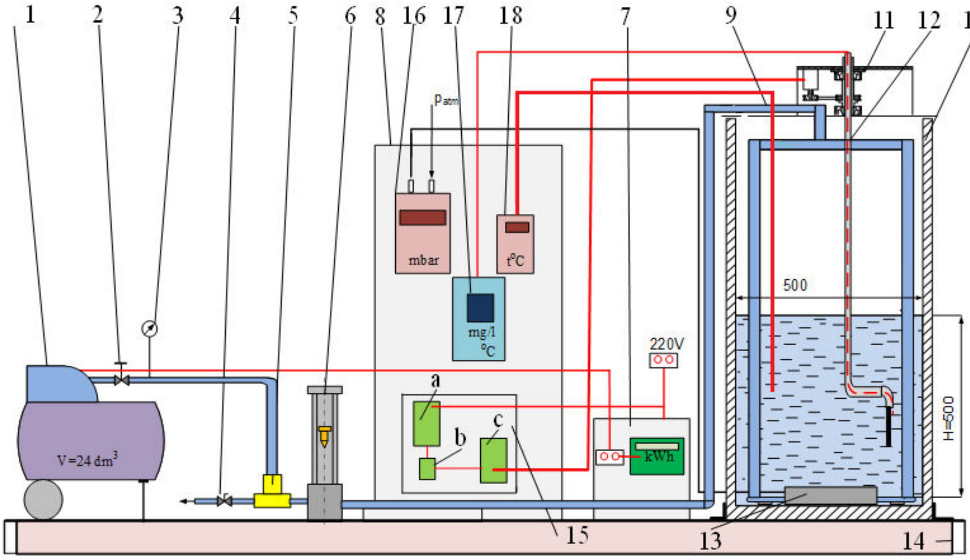

Fig. 11. The scheme of the experimental installation for researches on water oxygenation by introducing compressed atmospheric air into the water tank
1 - electro compressor with air tank; 2 - pressure reducer; 3 - manometer; 4 - connection for evacuating air into the atmosphere; 5 – T-joint; 6 - rotameter; 7 - electrical panel; 8 - panel with measuring devices; 9 - pipe for transporting compressed air to the bubble generator, 10 - water tank; 11 - mechanism of actuation of the probe; 12 - oxygenometer probe; 13 - bubble generator; 14 - support for installation; 15 - control electronics: a - power supply, b - switch, c - control element, 16 - digital manometer; 17 - oxygenometer; 18 - digital thermometer

In variant I, the compressed air supplied by a compressor (1) passes through a rotameter (6) so that through the pipe (9) it reaches the FBG (13).

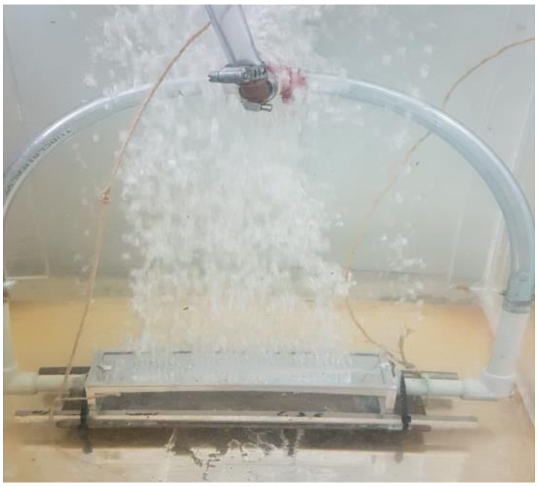

Fig. 12. Bubble curtain emitted by the fine bubble generator in operation

Figure 12 shows the bubble curtain emitted by FBG inserted in the water tank

3. Results and discussion

During the experimental researches on the operation of FBG in the two variants, the following remained constant: the area of the air outlet section in the water and the height of the water layer above the FBG (hydrostatic load).

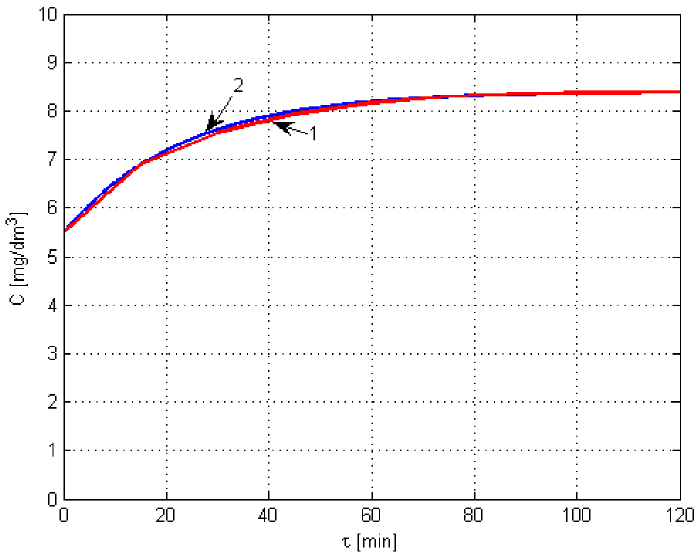

Fig. 13. Variation of the dissolved O_2 concentration in water as a function of time: C = f (τ)
1- theoretical results in the case of FBG with Ø 0.1 mm; 2-values measured in the case of FBG with Ø 0.1 mm

The experimental and theoretical curves are close, which means that the measurements are correct, confirming the superior capabilities of the oxygenation system.
Similar to the fine bubble generator with 152 orifices Ø 0.1 mm and for the fine bubble generator with 6 orifices Ø 0.5 mm the curves in figure 14 are obtained.

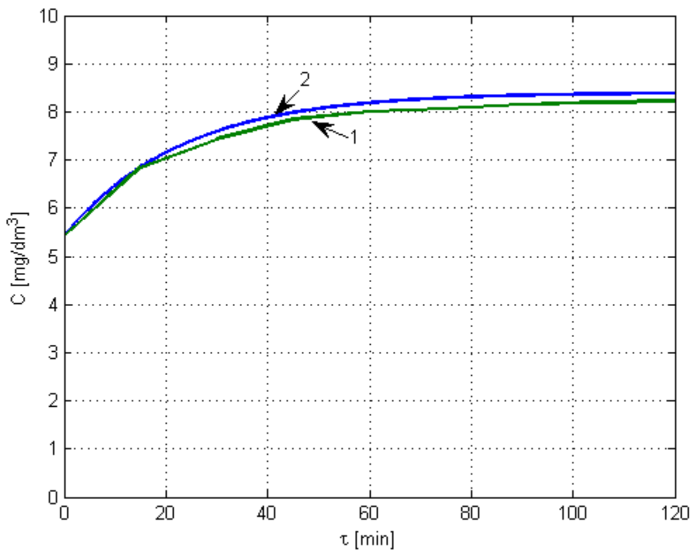

Fig. 14. Variation of the dissolved O_2 concentration in water as a function of time: C = f (τ)
1- theoretical results in the case of FBG with Ø 0.5 mm; 2-values measured in the case of FBG with Ø 0.5 mm

The experimentally determined values were graphically represented by the curves C = f (τ) (figure 15).

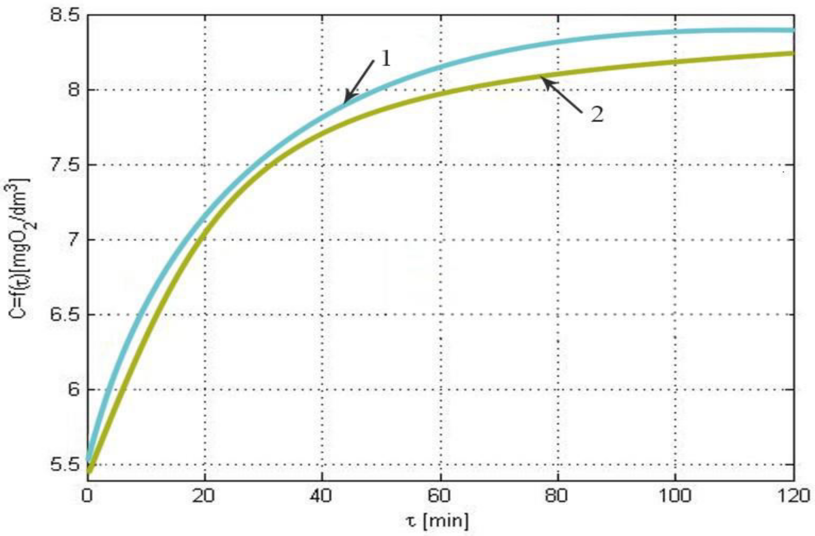

Fig. 15. Variation of the dissolved O2 concentration in water as a function of time: C = f (τ)
Measured values for variant I
Measured values for variant II

Figure 15 shows that variant I (curve 1) is more advantageous.

4. Conclusions

Aeration is necessary to improve water quality, to avoid the occurrence of oxygen deficiency in systems where there is a biochemical consumption of oxygen above the self-aeration capacity of water, to eliminate toxic gases that can be found in water and in the water treatment process.
The main purpose of water aeration, regardless of the industry and the reason for its use, is to increase or maintain an optimal level of dissolved oxygen in a water mass. The oxygen needed for the aeration process is taken from the atmospheric air and introduced into the water. For this aeration to be effective, a uniform dispersion of air in the volume of water must be ensured.
The pressurized air is dispersed in the form of bubbles by a specialized equipment, located at the bottom of the treatment tank.
So, the main purpose of aeration regardless of the industry and the purpose where it is used is to increase or maintain a high or optimal level of dissolved oxygen in a water mass to be used for various purposes or reintroduced into its natural circuit. The aeration process is used in the treatment and improvement of water quality, but also in many other fields including medicine, agriculture, fish farming, etc.

References

[1] Pătulea, Al. S. *The influence of functional parameters and the architecture of fine bubble generators on the efficiency of aeration installations / Influenţa parametrilor funcţionali şi a arhitecturii generatoarelor de bule fine asupra eficienţei instalaţiilor de aerare*. Doctoral thesis, Politehnica University of Bucharest, 2012.
[2] Căluşaru, I. M. *The influence of the physical properties of the liquid on the efficiency of the oxygenation processes / Influenţa proprietăţilor fizice ale lichidului asupra eficienţei proceselor de oxigenare*. Doctoral thesis, Politehnica University of Bucharest, 2014.
[3] Mateescu, G. M. *Hydro-gas-dynamics of fine bubble generators / Hidro-gazo-dinamica generatoarelor de bule fine*. Doctoral thesis, Politehnica University of Bucharest, Faculty of Mechanics and Mechatronics, 2011.
[4] Robescu, Dan, and Diana Robescu. *Methods, installations and equipment for the physical treatment of wastewater / Procedee, instalaţii şi echipamente pentru epurarea fizică a apelor uzate*. Bucharest, BREN Publishing House, 1999.
[5] Băran, Gh., and N. Băran. "Hydrodynamics of bubbles generated by porous diffusers / Hidrodinamica bulelor generate de difuzori poroşi." *Revista de Chimie* 54, no. 5 (2003): 436-440.

[6] Robescu, Dan, and Diana Robescu. *Processes, installations and equipment for water treatment / Procedee, instalaţii şi echipamente pentru epurarea apelor*. Bucharest, Lithographic Printing House of UPB, 1996.
[7] Stoianovici, S., and D. Robescu. *Mechanical processes and equipment for water treatment and purification / Procedee şi echipamente mecanice pentru tratarea şi epurarea apei*. Bucharest, Technical Publishing House, 1983.
[8] Berbente, C., and S. Mitran. *Numerical methods / Metode numeric*e. Bucharest, Technical Publishing House, 1997.
[9] Antia, H. M. *Numerical Methods for Scientists and Engineers*. Basel, Birkhauser Publisher, 2nd edition, 2002.
[10] Recktenwald, G. *Numerical Integration of Ordinary Differential Equations for Initial Value Problems*. Portland, Oregon, Portland State University, Department of Mechanical Engineering, 2006.
[11] Oprina, G., I. Pincovschi, and Gh. Băran. *Hydro-Gas-Dynamics Aeration systems equipped with bubble generators / Hidro-Gazo-Dinamica Sistemelor de aerare echipate cu generatoare de bule*. Bucharest, Politehnica Press, 2009.
[12] Băran, N., Al. S. Pătulea, and I. M. Căluşaru. "Design and building of a setup for the experimental research of fine bubble generators." *Termotehnica*, no. 2 (2011): 84-90.
[13] Băran, N., Al. S. Pătulea, and I. M. Căluşaru. "Computation of performance and efficienty of the water oxygenation process in non-stationary conditions." *Ecological Engineering and Environment Protection*, no. 3 (2012): 73-78.
[14] Houcque, David. *Applications of MATLAB: Ordinary Differential Equations (ODE)*. Ilinois, Robert R. McCormick School of Engineering and Applied Science, Northwestern University, 2007.
[15] Yang, Won Young, Wenwu Cao, Tae Sang Chung, and John Morris. *Applied Numerical Methods Using Matlab*. Wiley-Interscience, John Wiley & Sons, Inc., 2005.
[16] Miyahara, T., Y. Matsuha, and T. Takahashi. "The size of bubbles generated from perforated plates." *International Chemical Engineering* 23 (1983): 517-523.
[17] Oprina, G. *Contributions to the hydro-gas-dynamics of porous diffusers / Contribuţii la hidro-gazo-dinamica difuzoarelor poroase*. Doctoral thesis, Politehnica University of Bucharest, Faculty of Power Engineering, 2007.
[18] Mateescu, G., A. Marinescu, and N. Băran. "A new Constructing Fine Bubbles Generators." *Bulletin of The Transilvania University of Braşov* 2 (2009): 359-367.
[19] Băran, N., I. M. Căluşaru, and G. Mateescu. "Influence of the architecture of fine bubble generators on the variation of the concentration of oxygen dissolved in water." *Buletinul Stiintific al Universitatii Politehnica din Bucuresti, seria D, Inginerie Mecanică* 75, no. 3 (2013): 225-236.
[20] Căluşaru, Ionela Mihaela, Nicolae Băran, Alexandru Pătulea, and Gabriela Mateescu. "Theoretical and experimental researches regarding the modification of dissolved oxygen concentration in stationary waters." Paper presented at the International Conference on INnovation and Collaboration in Engineering Research (INCER-2012), Bucharest, Romania, July 2-4, 2012.
[21] Pătulea, Alexandru, Nicolae Băran, and Ionela Mihaela Căluşaru. "Measurements of Dissolved Oxygen Concentration in Stationary Water." *World Environment* 2, no. 5 (2012): 104-109, doi: 10.5923/j.env.20120205.02.

Hydraulic Installation for the Rotary Crane of a Railway Track Welding Machine

PhD Eng. **Ioan LEPĂDATU**[1,*], PhD Stud. Eng. **Ștefan ȘEFU**[1],
PhD Stud. Eng. **Ionela Mihaela BACIU**[1], Ec. **Laurențiu Valentin NICOLAE**[2],
Dipl. Eng. **Dănuț Florin MATEESCU**[2]

[1] National R&D Institute for Optoelectronics, Subsidiary Hydraulics and Pneumatics Research, Bucharest

[2] S.C. Proflex Automotive S.R.L.

* lepadatu.ihp@fluidas.ro

Abstract: *A railway track welding machine has several components in its structure, the most important being the welding head, which performs the electric flash-butt (end-to-end) welding of the train and tram tracks. Maneuvering the welding head and positioning it on the rails to be welded is done with the help of a rotary crane. This article presents the hydraulic installation from the structure of a railway track welding machine.*

Keywords: *Hydraulic installation, welding head, rotary crane, flash-butt welding*

1. Introduction

Flash- butt welding of train or tram tracks is done by a complex mechanical - electrical equipment called "welding head". To maneuver the welding head, this machine is equipped with a handling device with hydraulic arms. It is provided to support a load of about 4,500 kg at a length of 3… 4 m. This rotary crane has a pivoting capacity of 75° on each side of the center thus allowing welding of adjacent rails. This ability to pivot, together with the arm extension function, covers a wide operating area for the welding head.

The functions of the equipment are:

- lifting: up /down;
- extension: outside /inside;
- rotation: left / right.

2. Technical characteristics and performance of the rotary crane

- Maximum pressure: .... 160 bar;
- Maximum flow rate: .... 40 l / min;
- Supply voltage: .... 24 Vdc;
- Control voltage: .... 0 ... 10 V;
- Lifting cylinders:
  - piston diameter: .... 125 mm;
  - rod diameter: .... 50 mm;
  - stroke: .... 880 mm;
  - maximum pressure: .... 315 bar;
- Extension cylinders:
  - piston diameter: .... 60 mm;
  - rod diameter: .... 35 mm;
  - stroke: .... 1370 mm;
  - maximum pressure: .... 315 bar.
- Rotation mechanism
  - speed: …………………………..…… 3 rpm;
  - maximum torque: .... 800 Nm.

3. Presentation of the hydraulic installation of the rotary crane

The rotary crane of a railway track welding machine is shown in fig. 1.

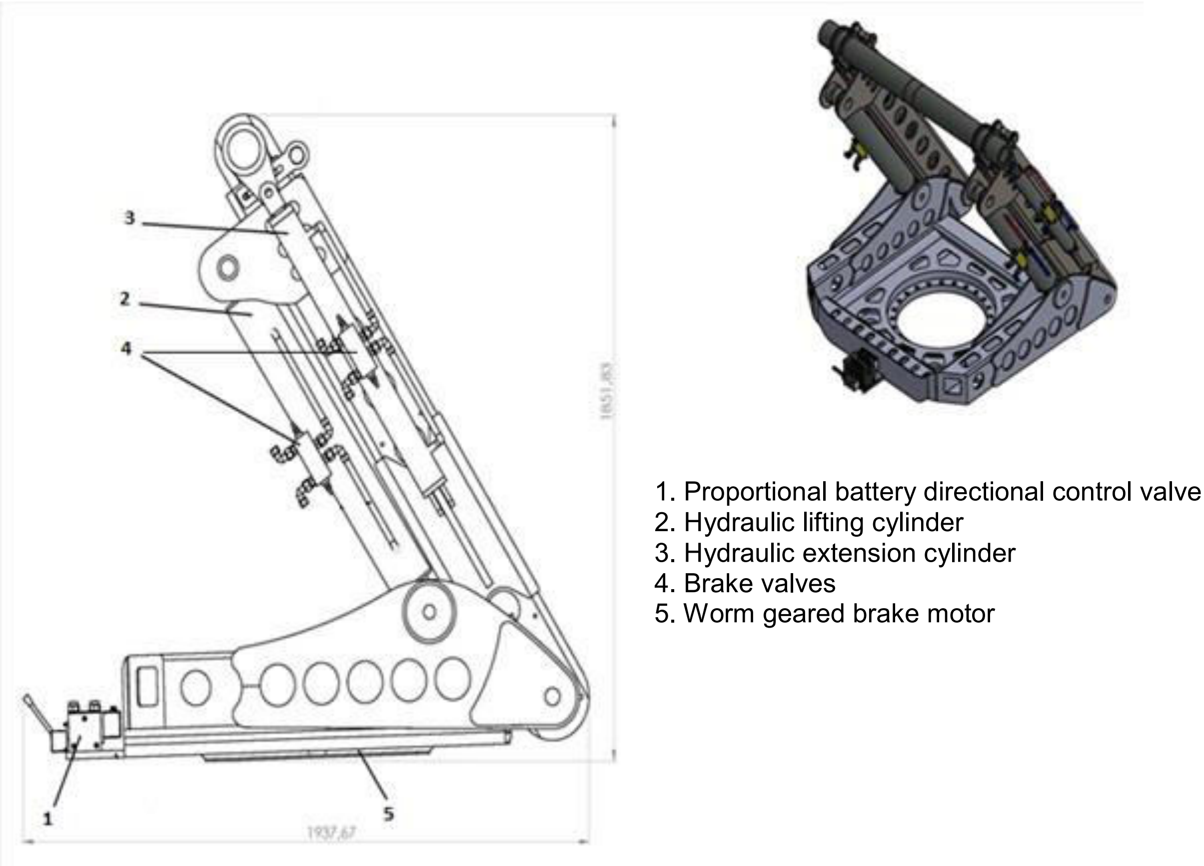

Fig. 1. The rotary crane of a railway track welding machine

The main components of the rotary crane hydraulic installation: battery directional control valve *1*, hydraulic lifting cylinder *2*, hydraulic extension cylinder *3*, brake valves *4*, and hydraulic gear reducer *5.*

3.1. Proportional battery directional control valve

Proportional battery directional control valve 1 (fig. 2) [1] is fixed on the crane platform. It is controlled by a digital electronic amplifier.

Fig. 2. Proportional battery directional control valve

3.2. Lifting hydraulic cylinder

Hydraulic cylinder [2, 3] for lifting the crane arm (hydraulic lifting cylinder *2*) (fig. 3) is articulated at the end of cylinder liner on the rotary platform, and at the end of rod - on the tilting arm of the crane.

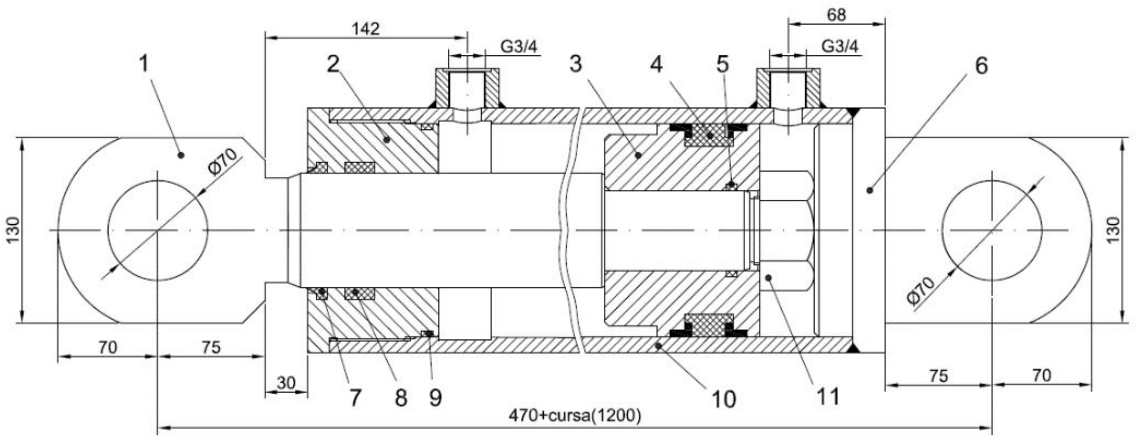

Fig. 3. Hydraulic lifting cylinder

3.3. Hydraulic extension cylinder

Hydraulic cylinder [2, 3] for extending the crane arm (hydraulic extension cylinder *3*) (fig. 4) is articulated at the end of cylinder liner on the tilting arm, and at the end of rod it is fixed on the extendable arm.

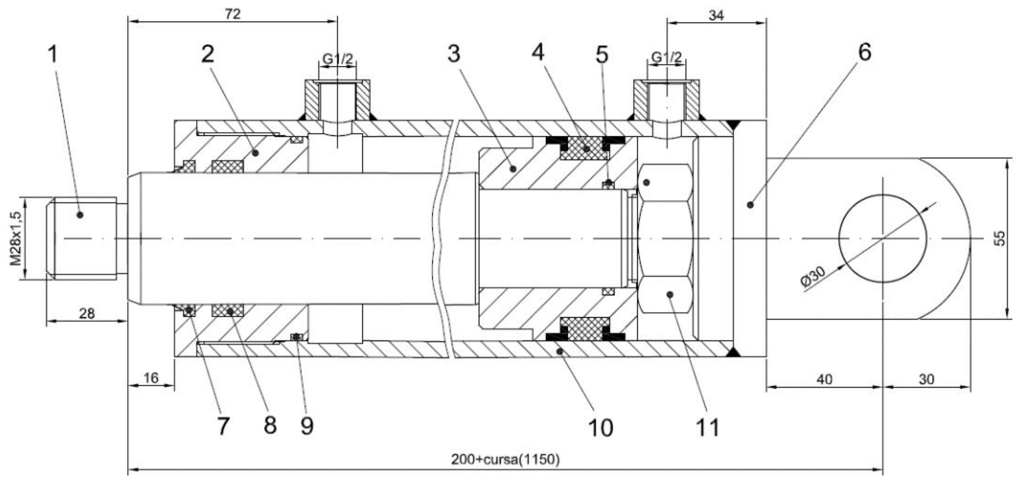

Fig. 4. Hydraulic extension cylinder

3.4. Brake valves

Brake valves [1, 4] *4* (fig. 5) are fixed on hydraulic cylinders *2* and *3*.

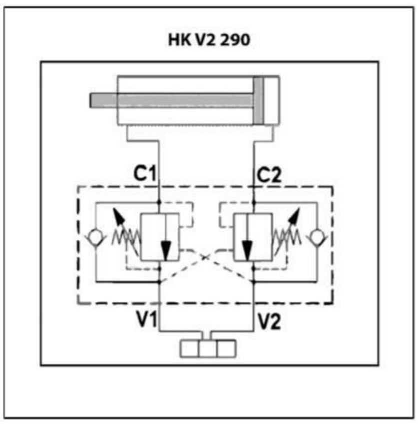

Fig. 5. Brake valves

3.5. Worm geared brake motor

Worm geared brake motor *5* (Fig. 6) [1, 5, 6, 7] is placed with the fixed part on the welding machine frame, and with the mobile part on the rotary platform of the crane.

Fig. 6. Worm geared brake motor

4. Operation of the rotary crane hydraulic installation

The functional role of the rotary crane within the structure of a railway track welding machine is to maneuver and position the welding head above the rails to be welded.
The diagram of the rotary crane hydraulic installation is presented in fig. 7 below.

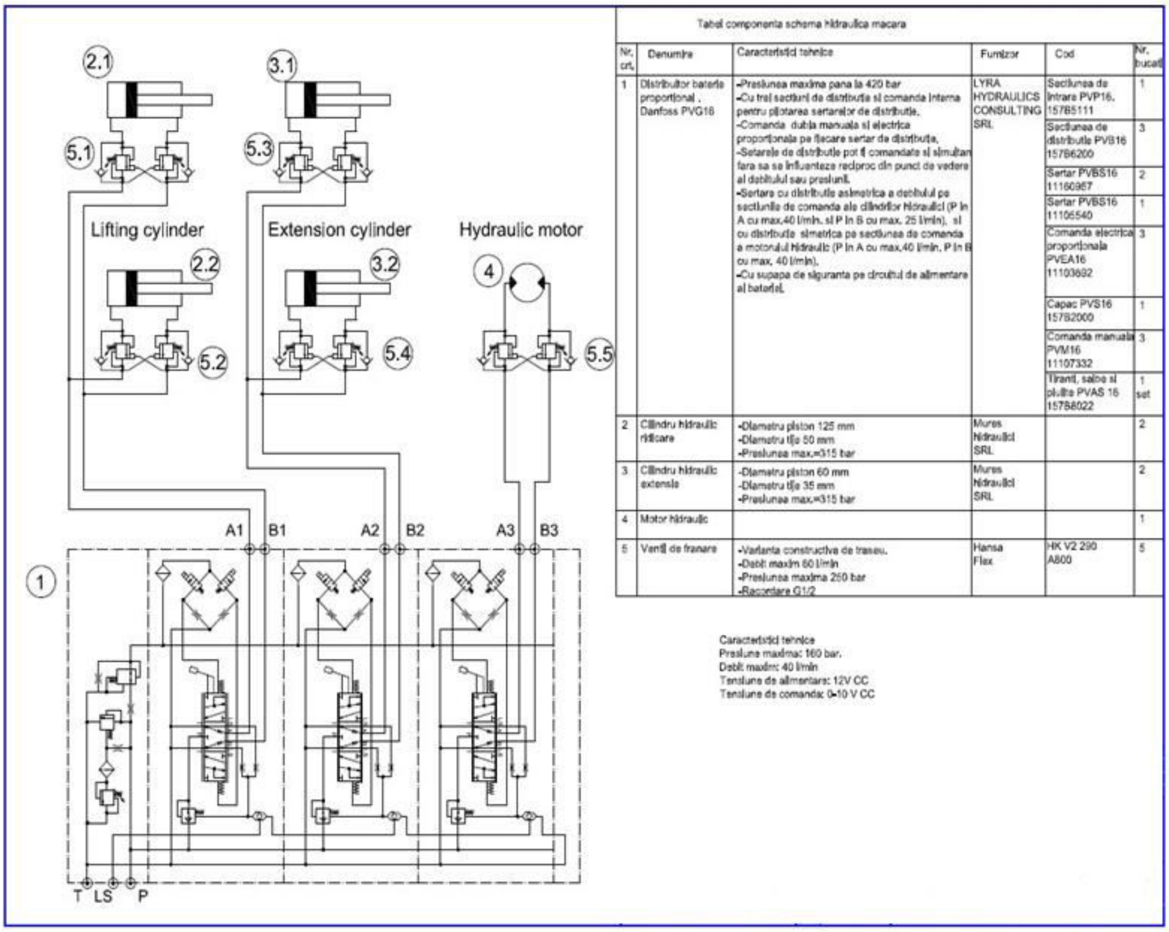

Tabel componenta schema hidraulica macara

Nr. crt.	Denumire	Caracteristici tehnice	Furnizor	Cod	Nr. bucati
1	Distribuitor baterie proportional , Danfoss PVG16	-Presiunea maxima pana la 420 bar -Cu trei sectiuni de distributie si comanda interna pentru pilotarea sertarelor de distributie. -Comanda dubla manuala si electrica proportionala pe fiecare sertar de distributie. -Sertarele de distributie pot fi comandate si simultan fara sa se influenteze reciproc din punct de vedere al debitului sau presiunii. -Sertare cu distributie asimetrica a debitului pe sectiunile de comanda ale cilindrilor hidraulici (P in A cu max.40 l/min. si P in B cu max. 25 l/min), si cu distributie simetrica pe sectiunea de comanda a motorului hidraulic (P in A cu max.40 l/min. P in B cu max. 40 l/min). -Cu supapa de siguranta pe circuitul de alimentare al bateriei.	LYRA HYDRAULICS CONSULTING SRL	Sectiunea de intrare PVP16. 157B5111	1
				Sectiunea de distributie PVB16 157B6200	3
				Sertar PVBS16 11160957	2
				Sertar PVBS16 11106540	1
				Comanda electrica proportionala PVEA16 11103692	3
				Capac PVS16 157B2000	1
				Comanda manuala PVM16 11107332	3
				Tiranti, saibe si piulite PVAS 16 157B8022	1 set
2	Cilindru hidraulic ridicare	-Diametru piston 125 mm -Diametru tije 50 mm -Presiunea max.=315 bar	Mures Hidraulici SRL		2
3	Cilindru hidraulic extensie	-Diametru piston 60 mm -Diametru tije 35 mm -Presiunea max.=315 bar	Mures Hidraulici SRL		2
4	Motor hidraulic				1
5	Ventil de franare	-Varianta constructiva de traseu. -Debit maxim 60 l/min -Presiunea maxima 250 bar -Racordare G1/2	Hansa Flex	HK V2 290 A800	5

Caracteristici tehnice
Presiune maxima: 160 bar.
Debit maxim: 40 l/min
Tensiune de alimentare: 12V CC
Tensiune de comanda: 0-10 V CC

Fig. 7. The diagram of the rotary crane hydraulic installation

Proportional battery directional control valve *1* directs flow from the pump to the lifting or extension cylinders and to the hydraulic motor that rotates the crane platform. The slide valves of the directional control valve make crossing sections proportional to size of the variable electrical signal (0 ... 10 V). The LS pressure signal is sent to pump which changes its capacity depending on the proportional electrical signal applied to the directional control valve. Possibility of achieving a variable flow rate actually means possibility of achieving variables speeds for lifting and extending the crane arm. Lifting and lowering of the crane arm is done by hydraulic cylinders *2.1* and *2.2*. Circuit *A1* performs lifting of the arm, and circuit *B1* - lowering. Brake valves *5.1* and *5.2* prevent accelerated lowering of the crane arm. Extension and retraction of the crane arm is done by hydraulic cylinders *3.1* and *3.2***.** Circuit *A2* performs extension of the arm, and circuit *B2* - lowering. Brake valves *5.3* and *5.4* prevent accelerated retraction of the crane arm. Rotating of the crane platform is done by hydraulic engine *4*. Circuit *A3* performs rotation in a direction, and circuit *B3* - in the opposite direction of rotation. Worm geared brake motor reduces the rotational speed of 105 rpm received from hydraulic motor to 1 rpm required to rotate the crane platform. Brake valve *5.5* prevents uncontrolled rotating of the rotary crane (under the action of the force of wind).

5. Conclusions

The hydraulic installation of the rotary crane within the structure of a train or tram tracks welding machine performs the intended functions:

- lifting: up / down;
- extension: outside / inside;
- rotation: left / right.

Acknowledgments

This paper has been developed in INOE 2000-IHP, as part of a project co-financed by the European Union through the European Regional Development Fund, under Competitiveness Operational Programme 2014-2020, Priority Axis 1: Research, technological development and innovation (RD&I) to support economic competitiveness and business development, Action 1.2.3 – Partnerships for knowledge transfer, project title: *Development of energy efficient technologies in niche applications of the manufacture of on-demand mechanical-hydraulic subassemblies and maintenance of mobile hydraulic equipment*, project acronym: MENTEH, SMIS code: 119809, Financial agreement no. 6 /25.06.2018, subsidiary contract no. 45 /17.01.2022.

References

[1] Rojek, Piotr. "Hydraulic systems of drilling machines and equipment designed in Komag." Paper presented at the 21st International Conference of Hydraulics and Pneumatics HERVEX, Calimanesti-Caciulata, Romania, November 5-7, 2014.

[2] Lepădatu, I., C. Cristescu, L. Dumitrescu, Al.P. Chiriță, R.I. Rădoi, and I.C. Dumitrescu. "Hydraulically operated assault ramp."/"Rampă de asalt acționată hidraulic." Paper presented at the 12th National Symposium on Construction Equipment SINUC, Bucharest, Romania, December 15-16, 2016.

[3] Lepădatu, I., C. Cristescu, I.C. Dumitrescu, M. Blejan, L. Dumitrescu, and Al.P. Chiriță. "Hydraulically driven assault double ramp." Paper presented at the 22nd International Conference of Hydraulics and Pneumatics HERVEX, Baile Govora, Romania, November 9-11, 2016.

[4] Cristescu, C., I.C. Dumitrescu, R.I. Rădoi, M. Blejan, I. Bălan, and I. Ilie. "Mobile equipment for simulation of side skidding at motor vehicles." Paper presented at the 21st International Conference of Hydraulics and Pneumatics HERVEX, Calimanesti-Caciulata, Romania, November 5-7, 2014.

[5] Popescu, M., S. Nicolaie, G. Oprina, R. Cîrnaru, A. Mituleț, R. Chihaia, and R. Mirea. "Improving the energy conversion efficiency of counter rotating wind turbines by using innovative generators." Paper presented at the 21st International Conference of Hydraulics and Pneumatics HERVEX, Calimanesti-Caciulata, Romania, November 5-7, 2014.

[6] Lepădatu, I., C. Cristescu, Al.P. Chiriță, and C. Mărculescu. "Four-wheel drive high efficiency hybrid transmission for multipurpose motor vehicles." Paper presented at the 23rd International Conference of Hydraulics and Pneumatics HERVEX, Baile Govora, Romania, November 8-10, 2017.

[7] Dumitrescu, L., Al.P. Chiriță, and C. Cristescu. "Working bench for reconditioning hydraulic cylinders." Paper presented at the 23rd International Conference of Hydraulics and Pneumatics HERVEX, Baile Govora, Romania, November 8-10, 2017.

ISSN 1453 – 7303 "HIDRAULICA" (No. 1/2022)
Magazine of Hydraulics, Pneumatics, Tribology, Ecology, Sensorics, Mechatronics

Overview of Multi-Position Cylinder

Dr. Eng. **Tiberiu AXINTE**[1,*], Dr. Eng. **George SURDU**[1], Eng. **Alexandru SAVASTRE**[1], Eng. **Victor BADANAU**[1], Eng. **Camelia PASCU**[1], Eng. **Nilgun MILIS**[2]

[1] Research and Innovation Center for Navy, Romania

[2] Politehnica University of Bucharest, Romania

*tibi_axinte@yahoo.com

Abstract: *This paper presents aspects related to the use of a cylinder with two piston rods. Beside a multi-position cylinder, it is a pneumatic actuator. In this article two kind of circuits using a multi-position cylinder are presented: one pneumatic circuit and one electro-pneumatic circuit. The pneumatic circuit comprises the following devices: compressed air supply, a start-up valve with filter control valve, a 5/2 way solenoid valve, a 3/2 way solenoid valve and a multi-position cylinder. Furthermore, an electro-pneumatic circuit comprises: compressed air supply, an air filter, a 5/2 way solenoid impulse valve, a 3/2 way solenoid valve, a multi-position cylinder, relay, lamp and a valve solenoid. The design and simulation of both schemes from this article is done in FluidSim software from Festo.*

Keywords: *Multi-position cylinder, pneumatic circuit, electro-pneumatic circuit, electrical scheme*

1. Introduction

Actuators are constructed by connecting two cylinders of the same piston diameter but of different maximum stroke. The maximum stroke of the second piston must be larger than that of the previous one. When moving back, an intermediate stop requires a particular control. The shorter maximum stroke is half of the maximum stroke, Fig. 1.

Fig. 1. Multi-position cylinder

The main characteristics of a multi-position cylinder, [1]:
- Mounting hole pattern to ISO 21287;
- 2...5 cylinders can be combined;
- Four position settings.

Adjustable parameters and symbol of a multiple position cylinder are shown in Fig. 2, below:

Designation	Range	Value	Unit	Symbol
Piston diameter	$10^{-3}...1$	$2\cdot10^{-2}$	m	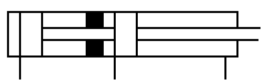
Piston rod diameter	$10^{-3}...1$	$8\cdot10^{-3}$	m	
Total stroke	$10^{-3}...2$	$2\cdot10^{-1}$	m	
Piston position	$10^{-3}...2$	0	m	
Intermediate position	$10^{-3}...1$	0	m	

Fig. 2. Adjustable parameters and symbol

2. The circuits with multi-position cylinder

A pneumatic installation is an interconnected set of devices that convert compressed air into mechanical work, [2].
In the table below the component devices used in the pneumatic scheme are presented.

Table 1: The devices of the first pneumatic scheme

Description	Number of components
Compressed air supply	1
Start-up valve with filter control valve	1
5/2 way solenoid valve	1
3/2 way solenoid valve	1
Multi-position cylinder	1

The first pneumatic circuit studied has one cylinder with two piston rods, Fig. 3.

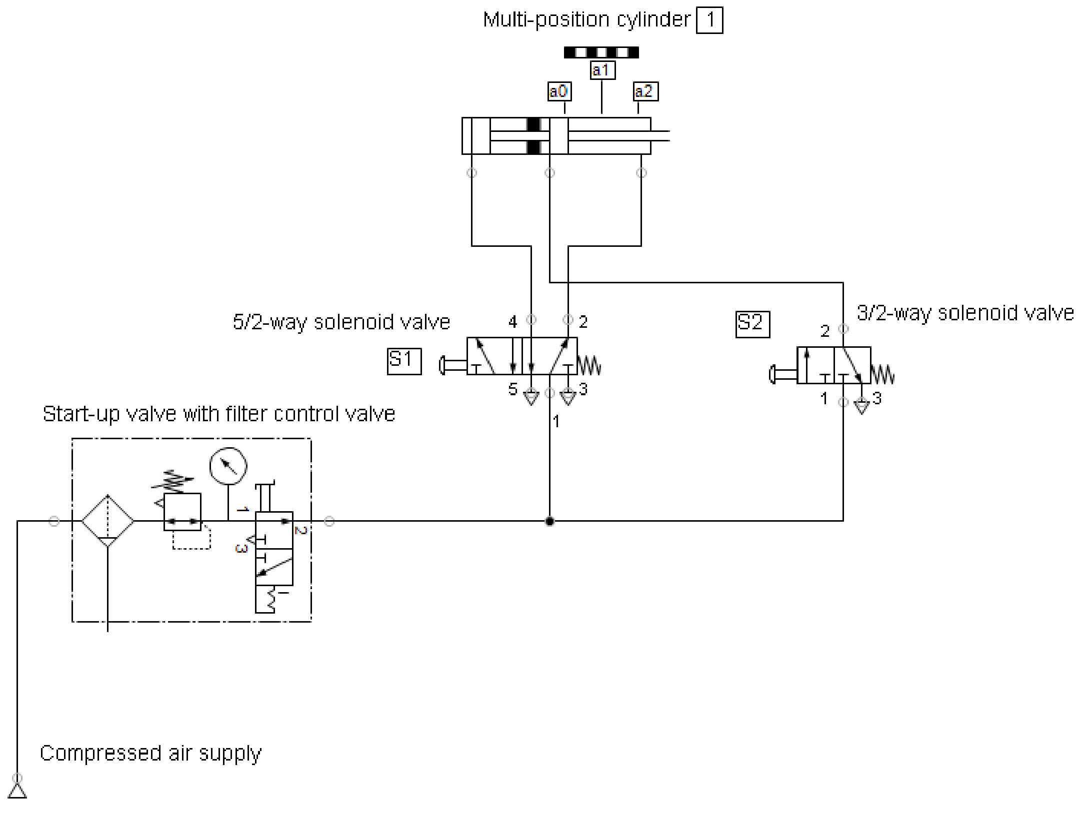

Fig. 3. Pneumatic circuit using multi-position cylinder

Operator presses the S1 button belonging to the 5/2 way solenoid valve with spring, [3].
Both piston rods move from point a0 to point a1. After that, both piston rods return from point a1 to point a0, because the 5/2 way valve has a spring, Fig. 4.

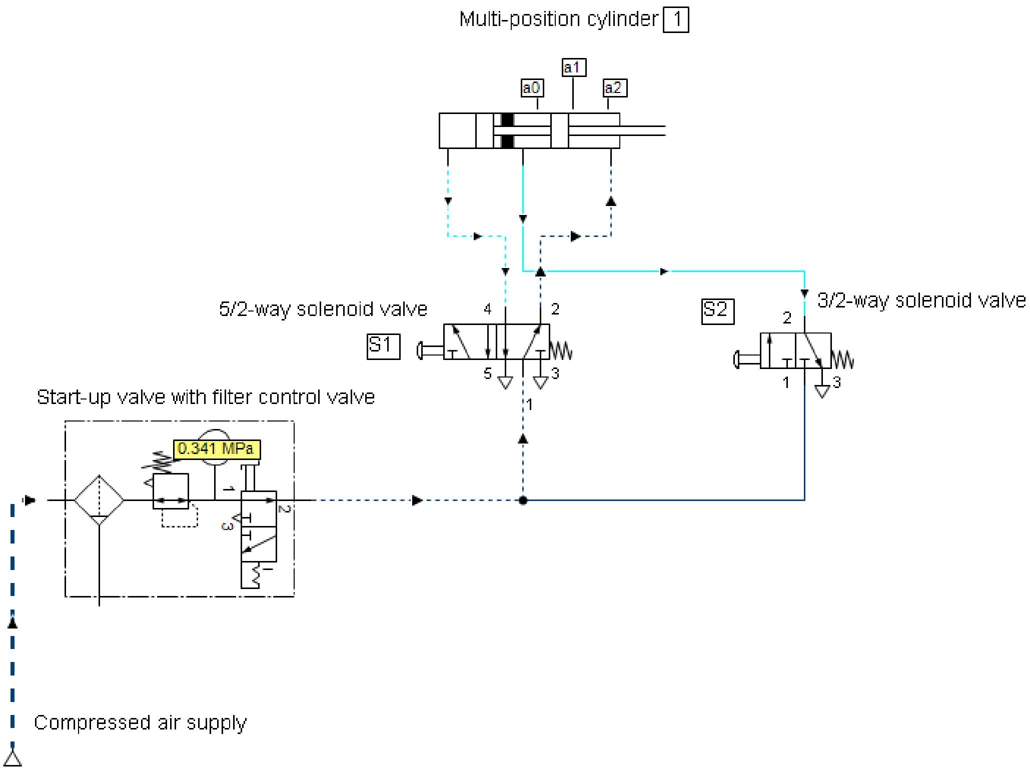

Fig. 4. Pneumatic scheme with multi-position cylinder. Simulation I

If operator presses S2 button belonging to the 3/2 way solenoid valve with spring, [4], the piston rod moves from point a0 to point a2. After that, this piston rod returns from point a2 to point a0, because of the spring of this 3/2 way solenoid valve, Fig. 5.

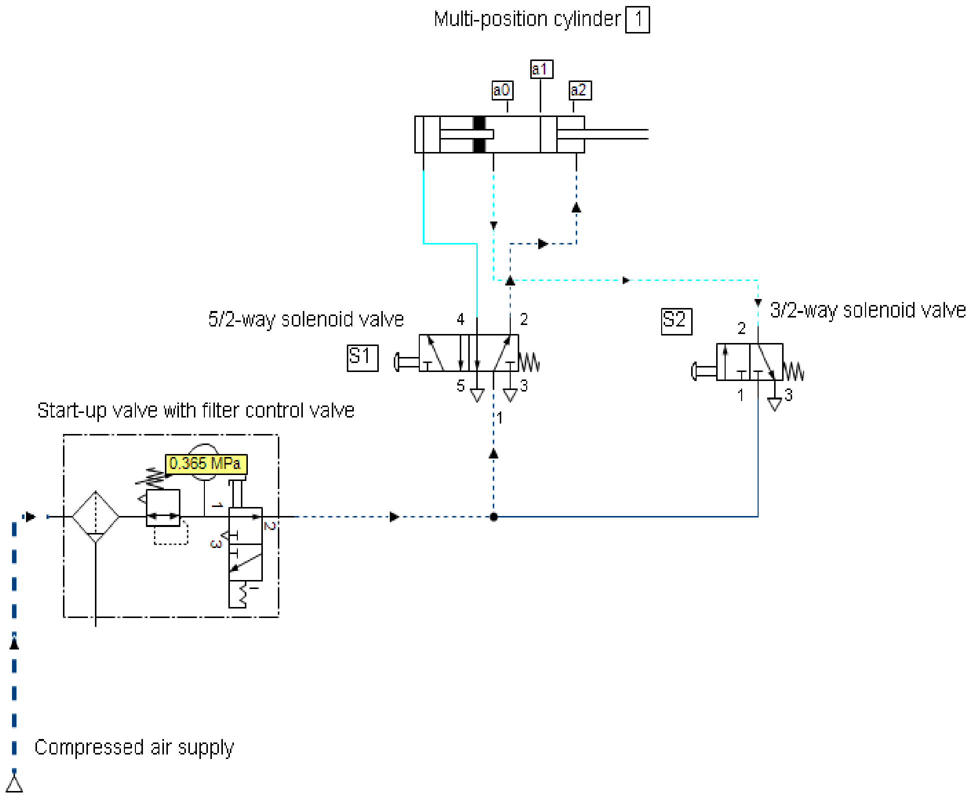

Fig. 5. Pneumatic scheme with multi-position cylinder. Simulation II

The diagrams given show variation of the following functional parameters of the multi-position cylinder 1 (Multi-cyl 1-1), Fig. 6:

- Position 1 – x1 [mm];
- Velocity 1 – v1 [m/s];
- Position 2 – x2 [mm];
- Velocity 2 – v2 [m/s].

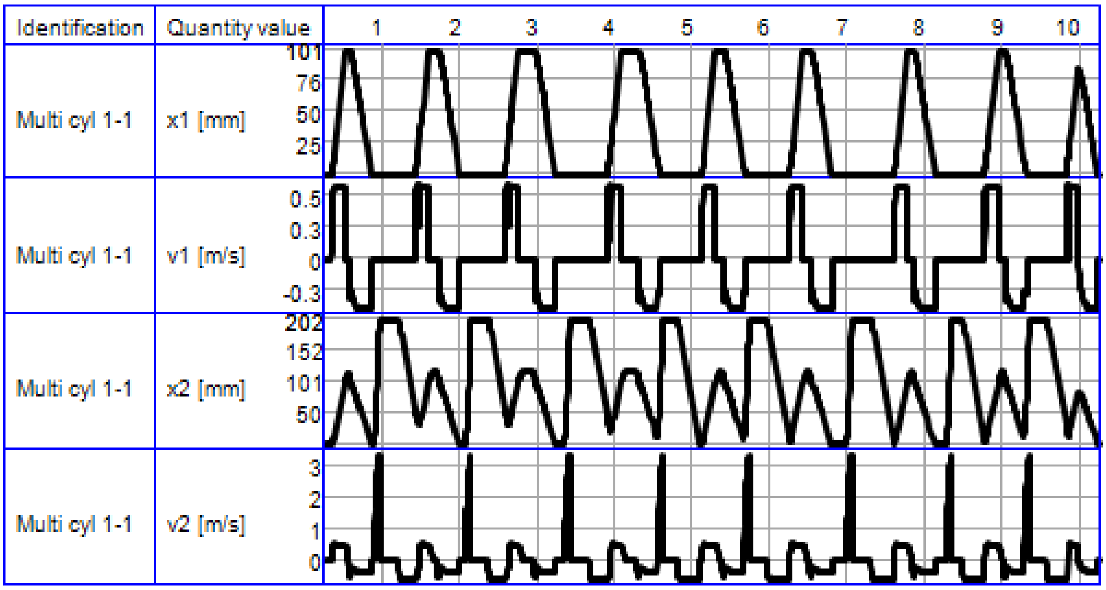

Fig. 6. Diagrams of parameters variations from the multi-cyl 1-1

Furthermore, an electro-pneumatic circuit with multi-position cylinder is studied, as in Fig. 7.

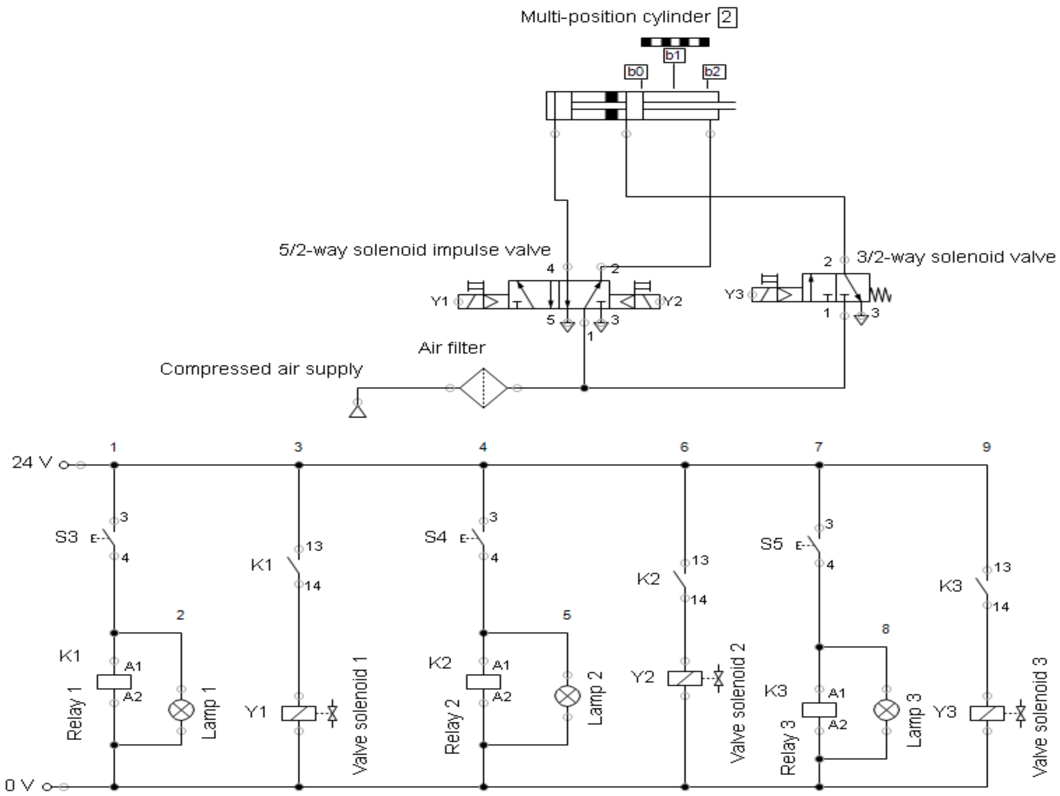

Fig. 7. Electro-pneumatic circuit using multi-position cylinder

Table 2 below shows the component devices used in the pneumatic scheme, [5].

Table 2: The devices of the electro-pneumatic scheme

Description	Number of components
Compressed air supply	1
Air filter	1
5/2 way solenoid impulse valve	1
3/2 way solenoid valve	1
Multi-position cylinder	1
Relay	3
Lamp	3
Valve solenoid	3

If operator presses S3 button, both piston rods of the multi-position cylinder (2) move from point b0 to point b1 and lamp 1 shows a yellow signal, Fig. 8.

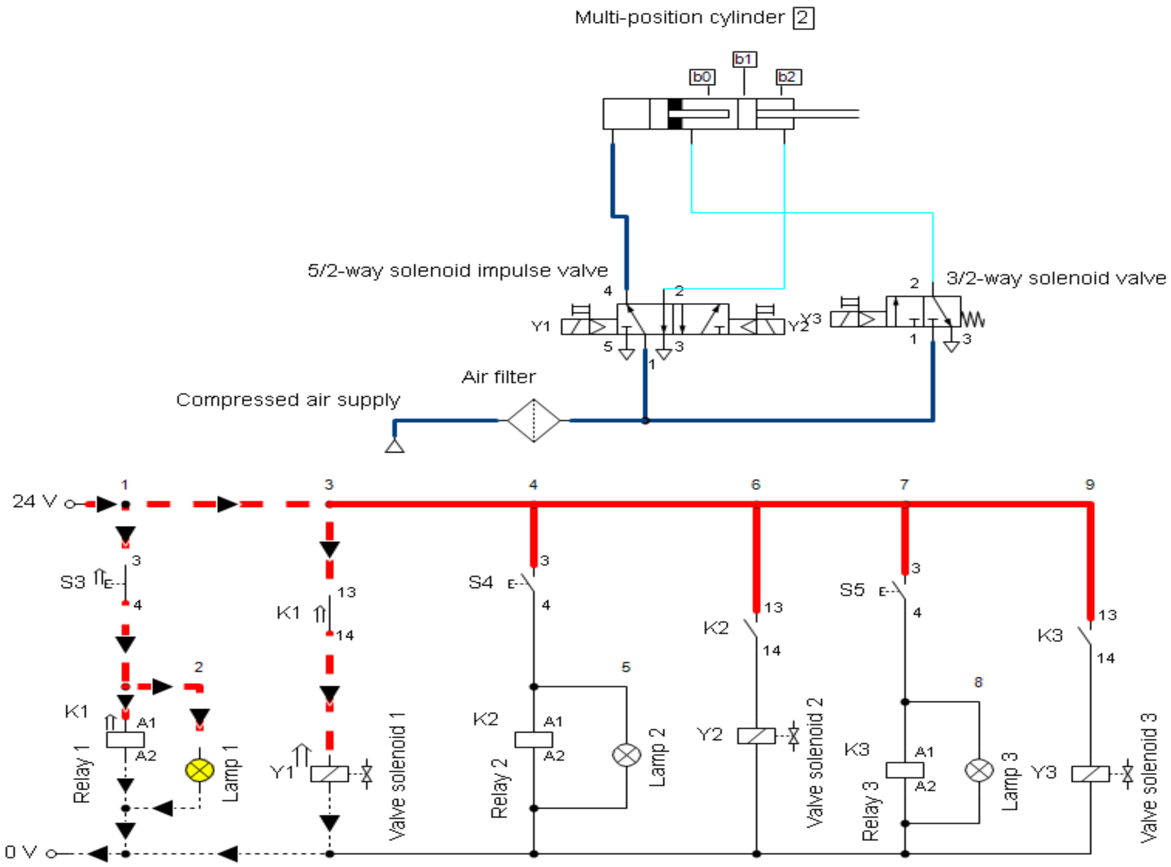

Fig. 8. Electro-pneumatic circuit using multi-position cylinder. Simulation I

If operator presses S4 button, both piston rods of the multi-position cylinder (2) move from point b1 to point b0 and lamp 2 shows green signal, Fig. 9.

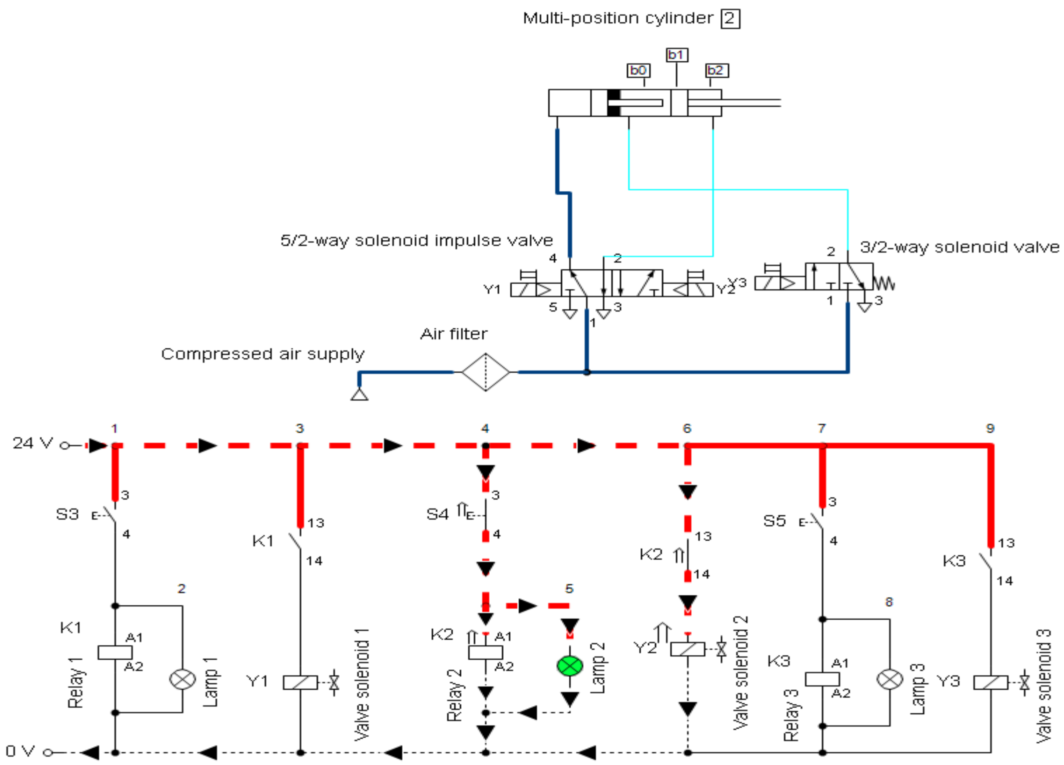

Fig. 9. Electro-pneumatic circuit using multi-position cylinder. Simulation II

Finally, if operator presses S5 button, the second piston rod of the multi-position cylinder (2) moves from point b1 to point b2. After that, this piston rod returns from point b2 to point b0, because of the spring of the 3/2 way solenoid valve and lamp 3 shows red signal, Fig. 10.

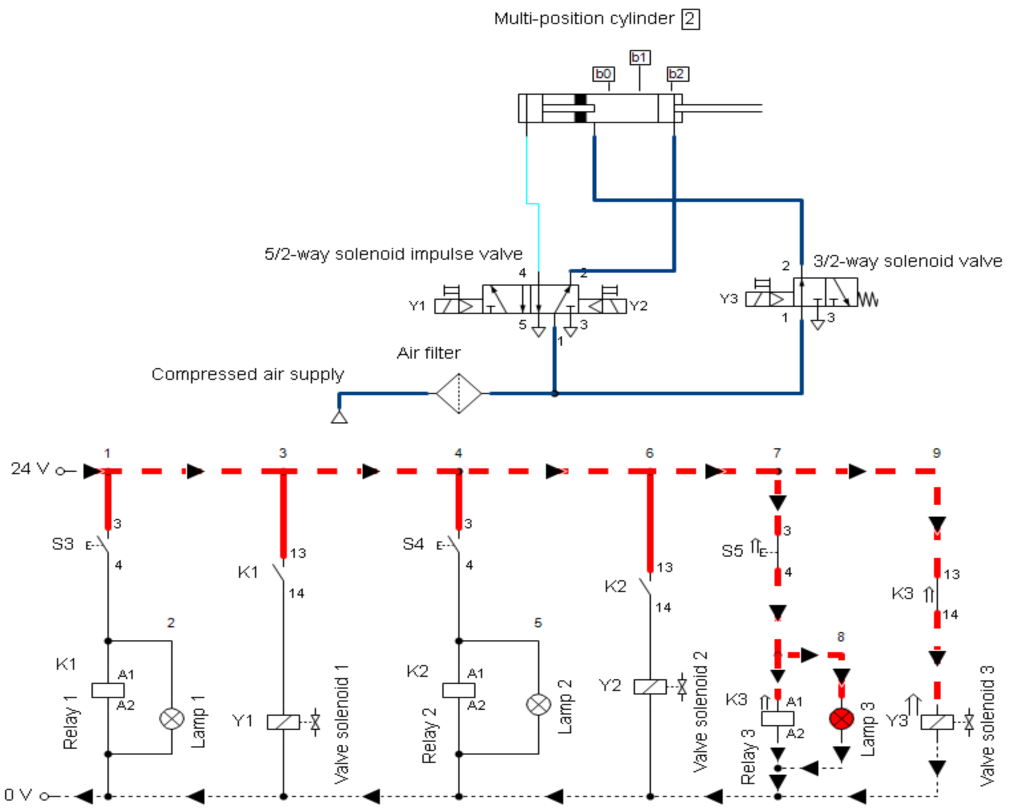

Fig. 10. Electro-pneumatic circuit using multi-position cylinder. Simulation III

3. Conclusions

The circuit schemes presented allow experimental verification of a multi-position cylinder. The main advantage of a multi-position cylinder is that this type of cylinder can use either one piston rod or both pistons rods. Using a single piston rod a small force is obtained in a reciprocating linear motion, but if a higher force is needed, then both pistons rods are used.
The presented pneumatic scheme has two simulations and the electro-pneumatic scheme has three simulations.
For a better choice of a multi-position cylinder in the design of pneumatic and electro-pneumatic installations, it is recommended that simulation methods should be used beforehand.

References

[1] www.festo.com.
[2] Figliolini, G., and P. Rea. “Design and test of pneumatic systems for production automation.” Paper presented at the 2004 Canadian Design Engineering Network (CDEN) Conference, Montreal, QC., Canada, July 29-30, 2004.
[3] Panaitescu, M., F.V. Panaitescu, and R.A. Dăineanu. “Analysis of Heat Flow and Transfer in The T Joint of a Steam Installation.” *Hidraulica Magazine*, no. 2 (June 2021): 29-41.
[4] Drumea, P., M. Blejan, L. Dumitrescu, M. Comes, I.C. Dutu, and I. Ilie. “Mechatronic system for air pressure control.” Paper presented at the 29th International Spring Seminar on Electronics Technology ISSE, St. Marienthal, Germany, May 10-14, 2006.
[5] Călimănescu, I., C.L. Dumitrache, and L. Grigorescu. “CFD analysis of a ball check microvalve.” Proc. *SPIE 9258 Advanced Topics in Optoelectronics, Microelectronics and Nanotechnologies VII* 9258 (February 2015): 570-575.

FLUIDAS

NATIONAL PROFESSIONAL ASSOCIATION OF HYDRAULICS AND PNEUMATICS IN ROMANIA

fluidas@fluidas.ro